FLORIDA STATE UNIVERSITY

COLLEGE OF ARTS AND SCIENCES

MEASUREMENT OF POLARIZATION OBSERVABLES IN VECTOR MESON PHOTOPRODUCTION USING A TRANSVERSELY-POLARIZED FROZEN-SPIN TARGET AND POLARIZED PHOTONS AT CLAS, JEFFERSON LAB

By

PRIYASHREE ROY

A Thesis submitted to the
Department of Physics
in partial fulfillment of the
requirements for the degree of
Doctor of Philosophy

2016

Priyashree Roy defended this thesis on November 01, 2016.
The members of the supervisory committee were:

Volker Crede

Professor Directing Dissertation

Tomasz Plewa

University Representative

Simon Capstick

Committee Member

Paul Eugenio

Committee Member

Harrison Prosper

Committee Member

The Graduate School has verified and approved the above-named committee members, and certifies that the thesis has been approved in accordance with university requirements.

"Our imagination is stretched to the utmost, not, as in fiction, to imagine things which are not really there, but just to comprehend those things which *are* there."

-Richard P. Feynman

ACKNOWLEDGMENTS

First off, I would like to thank my doctoral thesis advisor, Volker Crede, for being the best possible mentor one could ever wish for. His contribution in my professional as well as personal development goes beyond words. Apart from sharing his immense amount of knowledge in science, and providing me with a plethora of opportunities to further my career (such as providing me the opportunity to give many talks at conferences and collaboration meetings, writing recommendation letters, helping in establishing connections with other physicists etc.), he has inspired me to learn the art of enjoying life within as well as outside of the world of physics. Since doing a PhD takes a fairly long time, the work ethics and lifestyle of the mentor can potentially reflect in a significant way on his/her student's life. In this regard, I consider myself very fortunate to have worked with Volker, who has very strong work ethics and a very balanced lifestyle. I will certainly miss our (almost daily) conversations on a variety of interesting topics and the relaxed yet productive environment that he offers to his students. Many entertaining discussions on regular Friday lunches with him and the entire research group will always be remembered. None of this would have been possible without the tremendous support that I received from Simon Capstick and Laura Reina when I decided to switch my field of research from material science to hadronic physics. I owe a big thanks to them.

Many thanks to the hadronic physics group at Florida State University for their help in various ways. I would like to thank Paul Eugenio for involving me in the construction of a time-of-flight spectrometer for the GlueX experiment. It was very helpful in understanding how the detector works. Many thanks to Maurizio Bertoldi for training me in polishing the lightguides and wrapping the scintillators with ESR and tedlar. I am thankful to Alexander Ostrovidov for always resolving cluster-related issues at the earliest. I will always cherish the excellent camaraderie of my colleagues. I would like to thank Christopher Zeoli and Zulkaida Akbar for the many informative and motivating discussions which kept the enthusiasm up every day. Our group's company made the frequent twelve hour long drive to Jefferson Lab much less enduring. I am also very thankful to Sungkyun Park for bestowing many useful codes to me to help process the data and for his guidance during the initial years of my work. Many thanks to Andrew Wilson for sending replies to my queries about the Q-value method at his earliest. He helped me a lot with understanding the method. I would also like to thank the entire FROST-g9b run group for the constructive discussions every week about the

analysis. In particular, I would like to thank Eugene Pasyuk for providing valuable suggestions. I would also like to thank the CLAS-JLAB analysis review committee members: Kenneth Livingston, Veronique Ziegler and Evgeny Golovach, for spending a considerable amount of time to review my analysis. Many thanks to them for providing useful comments which helped in bringing the analysis to the finish line. I am very thankful to my dissertation committee members for taking time out from their busy schedule to consider this thesis. Special thanks to Simon Capstick for answering tons of questions that I asked while writing the section on theoretical predictions for the baryon spectrum.

A very important component of my life during the course of graduate studies was meeting many admirable people, some of whom, I hope, will remain life-long friends. Many thanks to Minseong Lee who taught me many important survival skills such as driving (a must in Florida), how to hold chopsticks to eat sushi, and many more. Many thanks also to Jonathan and Plamena for taking me to FSU musical shows and inviting me on every thanksgiving occasion. I am also very thankful to Zulkaida and Raditya for never giving up on insisting to join the international coffee hour gathering every Friday. I would like to thank Rebeka and Pampa for often taking out time from their busy schedule to come see me at my desk. I really appreciated it. Many thanks to Radhika and Daniel for being wonderful friends. I could not have explored Tallahassee without them. Also, due to our great team work in the kitchen every day, free food outside never tempted me. There are so many other people who came at different stages of my life as a graduate student to mould me into a better person. I am very thankful to each one of them.

Lastly but most importantly, I would like to thank my family for being my pillars of support. Heartiest thanks to my parents, Dev Dutta Roy and Baby Roy, for giving me the enthusiasm to live my dream and explore the world. My father was always deeply interested in fundamental science. His ideas and interesting conversations on a variety of scientific topics since my childhood days instilled interest in me for science. I would like to thank my mother for her love, kindness and always showing the bigger picture of life. Many thanks to my dear sisters, Priyamvada Roy and Indrika Roy, for believing in me. Finally, to Rakesh Yadav, no words can entirely express how thankful I am to you for always being there for me despite the distance for several years. Thank you so much for your love, valuable suggestions and immense support during tough times, and for rejoicing happy moments with me during good times.

TABLE OF CONTENTS

LIST OF TABLES

LIST OF FIGURES

ABSTRACT

The study of baryon resonances provides a deeper understanding of the strong interaction because the dynamics and relevant degrees of freedom hidden within them are reflected by the properties of the excited states of baryons. Higher-lying excited states at and above 1.7 GeV/c^2 are generally predicted to have strong couplings to final states involving a heavier meson, e. g. one of the vector mesons, ρ, ω, ϕ, as compared to a lighter pseudoscalar meson, e. g. π and η. Decays to the $\pi\pi N$ final states via $\pi\Delta$ also become more important through the population of intermediate resonances. We observe that nature invests in mass rather than momentum. The excited states of the nucleon are usually found as broadly overlapping resonances which may decay into a multitude of final states involving mesons and baryons. Polarization observables make it possible to isolate single-resonance contributions from other interference terms. The CLAS g9 (FROST) experiment, as part of the N^* spectroscopy program at Jefferson Laboratory, accumulated photoproduction data using circularly- & linearly-polarized photons incident on a transversely-polarized butanol target (g9b experiment) in the photon energy range $0.3 - 2.4$ GeV & $0.7 - 2.1$ GeV, respectively. In this work, the analysis of reactions and polarization observables which involve two charged pions, either in the fully exclusive reaction $\gamma p \to p\,\pi^+\pi^-$ or in the semi-exclusive reaction with a missing neutral pion, $\gamma p \to p\,\pi^+\pi^-\,(\pi^0)$ will be presented. For the reaction $\gamma p \to p\,\pi^+\pi^-$, eight polarization observables (I^s, I^c, P_x, P_y, $P^s_{x,\,y}$, $P^c_{x,\,y}$) have been extracted. The high statistics data rendered it possible to extract these observables in three dimensions. All of them are first-time measurements. The fairly good agreement of I^s and I^c obtained from this analysis with the experimental results from a previous CLAS experiment provides support for the first-time measurements. For the reaction $\gamma p \to p\omega \to p\,\pi^+\pi^-\,(\pi^0)$, five polarization observables (T, Σ, F, H, P) have been extracted, four of which are first-time measurements at all energies. This analysis thus represents a comprehensive program on vector-meson photoproduction: The ω is observed and studied directly from the data and the polarization observables for the (broad) ρ can be extracted from the double-pion reaction in a partial-wave analysis. The 13 polarization observables extracted in this analysis substantially augment the world database of polarization observables for these reactions and are expected to play a crucial role in identifying the contributing baryon resonances.

CHAPTER 1

INTRODUCTION

Developing an understanding of the myriad of natural phenomena around us is perhaps one of the most basic human instincts. There have been numerous situations in the past where the knowledge gained by such studies out of sheer inquisitiveness eventually became very useful for serving mankind. For example, until late 1600 electricity was mostly known out of intellectual curiosity. It was observed in nature in the form of lightning, numbing shocks from electric fish or sometimes (in case of static electricity) as a force of attraction when two objects were rubbed against each other. Now electricity has become the backbone of modern society. This and many other discoveries have shown time and again that although it can take a fairly long time to see the benefits of fundamental research, it is absolutely crucial for our development.

One of the forefronts of fundamental research at present is to understand the constituents of matter which we see everywhere around us. It is well known that the atomic nucleus consists of nucleons which are protons and neutrons. Numerous evidences have strongly suggested that these nucleons are made of quarks and gluons, however it is not clear how they interact to give rise to them. The theory which describes quark-gluon interactions, Quantum Chromodynamics (QCD), cannot be solved analytically in the low energy regime (non-perturbative regime) where the nucleons exist. Therefore, physicists resort to other tools to understand them. This chapter will provide a brief overview of QCD and a tool, namely baryon spectroscopy, utilized by physicists to get an insight into the basic properties of nucleons in the non-perturbative QCD regime. Furthermore, the absolute necessity to extract certain observables called 'polarization observables' in baryon spectroscopy will be explained. The motivation for extracting a set of these observables for ω and $\pi^+\pi^-$ photoproduction in this thesis will be discussed. It will be shown that this analysis will contribute significantly to the current status in our understanding of the resonant contributions to these reactions.

1.1 Quantum Chromodynamics

The universe consists of particles which interact with each other via force(s). Four fundamental forces have been observed in nature. They can be listed in an increasing order of their strength as follows: the gravitational force, the electroweak force, the electromagnetic force and the strong force. The electromagnetic force binds the constituents of an atom (electrons and the nucleus) together. The nucleus is further made of nucleons which are protons and neutrons. These sub-nuclear particles have been found to be a part of a big family of composite particles called 'hadrons' which were studied extensively since 1960's and, owing to their complexity, are a popular topic of research till date. It is now well established that hadrons are made of quarks (which are spin-1/2 fermions) and gluons (which are massless vector bosons). They interact via the strong force. The theoretical description of this force is given by a specific type of quantum field theory, known as Quantum Chromodynamics (QCD). The strong force is a short-range force which varies rapidly with distance. It exhibits two very peculiar features:

- Asymptotic freedom
- Confinement

Let us first discuss about asymptotic freedom. At short distances, or equivalently at high energies or momentum transfers Q, the quarks behave as if they are asymptotically free. This means that the strong coupling constant α_s, which is a measure of the strength of the strong force, vanishes asymptotically at short distances. This behavior of the strong force was first mathematically derived and thus discovered by David Gross and Frank Wilczek in 1973, and also independently by David Politzer in the same year. They received Nobel prize in 2004 for their extraordinary work. Note that asymptotic freedom could be mathematically derived since it occurs at high energies where QCD can be solved using perturbation theory. David Gross explained the mechanism using a simple analogy of magnetic screening [1]. Virtual quarks coming from quantum vacuum surround the bare quark and 'screen' or decrease the effective charge, analogous to diamagnets which 'screen' or decrease the applied external magnetic field. However, virtual gluons, being bosons, have the opposite effect. They 'anti-screen' or increase the effective charge, similar to paramagnets which align their magnetic dipoles parallel to the external field thereby increasing its strength. The effective charge is enhanced with larger distance as a thicker cloud of virtual gluons surrounding

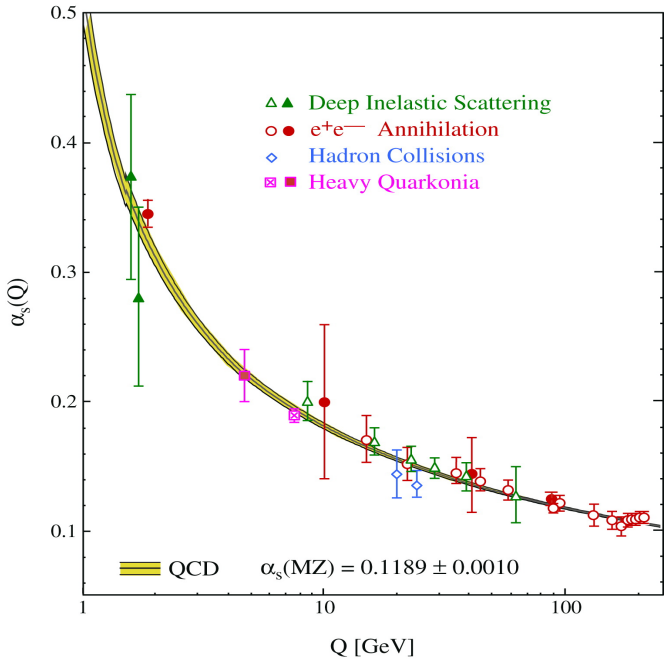

Figure 1.1: The strong coupling constant, α_s, as a function of the momentum transfer, Q, from different experiments. The open (closed) symbols represent α_s extracted from experimental measurements using next-to-leading (next-next-to-leading) order QCD calculations. The curves are the QCD predictions. The experimental results show evidence for asymptotic freedom at large momentum transfers (or short distances). Image source: [2].

the bare quark is created. This also means that the anti-screening effect decreases the effective charge (and hence the corresponding effective coupling) with shorter distances. The strong force is asymptotically free since the anti-screening effect of the virtual gluons overcomes the screening effect of the virtual quarks. This behavior has been experimentally confirmed in various high energy experiments as shown in Figure 1.1.

Quite opposite to asymptotic freedom, at large distances (or equivalently at low Q) the phenomenon of confinement is observed. In this energy regime, the quarks are so tightly bound to each other that they become inseparable. The amount of energy applied to separate the quarks within a hadron favors creation of new hadrons over isolation of the quarks. This happens in the non-perturbative energy regime where QCD cannot be analytically solved. Hence, no analytic proof for confinement of quarks exists at present. However, the concept of anti-screening, which was introduced to explain asymptotic freedom, also provides a good qualitative explanation for confinement. Frank Wilczek explained in his Nobel lecture that in the hypothetical situation where

we have an isolated quark, the energy of the cloud of virtual gluons surrounding the quark would keep increasing with distance due to anti-screening and diverge to infinity. This catastrophic divergence is prevented in reality by the presence of an antiquark whose anticloud overlaps with the quark's cloud in such a way that the total energy of the system stays finite. It is the phenomenon of confinement which gives stability to nucleons and nuclei in matter. At distances of the order of a femtometer, the strong force is approximately 137 times stronger than the electromagnetic force. Not only does this force bind the quarks and gluons very strongly at these distances, but in addition its residual effects also binds the protons and neutrons together within the nucleus. It is also worth mentioning here that although we cannot see free quarks in nature due to confinement, there are so many indirect evidences for their existence that they are considered as 'real' as electrons.

QCD, the theory of strong interaction, is in some respects similar to Quantum Electrodynamics (QED), the theory of electromagnetic interaction. For instance, each quark also has an antiquark (antiparticle of quark), just as a positron is the antiparticle of an electron. Gluons serve as the mediators of the strong interaction, similar to photons which are the mediators of the electromagnetic interaction. Furthermore, similar to the electric charge in QED, we have 'color charge' in QCD. Each quark carries a color charge and each antiquark carries an anti-color charge.

However, there are certain differences which make QCD much more complex than QED. A fundamental difference between QCD and QED is that in addition to quarks, gluons also carry color charge, whereas photons do not carry any electric charge. Therefore, gluons participate in the strong interaction in addition to mediating it unlike photons in QED. We have seen earlier that since virtual gluons in the quantum vacuum carry color charge they can influence the effective color charge, and since they are bosons they anti-screen the color charge. Without this property of the gluons the phenomena of confinement and asymptotic freedom would not have been observed in nature! Furthermore, unlike one electric charge in QED, there are three color charges. While the electric charge of a charged particle can be measured, the color charge of a color-charged particle cannot be measured due to confinement. The three color charges (anti-charges) are referred to as red (anti-red), green (anti-green) and blue (anti-blue); however it should be noted here that these charges are completely unrelated to the three primary colors of vision. These names are merely used to comprehend the idea of observing only 'color-neutral' hadrons. To explain this further, it is necessary to mention that all hadrons have the following components:

- a set of bare quarks which determine the quantum numbers of the hadron. They are called as 'valence' quarks,
- the gluons which are the quanta of the color field,
- an infinite number of bare quark-antiquark pairs which do not contribute to the quantum numbers of the hadron. They can be created from the quantum vacuum as well as from gluons. These quarks (antiquarks) are referred to as 'sea' quarks (antiquarks).

Based on the number of valence quarks, all established hadrons can be broadly classified into two groups : baryons and mesons. A baryon is a system of three valence quarks carrying a red, a green and a blue color, respectively to make it overall color-neutral. This is loosely analogous to a mixture of the three primary colors of vision which results in an overall 'white or colorless' state. The lowest mass baryons are the proton and the neutron. A meson is a system of a valence quark and a valence antiquark carrying a color and the corresponding anti-color, respectively in order to make it color-neutral. The lowest mass meson observed in nature is the pion.

1.2 Hadron Properties and Nomenclature

Hadrons are named based on their mass and a set of associated quantum numbers which describe their properties. These quantum numbers are the isospin I, the flavor quantum number, the total angular momentum quantum number J, the parity P and the charge conjugation quantum number C (for neutral mesons). The isospin quantum number tells us how many different charged states of the same particle (that is, the same mass, spin and parity) exist. For an isospin I, $(2I + 1)$ states, or equivalently third components of isospin (I_z), exist. For example, the nucleon has isospin $I = 1/2$ with the proton and the neutron as the two isopin projections.

The flavor quantum number refers to the quark content. Six quarks have been identified in nature and each of them has a unique flavor. By convention, the flavor quantum number is assigned the same sign as the electric charge of the quark:

- The up quark, denoted as u, has electric charge $= +2/3$ times the electron charge e. It has $I_z = 1/2$, as its flavor.
- The down quark, denoted as d, has charge$= -1/3\,(e)$. It is the isospin partner of the u quark and hence it has $I_z = -1/2$ as its flavor.

- The strange quark, s, has *strangeness* as its flavor. Each strange quark carries charge= $-1/3\,(e)$ and hence *strangeness* $S = -1$.
- The flavor for the charm quark, c, is its *charmness* C. The charge of the c quark is $+2/3\,(e)$ and hence $C = +1$.
- The flavor for the top quark, t, is its *topness* T. It carries a charge= $+2/3\,(e)$ and flavor $T = +1$.
- The bottom quark, b, has $-1/3\,(e)$ as its electric charge and *bottomness* $B = -1$ as its flavor.

Gluons do not carry any flavor, i.e. they are flavor neutral. Therefore, the strong force depends only on color and is flavor blind. The quarks u, d and s are usually referred to as 'light quarks' since they are the three lowest mass quarks among the six quarks. The other three quarks, c, b and t, are much heavier and are referred to as 'heavy quarks'. In this thesis, we will only work with light hadrons made of u and d quarks. Note that since free quarks do not exist in nature, the quark masses are merely parameters and their values depend on the method which is used to extract them from hadronic properties. The conventional values of mass quoted for the (bare) quarks accounts for only $\sim 1-3\%$ of the hadron mass. The rest of the mass comes from the energy of the color field.

The total angular momentum $\vec{J}$ is a vector sum of the orbital angular momentum $\vec{L}$ and the total spin $\vec{S}$. Therefore, the quantum number J can take values $|L-S|$, $|L-S+1|$, ... $|L+S-1|$, $|L+S|$. A meson can have spin $S = 0$ (when the quark and antiquark are anti-aligned), or 1 (when they are aligned). Thus, we see that mesons are bosons. A baryon can have spin $3/2$ when all three quark spins are aligned, or $1/2$ when one of the three quarks is anti-aligned. Thus, baryons are fermions.

The parity operator leads to an inversion of the spatial coordinates. For hadrons, the parity quantum number P serves as a good quantum number. It can have only two values, 1 or -1. If the state is invariant under spatial inversion, then $P = +1$ and the state is said to have 'even' parity. A state with $P = -1$ is said to have 'odd' parity. The parity of hadrons depends on L. For baryons, $P = (-1)^L$. Hence, the ground state baryons ($L = 0$) have '+' parity. For mesons, there is an additional factor of -1 since its quark and antiquark have opposite parities. Therefore, mesons have parity $P = (-1)^{L+1}$. The quantum numbers J and P can be experimentally measured. L and S can be inferred from them using the above relations.

Table 1.1: Light meson nomenclature based on their properties.

$q\bar{q}$ content & isospin	$^{2S+1}L_J =$ $PC =$	$^{1}_{(L\,\text{even})_J}$ $-+$	$^{1}_{(L\,\text{odd})_J}$ $+-$	$^{3}_{(L\,\text{even})_J}$ $--$	$^{3}_{(L\,\text{odd})_J}$ $++$
$u\bar{d}$, $u\bar{u} - d\bar{d}$, $d\bar{u}$ $(I = 1)$		π	b	ρ	a
$d\bar{d} + u\bar{u}$ and/or $s\bar{s}$ $(I = 0)$		η, η'	h, h'	ω, ϕ	f, f'

Another important operator is the particle-antiparticle conjugation. This operator changes the state of a particle to its antiparticle without changing the spatial and time coordinates. Therefore, it is also known as the charge conjugation operator. Among hadrons, it serves as a good quantum number only for neutral mesons. Its value is given by $C = (-1)^{L+S}$ where L and S are the orbital angular momentum and the spin quantum number, respectively of the neutral meson.

With the above knowledge about the quantum numbers, we can now understand the nomenclature for hadrons. For a meson, its mass, quark content and quantum numbers I, J^{PC} are sufficient to give it an unambiguous symbol. The mass (in MeV/c^2) is written in parentheses for mesons which decay strongly. However, it is omitted for the lightest meson resonances. Table 1.1 shows the nomenclature for the light mesons based on these properties. The mesons relevant for this thesis are the pions denoted as π (mass $\sim$ 140 MeV/c^2, $J^{PC} = 0^{-+}$), the ω meson (mass = 782 MeV/c^2, $J^{PC} = 1^{--}$), the ρ meson (mass = 770 MeV/c^2, $J^{PC} = 1^{--}$) and the η meson (mass = 547 MeV/c^2, $J^{PC} = 0^{-+}$). The ω and ρ mesons are examples of 'vector mesons', that is, mesons which have $J^{PC} = 1^{--}$. Note that the photon has the same J^{PC}.

For a baryon, the symbol is based on the isospin and the quark content. In this thesis, only baryons made of three u and/or d quarks are relevant. Those with isospin $I = 1/2$ are labeled as 'N' states and those with $I = 3/2$ are referred to as 'Δ' states. If the baryon decays strongly, its mass (in MeV/c^2) is written in parentheses together with the symbol. The quantum numbers J^P are also specified in the name. For example, the first excited state of the proton is the *Roper* resonance, denoted as $N(1440)1/2^+$. Here, 1440 MeV/c^2 is the mass and $1/2^+$ is the value of J^P of the resonance, and N denotes that it has $I = 1/2$. For completeness of light baryon nomenclature (i.e. baryons made of u, d and/or s quarks), the symbols for light baryons containing s quarks will be mentioned. If the baryon has one s quark, it is denoted by Λ (or Σ) symbol if the isopin is 0

(or 1). If the baryon has two s quarks, it is denoted by Ξ symbol. Such baryons have $I = 1/2$. A baryon with three s quarks is labeled as Ω. It has $I = 0$.

It is also worth mentioning here that in a strong interaction, P, I, C and all universal quantities associated with the system are conserved, such as the energy, linear and angular momentum, electric charge and baryon number of the system. The baryon number is given by $B =$ number of baryons $-$ number of antibaryons. The strong interactions which have been studied in details in this work are $\gamma p \to p\pi^+\pi^-$ and $\gamma p \to p\omega$ where ω decays strongly to $\pi^+\pi^-\pi^0$.

1.3 Baryon Spectroscopy

An intriguing question which remains unanswered in the non-perturbative QCD regime is how do quark-gluon interactions give rise to the excited states of hadrons? This leads to further questions such as what is the origin of confinement? What are the relevant degrees of freedom in excited hadrons and how do they evolve with energy? Since it is very difficult to solve QCD analytically in this energy regime, physicists use other smart tools to seek answers to these questions. One such essential tool is the spectroscopy of baryons, which means mapping out the excited states (also known as resonances) and studying them. Spectroscopy has played a vital role in our understanding of the atomic structure and its properties. While the basic idea in baryon spectroscopy is the same as atomic spectroscopy, it turns out that the former is much more complex than the latter, as we shall see later in this Chapter. Reference [3] provides a nice overview of the theoretical as well as experimental advances in our understanding of the light baryon spectrum.

From the baryon spectrum, the underlying symmetry can be revealed in the form of multiplets, for ground states as well as excited states. For example, the ground state mesons can be grouped into nonets (i.e. a group of nine states). Pions are a part of the pseudoscalar nonet (that is, $J^P = 0^-$) as shown in Figure 1.2 (left). The ρ meson and ω meson are a part of the vector meson ($J^P = 1^-$) nonet (Figure 1.2 (right)). The ground state baryons with $J^P = \frac{1}{2}^+$, such as the proton and the neutron, form an octet (i.e. eight members) and the $J^P = \frac{3}{2}^+$ baryons form a decuplet (i.e. 10 members). These are shown in Figure 1.3. The excited states can be grouped into various *supermultiplets*, as we shall see in the next section. The type of grouping gives an insight into the effective degrees of freedom of the system as well as provides clues for possible missing members of the multiplets. A perfect example is the prediction for the existence of the Ω baryon which was the

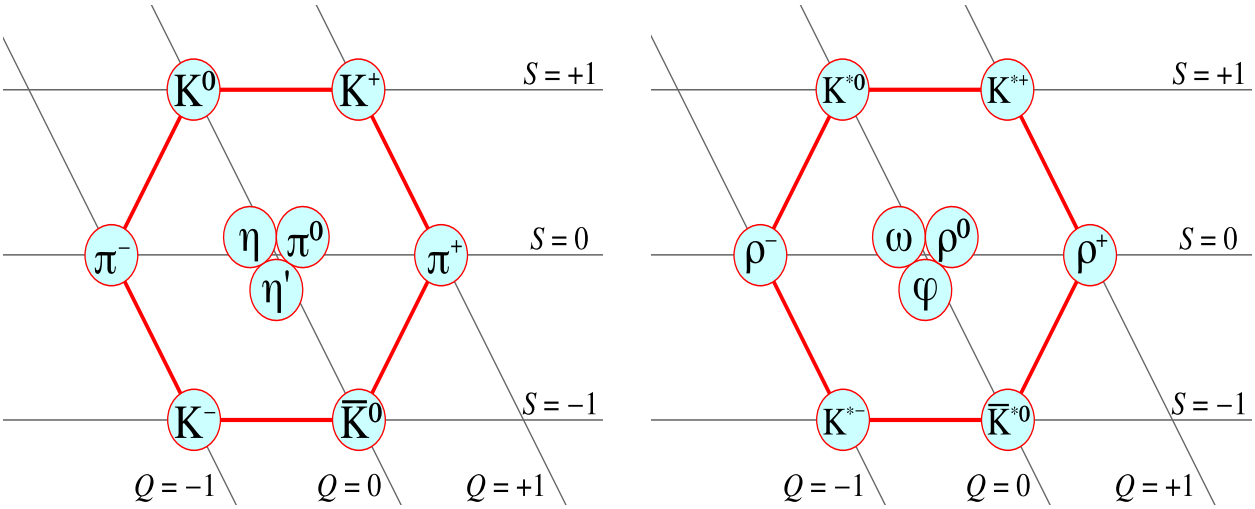

Figure 1.2: The ground state nonets for pseudoscalar mesons (left) and vector mesons (right). The symbol S denotes the strangeness and Q denotes the electric charge.

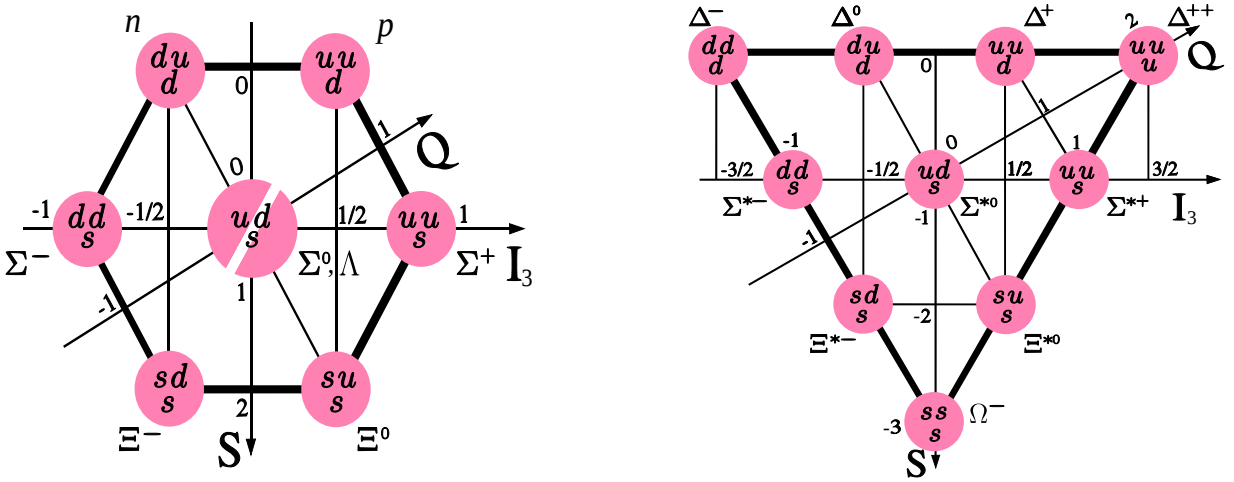

Figure 1.3: The baryon octet for spin-1/2 ground state baryons (left) and the baryon decuplet for spin-3/2 ground state baryons (right). Here, I_3 refers to the third component of isospin, S refers to the strangeness and Q refers to the electric charge.

only missing state of the ground state decuplet. The existence of the baryon was later confirmed experimentally.

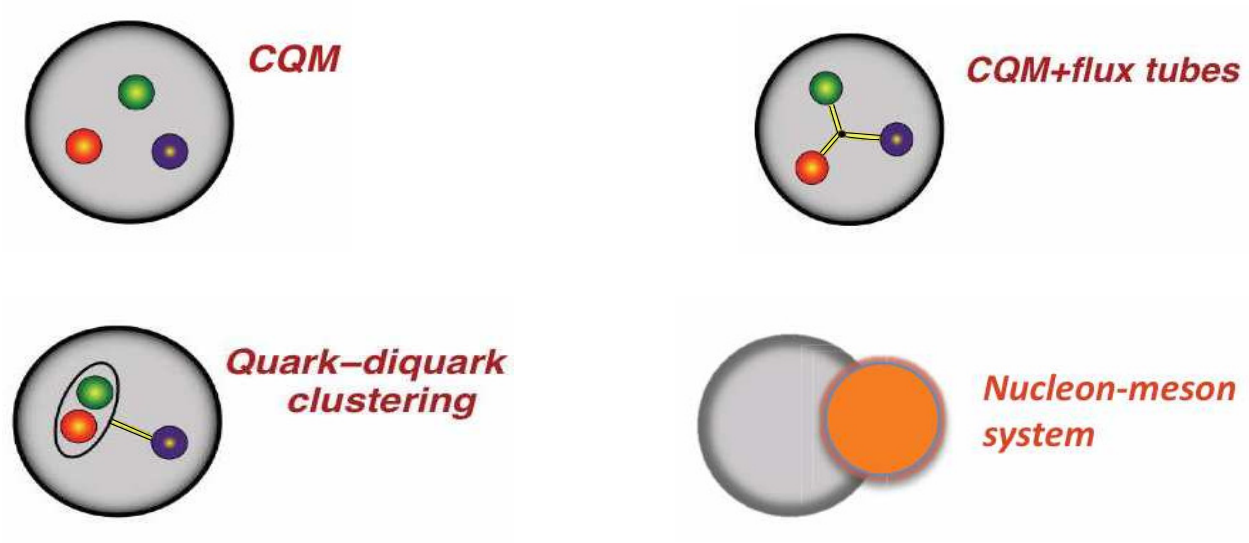

Figure 1.4: The figure shows various proposed pictures to describe the effective degrees of freedom in the excited states of baryons. They are the Constituent Quark Model (top left), the Constituent Quark Model with gluonic excitations (top right), the *static* quark-diquark model where a fixed pair of quarks remains static with respect to each other (bottom left), and the interaction of the ground state baryon with meson(s) (bottom right).

Baryon spectrum cannot be predicted by using pertubation theory. Therefore, phenomenological models and QCD-based lattice calculations are developed for theoretical understanding. An important point to note is that the full wave function of the baryon is given by:

$$\Psi = \Psi_{color}\,\Psi_{spin}\,\Psi_{space}\,\Psi_{flavor}. \tag{1.1}$$

Since all observed baryons are color singlet states, the color part of the wave function is always antisymmetric. This implies that the remaining part of the wave function, $\Psi_{spin}\,\Psi_{space}\,\Psi_{flavor}$, must be symmetric. All model descriptions and theoretical calculations incorporate this symmetry. Figure 1.4 shows various phenomenological models which have been proposed for describing the effective degrees of freedom in excited baryons and predicting the spectrum. They will be discussed briefly here.

The Constituent Quark Model (CQM): In this model (Figure 1.4 (top left)), the nucleon is considered as a system of only three 'constituent quarks' and nothing else. These quarks describe

the effective degrees of freedom of the system. The constituent quarks are essentially valence quarks 'dressed' with a cloud of the sea quark-antiquark pairs and gluons, such that sum of the masses of the constituent quarks becomes equal to the mass of the hadron. The interaction between the constituent quarks is model dependent. As an example, theoretical predictions from a Constituent Quark Model will be discussed in the next section.

CQM with Gluonic Excitations: In addition to the constituent quarks, gluons can also contribute to the effective degrees of freedom since they also carry color charge. Figure 1.4 (top right) depicts such a case. This approach leads to a higher density of excited states above $\sim$ 2 GeV than the Constituent Quark Model without any gluonic excitation. Hadrons with gluonic excitations are generally referred to as 'hybrid hadrons'. Observing such states in nature will give evidence for physics beyond the conventional quark model. Unfortunately, it is extremely difficult to identify hybrid baryons owing to the fact that they carry the same quantum numbers as the conventional qqq states. However, hybrid mesons can have exotic J^{PC}, thus providing an opportunity to unambiguously search for such states. Examples are 0^{--}, 0^{+-}, 1^{-+}, 2^{+-} and so on. These J^{PC} cannot be obtained if we follow the rules outlined in Section 1.2 for $q\bar{q}$ states. At present, the evidence for exotic mesons is weak at best. The GlueX experiment at Jefferson Lab is a dedicated experiment which aims at searching for and studying the properties of the exotic mesons.

The Static Quark-Diquark Model: Contrary to the above picture, one can imagine another modification of the Constituent Quark Model in which two of the three constituent quarks are 'frozen' with respect to each other, thereby reducing the effective degrees of freedom from three to two [4]. If the pair of 'frozen' quarks does not change with time, then such a description is referred to as the *static* quark-diquark picture (see Figure 1.4 (bottom left)). In this picture, calculations are simpler and there are fewer excited states above $\sim$ 1.7 GeV than what is predicted by the three-body system of the constituent quarks. However, some well known resonances cannot be accommodated in this picture, as we shall see in the next section.

Dynamically Generated Resonances: Another possible way of understanding the excited states is that they are dynamically generated by interactions between the ground state of the baryon and a meson or mesons [5]. For example, it is known that the energy difference between the first excited state of the proton, $N(1440)1/2^+$, and the ground state is about 500 MeV. This energy

can easily be imparted by a pion or two as it requires only $140 - 280$ MeV to create them. These pions can form a bound state with the baryon as shown in Figure 1.4 (bottom right). Such a state can be called as a dynamically generated excited state or resonance. Some resonances have been generated this way, such as the $N(1535)1/2^-$ and $N(1710)1/2^+$. The interpretation of the $N(1535)1/2^-$ resonance as being dynamically generated has gained preference over the quark model picture owing to the failure of the latter in explaining the unusually large coupling of this resonance to the $N\,\eta$ decay mode.

Lattice-QCD Calculations: An approach complementary to the phenomenological models is the *ab initio* computation within lattice-QCD, which is a discretized version of QCD. This method is gaining momentum with recent technological advances in computation as well as in lattice gauge theory. Lattice QCD uses a finite number of points in a Euclidean space lattice with periodic boundary conditions [3]. The quark fields are defined at lattice sites while the gluon fields are defined on the links between the lattice sites.

Three main factors which increase the computation time significantly are: reducing the lattice spacing, increasing the box-size and decreasing the quark masses. In fact, the computation time increases exponentially with the quark masses. The finite spacing introduces an ultraviolet cut-off for the momentum which is inversely proportional to the spacing, while the finite box-size introduces an infrared cut-off. Any result obtained on the discrete lattice is extrapolated to the continuum limit of infinite box-size and zero lattice spacing. The latter is done by tuning the bare coupling constant to zero according to the renormalization group. Due to computational limitations, the calculations are done at present with light quark masses that lead to a significantly higher pion mass. With further advancement in technology, getting an accurate prediction for the spectrum based on QCD using realistic pion masses will become feasible. Having a well-mapped baryon spectrum from experiments by that time will prove very useful in testing QCD in the non-perturbative regime.

1.3.1 Predictions for the Baryon Spectrum

The most prevalent phenomenological approach has been the Constituent Quark Models. There are various ways to describe the spin-dependent part of the inter-quark potential, such as using one-gluon exchange, instanton exchange or meson exchange mechanism. An example of a model based on one-gluon exchange is discussed in [6]. In this model, the spin-independent part of the

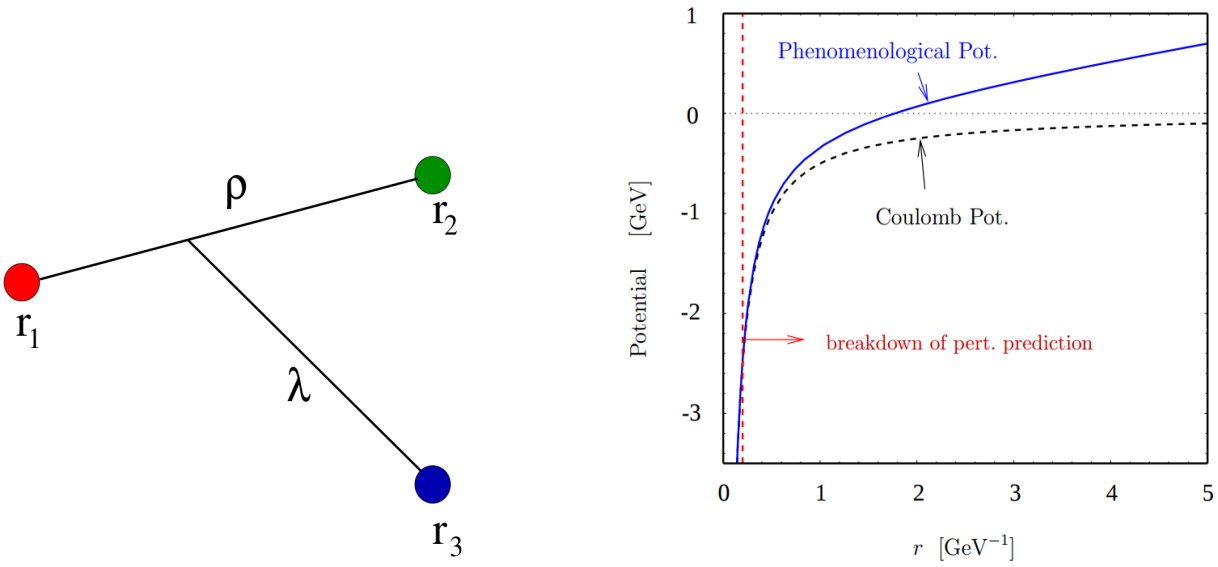

Figure 1.5: Description of a baryon in a Constituent Quark Model [6]. The spatial part of the wave function of the three-body system was described in terms of two harmonic oscillators, ρ and λ (left). The spin-independent part of the potential was defined as a combination of a linear positive potential at large distances to incorporate the phenomena of confinement, and a Coulomb potential to express the attractive behavior at short distances (right).

potential was approximated by a Coulomb and a linear form, as shown in Figure 1.5 (right). The divergence of the Coulomb potential to negative infinity was prevented by defining a finite size for the constituent quarks. The model was semi-relativistic, that is, the kinetic energies of the constituent quarks were treated relativistically, but Lorentz covariance was not imposed. The spatial part of the wave function was described in terms of two harmonic oscillators, ρ and λ as shown in Figure 1.5 (left). The ρ oscillator described the relative motion between quarks 1 and 2, whereas the λ oscillator described the motion of quark 3 relative to the (1, 2) quark pair.

Figure 1.6 shows predictions for the N^* spectrum using this model. The spectrum exhibits two main features. The first feature is that the excited states can be assigned to various multiplets, as mentioned in the previous section. The resonances can be classified into different excitation bands based on the quanta of excitation. These classifications are discussed in details in [3]. Each band can have a number of spin-flavor $SU(6)$ multiplets (where the degree 'six' comes from two spin

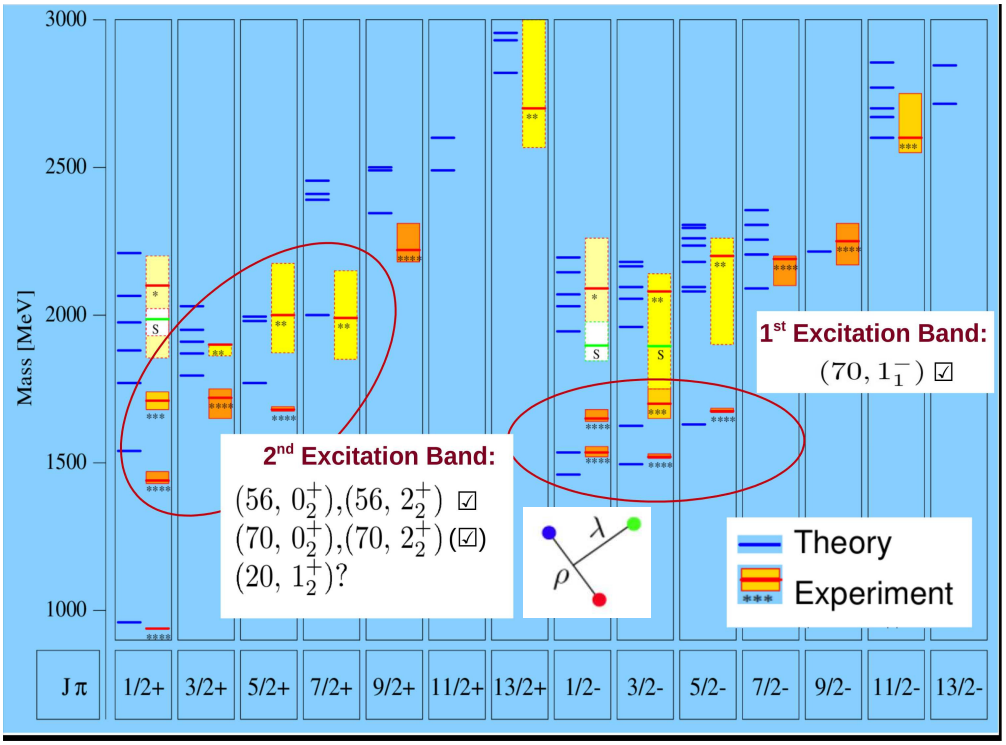

Figure 1.6: Predictions for the N^* spectrum from a Constituent Quark Model using one-gluon-exchange mechanism [6]. The left half of the picture shows states with + parity while the right half shows states with − parity, with $J_{\max} = 13/2$ for both parities. The blue lines represent the predicted states. The red lines represent the experimentally observed states and the height of the colored blocks corresponds to the uncertainties in the determination of their masses. The star-rating (as of 2010) below each red line is assigned based on the strength of evidence available for these states [7]; the number of $*$'s ranging from one for a poorly-known resonance to four for an established resonance. Different colors (for the blocks) have been used for different $*$ ratings to facilitate the identification of the poorly-known states and the well-known states. The nucleon ground state can be seen in the $J\,\pi = 1/2+$ column at 938 MeV/c^2. Two main features are seen from picture: 1) the states can be grouped into various supermultiplets, such as 56plets and 70plets, and 2) many predicted states above $\sim$ 1.7 GeV/c^2 have not been experimentally observed. Further details are discussed in the text.

projections and three flavors for light quarks). The possible supermultiplets are:

$$\mathbf{6} \otimes \mathbf{6} \otimes \mathbf{6} = \mathbf{56} \oplus \mathbf{70} \oplus \mathbf{70} \oplus \mathbf{20}. \tag{1.2}$$

The supermultiplets are specified by $(\mathbf{D}, L^P_N)$, where $\mathbf{D}$ represents the dimensionality, which is **56**, **70** or **20** in this discussion, L is the total angular momentum, N is the quanta of excitation and P is the parity. Each supermultiplet can, in turn, be decomposed into $SU(3)$ multiplets which are

the decuplets and the octets:

$$\begin{aligned} \mathbf{56} &= {}^4\mathbf{10} \oplus {}^2\mathbf{8}\,, \\ \mathbf{70} &= {}^2\mathbf{10} \oplus {}^4\mathbf{8} \oplus {}^2\mathbf{8} \oplus {}^2\mathbf{1}\,, \\ \mathbf{20} &= {}^2\mathbf{8} \oplus {}^4\mathbf{1}\,, \end{aligned} \tag{1.3}$$

where the superscript gives the total number of spin projections, $(2S+1)$, for each member of the $SU(3)$ multiplets. As we know from Section 1.2, for baryons S can take values 1/2 or 3/2 with two or four spin projections, respectively. Thus, Equation 1.3 shows, for example, that the **56**plet consists of 10 members, each having four spin projections, and eight members, each having two spin projections, leading to a total of 56 states. Furthermore, as we can see from Figure 1.3, each octet has one N, one Σ, one Λ and one Ξ state, amounting to a total of eight members if we include their isospin partners. Similarly, the decuplet consists of isospin projections of one Δ, one Σ, one Ξ and one Ω state. A supermultiplet is considered as completely filled if the underlying $SU(3)$ multiplets can be filled with the above mentioned states (which should also be experimentally confirmed) without ambiguity.

Excitation band 0: this corresponds to the ground state. It has one supermultiplet, $(\mathbf{56}, 0_0^+)$. The associated octet and decuplet are shown in Figure 1.3. This supermultiplet is completely filled.

Excitation band 1: this band has one quantum of angular excitation which is carried by either the λ or the ρ oscillator (Figure 1.5 (left)). It contains one supermultiplet, $(\mathbf{70}, 1_1^-)$. Since $L = 1$, the parity is $P = -1$. The possible values for J are (1/2, 3/2) for $L = 1$ and $S = 1/2$. These states are members of the ${}^2\mathbf{10}$, ${}^2\mathbf{8}$ or ${}^2\mathbf{1}$ multiplets of the **70**plet (see Equation 1.3). For example, $N(1535)1/2^-$ can be assigned to ${}^2\mathbf{8}$ and $\Delta(1620)1/2^-$ belongs to the ${}^2\mathbf{10}$ multiplet. Similarly, J can be (1/2, 3/2, 5/2) for $L = 1$ and $S = 3/2$. Such states are assigned to the octet, ${}^4\mathbf{8}$. An example is the state $N(1675)5/2^-$. Figure 1.6 shows the members of the band. The supermultiplet has been filled with N and Δ states, but filling the strange members remains difficult due to ambiguities in the assignment, poor evidence or unknown quantum numbers of the states.

Excitation band 2: This band can have one quantum of radial excitation. The corresponding supermultiplet is $(\mathbf{56}, 0_2^+)$. In this case, $L = 0$ and $P = +$. The Roper resonance, $N(1440)1/2^+$, is a member of the **56**plet. Another possibility is that one oscillator carries both quanta of excitation. Such states belong to $(\mathbf{56}, 2_2^+)$. Therefore, $L = 2$ and $P = (-1)^L = +$. This multiplet can be

completely filled with known N and Δ states, however the assignment is speculative. In addition, some of the strange members are missing.

It is also possible that both λ and ρ oscillators carry one quantum of angular excitation each. This gives $L = 0, 1, 2$. The corresponding multiplets are $(\mathbf{70}, 0_2^+)$, $(\mathbf{20}, 1_2^+)$ and $(\mathbf{70}, 2_2^+)$. It is interesting to observe that these multiplets are not consistent with the static quark-diquark picture since both oscillators need to be excited. In particular, $(\mathbf{20}, 1_2^+)$ is theoretically completely inconsistent. At present, it is possible to assign only two N states to this multiplet, but the assignment is merely an educated guess and the evidence for these two states is weak. The $(\mathbf{70}, 2_2^+)$ members have given some insight into the effective degrees of freedom. Recently, strong evidence was found for the resonance $N(1900)3/2^+$ [8],[9] and therefore it was promoted from $(**)$ to $(***)$ rating in 2012. This resonance can be assigned as member of a quartet of the $(\mathbf{70}, 2_2^+)$ multiplet, with the other three members being $N(1880)1/2^+$, $N(2000)5/2^+$ and $N(1990)7/2^+$. All of them are inconsistent with the static diquark model. Further evidence in support of the interpretation of the quartet as being resonances with both oscillators excited was reported in a recent study of the $\gamma p \to p\pi^0\pi^0$ reaction [10].

The second feature which stands out from Figure 1.6 is the overall comparison of the predictions with experimental measurements at low and high energies. We see that the number of experimentally observed states below $\sim$ 1.7 GeV/c^2 almost matches the number of predicted states. The masses, however, do not agree very well for some resonances, such as the Roper resonance. The predicted mass is significantly higher than the experimentally observed value, and the situation does not change much on using different exchange mechanisms between the constituent quarks. Recently, results from an experiment for π electroproduction on a proton suggested an interpretation for the state beyond the quark model. They observed that the state has strong contributions from the meson-baryon cloud at low momentum transfers (or large distances) [11]. It is also interesting to note that while the Constituent Quark Model provides a fairly good description of the light baryon spectrum at low energies, it predicts many more states than what we have experimentally observed at energies above 1.7 GeV. In fact, all phenomenological models, except for the static quark-diquark model, predict many more states at high energies than what has been experimentally observed so far.

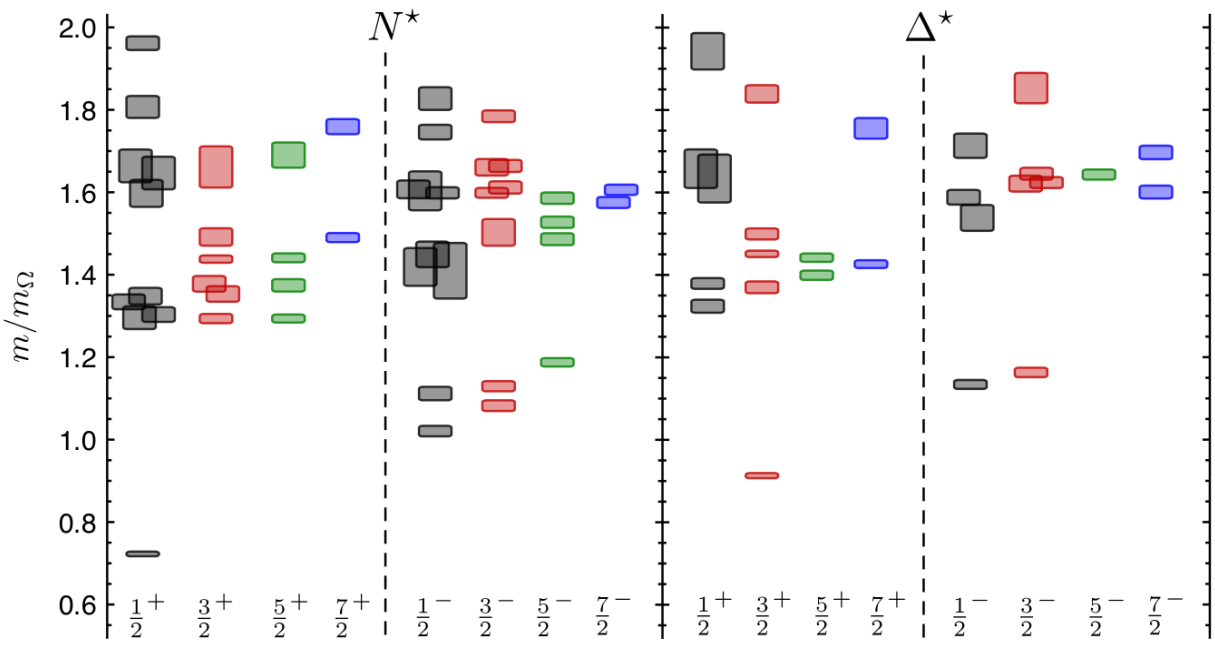

Figure 1.7: A lattice QCD prediction of the N and Δ spectrum, for $+$ as well as $-$ parities and J up to 7/2. The calculation was performed at a pion mass of 396 MeV/c^2. Image source: [12].

Lattice-QCD predictions have the advantage that they are calculated from first principles unlike the phenomenological models. A recent prediction for the light baryon spectrum, published in reference [12], is shown in Figure 1.7. It was obtained at $m_\pi = 396$ MeV/c^2. The lattice spacing in this calculation was ~ 0.123 fm and the box-size was ~ 2 fm. Even at a large pion mass, the spectrum exhibits $SU(6) \otimes O(3)$ symmetry, which is consistent with non-relativistic CQM. Furthermore, the number of low lying negative parity states as well as the first excited positive parity states matches CQM predictions. Overall, the lattice-QCD calculations also predict more resonances than experimental observations. Moreover, there does not appear to be any 'freezing' of the degrees of freedom as suggested in the static quark-diquark picture.

The above discussion clearly shows that most model-based as well as lattice-QCD calculations predict many resonances which remain experimentally undiscovered, especially at energies above 1.7 GeV. The idea of explaining this feature with the static quark-diquark model is fading away in the wake of experimentally finding resonances which are inconsistent with this picture and the lack of any sign of 'freezing' in recent lattice-QCD calculations.

An alternative explanation from the experimental aspect has been suggested, which is that these *missing* states perhaps do not couple strongly to the probes that have been predominantly used for spectroscopy. The known resonances have mostly come from πN scattering experiments. Photoproduction experiments have been conducted in the past, however they have mostly covered the energy regime below 1.7 GeV in center-of-mass. Moreover, most of the past analyses have focused on two body final states with light mesons, such as $p\pi$, $p\eta$ etc. It is predicted that the missing resonances predominantly couple to photon-induced reactions. They are also predicted to primarily decay through reactions that invest in mass rather than momentum, such as decays to multiparticle final states through the population of intermediate resonances, or decays to two-body final states involving heavier mesons (e.g. $p\omega$, $p\rho$) rather than the light mesons. These factors are the prime motivations for studying photon-induced reactions with $p\pi^+\pi^-$ and $p\omega$ final states at high energies in this analysis.

1.3.2 The Experimental Challenges in Baryon Spectroscopy

From an experimental point-of-view, finding the excited states of a baryon is much more challenging than finding atomic states. First off, baryon resonances are more unstable than atomic resonances, with the typical lifetime being of the order of 10^{-24} s for a strongly decaying resonance. This results in a large ΔE or width of the baryon resonance following Heisenberg's uncertainty principle:

$$\Delta E\,\Delta t \geq \hbar \tag{1.4}$$

From the above equation, the width comes out to be the order of 100 MeV which is larger than the average separation between the baryon resonances, thereby leading to highly overlapping states. The situation worsens as we go to higher energies. Figure 1.8 demonstrates the sharp contrast between an atomic and a baryonic cross section[1]. The latter cross section is shown for the πp scattering process. While all atomic resonances (shown in the top plot) are very narrow and thus can be easily distinguished in the spectrum, the overlapping nature of the baryon states (shown in the bottom plot) makes it very difficult to identify each resonance peak in the spectrum by eye. For example, the broad peak in the $\pi^- p \to X$ cross section lying in the region $W \in$ [1.4, 1.6] GeV (commonly known as the 'second resonance region') is actually comprised of three

[1] A cross section for a given reaction refers to the probability that it occurs at a certain energy.

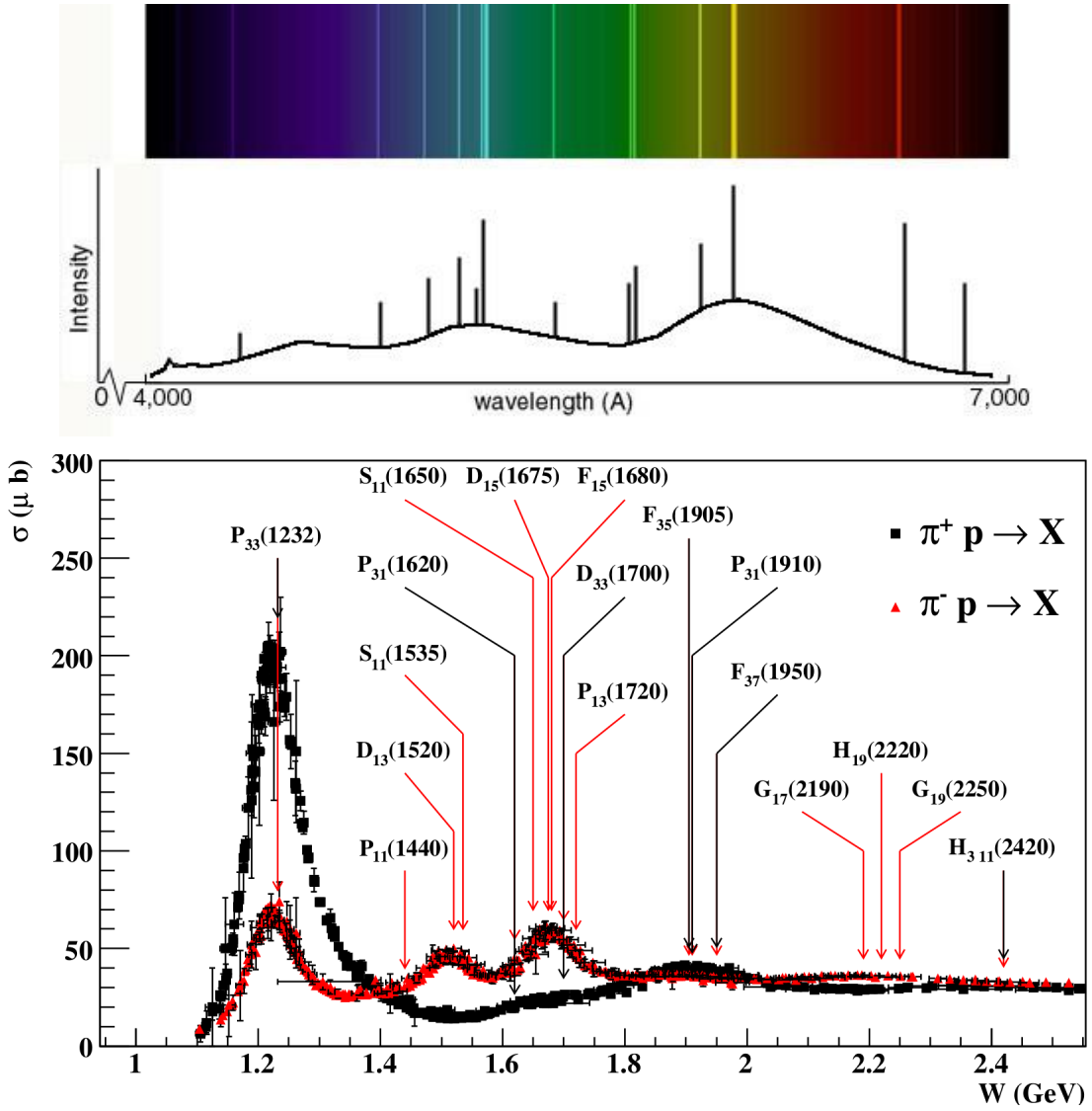

Figure 1.8: (Top) An example of an atomic spectrum. The resonance peaks are narrow and can be easily identified. (Bottom) Baryon cross sections from π^+ and π^- scattering off a proton. The x-axis is the center-of-mass energy, W, in GeV. The arrows show the nucleon resonances with a 4-star rating at various W. The resonances have been labeled using an old notation, $L_{2I\,2J}(M)$, where L is the orbital angular momentum of the πp system, I is the isospin, J is the spin and M is the mass of the resonance (in MeV/c^2). The picture shows that baryon peaks are broad and overlapping. Image source: [13].

resonances. In fact, at high energies the peaks get washed off due to highly overlapping states and another issue which makes baryon spectroscopy very difficult. The latter is related to the non-resonant contributions to the reaction, which are basically all those processes that do not

involve any excitation of the proton. For example, the proton can simply transfer a part of its four-momentum via exchange of some particles. Such processes are called 't-channel' processes. This is just one example out of many other non-resonant processes. Figure 1.9 shows Feynman diagrams for the resonant process (s-channel) and two non-resonant t-channel processes. Due to all these factors, merely having information on the unpolarized cross section is not sufficient to extract the resonant contributions to the reaction under study. Additional observables, called as Polarization Observables, are needed. These observables are discussed in more details in Section 1.3.3.

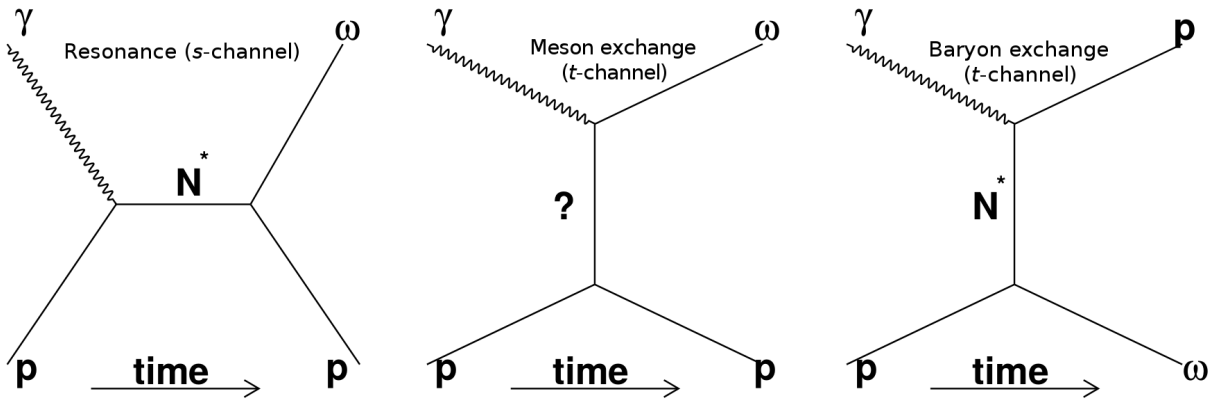

Figure 1.9: Feynman diagrams for (left) s-channel which is a resonant process, (middle) a t-channel process involving exchange of a meson, and (right) a t-channel process involving exchange of a baryon.

Furthermore, the proton can be excited using different type of probes such as a kaon beam, a pion beam, a photon beam etc. Resonances couple to different extent to different probes, as we mentioned in the earlier section. For example, Figure 1.8 (bottom plot) shows that in the cross section corresponding to $\pi^+ p \to X$, the contributions from $I = 1/2$ (i.e. N^*) resonances are suppressed (for example see the region $W \in [1.4, 1.8]$ GeV) since the reaction is an isospin filter. This happens because the $\pi^+ p$ system has $I = 3/2$ and $I_z = 3/2$, therefore X should also have the same I and I_z from isospin conservation. The $\pi^- p$ reaction, on the other hand, is sensitive to both N^* and Δ (i.e. $I = 3/2$) resonances. Being an isospin filter can be advantageous since it reduces complexity, however it also has the disadvantage of not being sensitive to some resonances. Therefore, to search for the resonances, experiments must be performed with a variety of probes. Most of the experiments conducted in the past have utilized a pion beam. It is absolutely crucial to

perform experiments with a photon beam in order to get access to those resonances which couple weakly to pions (especially in the high energy region) but more strongly to photons.

Another issue which complicates the situation is that when the photons interact with the proton, a zoo of particles come out, such as pions, photons, electrons etc. This is unlike atomic spectroscopy where the final state consists of photons only. At a time, only a subset of these particles can be chosen for study. Since a resonance can decay into a variety of final state particles, the probability of seeing a resonance depends on the probability of it decaying to the final state under study. Moreover, if a resonance-like feature observed in the reaction being studied indeed corresponds to a *true* resonance, it should be observed in many other reactions (if the decay of the resonance to those final states is allowed). Therefore, it is very important to study various reactions to well-establish resonances and better understand their properties.

1.3.3 Polarization Observables

In any given reaction, the scattering amplitudes from various contributing processes (resonant as well as non-resonant) are entangled with each other, therefore the phase information of the scattering amplitudes is required in addition to their magnitudes in order to disentangle them. However, the unpolarized cross section only gives information on the magnitude of the amplitudes which often leads to ambiguous solutions for the resonant contributions to the reaction. A good example which demonstrates such a situation is shown in Figure 1.10 (left plot). Different model predictions (SAID, MAID) as well as BnGa partial-wave fits provided a fairly good description of the $p\pi^0$ photoproduction cross section, thereby leading to ambiguous solutions.

Additional information can be extracted by performing polarized experiments and measuring the associated 'polarization observables'. They provide information on the phase of the scattering amplitudes. The resonances can then be extracted with minimal ambiguity from the unpolarized cross section and polarization observables using various interpretation tools. For instance, the polarization observable **E** (Figure 1.10 (right plot)), associated with a circularly-polarized beam and a longitudinally-polarized target, for the $p\pi^0$ photoproduction reaction revealed the discrepancies between the model predictions and experimental data which could not be seen solely based on the cross section.

The commonly used interpretation tools are model-based predictions and partial-wave fits (e.g. SAID, MAID, BnGa). The Bonn-Gatchina group (BnGa) maintains the largest experimental

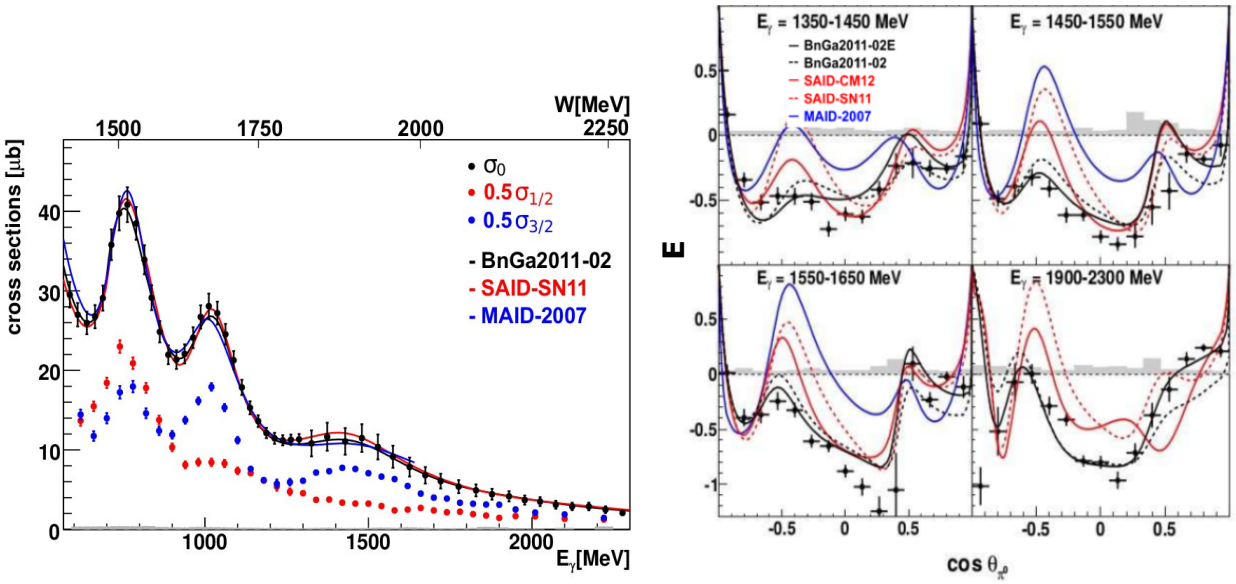

Figure 1.10: Experimental results and theoretical interpretations for the $p\pi^0$ photoproduction cross section (left) and the helicity asymmetry **E** as a function of $cos\theta_{\pi^0}$ (right) at various photon energies. The SAID, MAID and BnGa predictions provided a fairly good description of the total cross section, leading to ambiguous sets of solutions for the resonant contributions. However, serious discrepancies between the model predictions and experimental data were revealed by the **E** observable, which is highly sensitive to the contributing resonances. Note that the black solid curves are BnGa partial-wave fits to these data points. Image Source: [14].

database for a partial-wave analysis in a coupled-channel approach. In a partial-wave analysis, each process is constructed as a sum over the angular momentum states, or partial waves. A coupled-channel analysis simultaneously analyzes many reactions (such as available cross sections and polarization observables from many photon and pion-induced reactions) thus allowing for a consistent analysis. The baryon resonances are added as Breit-Wigner functions at various masses and with different quantum numbers until a good fit to the data is achieved. Another way to find the resonances is from model-based calculations for theoretical values of the polarization observables. Various resonant and non-resonant contributions are included in the model and the contributions are manipulated until the predictions match the experimental results.

1.4 Vector Meson and two-pion Photoproduction

In this analysis, a set of polarization observables for two separate reactions, $\vec{\gamma}\vec{p} \rightarrow p\pi^+\pi^-$ and $\vec{\gamma}\vec{p} \rightarrow p\omega$, with center-of-mass energies up to 2.1-2.3 GeV, have been extracted. There are several motivations behind this analysis. Firstly, they provide information on the photoproduction mechanism of ρ and ω vector mesons, respectively. The ρ meson has a very large width of about 145 MeV/c^2 due to which it is difficult to conduct a direct analysis of $\vec{\gamma}\vec{p} \rightarrow p\rho$ and extract the associated polarization observables. An alternate way is to extract them from the $\vec{\gamma}\vec{p} \rightarrow p\pi^+\pi^-$ reaction using a partial-wave analysis, since ρ decays to $\pi^+\pi^-$ with a 100% branching fraction. The photoproduction of vector mesons, and as a result the extraction of the resonant contributions to these reactions, have been under-explored in the past [15]. The FROST experiment offers a good opportunity to study them, which is very useful for the following reasons: they will aid in a better understanding of the properties of those resonances which contribute to these reactions, but are mostly known from other reactions (such as $N\pi$ scattering). Moreover, they are expected to reveal new high-mass resonances which are produced predominantly via photoproduction and decay primarily to two-body final states involving the (heavier) vector mesons as compared to the (lighter) pseudoscalar mesons.

An additional advantage of studying the $\gamma p \rightarrow p\pi^+\pi^-$ reaction is that it is highly expected to reveal many (yet unobserved) high-mass resonances as it is the dominant contributor to the photoproduction cross section at $E_\gamma \geq 0.8$ GeV, or equivalently $W \geq 1.5$ GeV (Figure 1.11). These high mass resonances are predicted to decay sequentially to three-pion final states via intermediate resonances, for example $\gamma p \rightarrow N^* \rightarrow \Delta^{++}\pi^- \rightarrow p\pi^+\pi^-$. Thus, this reaction has the potential to reveal missing resonances which are at the beginning of the decay chain, as well as those which serve as intermediate states in the chain. Evidence for such sequential decays has been recently found in the isospin channel with $p\pi^0\pi^0$ final state [10].

1.4.1 The ω Photoproduction Reaction on a Proton

This reaction can have two helicities for the beam, two for the target, three for the ω vector meson and two for the recoil proton, amounting to a total of $3 \times 2 \times 2 \times 2 = 24$ scattering amplitudes. Due to parity invariance,12 relations are obtained between these amplitudes, thereby reducing the number of independent amplitudes to 12. This implies that we need to perform

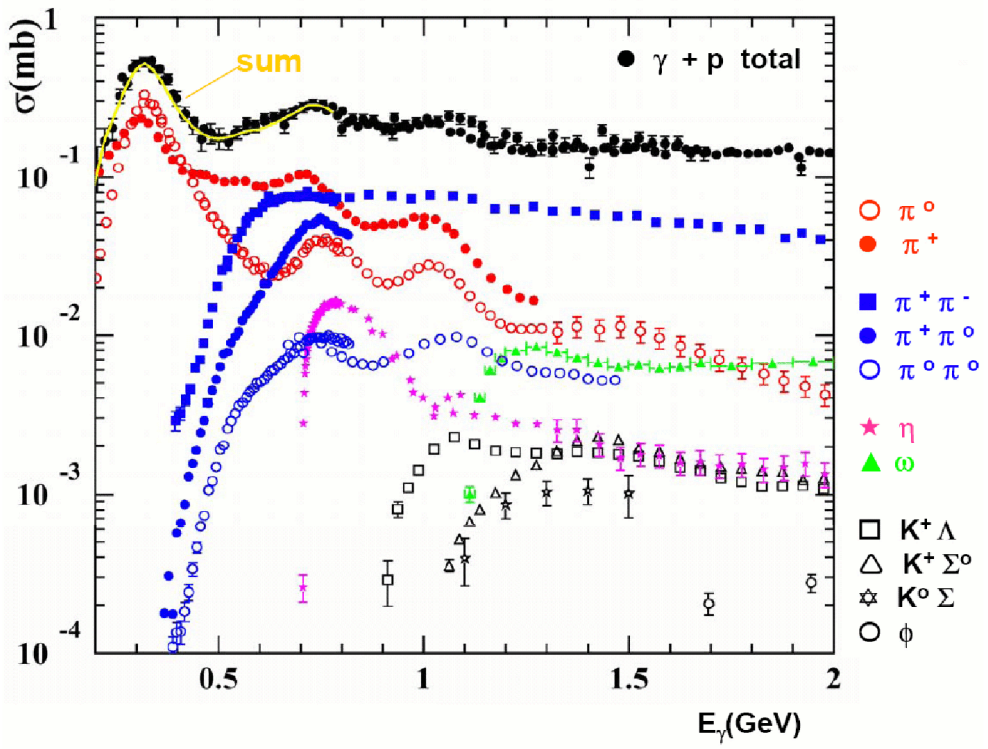

Figure 1.11: The plot shows the contribution from various reactions to the total photoproduction cross section off a proton. Beyond $E_\gamma = 0.8$ GeV, the biggest contribution comes from the $\gamma p \to p\pi^+\pi^-$ reaction.

23 independent measurements to fully determine the 12 scattering amplitudes (with one arbitrary phase) in each kinematic bin (the kinematic variables for this reaction are discussed in Section 4.1.1). However, it must be noted here that this number is valid only in the ideal situation of zero error bars on each measurement. In reality, we most likely need more observables. At present and perhaps also in the near future, the only feasible experiments for this reaction are double-polarization experiments with beam and/or target polarizations. It is very important to measure all these single and double-polarization observables as they are expected to impose tight constraints on models and partial-wave analyses which extract the underlying resonances, even though they are not sufficient to unambiguously determine the scattering amplitudes. In total, the reaction has 290 polarization observables (single-, double-, triple as well as quadrupole-spin observables expressed as bilinear products of the scattering amplitudes) associated with it since all initial and final-state particles can have spin [16]. Of course, a lot of these observables are redundant, however it is much

more difficult to identify them compared to the pseudoscalar meson case.

An advantage of studying this reaction is that it serves as an isospin filter being sensitive only to N^* resonances, thus partially reducing the complexity in identifying the resonant contributions. This is because the ω meson is an isoscalar particle ($I = 0$). Therefore, in $\gamma p \to X \to p\omega$, the $p\omega$ system has $I = 1/2$ and hence, due to isospin conservation, the resonance X should also have $I = 1/2$.

When only beam and target polarizations are measured, the differential cross section reduces to the form given by:

$$\begin{aligned}\frac{d\sigma}{dx_i} = \sigma_0 \{ (1 &- \delta_l \mathbf{\Sigma} \cos 2\beta) \\ &+ \Lambda_x (-\delta_l \mathbf{H} \sin 2\beta + \delta_\odot \mathbf{F}) \\ &- \Lambda_y (-\mathbf{T} + \delta_l \mathbf{P} \cos 2\beta) \\ &- \Lambda_z (-\delta_l \mathbf{G} \sin 2\beta + \delta_\odot \mathbf{E}) \} ,\end{aligned} \tag{1.5}$$

where x_i are the kinematic variables which are described in Section 4.1.1, δ_l ($\delta_\odot$) denotes the degree of linear (circular) polarization and Λ_x, Λ_y, Λ_z are the components of the target polarization with respect to the reaction plane (the axes are shown in Figure 4.1). The angle β denotes the angle between the direction of the linearly-polarized photon beam and the x-axis in the center-of-mass (reaction) plane. ($\mathbf{\Sigma}$, $\mathbf{T}$) and ($\mathbf{H}$, $\mathbf{P}$, $\mathbf{F}$, $\mathbf{G}$, $\mathbf{E}$) denote the single- and double-polarization observables, respectively.

Furthermore, there are observables called *Spin Density Matrix Elements* (SDMEs) associated with the decay distribution of the vector meson. They contain information about ω's polarization. The polarization observables can be expressed as a combination of these SDMEs [17].

Previous Measurements. The earliest measurements pertaining to this reaction were performed by SLAC and Daresbury in the 1970's [18], [19], [20]. They measured the unpolarized differential cross sections and SDMEs at high center-of-mass energies ($W \in [2.47, 2.9]$ GeV). Their results clearly showed that the t-channel exchange process dominates the production mechanism at these energies, which is expected since ω carries the same quantum numbers, J^{PC}, as the photon. In 2003, the CLAS collaboration [21] published differential cross section measurements in the energy range $W \in$ [2.6, 2.9] GeV. In the same year, the SAPHIR collaboration in Bonn [22] published

results on the differential cross section and the unpolarized SDMEs at $W \in [1.7, 2.4]$ GeV where 1.7 GeV is the reaction threshold. These results had better precision than the previous experiments and they also extended the kinematic coverage to the lower energy region. The SAPHIR authors concluded that s-channel processes were important to describe their data. In 2009, the CLAS collaboration [23] reported high-statistics and extensive measurements on the differential cross sections and the unpolarized SDMEs in the energy range $W \in [1.7, 2.8]$ GeV. The data was analyzed in a partial-wave model by the same authors [24] and a set of resonances were reported, as will be discussed below. In 2016, The CBELSA/TAPS collaboration [25] extracted and compared their results on the differential cross sections and the unpolarized SDMEs with the CLAS results. While the SDMEs from the two experiments agreed fairly well, an almost linear energy-dependent normalization discrepancy was observed for the differential cross sections. This issue remains unresolved. The A2 collaboration at MAMI [26] published in 2015 the first precise measurements of the differential cross sections near the reaction threshold with 15 MeV wide binning and full angular coverage.

While a lot of measurements have been carried out on the differential cross sections and the unpolarized SDMEs, only a few measurements with polarized beam-target have been performed till date. Furthermore, the precision and kinematic coverage of most of the existing measurements range from poor to fair. In 2015, Polarized SDMEs ρ^1 and ρ^2 were measured by the CBELSA/TAPS collaboration [25] in the energy range $W \in [1.74, 2.02]$ GeV. The beam asymmetry $\mathbf{\Sigma}$ was measured by the GRAAL collaboration in 2006 [27] from the reaction threshold to $W = 1.92$ GeV. The CBELSA/TAPS collaboration [28] reported results for this observable in 2008 in the range $W \in [1.7, 2.0]$ GeV, however with less precision and angular coverage. The two experimental results exhibited some inconsistencies which could possibly have been due to the reconstruction of ω from different decay modes. To investigate this, the GRAAL collaboration analyzed the three-pion as well as the radiative decay modes of ω and published very precise results for $\mathbf{\Sigma}$ in 2015 [29]. However, their results suffered from even severe discrepancies in some angle bins. Despite the inconsistencies, all three experiments reported large beam asymmetries, which confirmed the need for resonances to describe the data at these energies. Very recently, the CBELSA/TAPS collaboration published double-polarization results on the helicity asymmetry $\mathbf{E}$ from 1.7 GeV to 2.3 GeV in W, and on the observable $\mathbf{G}$ close to the reaction threshold [30].

Data Interpretation. The published data have been partial-wave analyzed by various groups to extract the underlying resonances. The earliest partial-wave analyses [31], [32] based on an effective Lagrangian approach confirmed the need for including resonances to describe the reaction and the need for polarization observables to test the predictions. In a pioneering coupled-channel approach in 2002, Penner and Mosel [33] included pion- and photon-induced reactions and extracted the first $N^* \to N\,\omega$ branching ratios. They found dominant contributions from $N(1710)1/2^+$ and $N(1900)3/2^+$ resonances. However, they observed smaller contributions from these resonances in a more recent coupled-channel analysis [34] which included the SAPHIR 2003 data on SDMEs [22], and strong contributions from $N(1680)5/2^+$ and $N(1675)5/2^-$. In 2009, M. Williams *et al.* [24] reported results from their partial-wave analysis which described the high-quality CLAS results on the differential cross sections and the unpolarized SDMEs [23] with reasonable accuracy. They observed strong contributions from $N(1680)5/2^+$ and $N(1700)3/2^-$ near threshold, and at least one higher mass resonance, $N(2190)7/2^-$. In addition, they reported suggestive evidence for $N(2000)5/2^+$ and a complicated structure, possibly comprising two close-by resonances, at around 1900 MeV.

The above analyses clearly showed that resonant contributions were important to describe the data. However, due to the lack of polarized data and/or a comprehensive PWA data base, different analyses predicted different sets of resonances and were also not sensitive to many resonances, particularly at high energies where the t-channel background dominates the process. Recently, more polarized measurements have been published, as has been discussed in the previous section. The new CBELSA/TAPS publications on polarization observables $\mathbf{\Sigma}$, $\mathbf{E}$, $\mathbf{G}$ and polarized SDMEs were included in the large BnGa data base containing pion and photon-induced reactions. The fit results from their PWA coupled-channel analysis was published early this year [35]. The inclusion of the polarized measurements, particularly the Σ and linearly-polarized SDMEs, led to a better understanding of the t-channel background, which in turn led to a significant improvement in their sensitivity to the contributing s-channel processes. They were able to extract branching ratios for 12 nucleon resonances. Notable contributions were reported from $N(1700)3/2^-$, $N(1720)3/2^+$, $N(1875)3/2^-$, $N(1880)1/2^+$, $N(1895)1/2^-$, $N(2000)5/2^+$, $N(2120)3/2^-$ and $N(2190)7/2^-$ resonances, four of which currently have a $(* *)$ rating. The complex structure of two resonances observed at around 1900 MeV by the CLAS-PWA was confirmed by them. They also observed that inclusion of at least one new state with a mass of about 2.2 GeV was required to obtain a good

description of the data. However, its quantum numbers remain ambiguous. Furthermore, small contributions from the partial waves $1/2^+$, $1/2^-$ and $3/2^-$ near threshold, and from $5/2^-$, $7/2^+$ and $7/2^-$ near 2 GeV were reported.

The importance of polarization observables is palpable from the above discussion. The sets of contributing resonances reported by the partial-wave analyses correspond to those which provide the best description of the available data. More data will provide tighter constraints and increase the sensitivity of the analysis techniques to the resonances. Our results from this work will significantly augment the database of polarized measurements for this reaction. In this analysis, the observables $\mathbf{\Sigma}$ (the beam asymmetry), $\mathbf{H}$ and $\mathbf{P}$ (double-polarization observables) have been measured from the reaction threshold to $W = 2.2$ GeV, while $\mathbf{T}$ (the target asymmetry) and $\mathbf{F}$ (a double-polarization observable) have been measured in the energy range $W \in [1.77, 2.48]$ GeV, although the statistics worsens after $W = 2.32$ GeV. All measurements, except for $\mathbf{\Sigma}$ below $W = 2.0$ GeV, are first-time measurements. A qualitative comparison of our results on $\mathbf{\Sigma}$ with existing results at low energies is discussed in details in Section 6.1.1.

1.4.2 The $\pi^+ \pi^-$ Photoproduction Reaction on a Proton

This reaction has $2 \times 2 \times 2 = 8$ scattering amplitudes associated with it. Including the differential cross section, the reaction has 64 polarization observables which can be expressed as bilinear products of the scattering amplitudes [36]. These observables arise from a combination of initial beam, initial proton and/or recoil proton polarization. Out of the 64 observables, only 15 are independent quantities. In the ideal situation, a set of 15 independent measurements, containing single-, double- as well as triple-polarization observables, need to be made at each kinematic point to provide sufficient constraints for the determination of the eight underlying scattering amplitudes. Note that each kinematic point is completely defined by five independent kinematic variables as discussed in Section 4.1.2. In reality, the measurements have finite uncertainties associated with them, therefore more polarization observables are required to provide additional constraints.

As mentioned in the previous section, currently it is only feasible to perform experiments with polarized beam and target. Without measuring the polarization of the recoil proton, the $\vec{\gamma}\vec{p} \to p\,\pi\pi$

differential cross section, $\frac{d\sigma}{dx_i}$, is given by [36]:

$$\begin{aligned}\frac{d\sigma}{dx_i} = \sigma_0 \{ (1 + \vec{\Lambda}_i \cdot \vec{\mathbf{P}}) \\ + \delta_\odot (\mathbf{I}^\odot + \vec{\Lambda}_i \cdot \vec{\mathbf{P}}^\odot) \\ + \delta_l [\sin 2\beta (\mathbf{I^s} + \vec{\Lambda}_i \cdot \vec{\mathbf{P}}^{\mathbf{s}}) \\ + \cos 2\beta (\mathbf{I^c} + \vec{\Lambda}_i \cdot \vec{\mathbf{P}}^{\mathbf{c}})] \} ,\end{aligned} \tag{1.6}$$

where x_i are the kinematic variables which are described in Section 4.1.2, σ_0 is the unpolarized cross section. $\vec{\Lambda}_i$ denotes the polarization of the initial proton and $\delta_\odot$ is the degree of circular polarization of the incoming photon beam, while δ_l is the degree of linear polarization. The angle β, equivalent to the angle in Equation 1.5, denotes the angle of inclination between the linearly-polarized photon beam relative to the x-axis in the center-of-mass production plane. It is defined as positive if the x-axis was rotated counter-clockwise from the beam polarization.

The two-meson final state equation (Equation 1.6) contains 15 polarization observables, not all of which are independent. $\mathbf{I}^\odot$, $\mathbf{I^s}$, and $\mathbf{I^c}$ arise from the beam polarization. The observables $\vec{\mathbf{P}}$ (having components $\mathbf{P_x}$, $\mathbf{P_y}$ and $\mathbf{P_z}$) describe the target asymmetries which arise if only the target nucleon is polarized, and $\vec{\mathbf{P}}^\odot$ as well as $\vec{\mathbf{P}}^{s,c}$ represent the double-polarization observables.

Previous Measurements and Data Interpretation. A vast amount of literature is available on the measurement of the total cross section and the invariant mass distributions of $\pi^+\pi^-$, $p\pi^+$ and $p\pi^-$ for this reaction. Reference [37] provides a nice summary of these measurements and their theoretical interpretations. As discussed earlier, the reaction can proceed in three different ways: $\gamma p \to N^* \to p\sigma \to p\pi^+\pi^-$, $\gamma p \to N^* \to p\rho \to p\pi^+\pi^-$ and $\gamma p \to N^* \to \Delta\pi \to p\pi^+\pi^-$. Various model calculations for the total cross section [38]-[40] found that the reaction is dominated by the Δ-Kroll-Ruderman background term (see Figure 1.12 (a)). Furthermore, Tejedor and Oset [38] suggested that Δ-Kroll-Ruderman term interferes with the sequential decay of $N(1520)3/2^-$ to the two-pion final state via $\Delta\pi$, leading to a peak-like structure in the total cross section between 0.6-0.8 GeV in photon energy. The invariant mass distributions also showed clear signals for $\Delta \to N\pi$ and $\rho \to \pi^+\pi^-$ contributions.

The polarization database for this reaction remains rather sparse. The only published polarized measurements are $\mathbf{I}^\odot$ measured using the CLAS detector at Jefferson Lab in the energy range

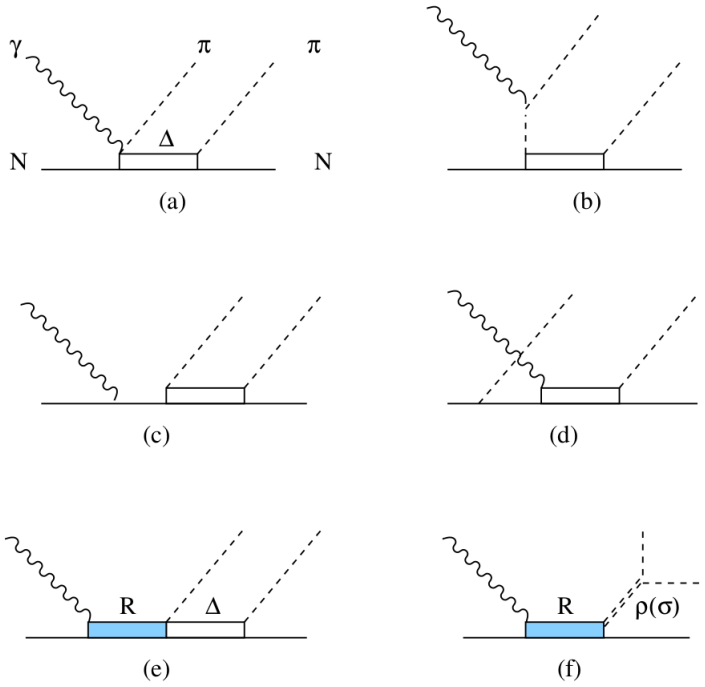

Figure 1.12: Feynman diagrams for two-pion photoproduction. a) Δ-Kroll-Ruderman term, b) Δ pion-pole term, c) Δ exchange term, d) direct Born term, e)-f) resonance terms. Image source: [43].

$W \in [1.35, 2.30]$ GeV [41] and at the MAMI accelerator in Mainz in the energy range $W \in [1.39, 1.55]$ GeV [42], and the helicity-dependent total cross-section difference (which is related to $\mathbf{P}_z^{\odot}$) measured by the GDH and A2 Collaboration at low energies [43]. Various model predictions exist for these observables, however none of them describe the experimental data well. Most models are based on the same effective Lagrangian scheme where the parameters for the resonant (Figure 1.12 (e) and (f)) and Born (background) terms (for example, Figure 1.12 (a)-(d)) are taken from other experiments or are treated as free parameters. The differences between various model predictions arise due to the different treatment of the background amplitudes. Extraction of resonances for this three-body final state reaction is very challenging due to the presence of a huge amount of background coming mainly from terms like Δ-Kroll-Ruderman which dominate the reaction.

More polarization observables are required to significantly improve the existing models. The CLAS collaboration has made a significant effort in this direction. High-statistics results on the beam asymmetries $\mathbf{I}^{\mathbf{s,c}}$ from CLAS-g8 [44] are in preparation for publication. The FROST exper-

iment at CLAS has provided access to the complete set of polarization observables associated with beam-target polarizations for this reaction and the extraction of the entire set is close to completion. In this work, eight polarization observables using the FROST data have been extracted in the energy range $W \in [1.5, 2.2]$ GeV. They are $\mathbf{I^{s,c}}$, $\mathbf{P_{x,y}}$ and $\mathbf{P^{s,c}_{x,y}}$. The high statistics data collected by the experiment made it possible to extract the observables as a function of three (out of the five) kinematic variables. It is highly expected that these new data will significantly aid in the study of sequential decays of the contributing resonances via intermediate states, and reveal many *missing* resonances.

The rest of the thesis is organized as follows. In Chapter 2, the experimental set up which was used to collect the data analyzed in this work will be discussed in details. In Chapter 3, the experimental conditions of all data sets, the identification of the photon and final-state particles, kinematic fitting, corrections, and additional cuts which were used to tune the data sets will be described. Moreover, details on the beam and target polarization will be provided. Chapter 4 will show the extraction of the polarization observables for the reactions $\vec{\gamma}\vec{p} \to p\pi^+\pi^-$ and $\vec{\gamma}\vec{p} \to p\omega$. Chapter 5 will discuss about the systematic uncertainties in our measurements due to various factors. The results from this analysis will be shown and discussed in Chapter 6. The thesis will conclude with a summary of this work and an outlook, presented in Chapter 7.

CHAPTER 2

THE FROST EXPERIMENT AT JEFFERSON LAB

In this work, data from the 'FROST-g9b' experiment has been utilized to obtain the polarization observables. In 'g9b', 'g' stands for *gamma* (i.e. the incident photons) and '9b' implies that this was the second iteration of the 9th approved photoproduction experiment. This chapter documents the key features of the experimental apparatus. The experiment was conducted in the year 2010 in Hall B of the Thomas Jefferson National Accelerator Facility (also known as Jefferson Lab), Virginia, using the Continuous Electron Beam Accelerator Facility (CEBAF). At the time of the experiment, the accelerator was capable of providing electron beam energies up to 5.5 GeV. The broad-range photon tagging facility in Hall B was able to tag photon energies ranging from 20% to 95% of the incident electron energy using the bremsstrahlung tagging technique. An indispensable feature of the FROST experiment, which was a double-polarization experiment, was the frozen-spin target. Butanol served as the ideal target material since it could be dynamically polarized. The experiment covered all possible combinations of beam and target polarizations. The FROST-g9b experiment, which was a subset of the FROST experiment, utilized a linearly- or circularly-polarized photon beam in combination with a transversely-polarized target. To detect the outgoing charged particles, which were created from the interaction of the photon beam with the target, the CEBAF Large Acceptance Spectrometer (CLAS) was utilized. It was a nearly-4π spectrometer optimized for hadron spectroscopy.

2.1 The Accelerator Facility at Jefferson Lab

CEBAF at Jefferson Lab serves as a unique 'giant microscope' to probe the atomic nucleus. It has a racetrack geometry with a circumference of about 7/8 of a mile. The accelerator was recently upgraded to provide a continuous electron beam with energies up to 12 GeV, however we will describe the facility as it was when the FROST experiment was performed. The facility had the following components: an electron injector, two linear accelerators (LINAC) consisting of 338 RF cavities in total, nine recirculation arcs made of magnets to bend the electron beam and an

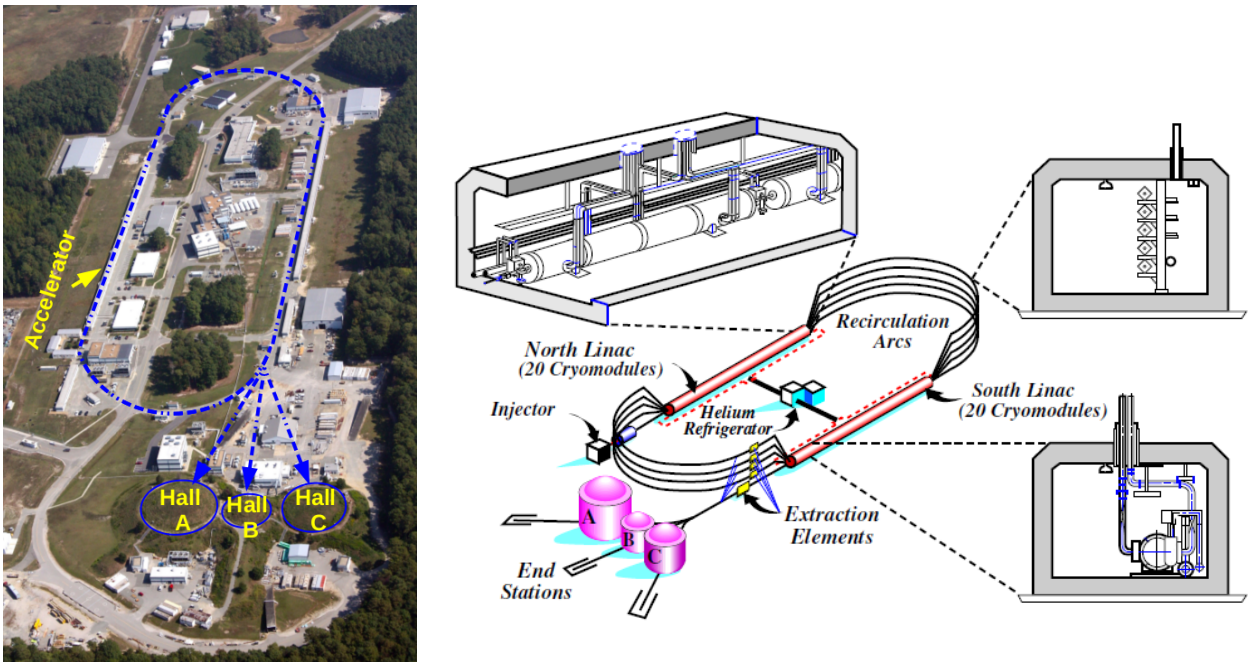

Figure 2.1: (Left) An aerial view of the accelerator site at the time of the FROST experiment. The racetrack shaped CEBAF accelerator and the three experimental halls are indicated on the picture. The FROST experiment was conducted in Hall B which is the smallest of the three halls. (Right) A schematic diagram of the accelerator facility showing its major components. Image source: [45].

RF separator to direct the beam to three different Halls: A, B and C. Figure 2.1 shows an aerial view of the accelerator site at the time of the FROST experiment as well as a schematic diagram showing its components.

Electrons were created in the Injector by shining pulsed lasers on a Gallium Arsenide photocathode at a frequency of 499 MHz (about a third of the accelerator frequency). This resulted in 2 ns bunches of unpolarized electrons. If longitudinally-polarized electrons were needed, then the light from the laser was circularly-polarized using two Pockel cells, prior to irradiating the photocathode with it. Three synchronized lasers were utilized to supply the beam simultaneously to the three halls, so that the characteristics of the beam could be tailored to each hall's requirement. The injector had nine radio frequency (RF) cavities which boosted the energy of the electrons to 45 MeV [46]. An optical chopper was used to cleanly separate the 2 ns bunches and the beam of electrons was then injected into the LINAC.

The two LINACs shown in Figure 2.1 were used to accelerate the electrons by ~ 500 MeV per

Figure 2.2: A picture of a cryomodule consisting of eight RF cavities. Image source: [45].

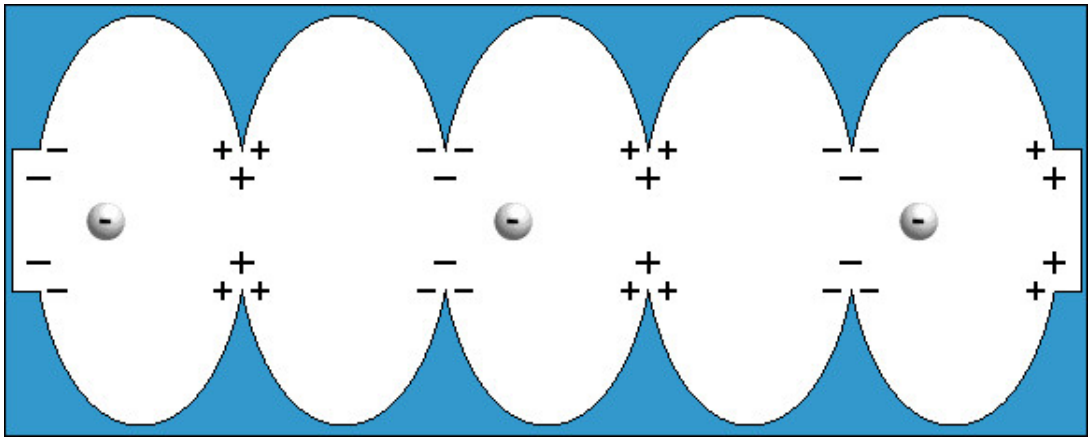

Figure 2.3: A diagram to illustrate the charge gradient across a cryomodule. Image source: [47].

pass. Since the facility allowed up to five passes in each LINAC, the maximum energy achieved was 5.5 GeV. Each LINAC consisted of 21 cryomodules, where each module was comprised of four sets of paired superconducting Niobium RF cavities, as shown in Figure 2.2. Thus, there were 168

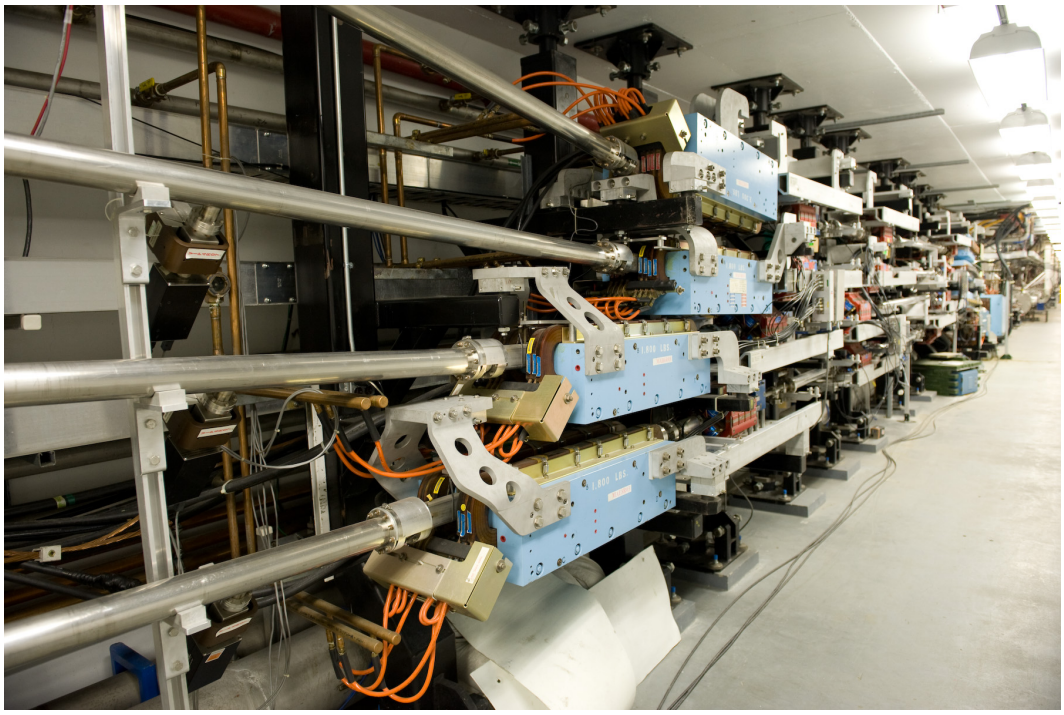

Figure 2.4: A picture of a recirculation arc used at CEBAF. The dipole magnets utilized to bend the electron beam are visible in the picture. Image source: [45].

cavities per LINAC. To sustain their superconductivity, they were immersed in liquid Helium and maintained at a temperature of 2 K. These cavities were used to accelerate the electron beam by producing a charge gradient along the length of the cryomodule, as shown in Figure 2.3. After passing through one LINAC, the electron beam was bent by using powerful dipole magnets in the recirculation arcs and directed to the other LINAC which further accelerated the electrons. Figure 2.4 shows a picture of a recirculation arc consisting of dipole magnets used at CEBAF. This way with each loop (two passes) the energy of the beam was boosted by about 1.1 GeV. A stronger magnetic field was required to bend the beam (by the same amount) as its energy increased. The beam was divided into five sub-beams based on energy (which depended on the number of loops the sub-beam had made) so that the five sub-beams could pass through different recirculation arcs before re-entering the LINACs. Once the beam achieved the desired energy, it was directed to the designated hall using an RF separator. In the rest of this chapter, we will focus on Hall B where the FROST experiment was conducted. The electron beam current in this experiment was maintained within the range $5 - 14$ nA, mainly to sustain the target polarization as well as to keep the event

rates within the limits of the detectors in Hall B. The typical electron beam luminosity was of the order of 10^{34} cm^{-2} s^{-1}.

2.2 The Bremsstrahlung Technique

Once the electron beam reached Hall B, it interacted with a radiator. The electromagnetic field of the radiator's nuclei applied a decelerating force on the electron which led to emission of a photon in order to conserve the total energy and momentum of the system. Such kind of radiation is known as 'Bremsstrahlung' which means 'braking radiation'. The typical photon beam luminosity achieved was of the order of 5×10^{31} cm^{-2} s^{-1}. Circularly-polarized photons were produced by irradiating an amorphous radiator, which was a thin gold foil of thickness 10^{-4} radiation length in this experiment, with longitudinally-polarized electrons. These photons exhibited a smooth energy distribution of the form $1/E_\gamma$, where E_γ refers to the photon energy. The degree of circular-beam polarization depended on the polarization of the incident electron beam, as will be discussed in Section 3.7.2. Therefore, it was important to precisely measure it. For this, a Møller polarimeter was utilized which was located upstream of the photon tagger described in the next section. It is based on the Møller (or elastic electron-electron) scattering process. The longitudinally-polarized electrons were scattered off polarized electrons of a magnetized 25 micron thick Permedur foil. The polarizations resulted in an asymmetric scattering distribution which was measured by two detectors, made of scintillators and photomultiplier tubes, located downstream of the target. Two quadrupole magnets were used to deflect the scattered electrons into the detectors. The electron beam polarization was proportional to the measured asymmetry and thus, could be determined. The polarimeter was used in special runs performed in-between the actual runs since the polarization measurements required special data acquisition settings.

To produce linearly-polarized photons, unpolarized electrons were incident on a well-oriented crystal radiator. A 50 μm diamond radiator was utilized in this experiment. The well-ordered structure of the crystal lattice led to a coherent scattering, which showed up as an enhancement on top of the $1/E_\gamma$ incoherent photon energy distribution [48]. The leading edge of the enhancement is referred to as the *coherent edge*. Most of the polarized photons resided within the enhancement, which was typically 200 MeV wide. A prototypical enhancement is shown in Figure 2.5. The

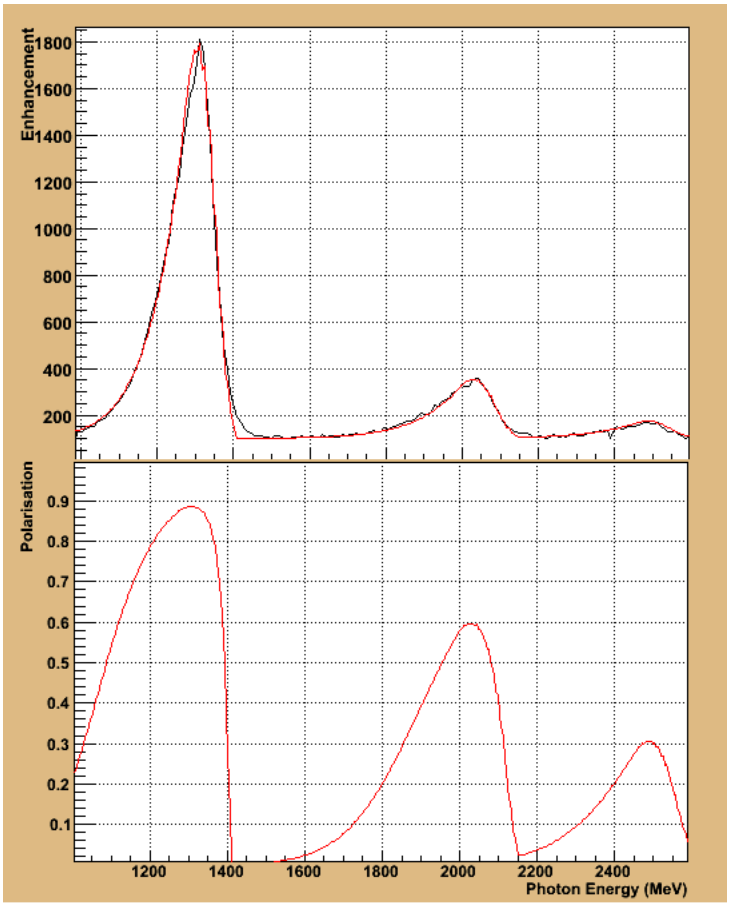

Figure 2.5: A prototypical example of an enhancement with coherent edge at 1.4 GeV (black curve). The peak was about 0.2 GeV wide. It was observed on top of the unpolarized $1/E_\gamma$ distribution and could be isolated by dividing the coherent spectrum by the spectrum obtained with an amorphous radiator. The red curve in the top plot is a fit to the data, and the bottom plot shows the corresponding degree of polarization extracted from the fit. The small peaks at higher energies originated from photons that scattered off other geometrically equivalent lattice planes in the radiator. Image source: [49].

experiment also collected data with unpolarized photons which were created by illuminating an amorphous carbon or gold radiator with unpolarized electrons.

The characteristics of the linear beam polarization were controlled by tuning various experimental parameters. By adjusting the lab azimuthal angle of the diamond crystal's lattice, an orientation of the scattering (or polarization) plane either parallel (PARA) or perpendicular (PERP) to the floor of the experimental hall could be achieved. The energy position of the coherent edge was adjusted by tweaking the small angles between the crystal lattice and the electron beam direction.

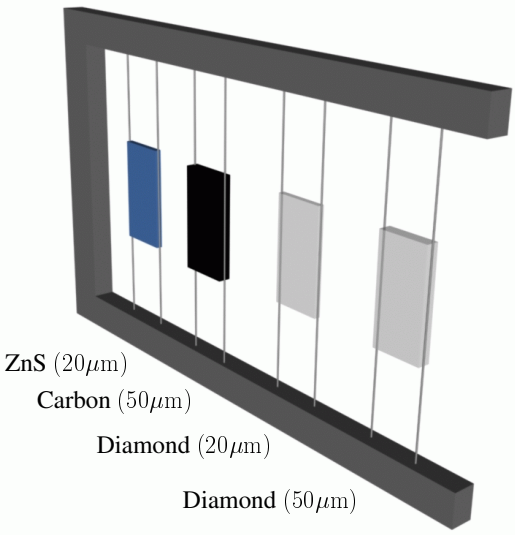

Figure 2.6: (Left) The goniometer used in Hall B to adjust the coherent edge position and orient the polarization plane of the photon beam parallel or perpendicular to the floor. (Right) A diagram of a target ladder containing various radiators. It was placed at the center of the goniometer. The required radiator could be moved into position when needed.

These fine adjustments were enabled by the use of a goniometer, which is shown in Figure 2.6 (left). It had an angular precision better than 10 μrad about the three orthogonal axes [50]. The available degrees of freedom are shown in Figure 2.7. A target ladder (Figure 2.6 (right)), which contained various radiators, was mounted at the center of the goniometer. This provided the flexibility to move different radiators into position as needed by the experiment.

As mentioned before, most of the polarized photons lied within the coherent peak. The ratio of polarized to unpolarized photons was improved further by tightening the beam collimation [48]; thus, a higher degree of polarization was obtained. For this purpose, a 2.0 mm active collimator made from nickel diskettes stacked in a cylindrical sheath of stainless steel was used. In this experiment, the linear beam-polarization was measured by fitting the enhancement. Details are discussed in Section 3.7.4. Figure 2.8 shows a schematic of the relative positions of the goniometer and the collimator with respect to the Photon Tagger which will be discussed in the next section.

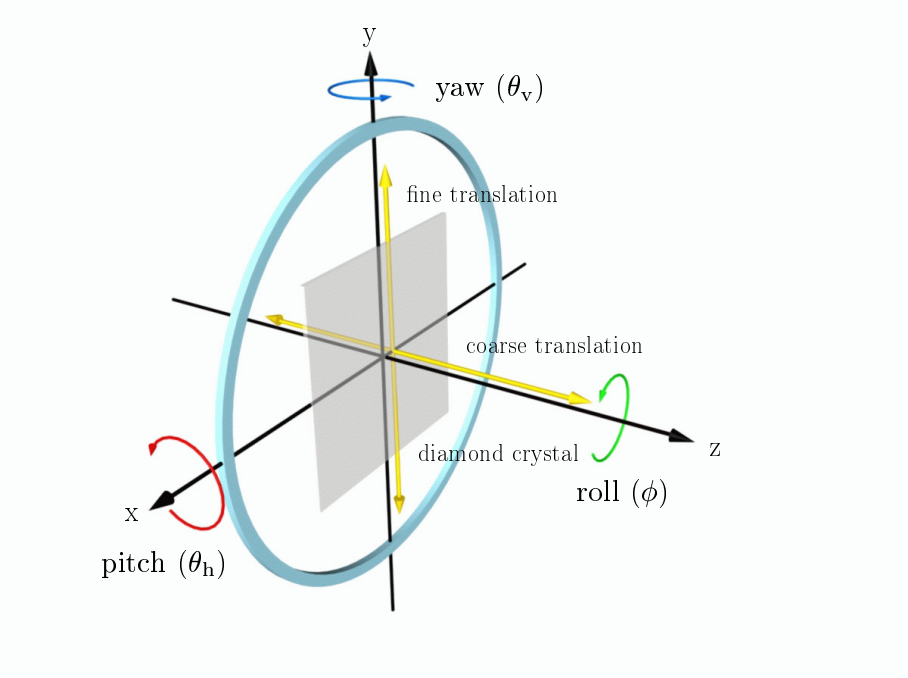

Figure 2.7: A schematic diagram illustrating the rotational and translational degrees of freedom available in the goniometer.

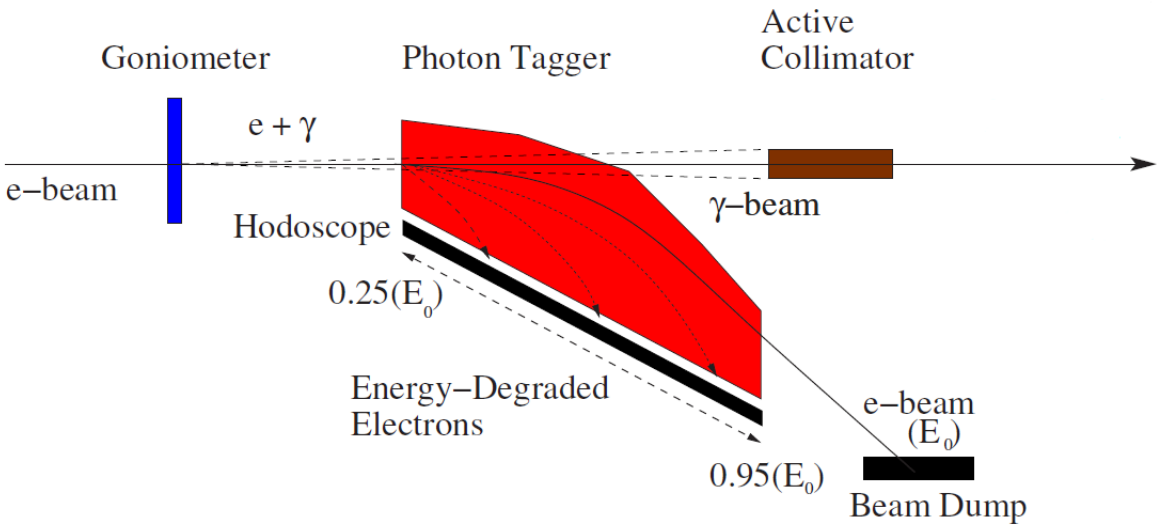

Figure 2.8: A schematic diagram showing the relative positions of the major parts of the experimental set up which was used for the production of high quality linearly polarized photons.

2.3 The Photon Tagger

The next important task was to bend the (scattered as well as unscattered) electrons away from the trajectory of the bremsstrahlung photons, and tag the energy and time of these photons. This was accomplished by using a Photon Tagger [51]. The Tagger consisted of a C-shaped magnet with an open-yoke design which was capable of producing a magnetic field up to 1.75 T in strength. The magnetic field was matched to the incident beam energy so that the unscattered electrons were directed to a beam dump and the scattered electrons (i.e. those which interacted with the radiator to emit a photon) were directed to the E- and T-counter planes in order to tag the energy and time of the produced photons. Figure 2.9 shows a schematic diagram of the Tagger hodoscope, along with the E- and T-counters.

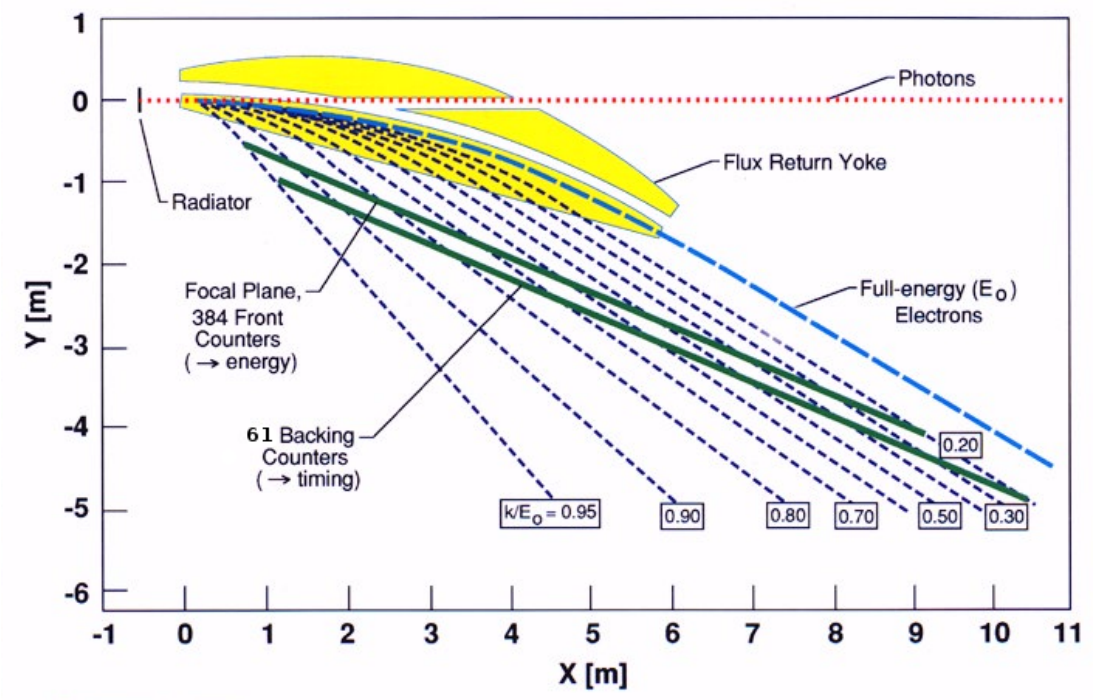

Figure 2.9: A diagram illustrating the overall geometry of the tagging system. The Tagger hodoscope is shown in yellow. The dashed black curves show the trajectories of the scattered electrons as they passed through the Tagger magnet. The photons emitted by these electrons traveled along the beam line which is shown using a red dotted line. The label at the end of each trajectory shows the fraction of the incident energy carried away by the associated photon. The two solid green lines denote the focal planes of the E- and T-counters of the Tagger. The blue dashed curve shows the path of the unscattered electrons that were directed to the beam dump. Image source: [51].

The energy of the photon, E_γ, was given by:

$$E_\gamma = E_{\text{incident}} - E_{\text{scattered}} \tag{2.1}$$

where E_{incident} refers to the energy of the electron incident on the radiator right after it came out of the accelerator, and $E_{\text{scattered}}$ refers to the energy of the scattered electron. Since E_{incident} was a known quantity, $E_{\text{scattered}}$ was the only missing information. To measure it, E-counters were utilized. The basic principle was as follows. The radius of curvature of the electron's trajectory due to the magnetic field was proportional to the electron's momentum. Therefore, by knowing the exact position of the electron on a plane, which was aligned with the optical focal point of the Tagger magnet, the momentum and energy of the electron could be determined precisely. This plane, called as the E-counter plane, was covered with 384 plastic scintillators which were 20 cm long, 4 mm thick and $6 - 18$ mm wide. The widths varied to ensure that the same momentum range was covered by all scintillators. Each scintillator covered 1/3rd of the neighboring scintillator's width, creating 767 separate channels to determine the scattered electron's position and hence its energy. This arrangement enabled tagging photons with energies from 20% to 95% of the incident electron beam energy, with a high energy resolution of $\frac{\Delta E}{E} = 0.001$.

Likewise, the T-counter plane, which was positioned 20 cm behind the E-counter plane and ran parallel to it, was utilized to accurately determine the time of the electron in the electron bunch, and hence the associated photon time. The T-plane consisted of 61 overlapping scintillator counters resulting in 121 separate channels. The counters were 2 cm thick, much thicker than the E-counter scintillators, to ensure sufficient light for precise timing. The widths (along the dispersion direction) were varied to compensate for the $1/E_\gamma$ behavior of the bremsstrahlung cross section, with 19 narrower counters covering $75 - 95\%$ of electron beam energy and the rest covering the range $20 - 75\%$. The lengths (transverse to the momentum plane) were varied from 20 cm at the high electron momentum end to 9 cm at the low momentum end. This arrangement enabled a timing resolution of ~ 100 ps.

2.4 The FROzen Spin Target (FROST)

For the g9b experiment, a target with transversely polarized protons was needed. The main factors governing the choice of the target material were: a high degree of target polarization,

resistance of the target polarization to the incident radiation and a long relaxation time. Taking these factors into consideration, 'frozen beads' of TEMPO ($C_9H_{18}NO$) doped butanol (C_4H_9OH) were used as the target material. The beads had a diameter of $1 - 2$ mm and were formed by dripping the doped butanol solution through a hypodermic needle into a bath of liquid nitrogen. The nuclei of the covalently bonded protons (i.e. protons of the hydrogen atoms in butanol) were polarized by the Dynamic Nuclear Polarization (DNP) technique. The FROST target system was a complex system with the following main components: a 5 T superconducting polarizing magnet, a cooling assembly which included a dilution refrigerator, a microwave system (for DNP), a Nuclear Magnetic Resonance (NMR) system (for measuring the target polarization), and a target insert. The entire assembly was mounted on a cart that could be easily rolled into and out of CLAS. Full details are available in [52] and [53]. A cutaway view of the polarized target system positioned inside the CLAS detector is shown in Figure 2.10. The CLAS detector is described in the next section.

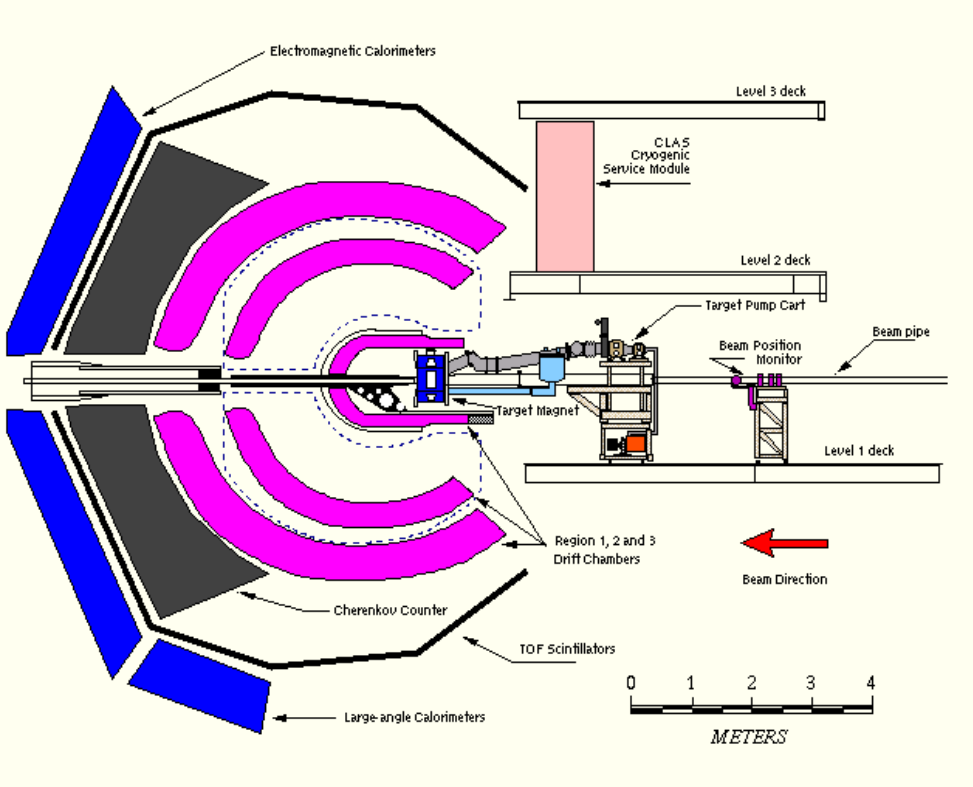

Figure 2.10: A cutaway view to illustrate the relative position of the polarized target system with respect to the CLAS detector during data taking. Image source: [53].

2.4.1 Polarizing the Target using the DNP Technique

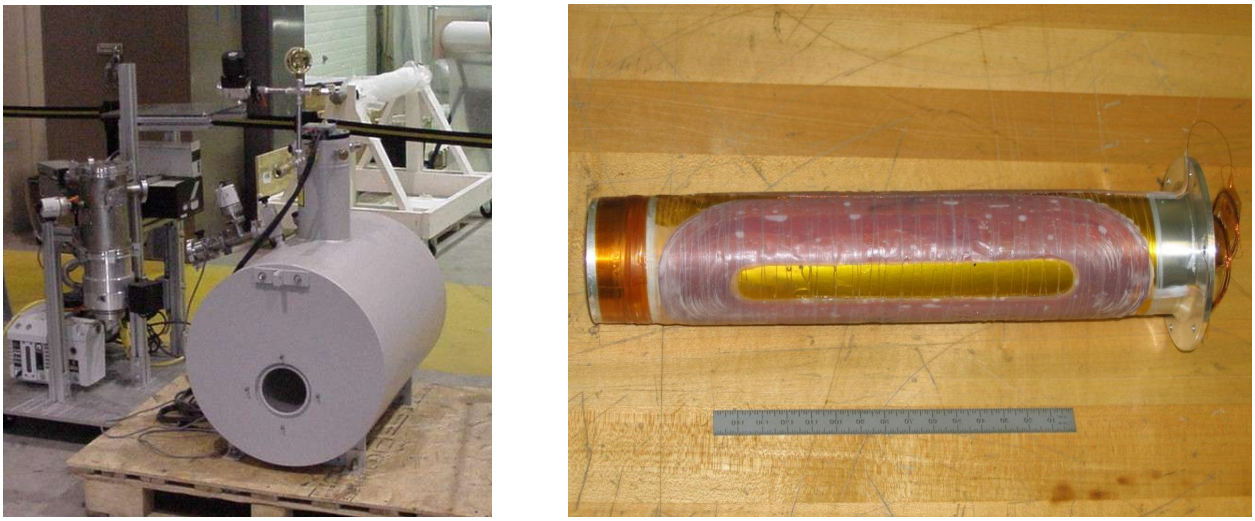

Figure 2.11: (Left) The solenoid polarizing magnet with a field of 5.0 T. (Right) The dipole holding magnet with a field strength of 0.5 T to sustain the transverse target polarization. Image source: [53].

The DNP technique is a well-established process that is used to polarize targets. It was employed as follows. The target was inserted into the bore of a superconducting polarizing magnet (see Figure 2.11 (left)) which was positioned 570 mm away from the center of the CLAS detector. The polarizing magnet was then energized to its full strength of 5 T. This process took about 40 minutes. The magnetic field was applied for a few hours to polarize the unpaired electrons in the TEMPO radicals while the target was maintained at $250-300$ mK temperature using a dilution refrigerator. A field-to-temperature ratio of 5 T/K or greater was desirable to achieve a high degree of nuclear polarization. In the next step, a microwave field was applied near the Electron Spin Resonance (ESR) frequency to flip their spins and the spin of the nearby protons of the hydrogen atoms in the butanol target. The electron spins relaxed back to a lower energy state in less than a millisecond due to the strong electron-lattice coupling and thus became available again for spin flips. However, the nucleon spin relaxation time was much longer ($\sim 10^3$ s). Therefore, they accumulated into one spin state, resulting in a net nuclear polarization. The direction of the nuclear spin could be set

either parallel or anti-parallel to the applied magnetic field, depending on whether the microwave frequency was set above or below the ESR frequency.

Once the polarization was complete, the microwave field was switched off and the target was cooled down to 60 mK using the dilution refrigerator, which is discussed in the next section. This took about 40 min. At this point, the polarizing field was ramped down and a small holding field of 0.5 T using a dipole magnet (made of 0.1 mm thick NbTi wire) was applied to sustain the transverse target polarization during data taking. The dipole holding magnet (shown in Figure 2.11 (right)) consisting of two racetrack-shaped coils, one on top of the other, were made with separate wires so that in case one of them failed, the other would continue generating magnetic field perpendicular to the beamline. It was placed within the FROST apparatus as shown in Figure 2.12. The polarizing magnet was then retracted and the target assembly was rolled into the center of CLAS.

The combination of high magnetic field and low temperature helped achieve a long relaxation time of 4000 hours without beam. With beam, the relaxation time decreased to 3400 hours, mainly due to the fact that the beam had a heating effect on the target. The target was re-polarized about once per week during the course of the experiment. The degree of the target polarization varied from 45% to 94% over the whole experiment, with the average being about 81%. It was measured using the NMR technique, whereby an RF frequency was swept through the proton Larmor frequency of 212.6 MHz. The resulting spin flips of the polarized protons altered the nuclear susceptibility of the target, which led to a change in the voltage across the circuit. The area under the plot of voltage versus frequency was proportional to the degree of polarization.

2.4.2 The Dilution Refrigerator

The cooling process was a multi-step process. The main components are shown in Figure 2.12. The temperature in the 4 K pot was about 4.2 K. In the 1 K pot, the temperature was about 1.5 K. In the distillation chamber, the temperature went down to about 0.8 K. To bring it further down, a ^{3}He-^{4}He horizontal dilution refrigerator was used. A schematic diagram of the refrigerator is shown in Figure 2.13. It utilized a process called evaporative cooling which can be summarized as follows. The mixing chamber of the refrigerator contained a mixture of ^{3}He-^{4}He. This mixture separated into two phases below 0.8 K: a 'concentrated phase' which was ^{3}He rich, and a 'dilute phase' which was ^{4}He rich or ^{3}He poor. The modus operandi was that since the specific heat of the dilute phase was higher (106 J/(mol K)) than the concentrated phase (22 J/(mol K)), therefore ^{3}He moving

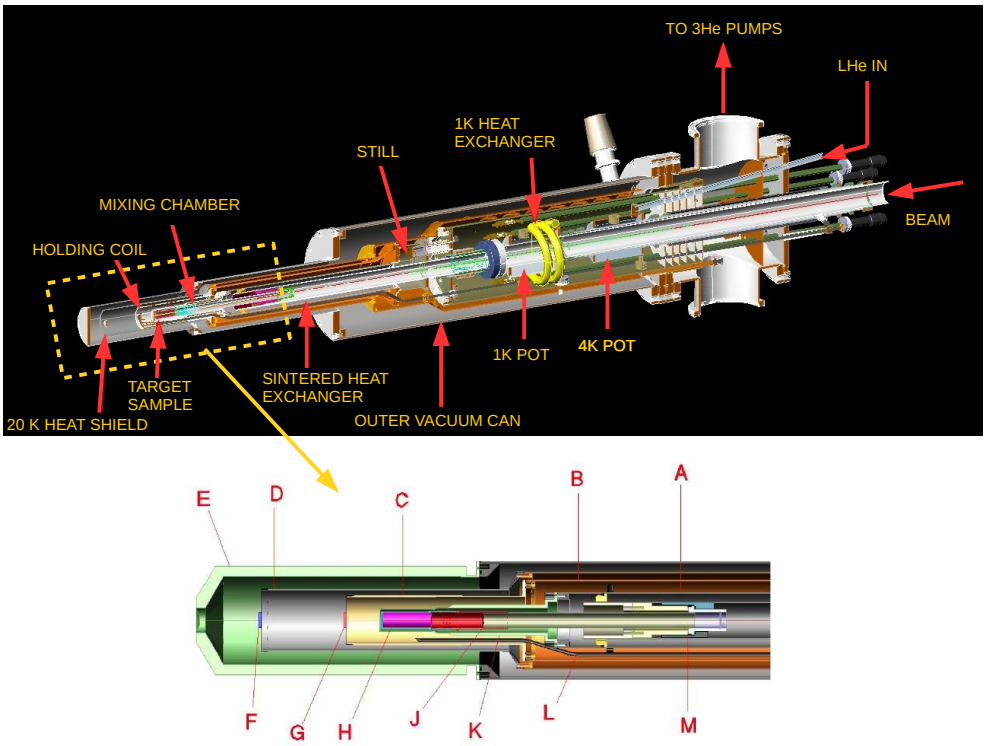

Figure 2.12: A cutaway view of the FROST apparatus showing the arrangement of the target sample, the holding coil and the cooling system including the dilution refrigerator. The enlarged section of the picture shows the following components: A) primary heat exchanger, B) 1 K heat shield, C) holding coil, D) 20 K heat shield, E) outer vacuum can (Rohacell extension), F) polyethylene target, G) carbon target, H) butanol target, J) target insert, K) mixing chamber, L) microwave guide, and M) Kapton coldseal. Image source: [53].

from the concentrated to the dilute phase would absorb energy from its surroundings. To facilitate such a flow, ^{3}He atoms were removed from the dilute phase, creating an imbalance. As the ^{3}He atoms from the concentrated phase moved to the dilute phase in order to re-establish equilibrium, they absorbed heat from the FROST target, which was placed right next to the mixing chamber (see Figure 2.13).

It must be mentioned here that the protons in the hydrogen atoms of the butanol target were polarized, but the protons bound within the nuclei of carbon and oxygen atoms were not. Events originating from these bound nucleons were considered as background events. Two additional targets, carbon and CH_2 (polyethylene) disks, were placed downstream of the butanol target to

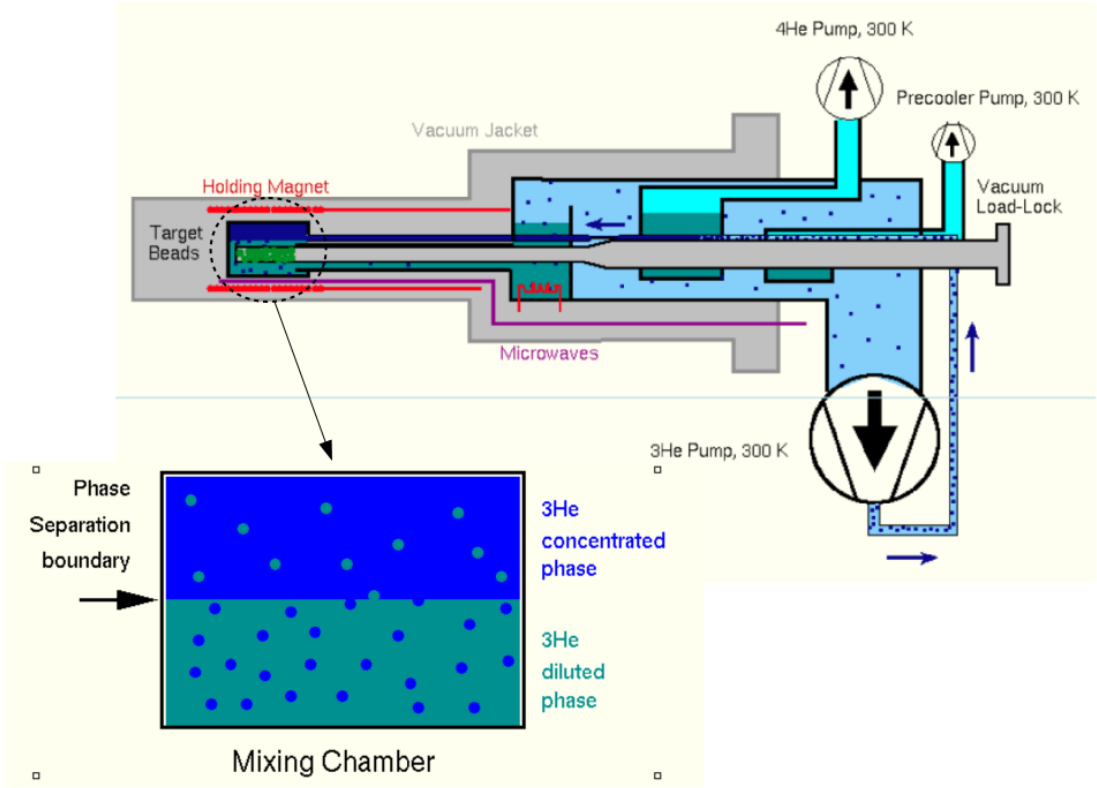

Figure 2.13: A schematic of the horizontal dilution refrigerator. Also shown in the picture are the locations of the target beads and the holding coil. Image source: [53].

understand the background, which included events originating from the bound nucleons of the FROST target. Further details are discussed in Chapter 3.

2.5 The CLAS Spectrometer

The main detector in Hall B was the CEBAF Large Acceptance Spectrometer. It was a multi-gap high acceptance magnetic spectrometer which was primarily used to detect charged particles of the final state. The electromagnetic calorimeter was not utilized in this analysis. It primarily served as an electron trigger in CLAS and hence was more suitable for electroproduction experiments. The detector was based on a non-homogeneous toroidal magnetic field, primarily pointing in the ϕ direction, to bend the charged particles and many sub-detectors to detect their tracks, as shown in Figure 2.14. The entire detection system had a six-fold symmetry about the beam-axis, covering almost 4π angle except for the forward hole for the beam and dead regions due to the presence of

structures like the beamline, support structure for the magnet etc. The major components of the CLAS detector are described below. Further details are available in [54].

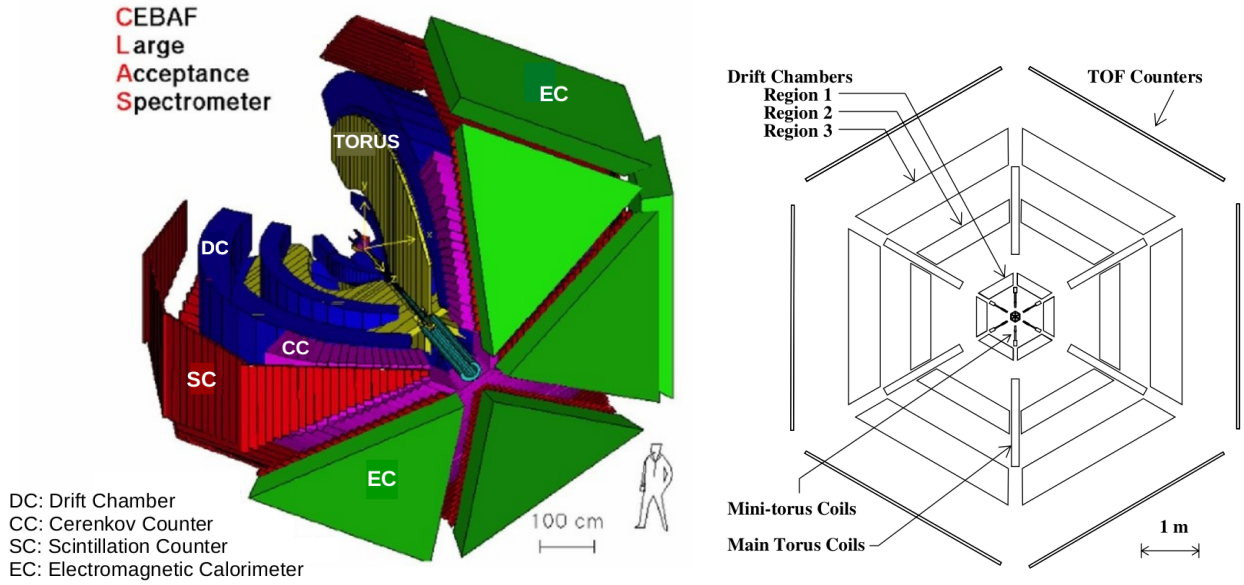

Figure 2.14: Schematic diagrams of the main components of the CLAS spectrometer. (Left) a 3D cutaway view and (right) a cross section perpendicular to the beam line. Th 'Mini-Torus' was not used in photoproduction experiments such as the FROST experiment. The six-fold symmetry of the spectrometer is visible in both diagrams. Image sources: [54], [45].

2.5.1 Torus Magnet

The Torus magnet provided a toroidal magnetic field which was required to bend the charged particles. Such a field ensured a large-angle coverage and in addition, created a field free zone around the target. The magnet consisted of six superconducting coils arranged in a toroidal fashion about the beam axis resulting in a magnetic field which mostly pointed in the ϕ direction, as shown in Figure 2.15 (left). Therefore, when acting on the charged particles, the force due to this field did not change their azimuthal angles. However, the field was not perfectly uniform. A deviation for the 'pure' ϕ direction was observed close to the coils. The effect of this deviation on the track of the charged particles was minimized by the circular inner shape of the coils. Figure 2.15 (right) shows the field mapping. The toroidal arrangement also geometrically divided the ϕ angle of CLAS into six symmetric sectors such that a particle that left the target and entered a sector remained within that sector.

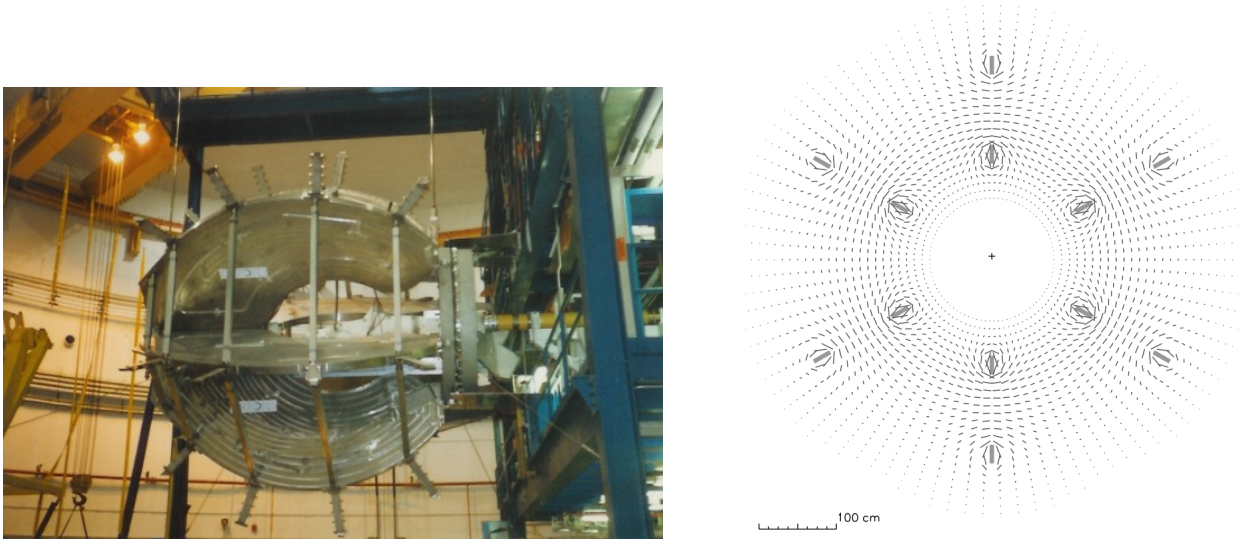

Figure 2.15: (Left) A picture of the Torus magnet during installation in Hall B. The kidney-shaped superconducting coils are shown in the picture. (Right) A map of the magnetic field vectors on a plane which is perpendicular to the beam line and centered on the target. The length of each line segment is proportional to the magnetic field strength at that point. The field vectors primarily point in the ϕ direction. The gray bars are the six coils in the cross section. Image sources: [54], [55].

The magnet was 5 m in diameter and 5 m long. The superconducting coils had four layers of 54 turns of aluminum-stabilized NbTi/Cu conductor. The coils were cooled to a temperature of 4.5 K by forcing super-critical helium through cooling tubes which were located at the edge of the windings. The Torus magnet was capable of handling a maximum current of 3860 A, which provided a magnetic field of 2.5 T in the forward direction and 0.6 T in the orthogonal direction. When the current was positive (negative), the magnetic field bent the negatively-charged particles towards (away) the beam line. The data collected in such configuration are referred to as inbending (outbending) data. The g9b data were inbending data taken at a Torus current of 1920 A.

2.5.2 Start Counter

Immediately surrounding the target assembly was a start counter. Its high timing resolution enabled an accurate determination of the start time for every trigger recorded by CLAS as well as each event's time. This information was utilized to calculate the $\beta = v/c$ of the final state charged particles, as will be discussed in Section 3.3.3. The start counter was divided into six sectors, each consisting of four 502 mm long scintillating paddles (see Figure 2.16). The resolution at the straight

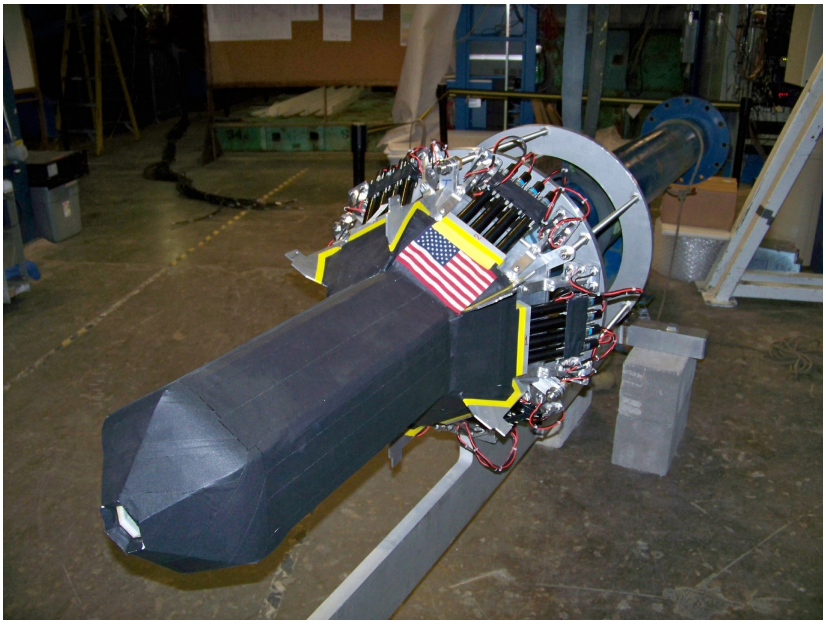

Figure 2.16: A picture of the Start Counter outside of CLAS. Each scintillator paddle was tapered to form a 'nose' at one end and attached to an acrylic light guide and a photomultiplier tube (PMT) on the other end. The PMT converted photon signals, originating from the interaction of charged particles with the scintillator as they traveled through them, into an amplified electric signal. Image source: [55].

section of each scintillator was ~ 290 ps while it was ~ 320 ps at the 'nose' portion. Further details are available in [56].

2.5.3 Drift Chambers

The Drift Chambers (DC) [57] were a sub-detector of the CLAS system, which were used to track charged particles as they traveled under the influence of the toroidal magnetic field. From the curvature of the trajectory of the charged particle, its momentum could be determined. The drift chambers were divided into six sectors in order to match the CLAS geometry and each sector was further divided into three regions based on the strength of the magnetic field, as shown in Figure 2.17. Region 1 was placed inside the Torus coils where the magnetic field was weak. Region 2 was mounted in between the coils, a region where the magnetic field was the strongest. Region 3 was positioned outside of the coils, where the magnetic field was weak again. This region tracked

the end-part of the particle's trajectory in the DC. This arrangement provided an angular coverage of 8° to 142° in the polar angle and an 80% coverage in the azimuthal angle.

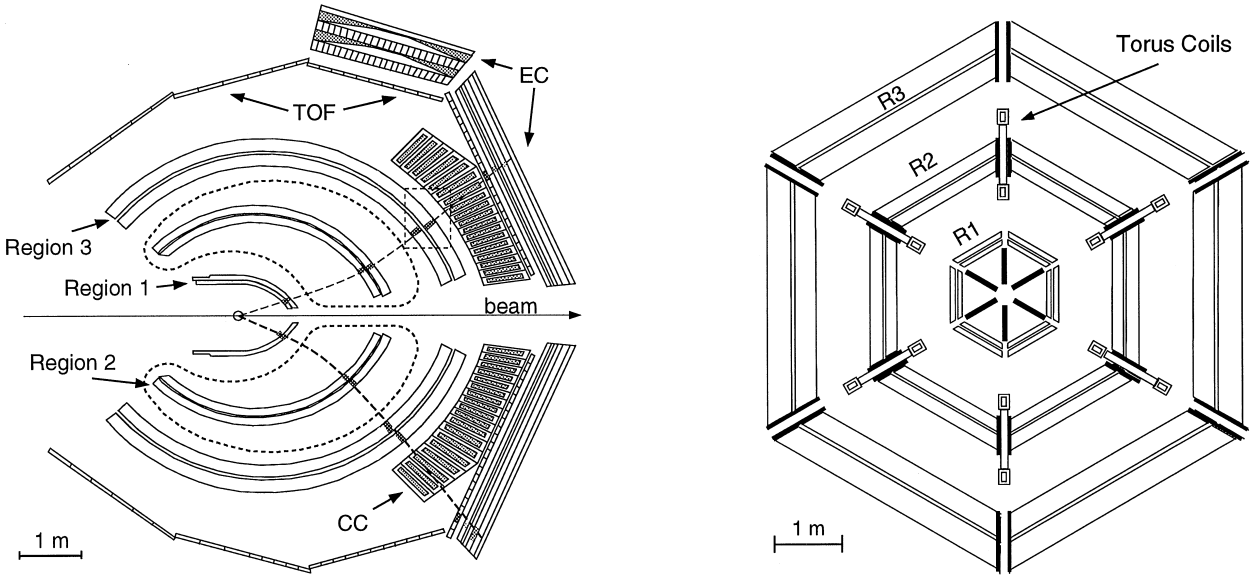

Figure 2.17: Schematic diagrams showing the arrangement of the three regions of the drift chambers in CLAS. (Left) A side view. The dotted lines show the projection of the Torus coils onto this plane. Also shown are the trajectories of two charged particles traversing the CLAS spectrometer. Notice the bend in their paths as they travel through the magnetic field of the drift chambers. (Right) A cross section perpendicular to the beam line showing the position of the three regions labeled 'R1', 'R2' and 'R3' with respect to the Torus coils. The six-fold symmetry of the chambers about the beam axis is visible in the diagram. Image source: [57].

Each region of the drift chamber consisted of layers of wires. In order to optimally fill the wedge-shaped volume between the Torus coils, the wires were run between two endplates, where each end plate was parallel to its neighboring coil's plane. The two end plates were thus tilted at 60° with respect to each other. This design led the wire directions to be almost perpendicular to the particle tracks, thus providing maximum sensitivity to the track's curvature. The wires were arranged in 'layers' of concentric circles. These layers were grouped into two 'superlayers', with each superlayer consisting of six layers of drift cells, as shown in Figure 2.18. The first superlayer was axial to the magnetic field, and the second was tilted at a 6° stereo angle around the radius of each layer to provide azimuthal information. The wires in each superlayer were arranged in a quasi-hexagonal pattern or cell with six 140 micron field wires made of gold-plated aluminum and one 20 micron

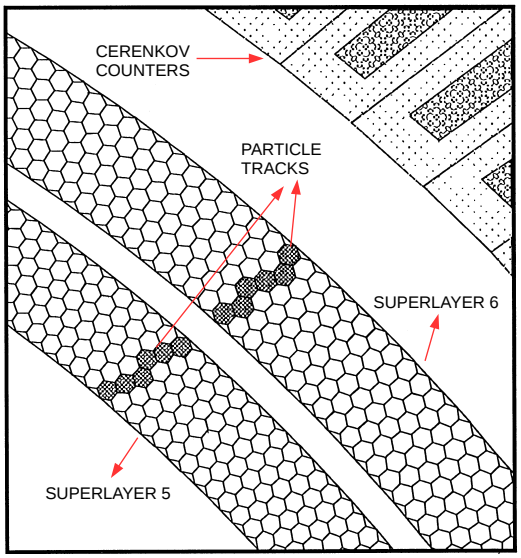

Figure 2.18: A schematic diagram showing the superlayers of Region 3 of the drift chambers. The shaded region shows the particle's trajectory as recorded by the (hexagonal) cells of the superlayers. Image source: [57].

sense wire made of gold-plated tungsten. The sense wire in each cell was kept at a positive potential, while the field wires were kept at a negative voltage. The hexagonal configuration offered a fair approximation of the ideal scenario of having circular cells in which the drift time to drift distance was independent of direction. This was a desirable feature in CLAS since the charged particles traveled through the chambers in all directions. The overall configuration contained $35,148$ sense wires. The chambers were filled with a 90% Argon and 10% carbon-dioxide mixture, due to its ionization properties and non-flammable nature.

2.5.4 Time-of-flight Scintillators (TOF)

As the name suggests, this sub-detector system provided the time at which the charged particles hit the TOF scintillators after traveling through the drift chambers. This information, when combined with the event start time at the target (from the Start Counter), provided the 'time-of-flight' through the toroidal magnetic field. Using this information and the track length from the drift chambers, the velocity of the charged particles was determined. The velocity and momentum of the particle, where the latter was determined by the drift chambers as discussed in the previous section, allowed the determination of the particle's mass. Furthermore, the charge was determined

by observing whether the particle bent towards or away from the beam line. Thus, the particle could be identified. The TOF counters had an angular coverage of 8° to 142° in the polar angle and nearly full coverage in the azimuthal angle.

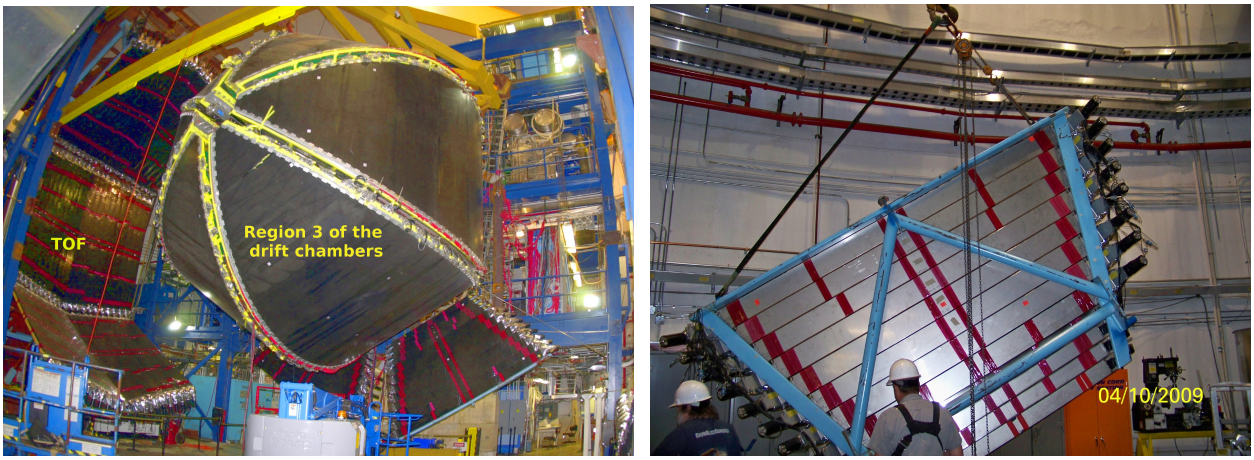

Figure 2.19: (Left) A photograph showing the time-of-flight detector as it was pulled away from the CLAS assembly during a maintenance period. (Right) A picture of a section of a time-of-flight panel during installation. Note the photomultiplier tubes attached to the ends of the scintillating paddles. Image sources: [45], [55].

The TOF detector was located approximately four meters from the target assembly. Like the other CLAS sub-detectors, the TOF system was divided into six panels, each containing 57 scintillating paddles of varying lengths and widths made of Bicron BC-408. Each bar was made two inches thick to provide 100% detection efficiency of minimum ionizing particles. Each end of the scintillator was connected to a photomultiplier tube (PMT). Figure 2.19 shows the TOF panels. The panels were positioned in a manner that placed each scintillator perpendicular to the particle tracks on an average. When a scintillator was hit by a particle, it absorbed its energy and scintillated, leading to creation of photons. The photons traveled through the scintillator into the PMTs which were attached to its ends. There the photon signal was converted into an electric signal and was amplified. The design provided an excellent timing resolution of 80 ps for the short counters and 160 ps for the long counters, surpassing the initial CLAS requirements. Full details on the TOF system is provided in [58].

2.6 The Beamline Devices

A number of beamline devices were placed upstream and downstream from the CLAS spectrometer to monitor the quality of the electron and the photon beam. The upstream devices monitored the beam quality. For example, the electron beam position monitors were used to monitor the x and y positions of the beam as well as the beam intensity. They inserted this information into the data stream every 20 s. Two electron beam monitors were used in photoproduction experiments such as FROST: one positioned just upstream of the goniometer and the other positioned just upstream of the tagger. The profile of the electron beam was determined using three Beam Profile Monitors, also known as Harp Scanners, located upstream of the CLAS target. These scanners were made of tungsten and iron crossed wires. To determine the beam profile, the scanners were moved across the beam line in the two perpendicular directions. Electrons scattered by the wires were detected by PMTs arranged around the beam line, and the distribution of the scattered electrons as a function of the wire position was used to determine the beam profile. Since this method involved intercepting the electron beam before it hit the target, it was performed in special runs. For the photon beam, a harp made of scintillating fibers was used downstream of the CLAS target.

The devices placed downstream of the CLAS detector, such as the Total Absorption Shower Counter (TASC), were used to measure the photon flux. Since these devices were not used in this analysis (see Section 3.8 for the photon flux determination in FROST-g9b), they will not be discussed here. Further details on the beamline devices are available in [54].

2.7 The g9b Trigger

Each sub-detector of CLAS had its own set of electronics to read out signals collected by it. However, not every signal measured by the individual sub-detectors corresponded to a physics event of interest. Instead, they could have potentially risen from cosmic rays, malfunctioning electronics etc. Therefore, to record only physics events and also minimize the dead time of the data acquisition system, a two-level trigger was employed in g9b. The Level 1 trigger required a hit in the same sector of both the Start Counter and the TOF. The Level 2 trigger required hits in at least four out of six superlayers of the drift chambers (so that the particle's trajectory could be reconstructed) in the same sector as the Level 1 trigger. This prevented recording false events, such as a cosmic ray event, which had accidental start counter and TOF coincidences. The Level 2 trigger, whose

processing time contributed directly to the dead time of the detector, was designed to be fast without compromising the accuracy with which the tracks were found in the drift chambers. In summary, for an event to be recorded, the two-level trigger system required the detection of at least one final-state charged particle's track in CLAS with momentum information. The trigger system is discussed in details in [54].

2.8 The Data Acquisition System (DAQ)

Once the trigger conditions were met, the DAQ wrote the detected signals to a magnetic tape. Events were recorded at a rate of $3 - 4$ kHz with a DAQ dead time (that is, the time when it was busy recording an event) of $15 - 20\%$. The average event size was about $3 - 5$ kB. Full information on the DAQ design and performance is available in [54]. The raw data containing electric signals from each detector, such as QDC (Charge to Digital Convertor) and TDC (Time to Digital Converter) channel IDs and values, were recorded on the tape in Bank Object System (BOS) format. In the next step, the raw data were converted into usable information such as momenta, angles, energies of the particles using reconstruction codes. Section 3.1 will further elaborate on the event reconstruction and selection. A total of 15.5 billion events were recorded in FROST-g9b (see g9b_runlist).

CHAPTER 3

EVENT SELECTION

3.1 The FROST Data Sets

This section summarizes the experimental conditions of the FROST data sets. The FROST experiment was carried out in two separate data-taking periods, FROST-g9a and FROST-g9b, based on the polarization of the target. The g9a experiment used a longitudinally-polarized target. Data for this experiment were taken between November 3th, 2007, and February 12th, 2008. In the g9b experiment, the target was transversely polarized. This experiment was performed from March-August 2010. Both g9a and g9b data sets were further divided into two major parts according to the polarization type of the incident photon beam: circular and linear polarization.

The data sets which have been used in this analysis of $\gamma p \to p\,\pi^+\pi^-$ and $\gamma p \to p\,\omega$ are shown in Table 3.1. The Tables 3.2, 3.3 (g9b - linear beam polarization) and 3.4 (g9b - circular beam polarization) show the experimental run conditions at which these measurements were performed. For the full details, see g9b_runlist. The data sets with a circularly-polarized photon beam were broken up into five different periods. [1]

Target magnet quench: On July 2, 2010, the target magnet accidentally quenched owing to a power outage in Hall C. This incident occurred right after completing the data acquisition of those g9b data sets which utilized a linearly-polarized photon beam. Due to the quench, the target

[1] A period was defined as a group of runs with similar conditions, such as the same target polarization or 1/2-wave plate status.

Table 3.1: The FROST data sets used in this analysis of $\gamma p \to p\,\pi^+\pi^-$ and $\gamma p \to p\omega$ reactions are indicated by ✓ marks.

Reaction	Transverse Target Polarization (g9b)	
	Linear Beam Polarization	Circular Beam Polarization
$\gamma p \to p\,\pi^+\pi^-$	✓	-
$\gamma p \to p\,\omega$	✓	✓

warmed up rapidly leading to a loss of the target polarization. Some quick fixes were carried out in order to resume data taking at the earliest possible. The quality of the data following the quench was studied in [59]. It was observed that the data taken after the quench had more background rendering the analysis more challenging. For this reason and the fact that the statistics of those data sets was fairly small, we did not include the post-quench data in our analysis.

The information included in the raw data consisted of QDC (Charge to Digital Convertor) and TDC (Time to Digital Converter) channel IDs and values. In a first step, the data had to undergo reconstruction, or be *cooked.* This process converted the data into physical quantities like particle IDs, positions, angles, energies, and momenta. The data calibration was carried out independently for each detector component of CLAS. After the detectors had been calibrated and the particle tracks had been reconstructed, the data were made available for physics analysis. Each event has its information organized in CLAS data banks [2]. These data banks contain not only the properties of the particles involved in a reaction but also information about detector hits.

Here we list some data banks that we will refer to in the later sections:

1. **GPID** [60] - This bank contains most of the details about the detected particles and the initial photon(s), such as the particle IDs, 4-vectors, β values ($= \frac{v}{c}$) of the particles, vertex of each particle, photon energy and other information from various detectors (like the Tagger, Time-of-Flight spectrometer, Start Counter and Drift Chambers).

2. **TAGR** - In this bank, information about all incident photons is stored. It comprises the energy of the photon(s), the time of the photon(s) after it was reconstructed in the Tagger, the time of the photon(s) after the RF correction, status of the photon(s) (used to identify which ones were not reconstructed properly), and the E- and T-counter ID information of the corresponding scattered electron.

3. **MVRT** - The MVRT bank contains event-vertex information. It was obtained by using tracking information (from the drift chambers and the time-of-flight scintillators) of each detected particle that constituted the event.

[2] http://clasweb.jlab.org/bos/browsebos.php?bank=gpid&build=64bit/STABL

Table 3.2: The experimental conditions of the g9b data sets with a linearly-polarized beam and a transversely-polarized target for the coherent edges at 0.9, 1.1, 1.3, 1.5, 1.7 GeV. The 200-MeV wide E_γ range right below the coherent edge was used in the analysis. In the column *"Target Pol. Sign"*, the first sign refers to the overall sign of the target polarization (+ or −) if the polarization was pointing away from (towards) the floor. The two signs within the brackets are the NMR and the holding magnet signs, respectively. PARA (PERP) denotes that the photon's electric field oscillated in a plane parallel (perpendicular) to the lab floor. AMO denotes data collected using unpolarized photons. This data was not used in our analysis.

Coherent Edge [GeV]	E_{e^-} [GeV]	Target Pol. Sign	Dates (in 2010)	Runs	Beam Pol. Setting	Total Events
0.9	3.08173	+(−, −)	04/19 - 04/24	62706 - 62761	PARA	214.2 M
					PERP	222.9 M
					AMO	70.5 M
		−(−, +)	04/29 - 05/03	62815 - 62844	PARA	144.8 M
					PERP	120.1 M
					AMO	30.0 M
1.1	3.08173	+(−, −)	04/24 - 04/27	62762 - 62796	PARA	242.1 M
					PERP	237.0 M
					AMO	40.4 M
		−(−, +)	04/27 - 04/29	62798 - 62814	PARA	121.5 M
					PERP	120.3 M
					AMO	42.2 M
1.3	3.08173	−(−, +)	05/03 - 05/06	62846 - 62876	PARA	209.5 M
					PERP	223.2 M
					AMO	54.5 M
		+(−, −)	05/15 - 05/18	63013 - 63059	PARA	376.7 M
					PERP	265.4 M
					AMO	73.2 M
1.5	5.07827	−(−, +)	05/07 - 05/11	62881 - 62953	PARA	357.6 M
					PERP	331.3 M
					AMO	98.6 M
		+(−, −)	05/11 - 05/15	62958 - 63012	PARA	237.3 M
					PERP	328.2 M
					AMO	76.1 M
1.7	5.07827	−(−, +)	05/18 - 05/22	63060 - 63118	PARA	372.4 M
					PERP	376.0 M
					AMO	83.2 M
		+(+, +)	05/27 - 06/01	63168 - 63220	PARA	344.1 M
					PERP	365.1 M
					AMO	79.9 M

Table 3.3: Experimental conditions of the g9b data sets with a linearly-pol. beam and a transversely-pol. target for the coherent edges at 1.9 & 2.1 GeV. The 200-MeV wide E_γ range right below the coherent edge was used in the analysis. In the column "Target Pol. Sign", the first sign refers to the overall sign of the target polarization (+ or −) if the polarization was pointing away from (towards) the floor. The two signs within the brackets are the NMR and the holding magnet signs, respectively. PARA (PERP) denotes that the photon's electric field oscillated in a plane parallel (perpendicular) to the lab floor. AMO denotes data collected using unpolarized photons. This data was not used in our analysis. Note that the $E_{e^-} = 5.57$ GeV data for these two coherent edges were also not used in the analysis because the tables to determine the degree of beam polarization were not available.

Coherent Edge [GeV]	E_{e^-} [GeV]	Target Pol. Sign	Dates (in 2010)	Runs	Beam Pol. Setting	Total Events
1.9	5.07827	−(−,+)	05/22 - 05/25	63119 - 63152	PARA	240.6 M
					PERP	199.2 M
					AMO	56.9 M
		+(+,+)	05/26 - 05/27	63154 - 63167	PARA	39.9 M
					PERP	82.5 M
					AMO	20.1 M
		+(+,+)	06/01 - 06/08	63221 - 63279	PARA	336.8 M
					PERP	272.3 M
					AMO	76.9 M
		−(−,+)	06/08 - 06/11	63281 - 63305	PARA	162.5 M
					PERP	166.1 M
					AMO	51.1 M
	5.57203	+(−,−)	06/28 - 06/29	63430 - 63441	PARA	35.9 M
					PERP	76.8 M
					AMO	10.4 M
		−(−,+)	06/29 - 06/30	63447 - 63454	PARA	61.1 M
					PERP	59.9 M
					AMO	10.0 M
2.1	5.07827	−(−,+)	06/11 - 06/15	63306 - 63348	PARA	243.7 M
					PERP	266.7 M
					AMO	60.2 M
		+(−,−)	06/15 - 06/21	63349 - 63404	PARA	314.6 M
					PERP	302.1 M
					AMO	88.0 M
	5.57203	+(−,−)	06/23 - 06/27	63407 - 63429	PARA	150.9 M
					PERP	156.5 M
					AMO	39.1 M
		−(−,+)	06/30 - 07/02	63455 - 63465	PARA	79.4 M
					PERP	40.5 M
					AMO	10.2 M

Table 3.4: The g9b data sets with a circularly-polarized photon beam and a transversely-polarized target, classified according to a wide variety of characteristics. The data are grouped in periods with similar run conditions. Each period contains data with both beam helicities (i.e., helicities parallel or antiparallel to the beam axis). In the "Target Pol. Sign" column, the two signs within brackets are the NMR and the holding magnet signs, respectively. The target polarization is given by the sign outside the brackets (+ or −) if the polarization was pointing away from (toward) the laboratory floor.

Target Pol. Type	Electron Beam Energy [GeV]	Dates	Target Pol. Sign	Runs	Period
Transverse (FROST-g9b)	3.082	03/19/10 - 03/23/10	$+(+,+)$	62207 - 62289	1
		03/24/10 - 03/30/10	$-(-,+)$	62298 - 62372	2
		03/30/10 - 04/05/10	$+(+,+)$	62374 - 62464	3
		04/07/10 - 04/13/10	$-(+,-)$	62504 - 62604	4
		04/13/10 - 04/19/10	$+(-,-)$	62609 - 62704	5

3.2 Reaction Channel and General Event Selection

The reaction channels of interest in this analysis are $\gamma p \to p\,\pi^+\pi^-$ and $\gamma p \to p\omega \to p\,\pi^+\pi^-\,(\pi^0)$. These three-track channels were broken up into different topologies as shown in Table 3.5. A topology is defined according to the detected particles in the final state: the two-particle final states (Topologies 1-3) and the three-particle final states (Topologies 4-5). A particle which was not detected in a given topology could be identified through the missing-mass technique. For this method, the Lorentz vectors of the incoming beam and the target were used. The four-momentum of a missing particle in the reaction was then determined from the measured three-momenta and the particle energies. The missing four-momentum was given by:

$$x^\mu \;=\; k^\mu \;+\; P^\mu \;-\; \sum_{i=1}^{2,3} p_i^\mu \,, \tag{3.1}$$

where k^μ and P^μ are the initial photon and target-proton four-momenta and p_i^μ are the four-momenta of the two or three detected final-state particles. The missing mass m_X was defined as:

$$m_X^2 \;=\; x^\mu x_\mu \,. \tag{3.2}$$

The missing-mass distribution was used for a data quality check after all corrections and cuts had been applied. The four-momentum vector x^μ in Equation 3.1 was used to complete the set of four-vectors for the Topologies 1, 2, 3 and 5 (Table 3.5).

Since the FROST experiment used a trigger which required at least one charged particle in CLAS, the trigger file allowed for the recording of a large variety of events. In order to analyze the specific topologies of the reaction $\gamma p \to p\,\pi^+\pi^-$, events were pre-selected based on the particles' identification number (PID), which was determined during the cooking process. Events that did not meet this requirement (Table 3.5) were ignored and subsequently omitted from the analysis. The calculation of the detected particles' masses, which was necessary to determine the PIDs of, used two independently-measured quantities, the momentum (p) and the velocity as a fraction of the speed of light (β). The magnitude of a particle's momentum was determined with an error of $< 1\,\%$ using information from the CLAS drift chambers (DC) [54]. The β of a detected final-state particle was determined with an error of up to $5\,\%$ [54] using a combination of the Start Counter (SC), the Time of Flight (TOF) spectrometer, and the particle's trajectory through CLAS. The detected particle's mass can then be calculated by:

$$m^2_{\text{particle } X} = \frac{p^2\,(1 - \beta^2)}{\beta^2}\,. \tag{3.3}$$

After the particle's mass had been calculated, it was compared to the masses of known particles (hadrons and leptons). If this calculated mass matched that of a known particle (within resolution),

Table 3.5: Classification of the reactions, $\gamma p \to p\,\pi^+\pi^-$ and $\gamma p \to p\,\omega \to p\,\pi^+\pi^-\,(\pi^0)$, using different topologies. Reconstructed particles were identified by their PID information from the GPID bank. We did not analyze Topology 3 because such events could not be distinguished from γn events.

Reaction	Topology	Reconstructed Particles				Missing Particle of Interest
		Total	p	π^+	π^-	
$\gamma p \to p\,\pi^+\,(\pi^-)$	1	2	1	1	0	m_{π^-}
$\gamma p \to p\,\pi^-\,(\pi^+)$	2	2	1	0	1	m_{π^+}
$\gamma p \to (p)\,\pi^+\pi^-$	3	2	0	1	1	m_p
$\gamma p \to p\,\pi^+\pi^-$	4	3	1	1	1	0
$\gamma p \to p\,\omega \to p\,\pi^+\pi^-\,(\pi^0)$	5	3	1	1	1	m_{π^0}

the PID associated with that mass was assigned to the final-state particle. This value could then be used to select certain final-states for analysis. In this analysis, the physical properties of the final-state particles (e.g. their 4-vectors, vertex information, etc.) were extracted from the GPID data bank. Photon and final-state particle selection was further improved by applying cuts and corrections (Section 3.3). We also used kinematic fitting (Section 3.5) to fine-tune the initial- and final-state momenta by imposing energy- and momentum conservation. Finally, to separate signal events from the remaining background, we used an event-based Q-factor method which is discussed in more details in Section 3.9.

Listed below in a short summary are the cuts and corrections that were applied to the FROST-g9b data in this analysis:

Cuts

- ◇ Vertex cuts:
  - (−3.0 - 3.0 cm) Butanol, (7.5 - 11.0 cm) C, (14.0 - 18.0 cm) CH_2
- ◇ Photon selection & accidentals (GPID[ ]. NGRF = 1 & GPID[ ].TAGRID equal for all tracks)
- ◇ Particle selection: $\Delta\beta = |\beta_{\mathrm{c}} - \beta_{\mathrm{m}}| \leq 3\sigma$
- ◇ Kinematic fitting: Confidence-level cut of CL > 0.001 for $\gamma p \to p\,\omega \to p\,\pi^+\pi^-\,(\pi^0)$

Corrections

- ◇ Time-of-Flight corrections
- ◇ Tagger-sag corrections (done in the cooking)
- ◇ ELoss corrections
- ◇ Momentum corrections
- ◇ Lab azimuthal angle corrections

The order in which these were applied to the data was quite flexible except for a few cases. For example, the time-of-flight corrections had to be applied before the β cuts. Momentum corrections were determined and applied after ELoss corrections. The following sections describe the cuts and corrections.

3.3 Photon and Particle Identification

3.3.1 Initial-Photon Selection (Cuts on Timing and Accidental Photons)

The electrons, which were used to produce the beam of polarized photons via bremsstrahlung radiation, were delivered from the accelerator into Hall B in the form of 2 ns bunches. Since each bunch contained many electrons, there were several potential photon candidates per recorded event that could have triggered the reaction inside the target. Random electron hits could also occur from various background sources (e.g. cosmic rays). These did not create bremsstrahlung photons but the hits were registered in the tagger scintillators. It was important to determine the correct photon in each event (out of about five candidates on average) because the corresponding photon energy was key to understanding the initial state of the event. The analysis steps taken in the photon selection were as follows:

1. The Start Counter time per track at the interaction point, t_{track}, was given by:

$$t_{\text{track}} = t_{\text{ST}} - \frac{d}{c\,\beta_{\text{calc}}}\,, \tag{3.4}$$

where t_{ST} was the time when the particle was detected by the Start Counter, d was the length of the track from the interaction point to the Start Counter [3], and $c\,\beta_{\text{calc}}$ was the calculated velocity of the particle. These (track) times can be averaged to give an event time, t_{event}.

The time at which a candidate photon arrived at the interaction point, t_γ, was given by:

$$t_\gamma = t_{\text{center}} + \frac{d'}{c}\,, \tag{3.5}$$

where t_{center} was the time at which the photon arrived at the center of the target and d' was the distance between the center of the target and the event vertex along the beam-axis. We did not consider the x- and y-coordinates of the event vertex because they were comparable to the vertex resolution. In this analysis, the t_γ values were obtained from GPID[].TPHO.

Both, t_γ as well as t_{event}, describe the time of the γp interaction – based on initial- and final-state particles, respectively. To find the correct initial photon, we can look at the corresponding time differences. The *coincidence time*, Δt_{TGPB}, was thus defined per photon as the difference between the Tagger time and the Start Counter time at the interaction point, $t_{\text{event}} - t_\gamma$. Since each event had several candidate photons, several Δt_{TGPB} values were available, which could be obtained from the TGPB bank. Figure 3.1 (left) shows an example distribution of the coincidence times, Δt_{TGPB}. The figure clearly shows the 2 ns

[3] The values of t_{ST} and d can be obtained from the GPID[].ST_TIME and GPID[].ST_LEN, respectively.

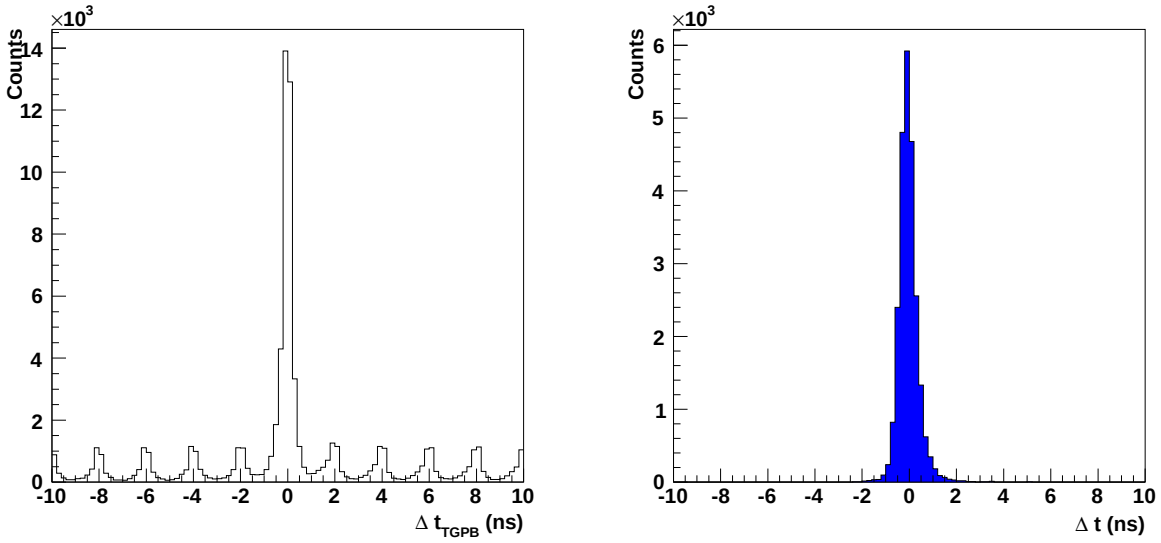

Figure 3.1: (Left) Example of a coincidence-time distribution, Δt_{TGPB}, from FROST-g9b (linear beam polarization) after applying all $\gamma p \to p\,\pi^+\pi^-$ topology and vertex cuts (events originated from the butanol target). The 2 ns bunching of the photon beam is clearly visible in the histogram. (Right) Distribution of $\Delta t = t_{\mathrm{event}} - t_\gamma$ for the selected photon (one entry per event). The event vertex time, t_{event}, was based on Equation 3.4; topology and vertex cuts were applied (see text for more details). We only considered events which had exactly one candidate photon in the same RF bucket per track; each identified track had to be associated with the same photon.

bunching of the photons that arrived at the target. For each track, the candidate photon that had the smallest coincidence time was determined and its energy and timing information, t_γ, were written to the track's GPID bank. The total number of photon candidates per track was also available. The photon selection itself was performed by the CLAS offline software in the cooking process. In this analysis, we used the energy of the selected photon but did not apply any further timing cuts.

2. Occasionally, events could have more than one candidate photon with $|\Delta t_{\mathrm{TGPB}}| < 1$ ns. In such cases, the photon selection cannot be made based on their time information. The fraction of these events is about $8-10\,\%$ in the FROST experiment. To prevent any ambiguity, only events with exactly one photon candidate in the same RF bucket for all selected tracks (GPID[].NGRF $= 1$) were considered in this analysis. In addition, we also ensured that the selected photon was the same for all reconstructed tracks (GPID[].TAGRID equal for all tracks). Figure 3.1 (right) shows an example of the coincidence time distribution for the selected initial photon (one entry per event).

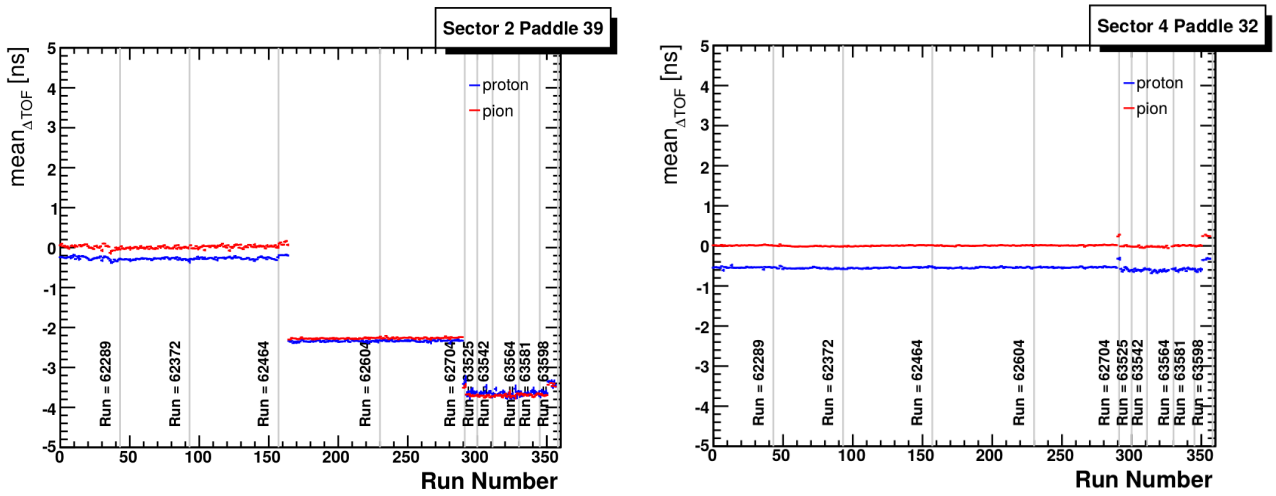

Figure 3.2: Time offsets, $\Delta(TOF)$ [ns], of protons (blue line) and pions (red line) versus run number [61]. (Left) Example for TOF Paddle 39, Sector 2. (Right) Example for TOF Paddle 32, Sector 4. The offsets vary with runs and are sometimes different for the different particles.

3.3.2 Time-of-Flight (TOF) Corrections

The FROST-g9b data sets required additional time-of-flight corrections at the analysis stage due to a laser-system malfunction which initially led to poor time-walk corrections. The collaborators at the University of South Carolina performed a detailed study [61] of time-of-flight offsets per paddle in every sector based on g9b runs with a circularly-polarized beam. Figure 3.2 shows the variation in the offsets of protons and pions for TOF Paddle 39 (Sector 2) and Paddle 32 (Sector 4) as examples. The offsets vary with run number and are sometimes even different for protons and pions. The TOF offsets were calculated according to:

$$\Delta(TOF) = \frac{d}{\beta_{\rm c}} - \frac{d}{\beta_{\rm m}}, \tag{3.6}$$

where d was the distance between the event vertex and the TOF paddle, $\beta_{\rm c}$ was calculated using the momentum and assumed mass of the particle, and $\beta_{\rm m} = \frac{v}{c}$ was determined from the TOF paddle and Start Counter information. The collaborators at the Catholic University of America determined the offsets for the FROST-g9b runs that utilized a linearly-polarized photon beam and also developed offline code [62] for all g9b runs to correct the observed offsets based on energy loss in the poorly-calibrated TOF paddles. Here is a short description of the procedure employed for the corrections [63]:

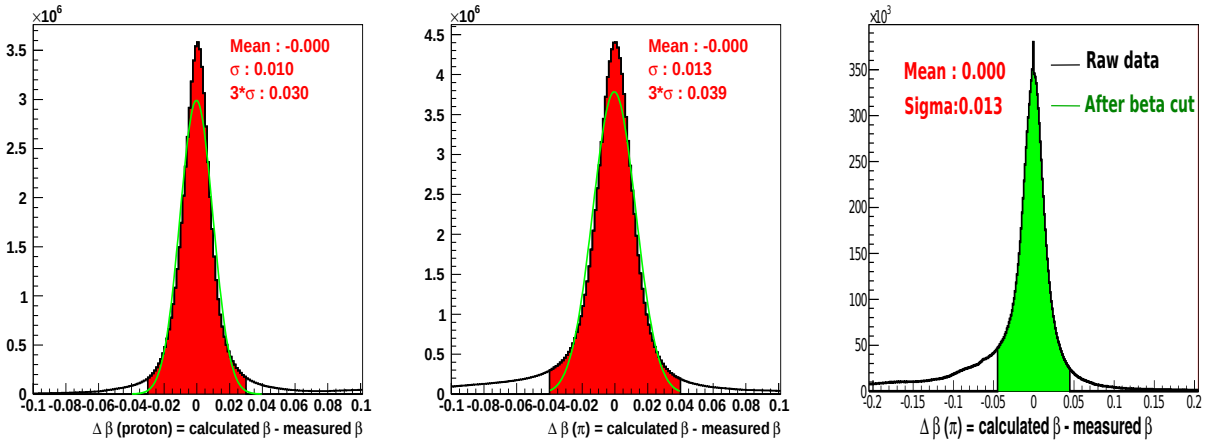

Figure 3.3: Distributions of $\Delta\beta = \beta_{\rm c} - \beta_{\rm m}$ for protons (left) as well as π^+ and π^- (right) from g9b experiment, where $\beta_{\rm c}$ was calculated based on the particle's assumed mass. Events in the center peak filled in red were selected after applying the $|\beta_{\rm c} - \beta_{\rm m}| \leq 3\sigma$ cut. See text for more details. The green distribution shows $\Delta\beta$ for pions before the time-of-flight corrections.

- Identify the double-pion reaction $\gamma p \to p\,\pi^+\pi^-$. This reaction has excellent statistics and is thus ideally suited for these studies.
- Determine the time offsets (time-shift corrections) and re-calculate the measured $\beta_{\rm m}$.
- Fit the *energy loss (dE) versus momentum* spectra of protons and pions for TOF and Start Counter paddles. Identify the proton and pion bands.
- Re-calculate $\Delta(TOF)$ using the new $\beta_{\rm m}$, and fit $\Delta(TOF)$ *versus energy loss* for the SC (TOF) paddles to determine an empirical 'time-walk' correction function.

In this analysis, we used the correction function – #include TSCtimeCorr.h – to simply determine the *corrected* $\beta_{\rm m}$ values as input to $\Delta\beta$ cuts in the selection of final-state tracks (Section 3.3.3).

3.3.3 Proton and Pion Selection

The photon energy for each event was selected according to the procedure outlined in Section 3.3.1. In the next step, the identification of the final-state particles, proton, π^+, and π^-, was needed. As mentioned in Section 3.2, we initially used particle ID information from the GPID bank and selected those events which belonged to the topologies of our interest (Table 3.5). For a more refined selection of the particles, we used the information on the measured and calculated β values

of each particle. The GPID bank contained the CLAS-measured momentum of a particle; a theoretical value, $\beta_{\rm c}$, for that particle could then be calculated from this measured momentum and an assumed mass. The β_c values for all possible particle types were compared to the CLAS-measured empirical $\beta_{\rm m} = \frac{v}{c}$ value. Particle identification then proceeded by choosing the calculated $\beta_{\rm c}$ closest to the measured $\beta_{\rm m}$. It must be mentioned that for the FROST-g9b runs, $\beta_{\rm m}$ was calculated after applying the TOF corrections discussed in the previous Section 3.3.2. Figure 3.3 shows the differences, $\Delta\beta = \beta_{\rm c} - \beta_{\rm m}$ for g9b runs. The red distributions represent our final results, whereas the green distribution (for pions) represents $\Delta\beta$ before the TOF corrections. The improvement is clearly visible, the $\Delta\beta_\pi$ peak is more symmetric and the spike at *zero* disappeared. Assuming a mass m for the particle, $\Delta\beta$ was given by:

$$\Delta\beta \;=\; \beta_{\rm c} \;-\; \beta_{\rm m} \;=\; \sqrt{\frac{p^2}{m^2 \,+\, p^2}} \;-\; \beta_{\rm m}\,. \tag{3.7}$$

The prominent peaks around $\Delta\beta = 0$ shown in Figure 3.3 correspond to the particles of interest. As is clearly seen in the figures, $\Delta\beta$ for the pions is broader than for the protons and a long tail

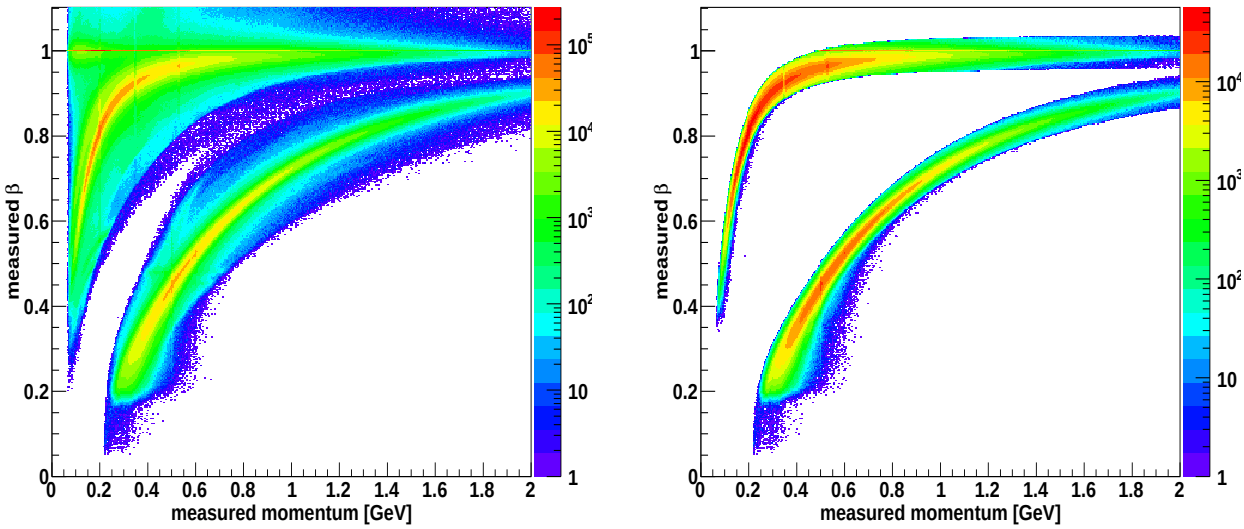

Figure 3.4: (Left) The measured $\beta_{\rm m}$ versus the measured momentum taken from GPID on a logarithmic color scale. Notice a thin horizontal line at one for electrons, and the broad stripes for pions (top) followed by protons (bottom). (Right) The measured $\beta_{\rm m}$ versus the measured momentum after applying the 3σ cut based on the difference $\Delta\beta \;=\; \beta_{\rm c} \;-\; \beta_{\rm m}$. Clean pion and proton bands are visible.

toward negative values for the pions is visible. When the GPID bank was created during the track reconstruction, electrons were not separated from pions. The long tail in the $\Delta\beta$ distributions for the pions represent these electrons which need to be filtered out. To identify the protons and pions, a loose cut on $|\beta_{\mathrm{c}} - \beta_{\mathrm{m}}|$ was applied. The cut was determined by fitting the main peak near $\Delta\beta = 0$ with a Gaussian and discarding all events outside a 3σ window, where σ was the Gaussian width. Thus, any event with a value of $|\Delta\beta|$ greater than 0.030 for the proton and 0.039 for the pions was filtered out of the FROST-g9b data sets. Figure 3.4 shows the measured momentum, p, versus the measured β_{m} for protons and pions before (a) and after (b) applying the $|\beta_{\mathrm{c}} - \beta_{\mathrm{m}}| < 3\sigma$ cut. The bands for the pions and protons (lower band) are clearly visible.

3.4 Vertex Cut

The FROST experiment had three different production targets and data were recorded simultaneously on all three of them: a butanol, a carbon, and a polyethylene target. The butanol target itself was 5 cm long and 3 cm in diameter. The carbon and polyethylene targets were 0.15 cm and 0.35 cm in length, respectively. The butanol target was located at the center of the CLAS spectrometer and the polyethylene target was located 16 cm downstream from the CLAS center. The carbon target was then placed further downstream at 9.5 cm. The z-vertex cuts applied in this analysis are shown in Table 3.6. The vertex cut in the x-y plane was chosen such that selected events originated no more than 3 cm from the z axis (beam line) (Fig. 3.5, left side).

Table 3.6: This table shows the z-vertex cut ranges which were applied in the FROST-g9b analysis to select events originating from the different production targets.

z-vertex range [cm]		
Butanol	C	CH_2
(−3.0, 3.0)	(7.5, 11.0)	(14.0, 18.0)

Figure 3.6 shows examples of event z-vertex distributions; the values were taken from the MVRT bank. The red line represents data containing all $p\,\pi^+\pi^-$ events, whereas the dashed blue line denotes the event distributions after the cuts on accidentals (Section 3.3.1) and $\Delta\beta$ (Section 3.3.3) were applied. The small peak between the carbon and the polyethylene target in g9b originated

from the end-cap of the heat shield. The carbon target resided inside the dipole magnet and the effect from a thin aluminized foil serving as the end-cap was visible as an additional small peak.

The vertex information in this analysis could be taken from either of the two banks, TBTR or MVRT. The difference in the vertex information came from the number of tracks used to reconstruct the vertex. The data in the TBTR bank was based on the vertex position of a single track, whereas the data in the MVRT bank represented event information (averaged vertex position) based on the tracking information of all available charged particles in the event. The MVRT vertex information was usually more accurate in multiple-track events (e. g. in double-pion photoproduction) since more tracks included in the reconstruction of the vertex location led to a higher degree of accuracy. In an ideal situation, both the TBTR and MVRT information should give similar results, which seemed to be a good approximation when looking at the vertex information for a larger data set. Figure 3.5 (right side) shows a *TBTR versus MVRT* z-vertex distribution. This plot was created using events which were selected after applying photon selection and $\Delta\beta$ cuts. The straight line for $V_z\ (TBTR) = V_z\ (MVRT)$ indicates the expected ideal situation, which was observed very well.

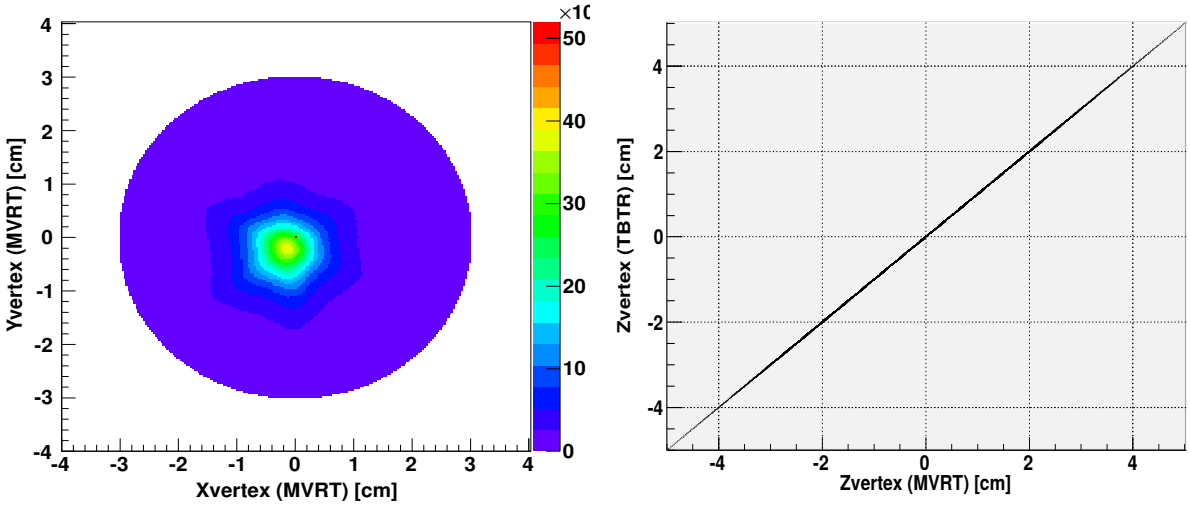

Figure 3.5: (Left) An example of a x- vs. y-vertex distribution from FROST-g9b data (900 MeV nominal coherent edge) based on $p\pi^+\pi^-$ events. A cut of $x^2 + y^2 < 9$ cm^2 was applied in the analysis. (Right) A comparison of the z-vertex reconstruction for the event from the MVRT bank and the z-vertex information for the proton from the TBTR bank is shown here. Photon selection cuts and $\Delta\beta$ cuts were applied before comparing the two vertex information. The straight line inclined at an angle of 45° showed that the two banks gave very similar results.

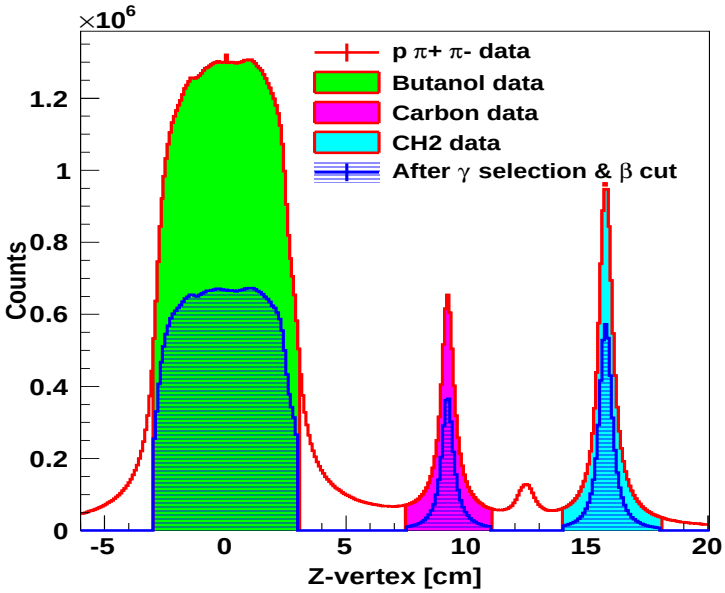

Figure 3.6: The z-vertex distribution (axis along the beam line) of all reconstructed particles in FROST-g9b; values from the MVRT bank. The positions of the three different targets are clearly visible. The small peak observed at ~ 12.5 cm originated from the end-cap of the heat shield. The red line denotes the data containing all $p\pi^+\pi^-$ events. The blue line denotes these events after applying cuts on accidentals and $\Delta\beta$.

The TBTR information for individual tracks was also available from the GPID banks. However, this analysis used the MVRT vertex information.

The use of the carbon target for signal-background separation: The carbon target was placed in the target cryostat to aid in the study of the background originating from bound nucleons in the butanol data. However, it was observed that the carbon target used in FROST-g9a was significantly contaminated with hydrogen. This effect manifested itself by the presence of a peak (around the pion mass) in the missing-pion mass distribution for events from the carbon target [64]. Figure 3.7 shows an example of the contamination using the $n\pi^+$ channel. The distribution from the ^{12}C target region showed a narrow peak at the mass of the neutron. Owing to the Fermi motion, such peaks should ideally be washed out and not be visible, as a broad enhancement at best. The source of the contamination remains unknown but it has been suspected to be due to a low-density build-up of ice (perhaps better: snow). The carbon data also suffered from low statistics. For these reasons, we developed an event-based method for the signal-background separation in the FROST

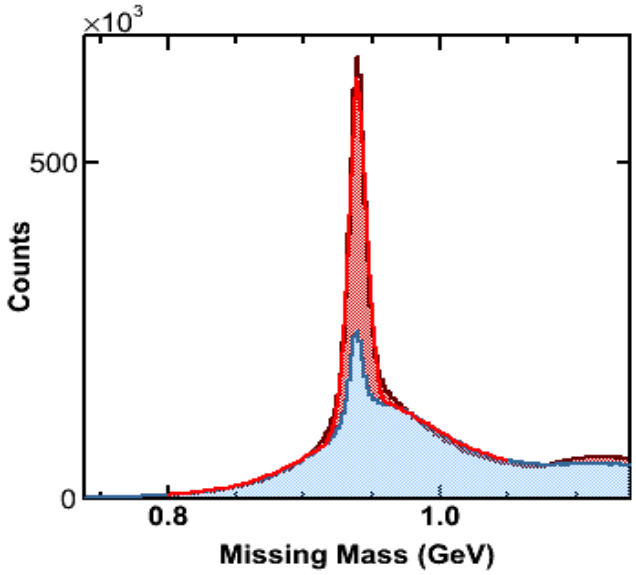

Figure 3.7: Example of a missing-mass distribution for the n π^+ channel from FROST-g9a data for $W = 1.25$ - 1.50 GeV, integrated over all angles. Events in the red histogram are from the butanol target and events in the blue histogram are from the ^{12}C target with z-vertex larger 5.0 cm and smaller than 7.5 cm. The blue histogram is scaled by 5.26. The distribution from the ^{12}C target region shows a narrow peak at the mass of the neutron. Courtesy of Steffen Strauch (University of South Carolina).

data which did not require any carbon information. The details are given in Section 3.9. The g9b data did not show any signs of a hydrogen contamination. To check the quality of our event-based technique, we compared the integrated background mass distributions from g9b butanol data with the integrated and scaled mass distributions from the g9b carbon data.

3.5 Introduction to Kinematic Fitting

The 4-vectors of the final-state particles were determined in the *cooking* or reconstruction phase. Kinematic fitting [65] slightly modified these *raw* 4-vectors by imposing energy-momentum conservation on the event as a physical constraint. In a brief summary, all measured components of the Lorentz 4-vectors (the magnitude of the momentum as well as the two angles used in the drift-chamber reconstruction – $p,\ \lambda,\ \phi$, respectively) in addition to the initial photon energy were modified within their given errors until the event satisfied energy-momentum conservation exactly. The determination of the correct error (or covariance) matrix was important in this fitting proce-

dure. The kinematically-fitted event had then several quantities which could be used to inspect the quality of the kinematic fitting: a pull value for each measured quantity and an overall χ^2 value. The latter could be converted to a confidence-level (CL) value to judge the goodness-of-fit. The pull distributions were used to evaluate the initial error estimation and to study systematics. It turned out that kinematic fitting provided an effective tool to determine kinematic corrections, e. g. momentum corrections. This is discussed in Section 3.6.

3.5.1 Confidence Level

To check the *goodness-of-fit* or the agreement between the fit hypothesis and the data, the fit χ^2 value was used. The corresponding CL value was defined as:

$$CL = \int_{\chi^2}^{\infty} f(z;n)\, dz\,, \tag{3.8}$$

where $f(z;n)$ was the χ^2 probability density function with n degrees of freedom. It denoted the probability distribution for certain external constraints, e. g. energy-momentum conservation or also a missing-particle constraint. In the ideal case where all events satisfied the fit hypothesis and the measured quantities were all independent and had only statistical uncertainties, the confidence-level distribution would be flat from $(0, 1]$. However, the real data had a confidence-level distribution which showed a peak near zero (Fig. 3.8, left side). This peak contained events which did not satisfy the imposed constraints. These events could be hadronic background events, poorly reconstructed events with significant systematic uncertainties, or events with misidentified particles. A cut on small CL values eliminated the majority of these background events while only a relatively small amount of good data was lost.

3.5.2 Pulls

A *pull value* is a measure of how much and in what direction the kinematic fitter has to alter a measured parameter – or to *pull* at it – in order to make the event fulfill the imposed constraint. All three fit parameters for every detected final-state particle had pull distributions. The pull value for the $i^{\,\text{th}}$ fit parameter was given by:

$$z_i = \frac{\epsilon_i}{\sigma(\epsilon_i)}\,, \tag{3.9}$$

where $\epsilon_i = \eta_i - y_i$ was the difference between the fitted value, η_i, and the measured value, y_i. The quantity σ represents the standard deviation of the parameter ϵ_i. Therefore, the $i^{\,\text{th}}$ pull can be

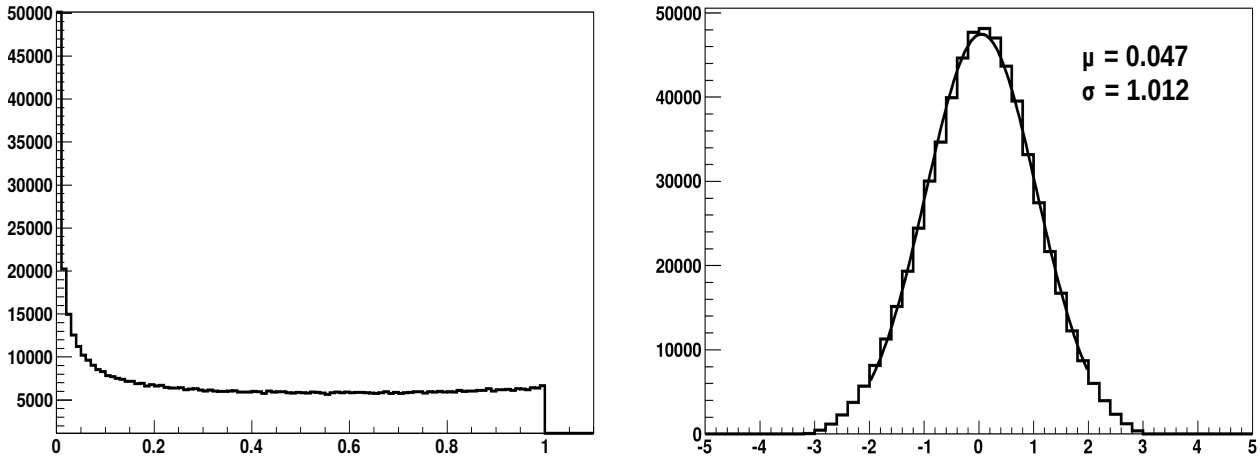

Figure 3.8: Example of results from kinematic fitting. Energy and momentum conservation was imposed on Topology 4 in the reaction $\gamma p \to p\,\pi^+\pi^-$. (Left) A confidence-level distribution. It peaks toward zero but flattens out toward one. (Right) A pull distribution of the incoming photon energy. Ideally, such a distribution is Gaussian in shape, centered at the origin ($\mu = 0$) and has a sigma of one ($\sigma = 1$).

written as:

$$z_i \;=\; \frac{\eta_i - y_i}{\sqrt{\sigma^2(\eta_i) + \sigma^2(y_i)}}\,. \tag{3.10}$$

The reaction $\gamma p \to p\,\pi^+\pi^-$ (using Topology 4, see Table 3.5) had three detected final-state particles: proton, π^+, and π^-. Since the reconstruction of each particle was based on three parameters, this topology had ten pull distributions including a pull for the initial photon energy. In the ideal case that the error matrix of these parameters was correctly determined and all remaining systematic errors were negligible, the pull distributions would be Gaussian in shape with a width of one ($\sigma = 1$) and centered at zero ($\mu = 0$); an example is shown in Figure 3.8 (right side). A systematic problem with the data in the quantity η_i would be observed as an overall shift away from zero. Similarly, if the errors of η_i were consistently (overestimated) underestimated, then the corresponding pull distribution would be too (narrow) broad, and the slope of the CL distribution toward $CL = 1$ would be (positive) negative. The errors of the measured parameters can be corrected from the pull distributions in an iterative procedure.

In our analysis, kinematic fitting served as an effective tool to fine-tune the final-state corrections. We used Topology 4 (all final-state particles detected) for this fine-tuning as described in Section 3.6.3.

3.6 Kinematic Corrections

3.6.1 Energy-Loss (ELoss) Correction

As charged particles traveled from the production vertex to the active components of the CLAS spectrometer, they lost energy through inelastic scattering, atomic excitation or ionization when interacting with the three kinds of targets, target walls, support structures, beam pipe, Start Counter, and the air gap between the Start Counter and the Region 1 Drift Chambers. Therefore, the momentum reconstructed from the drift chambers was smaller than the momentum of the particle at the production vertex. To account and correct for this, the 4-vectors of the final-state particles were modified event-by-event using the "ELoss" package, which was developed for charged particles moving through CLAS [66]. This ELoss package determined the lost momentum of each particle in the materials it had interacted with. In this procedure, the particle's 4-momentum – as measured by the Region 1 Drift Chambers – was used to track the particle back to the reaction

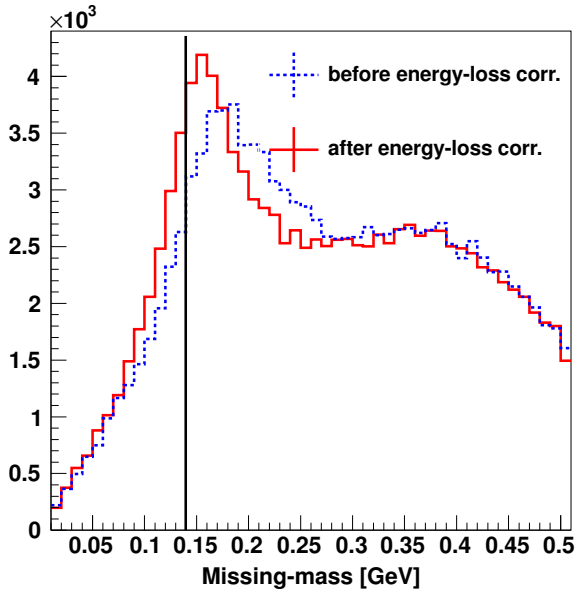

Figure 3.9: Missing-mass distributions from the butanol target before (dotted blue histogram) and after (solid red histogram) applying energy-loss corrections using the Topology $\gamma p \to p\,\pi^+(\pi^-)$. The vertical line denotes the mass of the π^-. In this example, the energy-loss corrections improved the peak position and made the width noticeably smaller. However, the peak was not positioned exactly at the π^- mass, yet; further corrections were needed. The picture was made using three runs from the FROST-g9b 1300-MeV data set (nominal coherent edge).

vertex in the target cell. The energy loss was then calculated based on the distance and the materials it traversed. The corresponding 4-vector was corrected by multiplying an ELoss correction factor to the magnitude of the momentum:

$$\begin{aligned} P_{(\,p\,,\,\mathrm{ELoss}\,)} &= \eta_p \cdot P_{(\,p\,,\,\mathrm{CLAS}\,)} \\ P_{(\,\pi^+\,,\,\mathrm{ELoss}\,)} &= \eta_{\pi^+} \cdot P_{(\,\pi^+\,,\,\mathrm{CLAS}\,)} \\ P_{(\,\pi^-\,,\,\mathrm{ELoss}\,)} &= \eta_{\pi^-} \cdot P_{(\,\pi^-\,,\,\mathrm{CLAS}\,)}\,, \end{aligned} \tag{3.11}$$

where $P_{(\,x\,,\,\mathrm{ELoss}\,)}$ is the momentum of the particle x after applying the energy-loss correction, $P_{(\,x\,,\,\mathrm{CLAS}\,)}$ is the raw momentum measured in CLAS and x is either the proton, π^+, or π^-. The parameters η_p, η_{π^+}, and η_{π^-} are the ELoss correction factors which modified the momentum by a few MeV, on average. The energy-loss correction improved the peak positions in the mass distributions, as can be seen from the example shown in Figure 3.9.

3.6.2 Tagger-Sag Correction

The energy of the incoming photons was determined by the Hall-B tagging system. It was observed in previous experiments that a physical sagging of the holding structure supporting the E-counter scintillator bars could be attributed to gravitational forces [67]. The consequence of this time-dependent sagging was a misalignment of the scintillator bars which led to a small shift of the scattered electron's energy [68]. In the FROST experiment, the tagger sag was taken into account and corrected in the offline reconstruction code. No further photon energy correction was applied.

3.6.3 Momentum Corrections

The FROST experimental setup was not absolutely perfect. For this reason, corrections of a few MeV had to be determined and applied to the final-state particles' momenta to account for unknown variations in the CLAS magnetic field (Torus Magnet) as well as inefficiencies and misalignments of the drift chambers. The initial g9b momentum corrections for the proton and the π^+ were determined by the collaborators at Arizona State University (ASU) [69] based on the single-track reactions $\gamma p \to p\,X$ and $\gamma p \to X\,\pi^+$, respectively. In a two-stage method, the proton and π^+ momenta were corrected such that the X-peak position did not show any azimuthal-angle dependence. We verified these corrections with the kinematic fitter developed at Florida State University by observing the quality of the pull distributions before and after applying the momentum corrections. The full details of the ASU approach are available in reference [69].

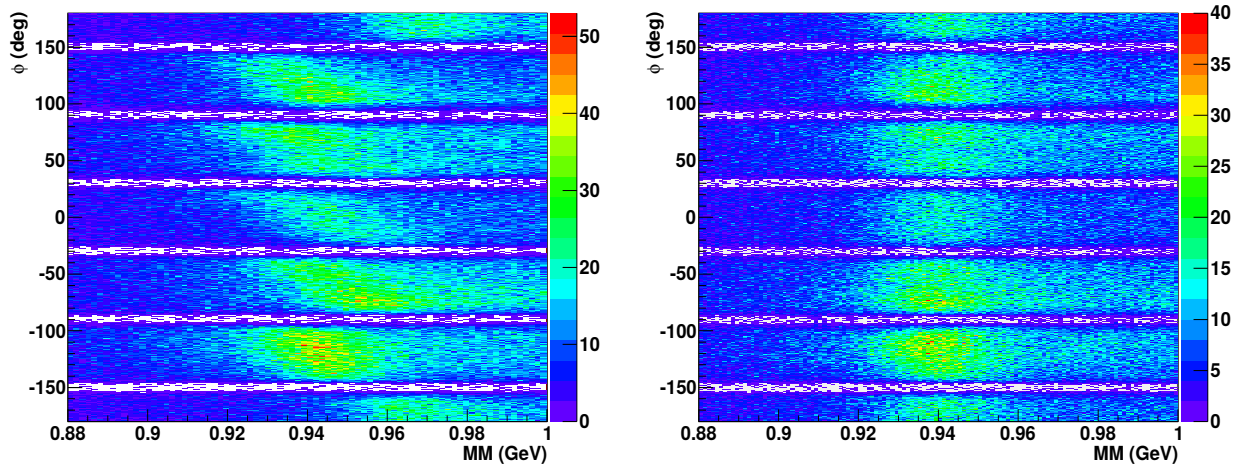

Figure 3.10: Azimuthal dependence in the lab frame of the missing mass X in the reaction $\gamma p \to \pi^+ X$ before (left) and after (right) applying momentum corrections for $E_\gamma \in [1.3, 1.4]$ GeV. The data shown are from the g9b data set with PARA beam and '+' target polarization.

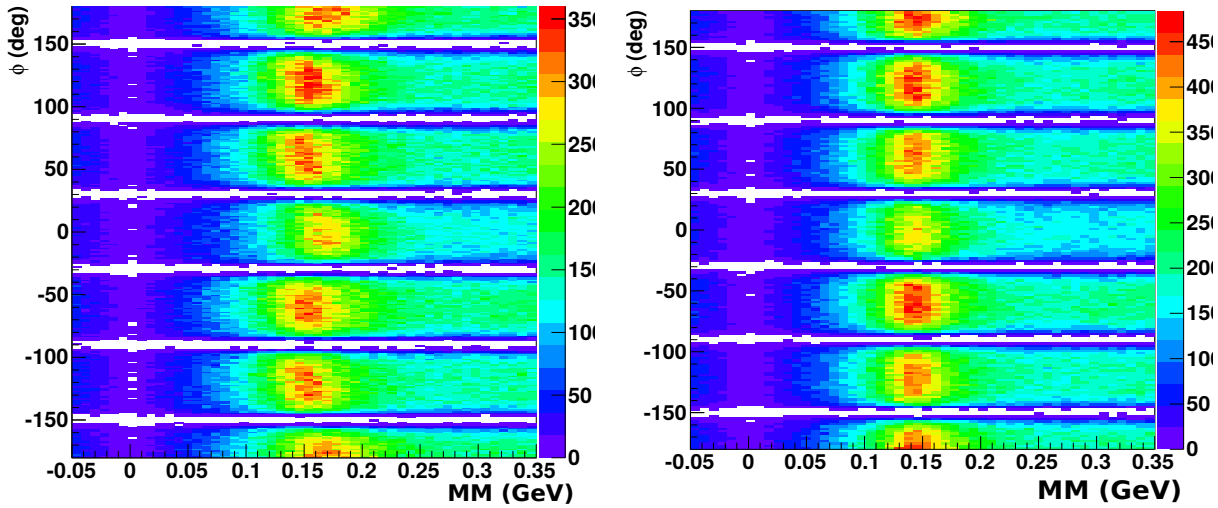

Figure 3.11: Azimuthal dependence in the laboratory frame of the missing mass X in the reaction $\gamma\, p \to p\, \pi^+\, X$ before (left) and after (right) applying momentum corrections for $E_\gamma \in [1.2, 1.3]$ GeV. The data shown are from the g9b data set with PARA beam and '+' target polarization.

We applied these initial ASU corrections on the g9b data. All data sets were then fine-tuned and momentum corrections were also determined for the π^-. In a first step, we studied the momentum

Table 3.7: The momentum binning of the final-state particles and our "fine-tuning" correction factors for the g9b data (utilizing circular beam polarization) after applying the initial ASU corrections.

Particle	Momentum Bin	Range [GeV]	Correction Factor
proton	1	≤ 0.5	1.037
	2	0.5 - 0.6	1.014
	3	0.6 - 0.7	1.006
	4	0.7 - 0.9	1.003
	5	> 0.9	1.001
π^+	1	≤ 0.2	1.005
	2	0.20 - 0.27	0.995
	3	0.27 - 0.35	0.996
	4	0.35 - 0.53	0.999
	5	> 0.53	1.002
π^-	1	≤ 0.2	1.005
	2	0.20 - 0.27	1.003
	3	0.27 - 0.35	1.003
	4	0.35 - 0.53	1.001
	5	> 0.53	1.001

distributions of each final-state particle, decided on five momentum ranges and binned the data accordingly. In a second step, we performed 4C kinematic fitting (Topology 4) and evaluated the pull distributions for the different momentum bins. The *fine-tuning* goal was to obtain pull distributions which were Gaussian in shape with a mean value = 0. As a matter of fact, only very small corrections were needed to achieve this goal. An iterative process was repeated until the pull distributions for proton, π^+, and π^- looked satisfactory. Table 3.7 gives the momentum ranges and the multiplicative factors we determined for the g9b data utilizing circular beam polarization; Tables 3.8 and 3.9 give the momentum ranges and the correction factors for the g9b data utilizing linear beam polarization.

Some representative distributions showing the rectification of the missing-mass dependence on $\phi_{\rm lab}$ after applying the momentum corrections are shown in Figures 3.10 (for the neutron in the

reaction $\gamma p \rightarrow \pi^+ X$) and 3.11 (for the π^- in the reaction $\gamma p \rightarrow p \pi^+ X$). The final pull and confidence-level distributions after applying all corrections are shown in Figures 3.12, and 3.13. Table 3.10 shows the final mean and σ values of Gaussian fits to the pull distributions that were integrated over all momentum bins after applying all corrections, including lab azimuthal and polar angle corrections. The angle corrections are explained in Section 3.6.4. The momentum corrections significantly improved the mean values of the momentum pull distributions; they had a much smaller effect on the other pulls. The azimuthal and polar angle corrections, on the other hand, improved the mean and the σ values of the λ and the ϕ pull distributions, respectively.

Table 3.8: The momentum binning of the final-state particles and our "fine-tuning" correction factors for the g9b data utilizing linear-beam polarization after applying the initial ASU corrections.

Particle	Mom. Bin	Range [GeV]	Correction Factor for different Coherent Edges				
			0.9	1.1	1.3 (5/3 - 5/6)	1.3 (5/15 - 5/18)	1.5
proton	1	≤ 0.5	1.013	1.023	1.012	1.015	1.000
	2	0.5 - 0.6	1.009	1.015	1.009	1.007	1.000
	3	0.6 - 0.7	1.006	1.008	1.006	1.003	1.000
	4	0.7 - 0.9	1.004	1.005	1.004	1.000	1.000
	5	> 0.9	1.002	0.999	1.002	0.998	1.000
π^+	1	≤ 0.2	1.000	1.000	0.998	0.995	1.000
	2	0.20 - 0.27	1.000	1.000	0.993	0.990	1.000
	3	0.27 - 0.35	1.000	1.000	0.993	0.990	1.000
	4	0.35 - 0.53	1.000	1.000	0.996	0.993	1.000
	5	> 0.53	1.000	1.000	1.003	0.999	1.000
π^-	1	≤ 0.2	1.000	1.000	1.000	0.998	1.021
	2	0.20 - 0.27	1.000	1.000	1.000	0.997	0.985
	3	0.27 - 0.35	1.000	1.000	1.000	0.997	0.982
	4	0.35 - 0.53	1.000	1.000	1.000	0.998	1.005
	5	> 0.53	1.000	1.000	1.000	0.998	0.991

Table 3.9: The momentum binning of the final-state particles and our "fine-tuning" correction factors for the g9b data utilizing linear-beam polarization after applying the initial ASU corrections.

Particle	Momentum Bin	Range [GeV]	Correction Factor for different Coherent Edges			
			1.7	1.9 (5/22 - 6/8)	1.9 (6/8 - 6/11)	2.1
proton	1	≤ 0.5	1.000	1.000	1.000	1.007
	2	0.5 - 0.6	1.000	1.000	1.000	1.005
	3	0.6 - 0.7	1.000	1.000	1.000	1.003
	4	0.7 - 0.9	1.000	1.000	1.000	1.003
	5	> 0.9	1.000	1.000	1.000	1.000
π^+	1	≤ 0.2	1.000	1.000	1.000	1.000
	2	0.20 - 0.27	1.000	1.000	1.000	1.000
	3	0.27 - 0.35	1.000	1.000	1.000	1.000
	4	0.35 - 0.53	1.000	1.000	1.000	1.000
	5	> 0.53	1.000	1.000	1.000	1.000
π^-	1	≤ 0.2	1.021	1.021	1.023	1.027
	2	0.20 - 0.27	0.985	0.985	0.986	0.988
	3	0.27 - 0.35	0.982	0.982	0.983	0.984
	4	0.35 - 0.53	1.005	1.005	1.006	1.007
	5	> 0.53	0.991	0.991	0.992	0.995

Table 3.10: Examples of final mean ($\bar{x}$) values and σ's of Gaussian fits to FROST pull distributions integrated over all momentum bins (Tables 3.7 & 3.8) after applying all corrections.

	proton			π^+			π^-			γ
	mom.	λ	ϕ	mom.	λ	ϕ	mom.	λ	ϕ	E
FROST - g9b (circular beam polarization: Period 3)										
$\bar{x}$	0.013	0.032	0.013	-0.023	-0.015	-0.024	-0.004	-0.032	-0.028	-0.021
σ	1.038	1.080	1.052	1.056	1.072	1.042	1.053	1.072	1.042	1.064
FROST - g9b (linear beam polarization: 1.3 GeV)										
$\bar{x}$	-0.006	0.044	-0.012	-0.040	-0.024	-0.029	-0.014	-0.041	-0.019	0.014
σ	1.031	0.981	0.975	0.968	0.969	1.018	0.973	0.980	1.007	1.015

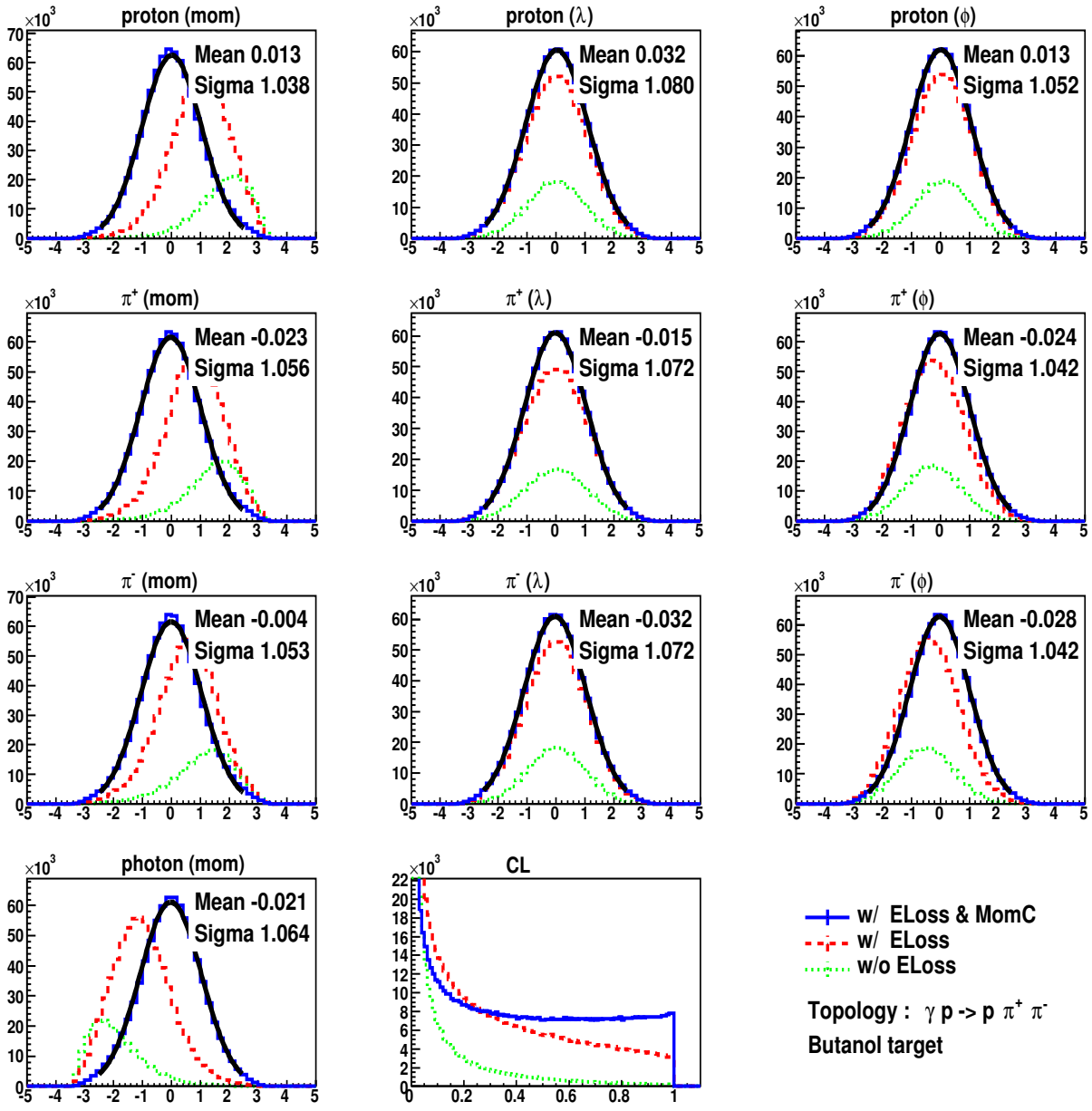

Figure 3.12: Examples of g9b pull and confidence-level distributions (Period 3, runs 62374-62464) from the butanol target at various stages in the analysis. The green-dotted line was made from the raw data without applying any corrections. After the ELoss package was applied, the red-dashed line was obtained. A significant improvement was observed, in particular for the momentum pulls. Finally, momentum and angle corrections (Section 3.6.4) were applied and the blue-solid histograms were obtained. These pull and the confidence-level distributions are based on Topology 4, $\gamma p \to p\pi^+\pi^-$, with a 5 % confidence-level cut applied. The lines represent Gaussian fits to the data; the mean and σ values of the fits can also be found in Table 3.10.

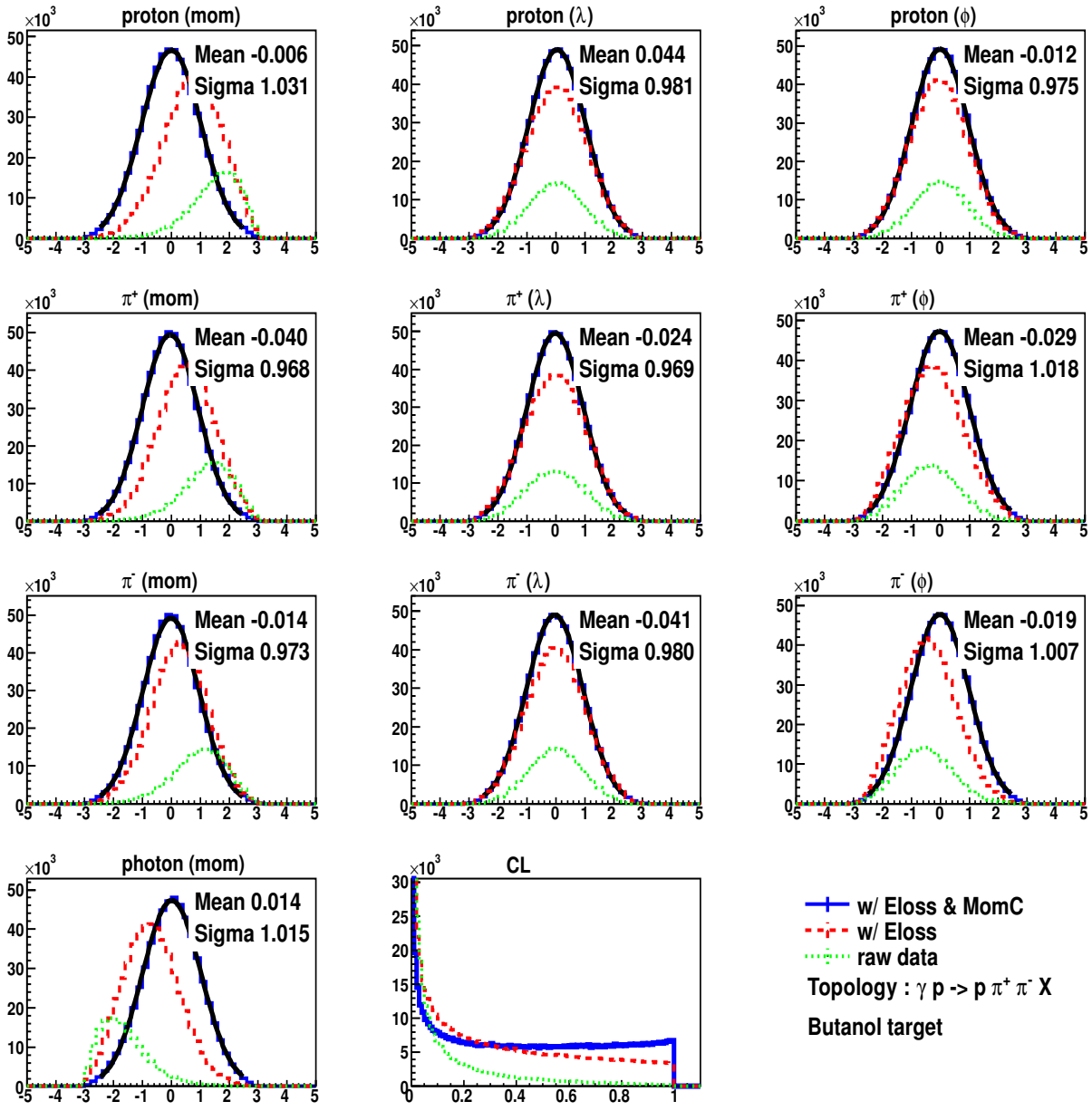

Figure 3.13: Examples of g9b pull and confidence-level distributions (1.3 GeV coherent edge) from the butanol target at various stages in the analysis. The green-dotted line was made from the raw data without applying any corrections. After the ELoss package was applied, the red-dashed line was obtained. A significant improvement was observed, in particular for the momentum pulls. Finally, momentum and angle corrections (Section 3.6.4) were applied and the blue-solid histograms were obtained. These pull and the confidence-level distributions are based on Topology 4, $\gamma p \to p\pi^+\pi^-$, with a 5 % confidence-level cut applied. The lines represent Gaussian fits to the data; the mean and σ values of the fits can also be found in Table 3.10.

3.6.4 Lab Azimuthal and Polar Angle Corrections

We initially observed that the λ-pull distributions of the final-state particles from the FROST-g9b data exhibited a sinusoidal behavior with respect to the lab azimuthal angle, ϕ_{lab} (derived from their respective momentum vectors). Since the tracking parameter λ is closely related to the azimuthal angle in the lab coordinate system, this indicated that the measured azimuthal angles from the momentum vectors needed corrections. It should be noted here that these modulations in the λ pull distributions are not an effect of the beam and target polarizations. In the ideal case, the pull distributions in each ϕ_{lab} sector should be centered at zero, independent of the type of the beam and target polarizations. It was important to correct the azimuthal angles in FROST-g9b (which had a transversely-polarized target) since the final observables were extracted by fitting the ϕ_{lab} angular distributions.

The ϕ pull distributions showed relatively smaller but also non-zero modulations with respect to the lab azimuthal angle ϕ_{lab} (see Appendix A). This suggested that corrections were also required for the lab polar angles θ_{lab} (derived from the momentum vectors) which are closely related to the ϕ tracking parameter.

Upon developing correction functions, we observed that the modulations were related to the magnetic field of the dipole holding magnet (introduced in Section 2). The data with a negative sign for the holding field showed modulations that were 180° out-of-phase with the modulations seen in the data with a positive sign for the holding field (see Appendix A). Our observations were consistent with the expected effects of a magnetic dipole field (about 0.5 T in magnitude) on charged particles which broke the ϕ_{lab} invariance of the system. The magnetic forces of the holding field were not taken into account during the track reconstruction and needed to be corrected. The deflection caused by the magnetic force on a charged particle depended on many factors such as the x-, y- and z-components of the particle's velocity, the initial azimuthal angle and the time-of-flight of the particle. This represented a complicated multi-dimensional problem which was almost impossible to solve at this stage in the analysis. To simplify the situation, we developed corrections for the final-state particles only as a function of β_z. The reason for choosing β_z was that the component of the magnetic force that affected the azimuthal angle depended only on the z-component of $\vec{\beta}$. The details of the procedure used for the determination of the correction functions are given in Appendix A. Figure 3.14 shows examples of the mean values of the λ pull distributions versus ϕ_{lab}

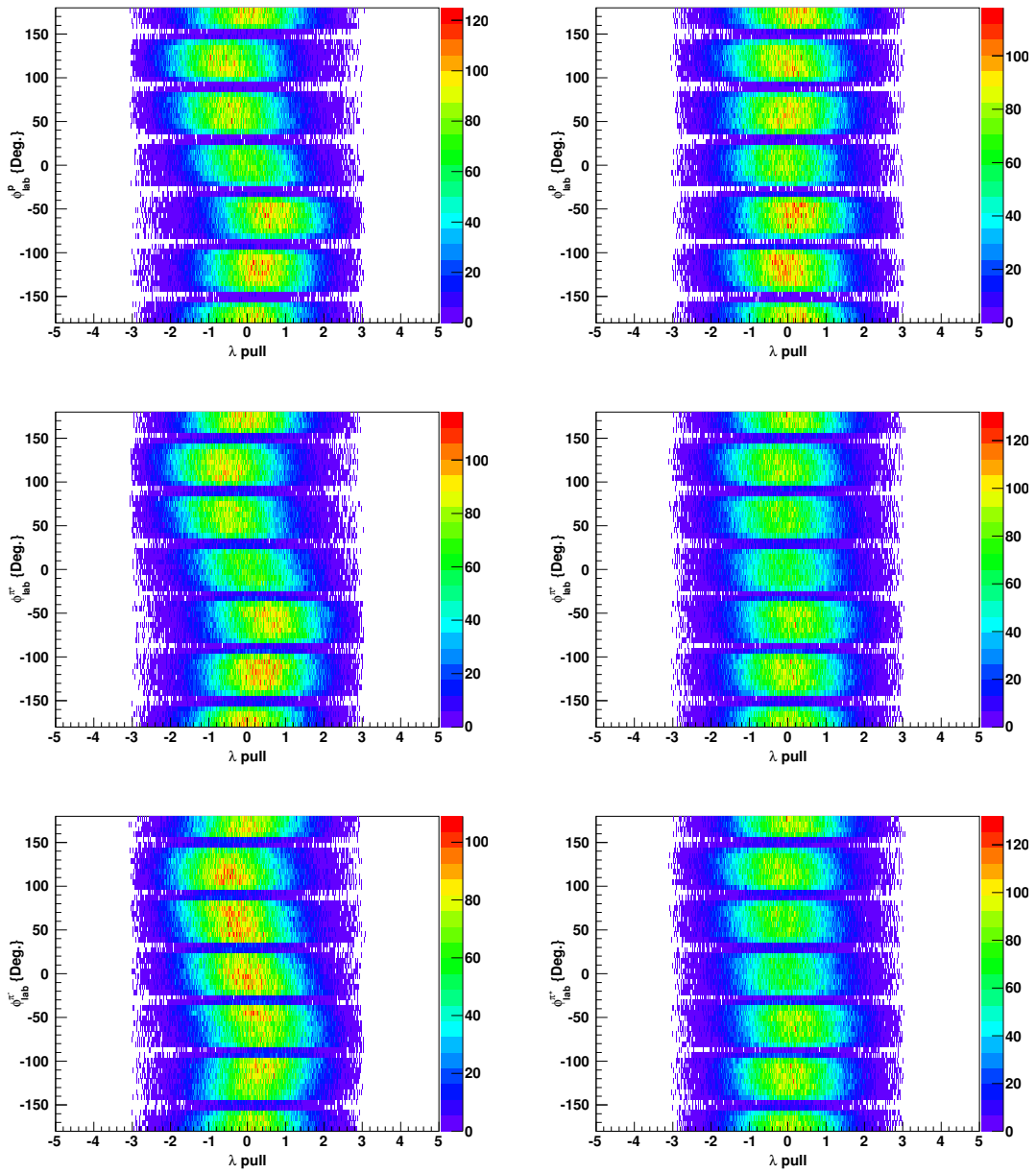

Figure 3.14: (Left column) Mean values of the λ pull distributions versus the lab azimuthal angle from Topology 4 of FROST-g9b (1.5 GeV coherent-edge data set) for the proton (top), π^+ (center) and π^- (bottom) after applying energy-loss and momentum corrections. The modulations observed in these plots indicated that the azimuthal angles (from the momentum vectors) in the lab system required separate corrections for each particle. (Right column) The same distributions after applying the angle corrections. The initial modulations were successfully corrected.

before (left column) and after (right column) applying the corrections (1.5 GeV data set). The modulations were successfully removed.

The corrections also improved the overall kinematics. This was evident from the σ values of the Gaussian fits to the integrated λ and ϕ pull distributions. Before applying the angle corrections, the modulations led to a larger width of the pulls (Table 3.11). After the corrections were applied, the σ values came closer to the ideal value of *one* as shown in the table. The mean values of the pulls also improved. Note that we used the same corrections for the linearly- as well as the circularly-polarized g9b data.

Table 3.11: Examples of the final (ELoss and momentum corrections included) mean and σ values of Gaussian fits to FROST pull distributions before and after applying angle corrections. The corrections improved the quality of the λ and ϕ pull distributions, thereby improving the overall kinematics of the events.

	proton			π^+			π^-			γ
	mom.	λ	ϕ	mom.	λ	ϕ	mom.	λ	ϕ	E
FROST - g9b (1.5 GeV data set), without angle corrections										
$\bar{x}$	0.040	0.061	-0.015	-0.016	0.001	-0.058	0.004	-0.078	-0.053	-0.047
σ	1.028	1.114	1.094	1.052	1.093	1.049	1.041	1.104	1.049	1.044
FROST - g9b (1.5 GeV data set, with angle corrections										
$\bar{x}$	0.035	0.046	-0.001	-0.008	-0.013	-0.031	-0.001	-0.052	-0.045	-0.039
σ	1.026	1.076	1.054	1.046	1.062	1.027	1.032	1.066	1.028	1.048

3.6.5 Bad or Malfunctioning Time-of-Flight Paddles

Some TOF paddles of the CLAS spectrometer were dead or malfunctioning during the experiment. Reference [59] contains an extensive study on bad TOF paddles in FROST-g9b using single-track events. These paddles were identified by studying the reconstructed mass versus TOF counter number for all six sectors. The identified bad paddles are listed in Table 3.12. However, in this analysis we did not remove them because the final observables were extracted by forming asymmetries in which the data were used for the acceptance correction. The poor efficiency of the

bad paddles canceled out in the ratios. The table is given in this document for completeness and future reference.

Table 3.12: The list of bad time-of-flight paddles.

Sector Number	Bad TOF Paddles in g9b
1	none
2	24, 44, 45, 49, 51
3	22, 38
4	15, 48, 49, 53
5	22, 50-55
6	12, 13, 49, 53, 56

3.7 Event Statistics after Applying all Cuts and Corrections

The process of developing and applying energy, momentum and other necessary corrections such as angle corrections during the course of this analysis served the purpose of correcting for the effects of the experimental setup, therefore resulting in a data set that was as nature intended it. Additionally, determining and enforcing cuts used in the analysis served not only to remove the remaining instrumental effects of the experimental setup but also to remove the contributions from physics events not of interest to the analysis (the hadronic or electromagnetic background). Through the application of the proper vertex position, photon and particle identification variables, this background could be reduced considerably. However, the FROST experiment used a "dirty" polarized target (about 86.5 % of the nucleons in butanol are from carbon and oxygen), the free-proton events from the butanol – after removing some of the background – still had contributions from bound nucleons. These bound-nucleon contributions still need to be taken care of.

As an example, Table 3.13 shows how many events survived after applying various cuts on the (coherent edge) 1.3 GeV data set from FROST-g9b with PARA and PERP beam polarization settings. The number quoted within parentheses shows the percentage of surviving events. Applying a vertex cut to select events originating from the butanol target, filtered out the maximum chunk (93.5 %) of the data. Note that Topology 1 resulted in the largest yield compared to the other three topologies in the two-pion analysis.

Table 3.13: The table shows the statistics of surviving events after various cuts were applied to the g9b-1.3 GeV data set with PARA & PERP settings (AMO data set not considered here).

Cuts	# of Events (% of Events)			
No cut	1.031e09 (100)			
Vertex Cut (Butanol Events)	6.74e07 (6.5)			
Vertex Cut + Topology Cut	Topology 1	Topology 2	Topology 3	Topology 4
	2.05e07 (1.99)	1.99e07 (1.93)	1.71e07 (1.66)	1.00e07 (0.97)
Vertex Cut + Topology Cut + Photon Selection Cuts	1.16e07 (1.13)	9.83e06 (0.95)	1.12e07 (1.09)	6.30e06 (0.61)
Vertex Cut + Topology Cut + Photon Selection + β Cut	8.43e06 (0.82)	7.72e06 (0.75)	6.54e06 (0.63)	4.01e06 (0.39)

3.7.1 Beam and Target Polarization

3.7.2 Circularly-Polarized Photon Beam - Degree of Polarization

Circularly-polarized photons were produced via bremsstrahlung of longitudinally-polarized electrons from an amorphous radiator, as discussed in Chapter 2. The degree of circular polarization of these bremsstrahlung photons, $\delta_{\odot}$, could be calculated from the longitudinal polarization of the electron beam, δ_{e^-}, multiplied by a numerical factor. Using $x = E_{\gamma}/E_{e^-}$, the degree of polarization was given by [70]:

$$\delta_{\odot}(x) \;=\; \delta_{e} \;\cdot\; \frac{4x - x^2}{4 - 4x + 3x^2}\,. \tag{3.12}$$

Figure 3.15 shows that the degree of circular polarization is roughly proportional to the photon beam energy. In this figure, the photon energy, E_{γ}, is given as a fraction of the electron beam energy, E_{e^-}. In the g9b experiment, the electron beam energy was 3.082 GeV for all the runs that we used in this analysis. The degree of electron beam polarization, δ_{e^-}, was determined from Møller measurements, discussed in details in Section 2.2. Table 3.14 summarizes these measurements for different runs. The average value for δ_{e^-} was $87.10 \pm 1.50\,\%$. We determined the degree of photon beam polarization on an event basis using our knowledge of the photon energy of the event, the average degree of electron beam polarization and Equation 3.12.

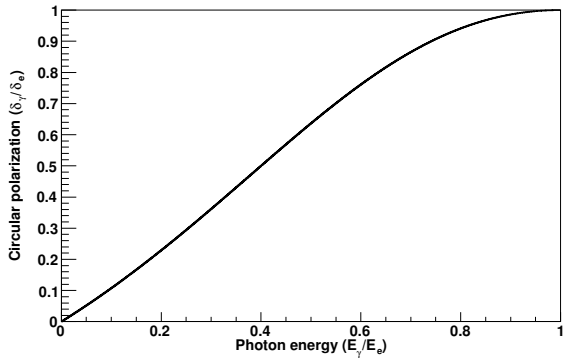

Figure 3.15: Degree of circular polarization in units of $[\delta_\gamma/\delta_{e^-}]$ as a function of photon energy.

Table 3.14: Møller measurements of the electron beam polarization and average values.

Experiment	Electron-Beam Energy E_{e^-}	Date	Run Number	Electron-Beam Polarization δ_{e^-}	
					Average
FROST-g9b	3.082 GeV	Mar. 22, 2010	62271	$+84.72 \pm 1.71$	87.10 ± 1.50
				-86.51 ± 1.49	
		Mar. 24, 2010	62305	$+88.09 \pm 1.47$	
				-88.98 ± 1.48	
		Apr. 08, 2010	62530	$+88.08 \pm 1.48$	
				-86.49 ± 1.38	
		Apr. 19, 2010	62704	$+86.76 \pm 1.36$	
				-86.94 ± 1.30	

3.7.3 Circularly-Polarized Photon Beam - Orientation of the Helicity States

The direction of the beam polarization depended on the condition of the half-wave plate (HWP) which was either IN or OUT. In each period, the longitudinal polarization of the electron beam was flipped pseudo-randomly at a rate of $30 - 940$ Hz. Occasionally, the HWP was inserted in the circularly-polarized laser beam of the electron gun to reverse helicities and thus, the beam polarization phase was changed by 180°. The HWP was inserted and removed at semi-regular intervals throughout the experimental run to ensure that no polarity-dependent bias was manifested in the measured asymmetries. Corrections to the helicity state (including HWP settings) were

taken into account during the reconstruction process and the CORRECTED helicity information was available for the analysis in the trigger bit 29 of the HEAD bank. Trigger bit 30 of the same bank was used as a flag to indicate whether the beam helicity information required corrections. We used the code provided on the FROST website [74]:

```
int cntrlmask = 0x40000000;    // bit30 flag for corrected helicity
int helmask   = 0x20000000;    // bit29 corrected helicity bit
if ( !(HEAD[0].TRIGBITS & cntrlmask) ) continue;
int helicity = (HEAD[0].TRIGBITS & helmask) ? 1 : -1;
```

3.7.4 Linearly-Polarized Photon Beam - Degree of Polarization

Linearly-polarized photons were produced in the FROST experiment by using the coherent bremsstrahlung technique whereby the electron beam scattered coherently from a diamond crystal radiator. In this technique, the coherent scattering led to an enhancement (also called the *coherent peak*) in the photon energy spectrum. As discussed in details in Section 2.2, the coherent edge, the orientation of the linear beam-polarization and the degree of the beam polarization were controlled by various experimental conditions.

The degree of beam polarization was determined by fitting the measured enhancements obtained from the tagging spectrometer with a coherent bremsstrahlung calculation developed at the University of Glasgow [71, 72]. A typical fit is shown in Figure 3.16. The corresponding polarization was determined from the fitted parameters as a function of photon energy (or tagger channel) and a polarization "lookup table" was created. Ideally, for a given electron beam energy, polarization plane orientation and nominal coherent-edge setting, only one polarization table should be needed. In practice, the coherent edge drifted with time, due to small changes in the angle between the beam and the crystal lattice. Hence, many polarization tables were required, and the appropriate table was selected on the basis of the coherent edge position, which was measured every 2s.

In the analysis, the event-by-event information on the coherent edge position was available from the EPIC bank. Events were discarded if the actual coherent edge position was greater than the nominal edge setting (in MeV) + 100 MeV. The appropriate polarization table was then selected based on the nominal edge setting, electron beam energy, polarization plane orientation and the actual coherent edge value. The degree of the beam polarization corresponding to the tagger *E_id bin* associated with the event's photon was obtained from the selected table. Events were only

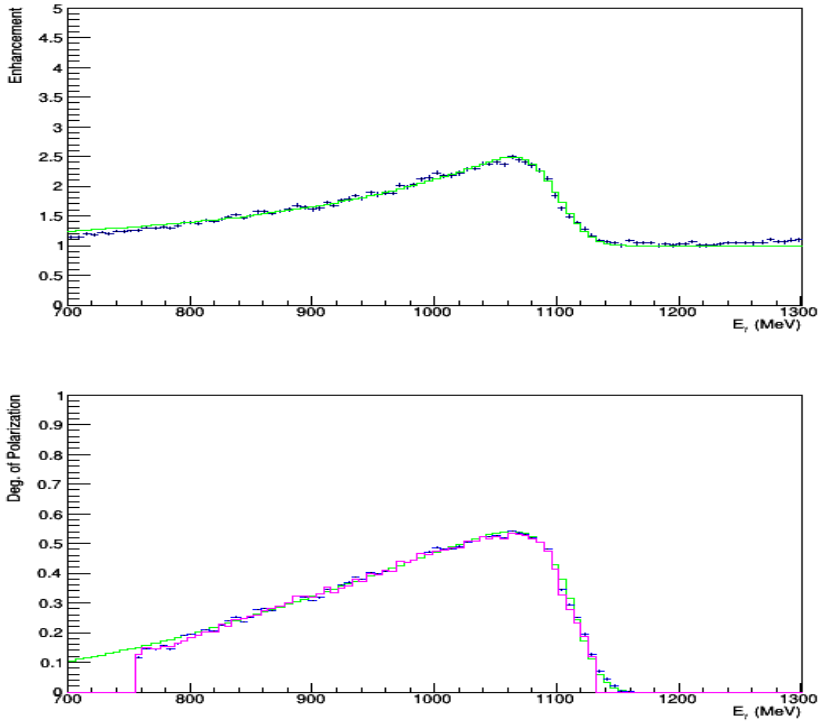

Figure 3.16: An enhancement peak (top) and the corresponding degree of beam polarization (bottom) from the 1100 MeV nominal coherent edge data set of FROST-g9b with PERP beam setting (data points shown in blue in the picture). The fit to the enhancement is shown in green. The actual coherent edge is located at 1099.0 MeV in this example. Figure taken from [73].

kept if the polarization was available and the value was between 0.0 and 1.0. The degree of linear polarization varied from $\sim 40\,\%$ to about $60\,\%$ in the g9b data sets.

3.7.5 Beam-Charge Asymmetry in Data Sets with Circularly-Polarized Photons

The electron-beam polarization was toggled between the h^+ and the h^- helicity state at rates of 943.396 Hz, 239.981 Hz, and 29.560 Hz, depending on the requests of the experiments involved during the data-taking [74]. At these large rates, the photon-beam flux for both helicity states should be the same, on average. However, small beam-charge asymmetries of the electron beam could cause instrumental asymmetries in the observed *hadronic* asymmetries and had to be taken into account. The beam-charge asymmetry could be calculated from the luminosities of helicity-plus

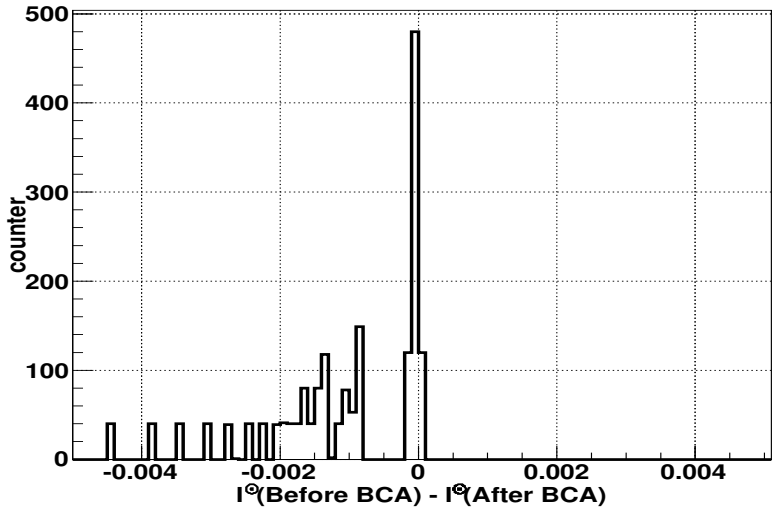

Figure 3.17: Comparison between the polarization observable $\mathbf{I}^{\odot}$ before and after applying the correction for beam-charge asymmetry. Image source: [75].

and helicity-minus events:

$$\Gamma^{\pm} = \alpha^{\pm}\,\Gamma = \frac{1}{2}\,(1 \pm \bar{a}_c)\,\Gamma\,, \tag{3.13}$$

where Γ was the total luminosity. The parameter $\alpha^{\pm}$ was used to find the helicity-plus and helicity-minus luminosities, $\Gamma^{\pm}$, from the total luminosity. This parameter depended on the mean value of the electron-beam charge asymmetry, $\bar{a}_c$. Figure 3.18 shows examples of the beam-charge asymmetry for g9b runs. The beam-charge asymmetry was typically less than 0.2 % [74]. Since the beam-charge asymmetries were very small, they could be considered negligible. For example, the effect of the beam-charge asymmetry on the polarization observable $\mathbf{I}^{\odot}$ using the FROST-g9a data was investigated and found to be negligible, as shown in Figure 3.17.

3.7.6 Target Polarization

In FROST-g9b, the target was transversely-polarized and was polarized a total of 19 times, about once per week. The target was most often polarized in the negative spin state (15 times) because it reached a higher starting polarization ($-92\,\%$) than the positive spin state ($83\,\%$). Therefore, the orientation of the target spins with respect to the beam was usually determined by the direction of the transverse holding field. The relaxation time during g9b was somewhat higher,

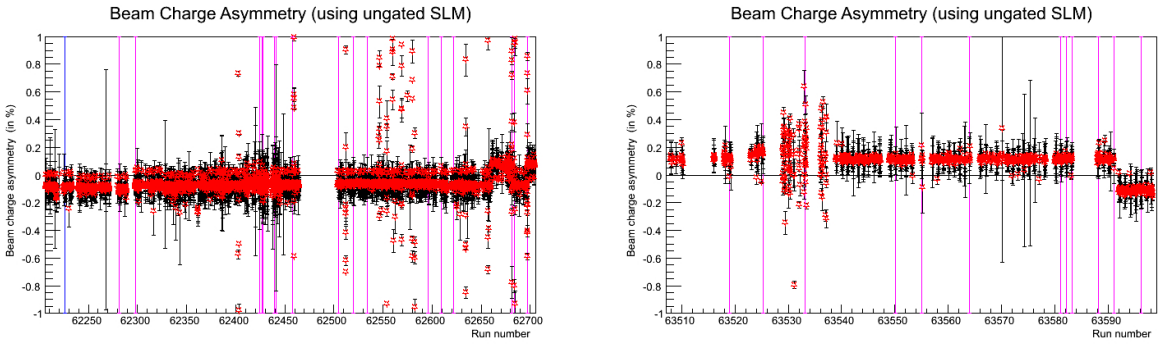

Figure 3.18: Examples of the beam-charge asymmetry for (left) earlier g9b runs, 62225-62704, and (right) later g9b runs, 63508-63598. The values are typically smaller than 0.2 %. Pictures from [74].

about 3400 hours for positive polarization with beam and 4000 hours without. The relaxation time for the negative spin state was once again about half that of the positive. The final two weeks of g9b were run with a super-fluid leak between the mixing chamber and beam pipe. This reduced the starting polarization (three polarization cycles) to an average of only 69 %, and the relaxation time decreased by about a factor of seven, necessitating bi-weekly polarizations [52].

The collaborators at the University of South Carolina determined the target polarization from NMR measurements [76]. The basic principle behind this technique is discussed in Section 2.4. The results for each g9b run including uncertainties are given in the g9b_runlist. Figure 3.19 shows the magnitude and direction of the target polarization in each FROST-g9b run. The target polarization varied from about 45 % to 94 % over the whole experiment with a typical uncertainty of ~ 1.7 %. The average polarization was found to be about 81 %. A positive (negative) sign for the target polarization denotes that the polarization pointed away from (towards) the floor of the experimental Hall.

The average degree of target polarization in each period was used in the analysis rather than run-by-run polarization values. For further details please see Section 4.4.2.

Target Polarization Offset-Angle Calibration The transverse magnetic field of the holding magnet was inclined at a nominal angle of $\sim 60°$ with respect to the floor of the experimental hall but the extraction of the polarization observables required an accurate determination of this offset. It was not possible to find the angle during the experiment since the coils of the dipole holding magnet were attached to the target cryostat and could not be monitored while the target was in

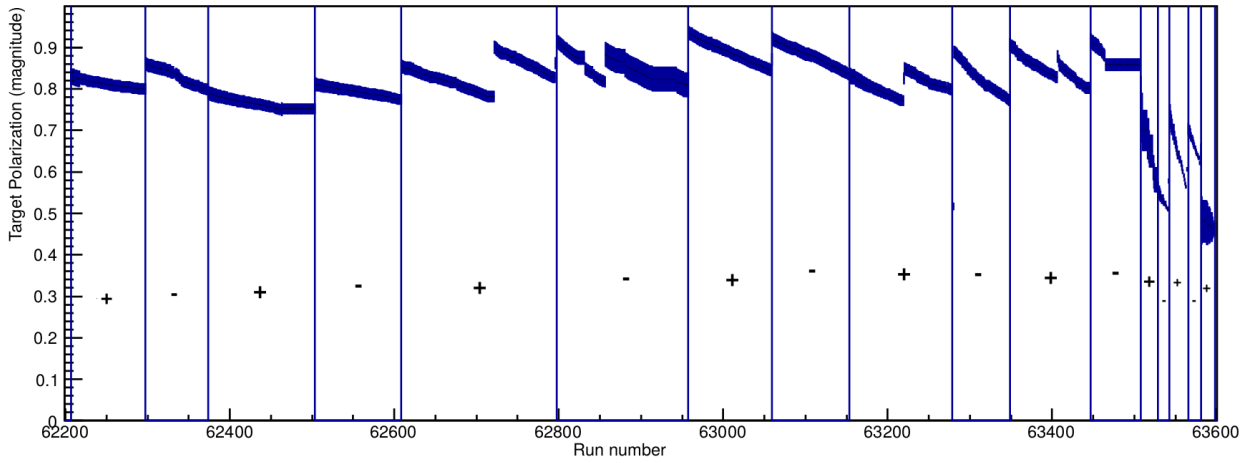

Figure 3.19: Target polarization versus run number in g9b. Image source: [59].

place. However, it was possible to extract the offset experimentally by introducing it as a parameter in the fits of high-statistics azimuthal-angle distributions. Individual studies were carried out by the collaborators at Arizona State University (ASU) as well as the Catholic University of America (CUA), and by us (see Appendix E).

ASU performed a detailed study using a high statistics reactions, $\gamma p \to n\pi^+$ and $\gamma p \to p\pi^0$, over a range of energy and polar angle bins [77], [78]. The yields were fitted to the equation:

$$Y \;=\; N_\gamma\,\sigma_0\,(1 \,+\, P_t T \sin\alpha \,+\, P_t P_\gamma F \cos\alpha) = N_\gamma\,\sigma_0\,(1 \,+\, P_t T \sin(\phi - \phi') \,+\, P_t P_\gamma F \cos(\phi - \phi'))\,, \tag{3.14}$$

where N_γ was the normalizing photon-flux factor, P_γ and P_t were the beam and target polarizations, respectively, α was the angle of inclination of the target polarization with respect to the center-of-mass production plane (see Appendix B), ϕ was the azimuthal angle of the outgoing meson and $\sigma_0,\ T,\ F,\ \phi'$ were the fit parameters. The weighted average of ϕ' came out to be $-63.9 \pm 0.4°$. The magnitude of ϕ' was also consistent with the CUA result [59]. CUA extracted the angle by studying the raw target asymmetry for the reaction $\gamma p \to \pi^+ X$.

Furthermore, the use of Equation 3.14 for the reaction $\gamma p \to p\eta$ using g9b data gave results for T which were consistent with previously published results [78]. This provided an unambiguous determination of the target offset. From Figure **??** we see that the angle α is related to the target offset angle ϕ_0 as $\alpha = 180° - \phi^p_{CLAS} + \phi_0$. This reduces Equation 3.14 to (let us only focus on the

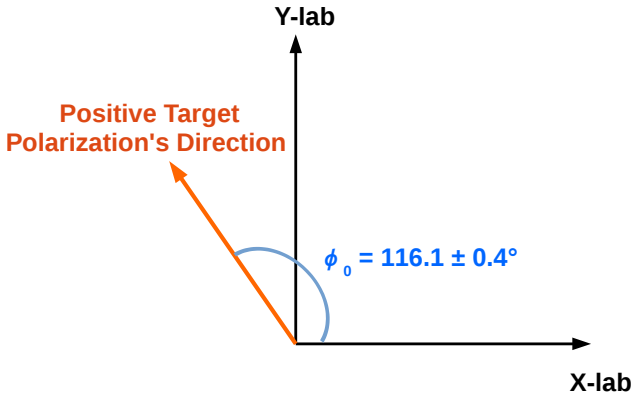

Figure 3.20: A schematic of the offset angle in the lab frame when the target polarization direction is denoted as "+". The z-axis is defined in the direction of the incoming photon beam.

part which involves T):

$$\begin{aligned} Y &= N_\gamma \, \sigma_0 \, (1 + P_t T \sin(180^\circ - \phi^p_{CLAS} + \phi_0)) \\ &= N_\gamma \, \sigma_0 \, (1 - P_t T \sin(\phi^p_{CLAS} - 180^\circ - \phi_0)) \\ &= N_\gamma \, \sigma_0 \, (1 - P_t T \sin(\phi^\eta_{CLAS} - \phi_0)) \\ &= N_\gamma \, \sigma_0 \, (1 + P_t T \sin(180^\circ + \phi^\eta_{CLAS} - \phi_0)) \\ &= N_\gamma \, \sigma_0 \, (1 + P_t T \sin(\phi^\eta_{CLAS} - (\phi_0 - 180^\circ))) \end{aligned} \tag{3.15}$$

On comparing Equations 3.14 and 3.15 we see that $\phi_0 = \phi' + 180^\circ = -63.9^\circ + 180^\circ$. Therefore the target offset was, $\phi_0 = 116.1^\circ \pm 0.4^\circ$ from the x-axis in the lab frame (Figure 3.20).

3.8 Normalization

To extract experimental asymmetries, it was necessary to appropriately combine data sets with different beam and/or target polarizations. Since the number of runs included in each data set was different and each run also had a different number of events, a normalization factor was needed to adjust the imbalance. The total number of events included in the raw data (no cuts applied and no particular final state selected) was roughly proportional to the initial number of photons. A normalization factor, denoted as:

$$N = \frac{\Phi_1 \, (\text{data set}_1)}{\Phi_2 \, (\text{data set}_2)} \, , \tag{3.16}$$

could thus be defined as the ratio of the initial number of photons for two data sets or alternatively, as the ratio of the raw events from one of the targets. The photon flux information in CLAS analyses were stored in "gflux" files. Full details on the method to determine the photon flux is available in [79]. The general idea was as follows. The first step was to find out the number of "good" electron hits (when left and right hits of a T-counter matched with a hit in the E-counter of the tagger) during the time when the detector was ready to record data. This number was multiplied with a factor called the "tagging ratio" which was equal to the percentage of "good electrons" that produced a real photon which could cause a physics event. Not all "good electrons" may have a real photon associated with them due to a number of reasons, such as dispersion of the beam, bad collimation downstream of the radiator and Møller scattering. In order to determine the ratio, the number of real photons in a low intensity beam (10% of the production beam current) was measured by placing a Total Absorption Shower Counter (TASC) directly in the photon beam. The beam was operated at low intensity to prevent overloading of the TASC. The tagging ratio was then determined and it was assumed that this ratio was independent of the beam intensity. It was observed that the ratio was T-counter dependent, varying from $75 - 81\%$ over all counters, but with only approximately 1% spread for each counter. In addition to the tagging ratio, a small correction due to the loss of photons from the target to the TASC was also included in the photon flux calculation.

While it was certainly preferable to use the photon flux from the gflux files, this information was not available in g9b. Therefore, we determined the normalization factors by utilizing the information on the total number of reconstructed events from the different targets (after applying cuts on accidentals) since this number was considered proportional to the photon flux Φ. The factors were separately determined for the C and CH_2 targets. We used events from all reactions rather than from the reactions of our interest so that the normalization factors were independent of the physics dynamics we wanted to extract. It is worth mentioning here that in FROST-g9a gflux files were available. Therefore, it was possible to compare the flux normalization obtained using this method with the flux normalization determined using the gflux files (see Appendix D). It was found that the normalization factors obtained from the two methods were consistent, differing by only less than 2%.

Circular beam polarization Five periods were defined as shown in Table 3.4. All five periods had the same accelerator energy $E_{e^-} = 3.082$ GeV. We merged Periods 1 & 3 because both had very similar experimental conditions. The merged data set will be referred to as *period 13*. Given the nature of the g9b polarization, we needed to fit ϕ_{lab} distributions to extract the observables. It was thus more practical to combine data sets with similar run conditions to increase the statistics and to then do the fitting. As discussed in Section 3.6.4, the two different holding field directions showed small kinematical differences. To reduce the corresponding systematic uncertainty, we used: combination132 of Periods 13 & 2 and combination45 of Periods 4 and 5. The separately-determined normalization factors were again found to be independent of energy. Table 3.15 shows the normalization factors that were determined for each period combination using the C and CH_2 targets. Those obtained from the CH_2 target were used in the analysis since the holding-magnet's field was negligible at this target location. We have used the difference observed for the two targets as the systematic uncertainty for the normalization factor.

Linear beam polarization Each (nominal) coherent edge data set had four subsets that corresponded to the four beam-target polarization orientations (Tables 3.2 and 3.3). The normalization factors for the subsets were determined using both the carbon as well as the CH_2 target. The data were divided into 100-MeV wide energy bins. We combined overlapping energy regions between different coherent-edge data sets, provided that they had the same electron beam energy and target-polarization orientation. One such bin was the 1.6 - 1.7 GeV energy bin from the 1.7 and 1.9 GeV (nominal) coherent edge data sets where the electron beam energy was 5.078 GeV. Table 3.16 shows the normalization factors for all coherent edge data sets. The ratios obtained from the CH_2 target were used during the extraction of asymmetries for the same reason as mentioned before. The systematic uncertainties were derived from comparing the results from the two targets.

Table 3.15: The normalization factors obtained from the C and CH_2 targets for combination132 and combination45 of the g9b data sets using circularly-polarized photons.

Target	ratio $N = \Phi(+)/\Phi(-)$	
	per-13/per-2	per-5/per-4
C	1.83	0.77
CH_2	1.83	0.76

Table 3.16: The normalization factors of the subsets (based on beam-target polarization orientations) for each coherent edge setting in the g9b experiment. The factors were separately obtained for the C and CH_2 targets. Each coherent edge data set was divided into 100-MeV wide energy bins. As an example, "$\Phi(\|,+)$" denotes that the photon flux of the subset had a 'PARA' beam polarization and a '+' target polarization.

Coh. Edge [GeV]	E_γ Bin [GeV]	Normalization Factors							
		C Target				CH_2 Target			
		$\frac{\Phi(\|,+)}{\Phi(\|,-)}$	$\frac{\Phi(\perp,+)}{\Phi(\perp,-)}$	$\frac{\Phi(\|,+)}{\Phi(\perp,+)}$	$\frac{\Phi(\|,-)}{\Phi(\perp,-)}$	$\frac{\Phi(\|,+)}{\Phi(\|,-)}$	$\frac{\Phi(\perp,+)}{\Phi(\perp,-)}$	$\frac{\Phi(\|,+)}{\Phi(\perp,+)}$	$\frac{\Phi(\|,-)}{\Phi(\perp,-)}$
0.9	0.7-0.8	1.441	1.748	0.809	0.981	1.437	1.744	0.808	0.980
	0.8-0.9	1.403	1.796	0.875	1.121	1.399	1.799	0.875	1.125
1.1	0.9-1.0	1.934	1.932	0.846	0.845	1.938	1.943	0.845	0.847
	1.0-1.1	1.937	1.840	0.965	0.916	1.921	1.832	0.964	0.919
1.3	1.1-1.2	1.248	0.947	1.215	0.922	1.237	0.947	1.214	0.930
$1.3+1.4$	1.2-1.3	0.785	0.785	0.984	0.984	0.792	0.786	0.996	0.988
1.5	1.3-1.4	0.508	0.733	0.704	1.016	0.510	0.735	0.706	1.018
	1.4-1.5	0.499	0.695	0.798	1.112	0.494	0.692	0.794	1.112
1.7	1.5-1.6	0.880	0.975	0.819	0.907	0.889	0.983	0.823	0.910
$1.7+1.9$	1.6-1.7	0.919	0.990	0.917	0.987	0.921	0.997	0.912	0.988
1.9	1.7-1.8	0.913	0.977	0.977	1.046	0.931	0.981	0.984	1.037
$1.9+2.1$	1.8-1.9	1.224	1.174	0.971	0.931	1.226	1.173	0.962	0.920
2.1	1.9-2.0	2.038	1.599	1.042	0.817	2.026	1.623	1.034	0.829
	2.0-2.1	2.147	1.542	1.200	0.862	2.143	1.541	1.197	0.861

3.9 Signal-Background Separation: Dilution Factors & Q-Factor Method

Frozen beads of butanol (C_4H_9OH) *were used for the target material. The butanol was doped with the nitroxyl radical TEMPO at a concentration of* 2.0×10^{19} *spins* cm^{-3} *for dynamic polarization. Water (0.5 % by weight) was added to the solution before freezing in order to avoid a crystalline solid* [52]. Figure 3.21 (left) shows a photograph of the target material. When the butanol was polarized, only the 10 *free* hydrogen nucleons of the butanol could be polarized. In the analyses, contributions from free-proton events had to be separated from contributions of events off

bound nucleons. The latter were subject to Fermi motion and missing-mass distributions showed no particular structures since the particle peaks were broadened and mostly washed out. This is illustrated in Figure 3.21 (right). A *dilution factor* describes the signal fraction and is generally defined as the ratio of the free-proton contribution to the full butanol cross section. A simple calculation based on the chemical formula of butanol yields $10/74 = 0.135$ as the ideal or *naive* dilution factor. In practice, effective dilution factors are usually determined from mass distributions. Since different signal peaks can be used, these factors are reaction dependent and are generally larger than the ideal factor after the application of various selection cuts, which reduce background and can alter the relevant mass distributions.

In addition to the polarized butanol, two additional targets were installed in the cryostat for background and dilution studies. A 1.5 mm thick carbon disk and a 3.5 mm thick CH_2 disk were mounted on the 1 K and 20 K heat shields, approximately 9.5 cm in g9b and 16 cm downstream of the butanol sample, respectively.

3.9.1 Determination of the Dilution Factor

Figure 3.22 (left) shows an example of a missing-mass distribution. The black solid line denotes butanol events after all corrections and selection cuts. An additional $CL > 5\,\%$ cut resulted in the

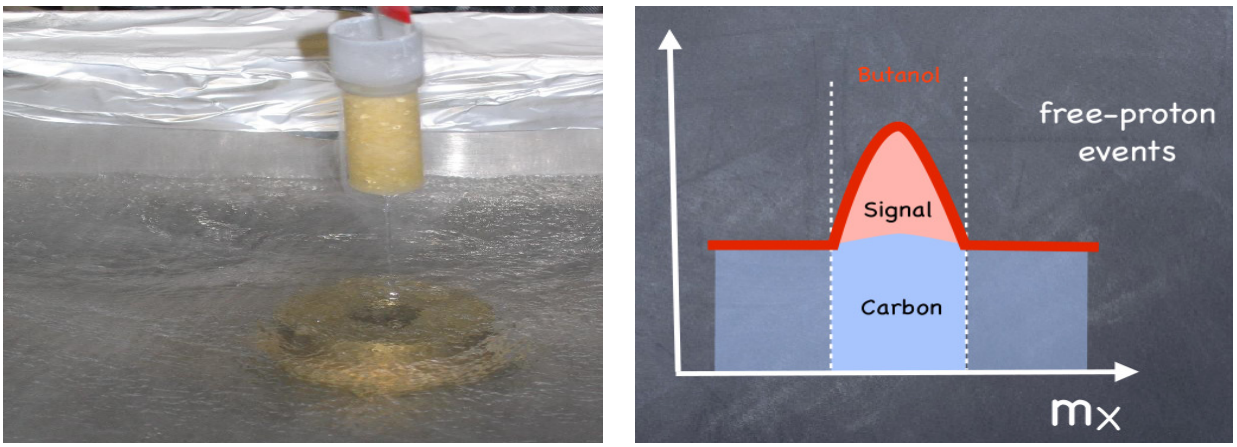

Figure 3.21: (Left) The polarized target material consisted of 1.5 mm beads of frozen Butanol doped with the paramagnetic radical TEMPO. They were contained within a 15×50 mm Kel-F cup. Here the beads had just been loaded into the cup (under liquid nitrogen) and were ready to be attached to the target insert. (Right) An schematic illustration of the dilution factor.

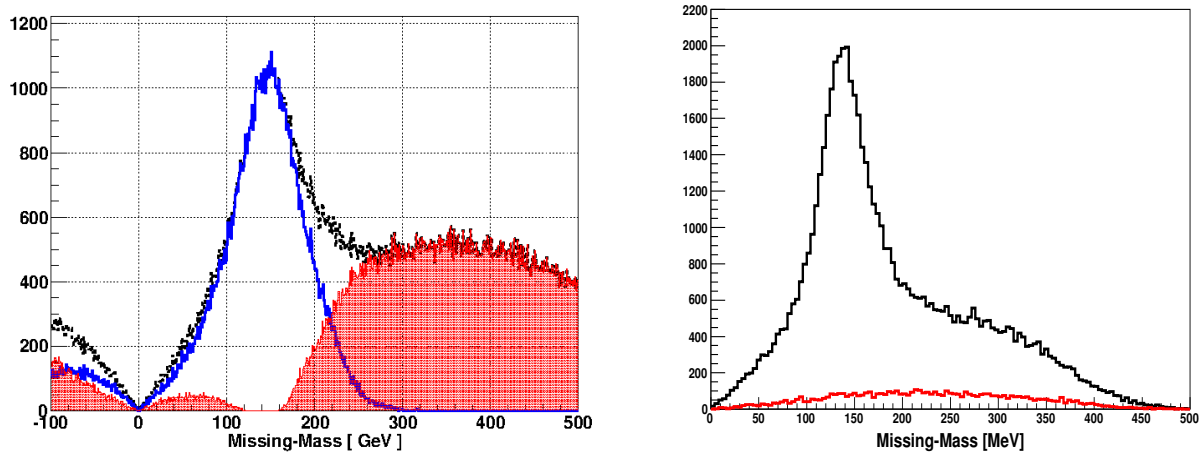

Figure 3.22: (Left) An example of a mass distribution from the butanol target for topology 1 (π^- missing in all $p\pi^+\pi^-$ events). The black curve shows the mass distribution after applying photon selection cuts, particle selection cuts and energy-momentum corrections. The blue curve represents events which survived after applying a $CL > 5\%$ cut and the red filled plot shows the events which did not survive this cut. A lot of background events remained in the blue distribution which could be assigned to kinematically-good events originating from bound nucleons of the butanol target. (Right) Missing π^- mass distributions for the reaction $\gamma p \to p\,\pi^+\pi^-$ from the butanol (black curve) and carbon (red curve) targets.

blue distribution. Since the various topologies in the reaction $\gamma p \to p\,\pi^+\pi^-$ from hydrogen could be considered background free (see [44]), the remaining background in the blue distribution could be assigned to contributions from bound nucleons. In the $\omega \to \pi^+\pi^-\pi^0$ channel based on Topology 5, competing hadronic reactions also contributed to the background, particularly the two-pion final state with a reconstructed *fake* π^0.

Traditionally, signal-background separation is carried out in a binned analysis by determining dilution factors for each kinematic bin. The procedure is based on comparing corresponding mass distributions from butanol and carbon. It is assumed that bound-nucleon events from ^{12}C and ^{16}O nuclei in the butanol behave very similarly, and can be appropriately subtracted using the data from the carbon target. Figure 3.22 (right) illustrates the procedure using the example of a missing-π^- mass distribution. The black (red) solid line shows the distribution from butanol (carbon). The carbon distribution needs to be scaled to match the butanol outside the signal region. The background can then be subtracted by either using the carbon data directly or by fitting the carbon and using the analytic description of the carbon distribution.

The equation to calculate the dilution factor D in a particular W bin is given by:

$$D\,(W) \;=\; 1 \;-\; \frac{s\,N_C\,(W)}{N_{C_4H_9OH}\,(W)}\,, \tag{3.17}$$

where $s\,N_C$ is the number of scaled carbon events, $N_{C_4H_9OH}$ is the number of butanol events, and the parameter s is the carbon scale factor. The method to determine the scale parameters, usually referred to as *phase space scale factors*, is described in [80] and was used by other FROST members.

Since the carbon data in the g9a experiment suffered from a hydrogen contamination of unknown origin [64] and the carbon statistics was also generally poor, we developed a technique which allowed us to subtract the bound-nucleon background without using information from the other targets. This so-called "Q-factor" method was based on a powerful multivariate analysis technique and was previously used for the analysis of CLAS hydrogen (g11a) data [81].

The Q-factor method and the machinery developed at FSU had the following salient features and advantages:

- The method was a generalization of the traditional one-dimensional side-band subtraction method to higher dimensions without having to bin the data.
- The results were event-based quality factors which could be considered event-based dilution factors and denoted the probability for an event to be a signal rather than a background event. The event-based Q-factors could then be used as weights in any distribution such as mass distributions, cross sections and asymmetries. Therefore, it also facilitated the performance of event-based PWAs and other interpretation techniques.
- Since the photoproduction of two pseudoscalar mesons required five independent kinematic variables, the Q-factors allowed us to quickly re-display the asymmetries for a different choice of kinematic variables without having to repeat the analysis and find new dilution factors each time.
- The Q-factor machinery developed at FSU was user-friendly and sufficiently general to perform background subtraction for both reactions, $\gamma p \to p\,\pi^+\pi^-$ and $\gamma p \to p\,\omega \to p\,\pi^+\pi^-\pi^0$.

3.9.2 General Description

In this event-based method, the set of coordinates that described the multi-dimensional phase space of the reaction were categorized into two types: *reference* and *non-reference* coordinates. The signal and background shapes had to be known *a priori* in the reference coordinate but this

knowledge was not required in the non-reference coordinates. Mass was typically chosen as the reference coordinate. For each event, we then set out to find the N_c nearest neighbors in the phase space of the non-reference coordinates. This was similar to binning the data using a dynamical bin width in the non-reference coordinates and making sure that we had N_c events per fit.

The mass distribution of the N_c events (including the candidate event) in the reference coordinate was then fitted with a total function defined as:

$$f(x) = N \cdot [f_s \cdot S(x) + (1 - f_s) \cdot B(x)], \tag{3.18}$$

where $S(x)$ denoted the signal and $B(x)$ the background probability density function. N was a normalization constant and f_s was the signal fraction with a value between 0 and 1. The Roofit package of the CERN ROOT software [82] was used for the fit procedure. Since N_c was usually a small number (of the order of a few hundred events), an unbinned maximum likelihood method was used for the fitting. The Q-factor itself was then given by:

$$Q = \frac{s(x)}{s(x) + b(x)}, \tag{3.19}$$

where x was the reference-coordinate value of the candidate event, $s(x) = f_s \cdot S(x)$ and $b(x) = (1 - f_s) \cdot B(x)$. The Q-factor could then be used as an event weight to determine the signal contribution to any physical distribution.

3.9.3 The Q-Factor Method for the $\gamma p \to p\,\omega$ Reaction

The kinematic variables which described the reaction $\gamma p \to p\,\omega$ were the incoming photon energy, E_γ, the center-of-mass angle of the outgoing ω, $\cos\theta^{\omega}_{\mathrm{c.m.}}$ and the lab azimuthal angle of the recoil proton, $\phi^{p}_{\mathrm{recoil}}$ (since angular distributions in this angle were fitted to extract the polarization observables). Furthermore, since we reconstructed the ω from its decay into $\pi^+\pi^-(\pi^0)$, we also considered the relevant kinematic variables which described the five-dimensional phase space of the 3π system. The decay was described by five independent kinematic variables but we only chose three of them since the decay amplitude was only sensitive to these three variables [13]. The choice was:

- The two angles of the ω meson in the helicity frame, $\cos\theta_{\mathrm{HEL}}$ and ϕ_{HEL}, and
- The parameter $\lambda \propto |\,\vec{p}_{\pi^+} \times \vec{p}_{\pi^-}\,|^2$ [13].

The five non-reference coordinates and their maximum ranges used in the Q-factor method are summarized in Table 3.17.

Table 3.17: The non-reference coordinates Γ_i and their ranges Δ_i. Here,"Q" denotes the total kinetic energy of the $\pi^+\pi^-\pi^0$ system.

Γ_i	Non-Reference Coordinate	Maximum Range Δ_i
Γ_0	$\cos\Theta^{\text{proton}}_{\text{c. m.}}$	2
Γ_1	$\cos\theta_{\text{HEL}}$	2
Γ_2	ϕ_{HEL}	2π [radians]
Γ_3	λ	$Q^2(\frac{Q^2}{108}+\frac{mQ}{9}+\frac{m^2}{3})$
Γ_4	ϕ^p_{recoil}	π [radians]

For the signal-background separation in the $\omega \to \pi^+\pi^-\pi^0$ analysis, we initially applied a small $CL > 0.001$ cut (from kinematic fitting) on the $\gamma p \to p\,\pi^+\pi^-\,(\pi^0)$ final state. This loose CL cut significantly reduced the background, in particular from $\gamma p \to p\,\pi^+\pi^-$. We then used the event-based technique to select ω events.

The data were divided into sub-datasets based on the photon energy (100-MeV wide bins) and beam-target polarization orientations. We chose 300 nearest neighbor events for each signal candidate in the phase space spanned by the non-reference coordinates. The $\pi^+\pi^-\,(\pi^0)$ invariant mass distribution of these 300 events was fitted using the unbinned maximum-likelihood technique. Since the natural width of the ω meson is 8.49 MeV which is at the level of the detector resolution, we chose a Voigtian function for the signal pdf. The Voigtian function was a convolution of a Gaussian, which was used to describe the resolution, and a Breit-Wigner, which described the natural line shape of the resonance. The background shape was modeled with a second-order Chebychev polynomial. The phase space close to the ω production threshold ($E_\gamma \in [1100, 1300]$ MeV) had a fairly sharp cut-off on the right-hand side of the omega-signal peak. Hence, we used the product of an Argus function and a second-order Chebychev polynomial to describe the mass distributions. The Argus pdf is a standard function which is typically used to describe the edge of the phase space in multi-body decays near threshold [82]. The Chebychev pdf was again used to describe the smooth shape of the phase space away from the edge.

Table 3.18 shows the parameters of the signal and background pdfs and the constraints imposed on them. The two pdfs were used to construct a total pdf (see Equation 3.18) and the Q-factor of the signal candidate was extracted using Equation 3.19. Figure 3.23 shows an example of a fit to an invariant $\pi^+\pi^-$ (π^0) mass distribution of 300 events. The figure shows a comparison of the data with appropriately normalized signal and background pdfs after the fit parameters were determined in the unbinned maximum likelihood fit.

Quality Checks A quality check of our event-based technique was provided by the following. Once the fit parameters were determined in an individual likelihood fit, we performed a least-square fit of the same mass distribution from the 301 events. On the one hand, this allowed us to display the fit functions shown in Figure 3.23. On the other hand, we were able to plot the distribution of all reduced-χ^2 values as another goodness-of-fit measure. Figure 3.24 shows several goodness-of-fit measures for the three energy bins $E_\gamma \in [1200, 1300]$ MeV, $E_\gamma \in [1300, 1400]$ MeV, and $E_\gamma \in [1400, 1500]$ MeV. The reduced-χ^2 distributions in the left column peak fairly close to the ideal value of *one*. We observed a transition from peak values above *one* to peak values below *one* around 1.4 GeV. The signal statistics gradually decreased toward higher energies and we concluded

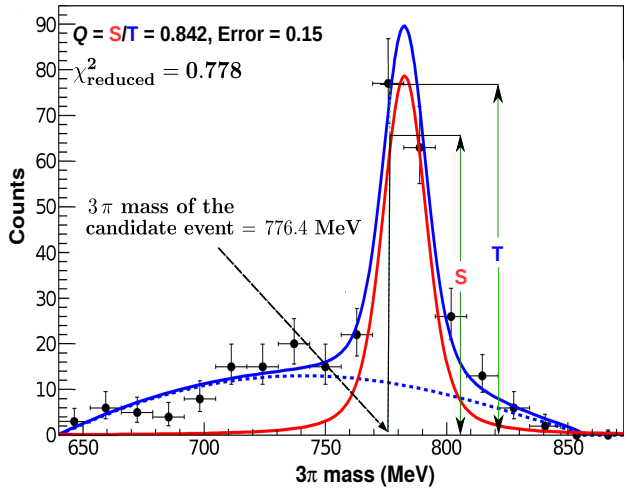

Figure 3.23: A typical example of a $\pi^+\pi^-\pi^0$ mass distribution of 300 nearest-neighbors for a chosen butanol event with $E_\gamma \in [1.2, 1.3]$ GeV. The blue solid line represents the total fit, the red solid line the signal, and the blue dotted line the background function. The "seed" value gave the 3π mass of the signal candidate. The Q-factor was given by S/T where S (T) was the height of the signal pdf (total pdf) at the "seed" value.

Table 3.18: Parameters of the signal and background probability-density functions and the constraints imposed on them. Above 1.3 GeV, a Voigtian was used to describe the signal and a Chebychev polynomial was used to describe the background. Near threshold, a product of Argus and Chebychev was used to describe the background. For m_0, the values in parentheses applied to $E_\gamma \in [1.2, 1.3]$ GeV.

	Parameters	Initial Value	Constraints
Voigtian pdf	Mean, μ	782.65 MeV	770.0 - 800.0 MeV
	Gaussian width, σ	~ 10 MeV	1-20 MeV
	Decay width, Γ	8.49 MeV	Fixed parameter
Chebychev pdf	c_0	0.2	-0.50 - 1.0
	c_1	~ -0.2	-1.00 - 1.0
	c_2	-0.005	-0.01 - 0.1
Argus pdf	m_0 (edge of phase space)	810.0 MeV (840.0 MeV)	± 10 MeV (± 30 MeV)
	c (curvature of Argus)	-0.001	Fixed parameter
Chebychev pdf	c_0	0.2	-0.50 - 1.0
	c_1	-0.2	-1.00 - 1.0
	c_2	-0.02	Fixed parameter

that the fitter started to describe statistical fluctuations. This resulted in over-constrained fits and smaller reduced χ^2 values, on average.

Since the ω decay amplitude is proportional to the parameter λ [13], the λ distribution of the identified signal events should have a linear slope. Figure 3.24 (right column) shows these distributions for the same energy bins as in the left column. The (red) signal distribution was generated by weighting event-by-event the (black) butanol distribution with the Q-values; the (blue) background distribution was generated by weighting the butanol distribution with $1 - Q$. Some small deviations from the expected linear behavior could be observed at small λ values. Since the background from butanol was complicated, the shape was not well described. Some ω events off bound nucleons likely contributed and a flat background distribution (as is typically the case for hydrogen) could not be expected.

Finally, representative g9b (circular beam polarization), and g9b (linear beam polarization) ω-mass distributions including the Q-factor fit results are presented in 3.25 & 3.26, and 3.27, respectively.

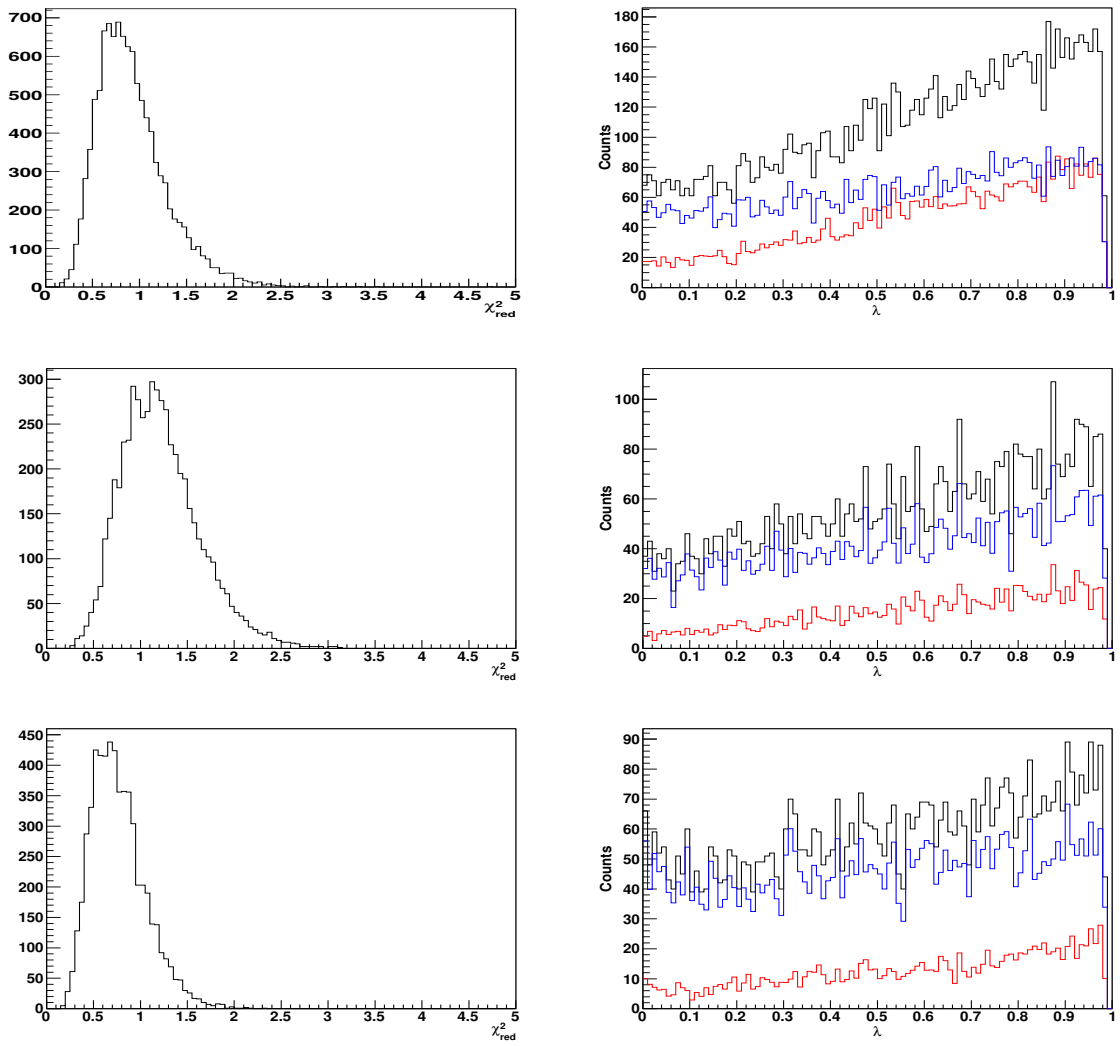

Figure 3.24: (Left column) Examples of reduced-χ^2 distributions from g9b (PARA beam & '+' target polarization) for (from top to bottom) $E_\gamma \in [1.2, 1.3]$ GeV, $E_\gamma \in [1.3, 1.4]$ GeV, and $E_\gamma \in [1.4, 1.5]$ GeV. (Right column) Examples of λ distributions for the same energy bins. The black line denotes the butanol, the red line the signal, and the blue solid line the background distribution.

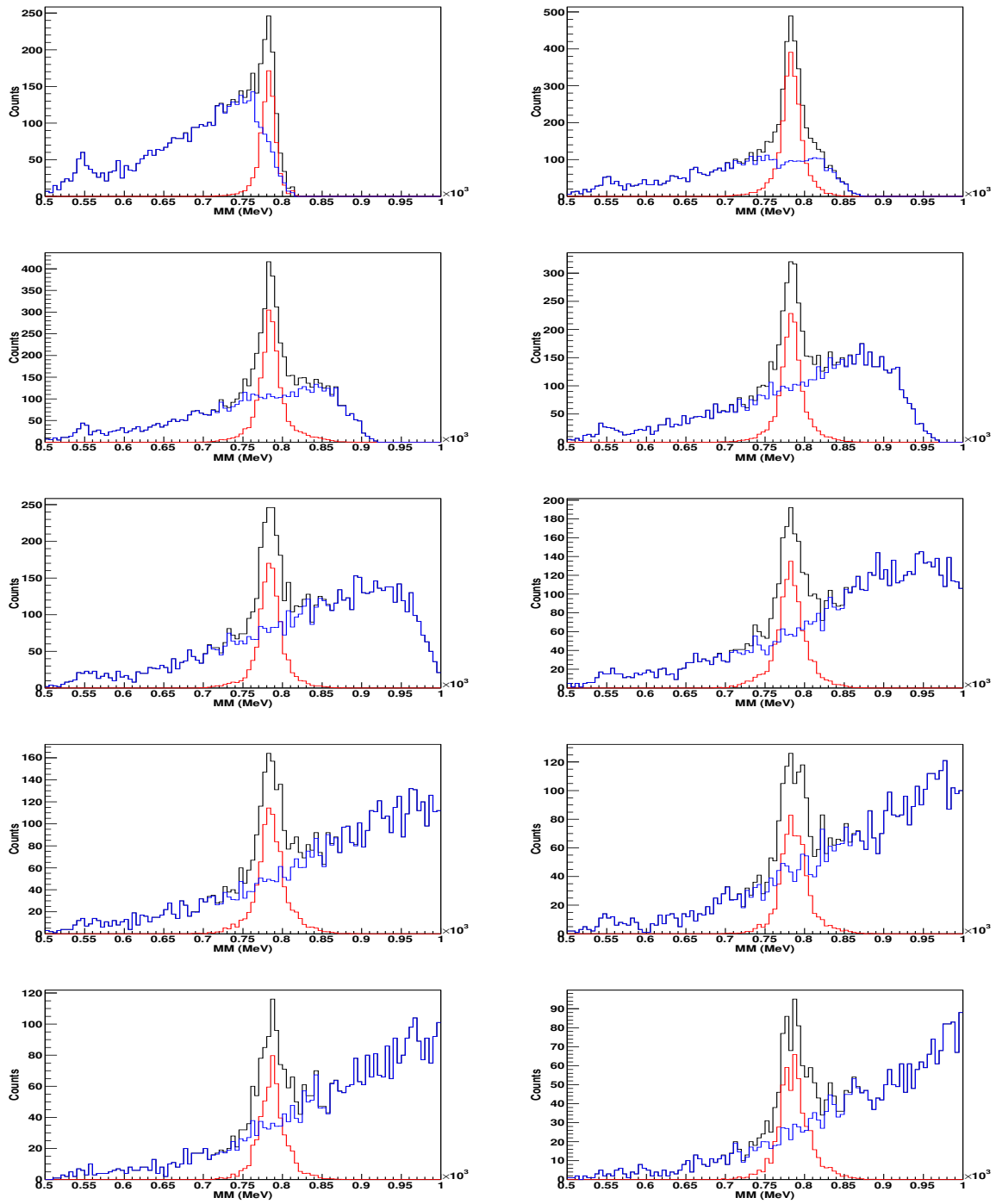

Figure 3.25: Examples of g9b (circular beam polarization) invariant $\pi^+\pi^-\pi^0$ distributions for the reaction $\gamma p \to p\,\omega$ (Period 3, positive beam helicity). Shown are 100-MeV wide energy bins starting at $E_\gamma \in [1100, 1200]$ MeV (top left), $E_\gamma \in [1200, 1300]$ MeV (top right), etc. The background description at threshold was challenging close to the reaction threshold. We refer to Section 5.1 for a discussion on the corresponding systematic uncertainty.

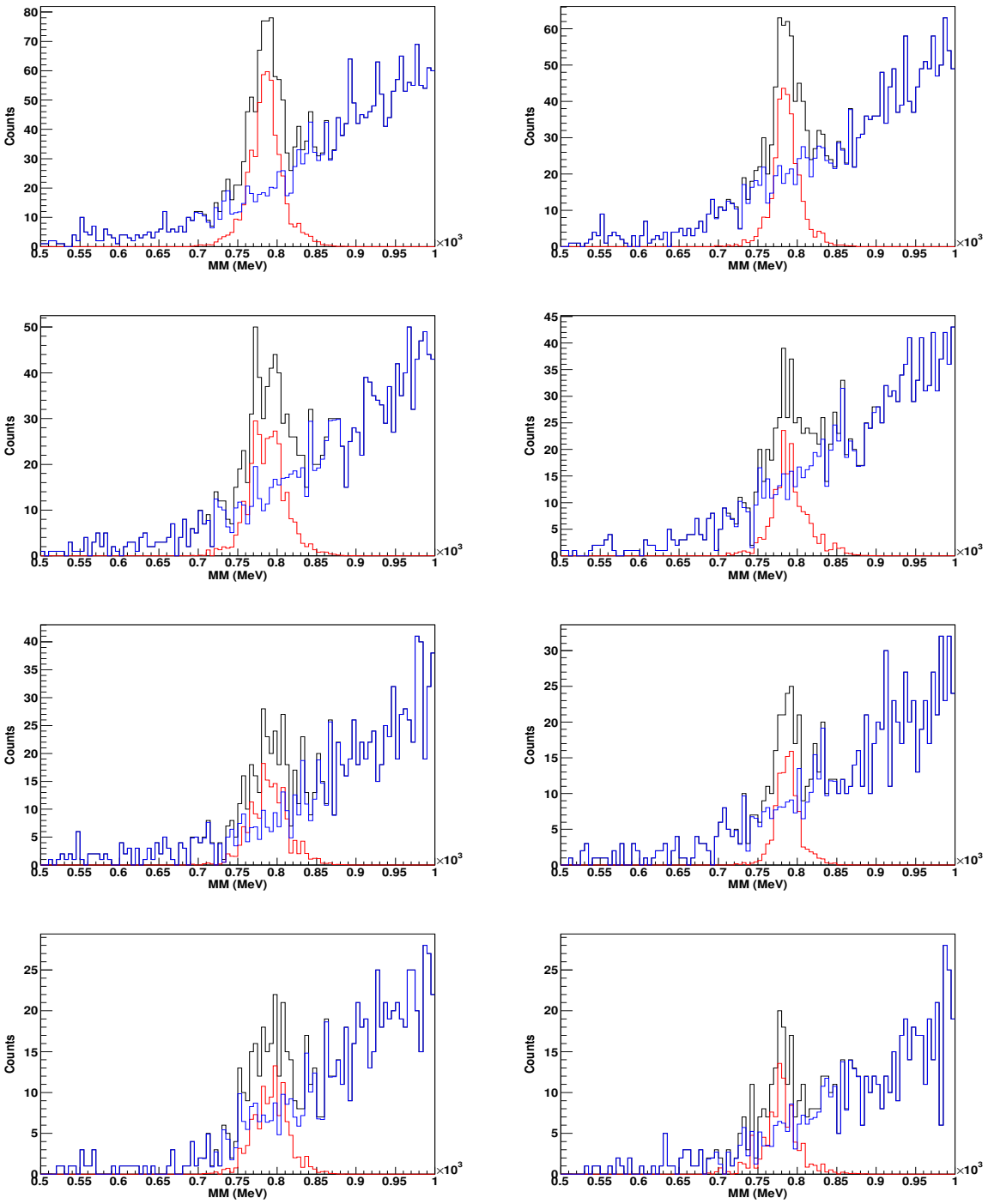

Figure 3.26: Continuation of Figure 3.25 (previous page). Examples of g9b (circular beam polarization) invariant $\pi^+\pi^-\pi^0$ distributions for the reaction $\gamma p \to p\omega$ (Period 3, positive beam helicity). Shown are 100-MeV wide energy bins starting at $E_\gamma \in [2100, 2200]$ MeV (top left), $E_\gamma \in [2200, 2300]$ MeV (top right), etc.

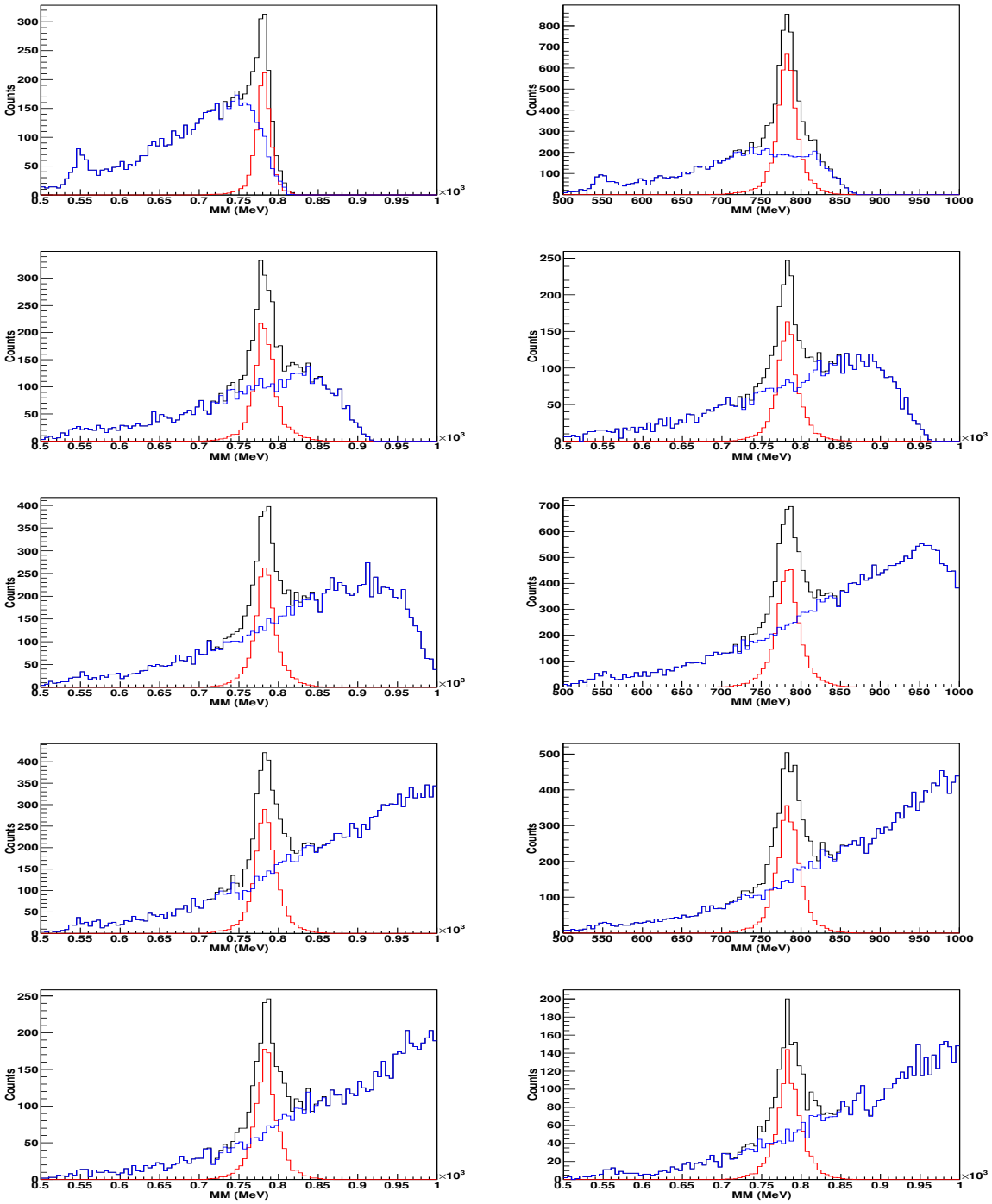

Figure 3.27: Examples of g9b (linear beam polarization) invariant $\pi^+\pi^-\pi^0$ distributions for the reaction $\gamma p \to p\,\omega$ (beam polarization PARA & target polarization +). Shown are 100-MeV wide energy bins starting at $E_\gamma \in [1100, 1200]$ MeV (top left), $E_\gamma \in [1200, 1300]$ MeV (top right), etc. The background description at threshold was challenging close to the reaction threshold. We refer to Section 5.1 for a discussion on the corresponding systematic uncertainty.

3.9.4 The Q-Factor Method for the $\gamma p \to p\,\pi^+\pi^-$ Reaction

In the two-pion reaction, the following five kinematic variables were chosen to define the five-dimensional kinematic phase space:

- The overall center-of-mass angle of the proton, $\cos\Theta_{\mathrm{c.m.}}$,
- A mass, $m_{\mathrm{p}\pi^+}$ or $m_{\mathrm{p}\pi^-}$ or $m_{\pi^+\pi^-}$,
- The incoming photon energy, E_γ, or the overall center-of-mass energy, W, and
- The polar and azimuthal angles, $\theta^*_{\pi^+}$ and $\phi^*_{\pi^+}$, in the rest frame of the $\pi^+\pi^-$ system. [4]

In addition, we fitted $\phi^{lab}_{\pi^+}$ modulations to extract the final observables. Accordingly, we chose five non-reference coordinates (denoted by Γ_i) for this reaction. They are listed in Table 3.19. For each candidate event, the events closest in the kinematic phase space defined by the five non-reference coordinates were selected to perform event-based unbinned maximum likelihood fits [82] in the remaining fifth variable. In our analyses, we performed fits of the missing-π^- mass in Topology 1, the missing-π^+ mass in Topology 2, and the missing-proton mass in Topology 4 (by artificially leaving out the proton). We chose the proton in Topology 4 because the missing-nucleon peak was much narrower than the missing-pion peak. In particular at lower energies, this allowed for more background on both sides of the signal peak to constrain the fits. At higher energies, either a missing-π or the missing-proton peak worked reasonably well. At the end, we used the missing-π^- peak only for the g9b data above 1600 MeV. We did not analyze γp events with a missing proton (Topology 3) because such events could not be distinguished from γn events.

To locate the nearest-neighbor events, the following equation describing the distance between event a and b, D_{ab}, was used:

$$D^2_{ab} = \sum_{i=1}^{4} \left(\frac{\Gamma^a_i - \Gamma^b_i}{\Delta_i} \right)^2 , \tag{3.20}$$

where Γ_i was the i^{th} non-reference coordinate and Δ_i was the maximum range of the non-reference coordinate Γ_i. Table 3.19 also shows the maximum ranges of these kinematic variables.

The data were first divided into sub-datasets based on the photon energy (100 MeV wide bins) and beam-target polarization settings. The Q-factor machinery was then applied to each sub-dataset separately. This enabled us to parallelize the procedure by submitting multiple jobs, thus

[4] See Section 4.1.2 for a full discussion of the $\gamma p \to p\,\pi^+\pi^-$ kinematics.

Table 3.19: The non-reference coordinates Γ_i and their ranges Δ_i used in the Q-factor method.

Γ_i	Non-Reference Coordinate	Maximum Range Δ_i
Γ_0	Photon Energy E	100 [MeV]
Γ_1	$\cos\Theta^{\text{proton}}_{\text{c. m.}}$	2
Γ_2	$\phi^*_{\pi^+}$	2π [radians]
Γ_3	$\cos\theta^*_{\pi^+}$	2
Γ_4	$\phi^{lab}_{\pi^+}$	π [radians]

Table 3.20: Parameters of the signal and background probability-density functions and the constraints imposed on them. A Gaussian pdf was used to describe the signal and a second-order Chebychev polynomial was used to describe the background. Values in parentheses applied to $E_\gamma > 1200$ MeV.

	Parameters	Initial Value	Constraints	Initial Value	Constraints
Gaussian pdf	Mean, μ	140.0 MeV	$\pm$ 20 MeV	938.0 MeV	$\pm$20 MeV
	Width, σ	28.5 MeV	$\geq$ 2 MeV	10 MeV	$\geq$ 2 MeV
Chebychev pdf	c_0	0.2	-0.5 - 1.0	0.2	-0.5 - 1.0
	c_1	-0.5	-1.0 - 1.0 (-0.5 - 0.5)	-0.1	-1.0 - 1.0 (-0.5 - 0.5)
	c_2	-0.01 (0.05)	-1.0 - 1.0 (-0.01 - 0.1)	-0.01 (0.05)	-1.0 - 1.0 (-0.01 - 0.1)

significantly reducing the time consumption. We chose 300 nearest neighbors for each candidate event (excluding the candidate itself). In the missing π^- or π^+ mass distributions from the butanol target, a clear peak near 139.5 MeV for the pion could be seen. Since the peak was much broader than the natural width of the π^-, a Gaussian resolution function was used for the signal probability-density function (pdf). The same argument applies to the missing-proton peak. For the background pdf, we chose a second-order Chebychev polynomial. The parameters and the constraints imposed on the fit are shown in Table 3.20. The total pdf was constructed from the signal and background pdfs (Equation 3.18) and the Q-factor of the candidate event was determined according to Equation 3.19.

Quality Checks Although the carbon target was placed in the target cryostat for background studies, we did not use the mass distributions from carbon to define the background pdf because of its low statistics which introduced large fluctuations in the background function. However, to check the quality of the Q-factor method, we compared the scaled mass distributions from carbon with the background mass distributions obtained by weighting each event with $1 - Q$. The carbon distributions were scaled to the butanol background sufficiently-far away from the pion peak in a fitting procedure. An example of the good agreement between the butanol and the scaled carbon is shown in Figure 3.28 (left). The right side shows the method to determine the scale factor.

Further examples for the three different topologies at different energies are shown in Figure 3.30. Some small discrepancies were observed between the scaled carbon distributions and the butanol. In the lower-energy range (top row) for example, our background description in the signal region appeared to overestimate the carbon distribution for missing masses $\lesssim$130 MeV/c^2, whereas it seems to underestimate the carbon distribution for missing masses above. We believe that the disagreement originates from the behavior of carbon which is still not well understood. For example, we observed that the curvature in the carbon distribution changed from concave in the mass range 20 - 110 MeV/c^2 to convex beyond about 110 MeV/c^2. Given the different target positions and the unknown hydrogen contamination of the g9a carbon data, there is no obvious reason why the carbon distributions should *perfectly* match the actual background from the butanol.

Another quality check of our event-based technique was provided by the distribution of all reduced-χ^2 values obtained after performing least-square fits of the mass distributions from 301 events per seed event, using the pre-determined values of the fit parameters from the likelihood fits. Figure 3.29 shows an example of such a reduced-χ^2 distribution obtained from all Q-factor fits in the chosen data set (corresponding to Figure 3.28). The distribution peaks near the ideal value of *one*, which showed that our technique worked effectively.

Finally, examples of g9 mass distributions for the two-pion channel including the Q-factor fit results are shown on the following pages (Figures 3.31-3.32). The figures present the full statistics for the selected data sets of particular beam and target polarization. Without any loss of generality, they serve as representative distributions for all of the FROST data we analyzed. Presented are data for PARA and positive target polarization. In all figures, the left column represents Topology 1, the middle column Topology 2, and the right column Topology 4.

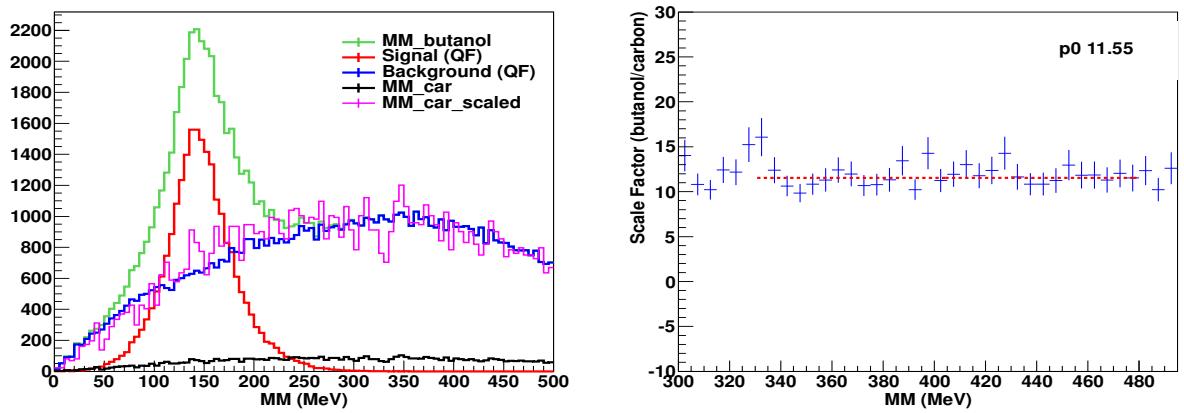

Figure 3.28: (Left) Example of a g9b missing-mass distribution for $E_\gamma \in [1.2, 1.3]$ GeV. The green distribution denotes the butanol data, the red distribution the signal (data weighted with Q), and the blue distribution shows the background (data weighted with $1 - Q$). The carbon and scaled carbon distributions are given by the black and the magenta distributions, respectively. (Right) A zero-order fit of the butanol/carbon ratio in the mass range $[300, 500]$ MeV to determine the scale factor.

At very low energies, $E_\gamma \in [500\,, 700]$ MeV, the typical Topology 2 distributions showed more background to the left of the signal peak than could be observed for Topology 1, where the signal essentially covered the available phase space. For this reason, a reliable background subtraction was not possible for Topology 1 below 700 MeV. For Topology 4, we used the missing-proton peak because it was narrower than the missing-π peak. At higher energies, both approaches worked

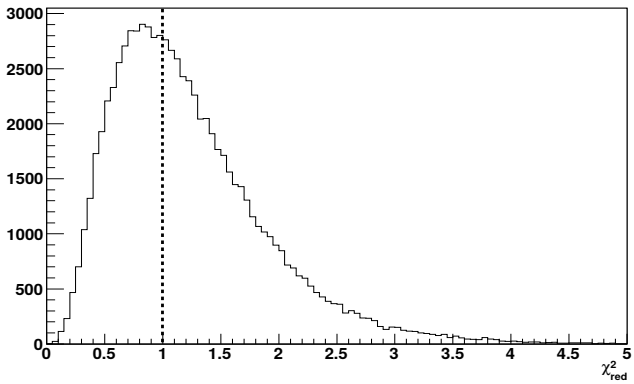

Figure 3.29: Example of a reduced-χ^2 distribution from the data shown in Figure 3.28.

fine but we used the missing-π^- peak above 1600 MeV (Fig. 3.32). Moreover, the Topology 4 background generally exhibited small peak-like structures around the tails of the signal peak. The higher-mass structure was also observed in carbon (e.g. Fig. 3.30) and turned out to be a true feature of the background. Unfortunately, the lower-mass structure appeared to be an associated consequence of the fitting at low energies. However, the effect had no noticeable impact on the final observables and for this reason, we considered it negligible.

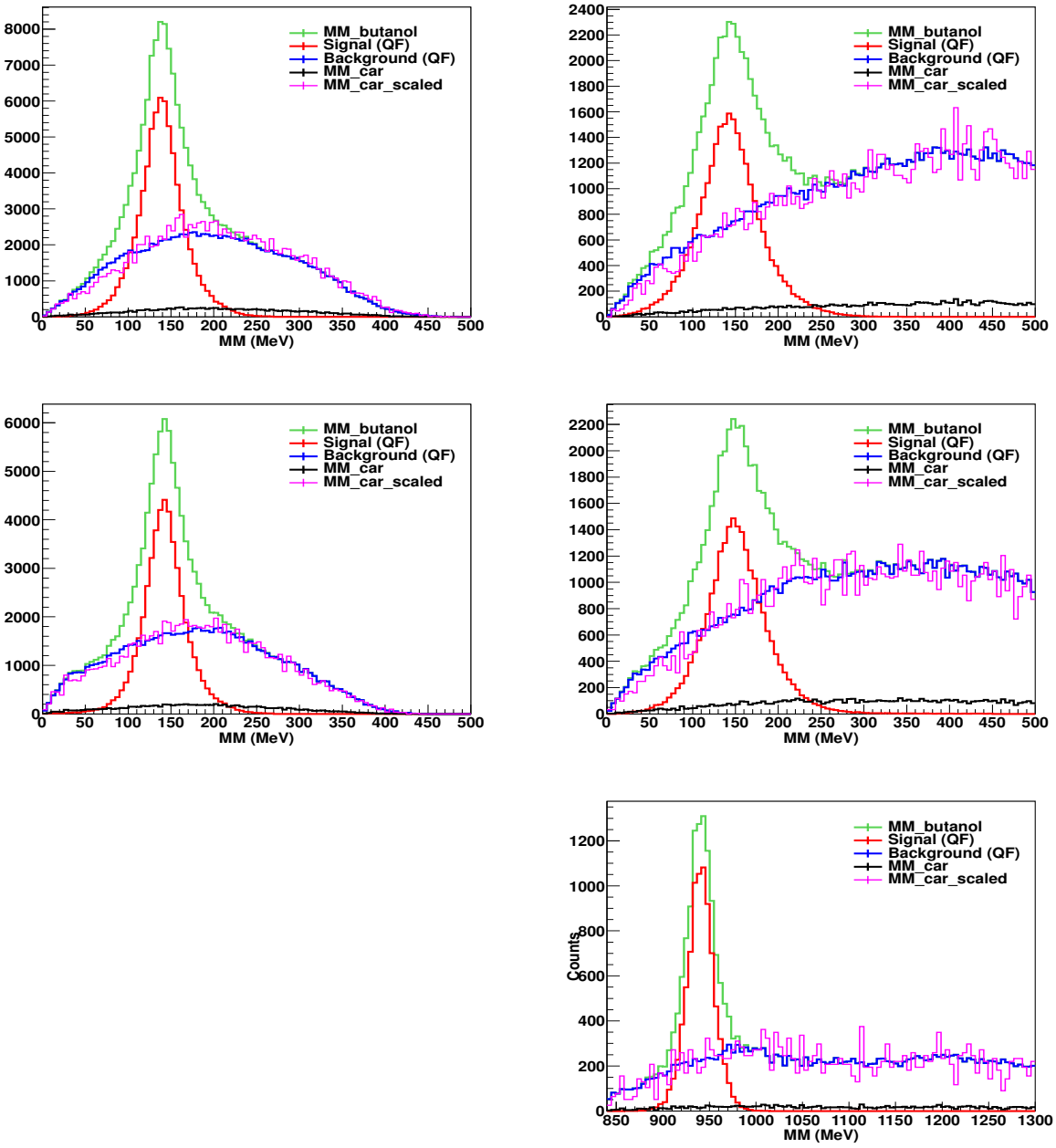

Figure 3.30: Examples of g9b missing-mass distributions for $E_\gamma \in [0.8, 0.9]$ GeV (left) as well as $E_\gamma \in [1.5, 1.6]$ GeV (right); shown are Topology 1 (top), Topology 2 (center), & Topology 4 (bottom). The green distribution denotes the butanol data, the red distribution the signal (data weighted with Q), and the blue distribution shows the background (data weighted with $1 - Q$). The carbon and scaled carbon distributions are given by the black and the magenta distributions, respectively.

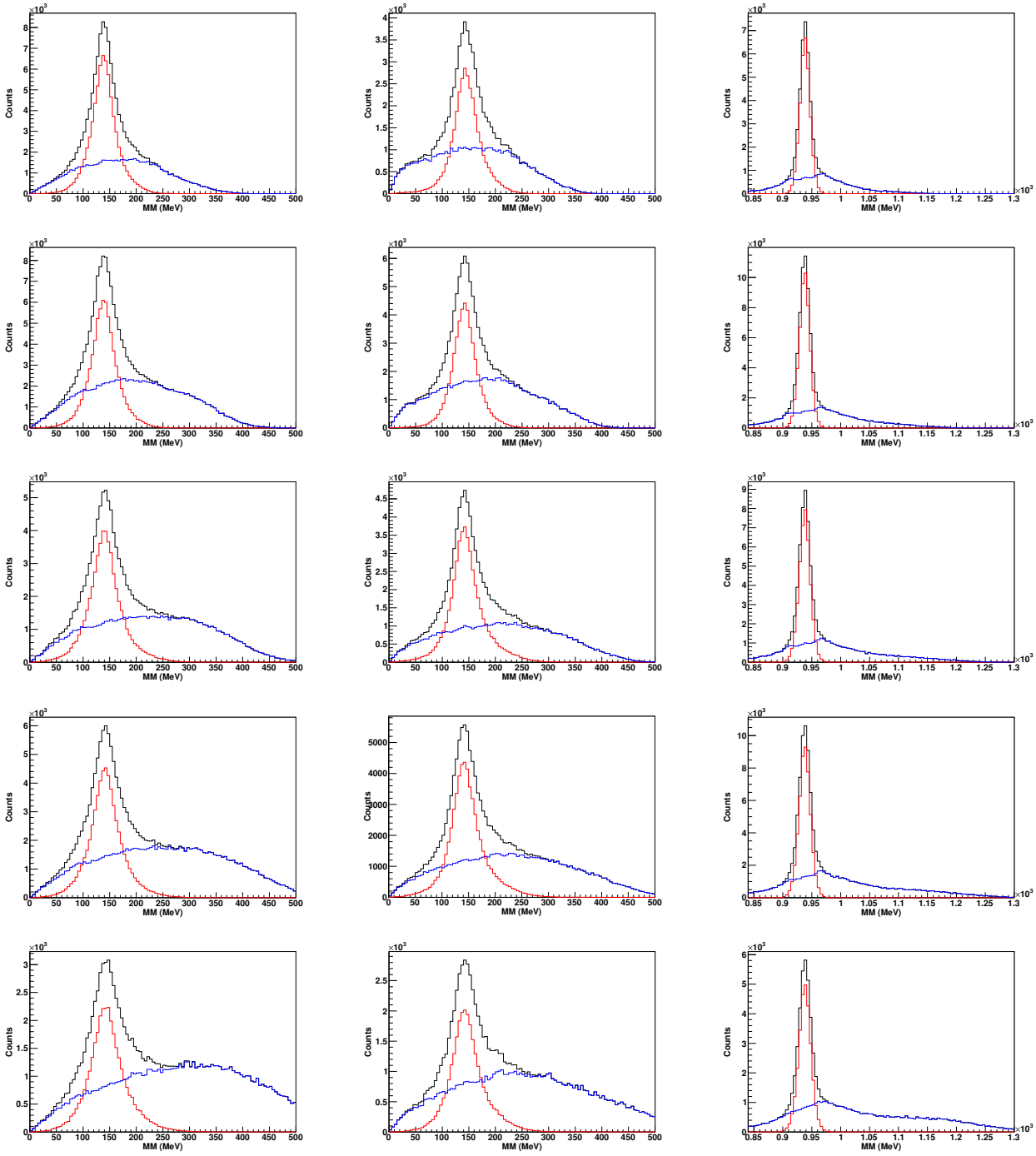

Figure 3.31: Examples of g9b missing-mass distributions for the two-pion reaction $\gamma p \to p\,\pi^+\pi^-$ (beam polarization PARA & target polarization +). The individual rows show the energy bins 700-800 MeV, 800-900 MeV, 900-1000 MeV, 1000-1100 MeV, 1100-1200 MeV. The three columns represent Topology 1 (left), Topology 2 (center), Topology 4 (right). See text for more details.

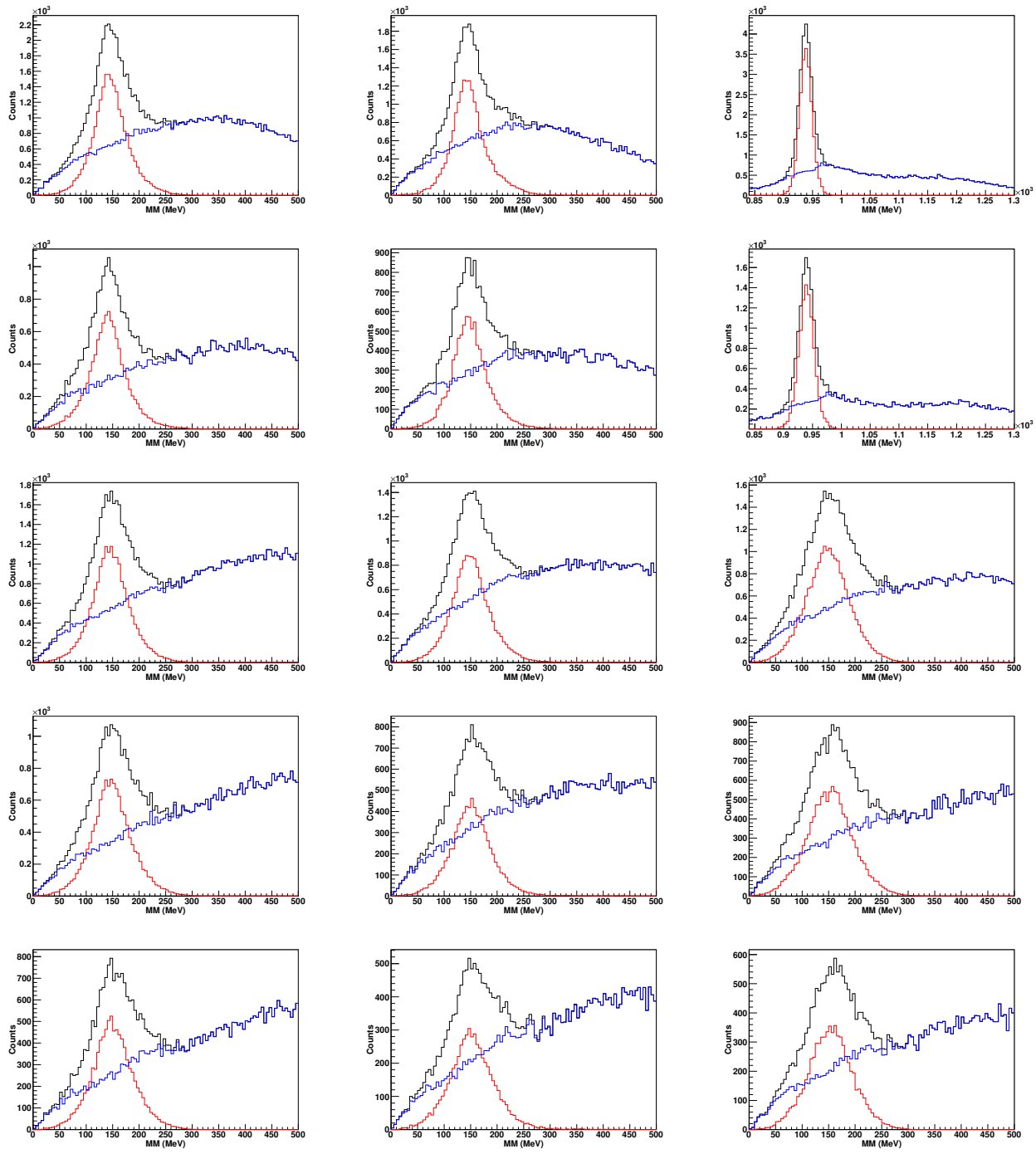

Figure 3.32: Examples of g9b missing-mass distributions for the two-pion reaction $\gamma p \to p\pi^+\pi^-$ (beam polarization PARA & target polarization +). The individual rows show the energy bins 1200-1300 MeV, 1400-1500 MeV, 1600-1700 MeV, 1800-1900 MeV, 2000-2100 MeV. The three columns represent Topology 1 (left), Topology 2 (center), Topology 4 (right). Note that we used the missing-pion peak above 1600 MeV in Topology 4. See text for more details.

CHAPTER 4

GENERAL PHYSICS ANALYSIS

After all corrections and cuts were applied and signal-background separation was carried out, the extraction of polarization observables from the carefully selected events could commence. This chapter presents the methodology utilized in the extraction of single- and double-polarization observables from the experimental data.

4.1 Data Description and Kinematics

4.1.1 Binning and Angles in the $\gamma p \to p\,\omega$ Analysis

The kinematics of ω photoproduction off the proton could be completely described by two variables. We chose these variables to be the incoming photon energy, E_γ, and the cosine of the polar angle of the ω meson in the center-of-mass frame, $\cos\Theta^{\omega}_{\text{c.m.}}$, where the z-axis was defined along the incoming photon beam (see Figure 4.1). Alternatively, we also chose $\Theta^{\omega}_{\text{c.m.}}$ instead of its cosine rendering possible a direct comparison with recently published results from the GRAAL collaboration [29]. The data were binned in 100-MeV wide E_γ bins, which covered an energy range from 1100-2100 MeV (when the photon beam was linearly polarized) or 1100-2800 MeV (when the beam was circularly polarized). For all polarization observables except for **H** and **P**, the $\Theta^{\omega}_{\text{c.m.}}$ or $\cos\Theta^{\omega}_{\text{c.m.}}$ variable was binned in nine or 10 bins depending on statistics. Note that CLAS had a poor acceptance for three-track events in the very forward and backward directions in the center-of-mass frame. This was taken into consideration when defining the bins. In total, we used 96 (160) bins in Topology 5 when the data had a linearly- (circularly-)polarized photon beam.

In the extraction of the double-polarization observables **H** and **P**, only five bins were used for $\cos\Theta^{\omega}_{\text{c.m.}}$ since the asymmetries, from which the observables were extracted, had a more complicated form involving products of sine and cosine terms and two associated fit parameters; this is discussed in Section 4.4.3. The use of wider bins increased statistics and hence, improved the quality of the fits (though at an accepted small loss of angular information).

4.1.2 Binning and Angles in the $\gamma p \to p\,\pi^+\pi^-$ Analysis

The kinematics of $\gamma p \to p\,\pi^+\pi^-$ required a selection of five independent kinematic variables. For this analysis, $\cos\Theta_{\text{c.m.}}$, a mass ($m_{p\pi^+}$, $m_{p\pi^-}$, or $m_{\pi^+\pi^-}$), the photon energy, E_γ, as well as θ_{π^+} and ϕ_{π^+} were chosen. The latter two angles denoted the polar and azimuthal angles of the π^+ in the rest frame of the $\pi^+\pi^-$ system. A diagram showing the kinematics of the reaction can be seen in Figure 4.2. The blue plane represents the center-of-mass production plane composed of the initial photon and the recoil proton, whereas the red plane represents the decay plane formed by two of the final-state particles.

The angle ϕ^* shown in Figure 4.2 was a kinematic variable unique to a final state containing two pseudoscalar mesons. It described the orientation of the decay plane with respect to the production plane. It was also given by the azimuthal angle of one of the particles from the chosen pair in this pair's rest frame. In our analysis, we chose the π^+ meson (the corresponding azimuthal angle will be denoted as ϕ_{π^+} instead of ϕ^*). The angle ϕ_{π^+} was calculated via two boosts. The first being a boost along the beam axis into the overall center-of-mass frame. The second boost occurred along the axis anti-parallel to the recoiling proton and resulted in the two-π rest frame, wherein the two final-state pions departed back-to-back. Mathematically, ϕ_{π^+} was uniquely determined by

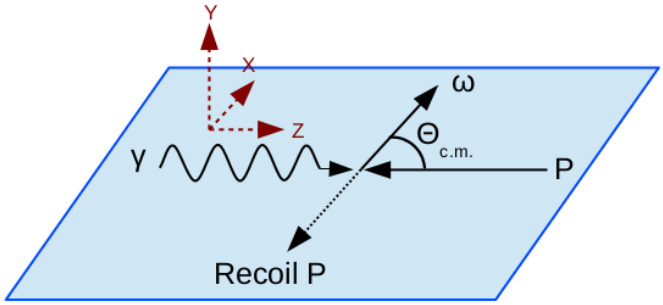

Figure 4.1: A diagram describing the kinematics of the reaction $\gamma p \to p\,\omega$. The blue plane represents the center-of-mass production plane composed of the initial photon and the recoil proton. The angle $\Theta_{c.m.}$ denotes the angle between the initial proton and the ω meson in the center-of-mass system. The z-axis is chosen to be along the direction of the incoming photon beam. The y-axis is defined as $\hat{y} = \frac{\hat{p}_{rec}\times\hat{z}}{|\hat{p}_{rec}\times\hat{z}|}$, where $\hat{p}_{rec}$ is a unit vector along the momentum of the recoil proton. The x-axis then lies on the production plane.

the following expression:

$$\cos\phi_{\pi^+} \;=\; \frac{(\vec{p}\times\vec{a})\;\cdot\;(\vec{b}_2\times\vec{b}_1)}{|\vec{p}\times\vec{a}|\;|\vec{b}_2\times\vec{b}_1|}\,, \tag{4.1}$$

where $\vec{p}$, $\vec{a}$, $\vec{b}_1$, and $\vec{b}_2$ were the initial-state proton, the recoil proton, the π^+ and π^-, respectively.

The FROST-g9b data were binned in three independent kinematic variables: the incoming photon energy, E_γ, θ_{π^+} and ϕ_{π^+}. We used 100-MeV wide photon energy bins, covering an energy range from 700-2100 MeV. The binning in θ_{π^+} and ϕ_{π^+} for the single-polarization observables was different from the binning for the double-polarization observables. The reason was that the asymmetries between doubly-polarized data sets had a more complicated angular distribution and hence, more statistics per kinematic bin was needed to obtain good fits. In this thesis, the single-polarization observables are displayed using 10 bins in θ_{π^+} and also 10 bins in ϕ_{π^+}, thereby giving us 1400 bins per final-state topology. On the other hand, the double-polarization observables are given in *quasi* three dimensions. We chose two bins in θ_{π^+} and 10 bins in ϕ_{π^+}, resulting in a total of 280 bins per final-state topology.

4.2 The $\vec{\gamma}\,\vec{p}\to p\,\omega$ Polarization Observables

In this analysis, the reaction rate for data with a linearly- as well as circularly-polarized photon beam and a transversely-polarized target reduced from the form shown in Section 1.4.1 to:

$$\begin{aligned}\frac{d\sigma}{dx_i} \;=\; \sigma_0\,\{\,(\,1\;-\;\delta_l\,\mathbf{\Sigma}\cos 2\beta)\\ &+\;\Lambda\cos\alpha\,(-\delta_l\,\mathbf{H}\sin 2\beta\;+\;\delta_\odot\,\mathbf{F})\\ &-\;\Lambda\sin\alpha\,(-\mathbf{T}\;+\;\delta_l\,\mathbf{P}\cos 2\beta)\,\}\,.\end{aligned} \tag{4.2}$$

Here, x_i denoted the kinematic variables, δ_l ($\delta_\odot$) denoted the degree of linear (circular) polarization, Λ denoted the target polarization and ($\mathbf{\Sigma}$, $\mathbf{H}$, $\mathbf{F}$, $\mathbf{T}$, $\mathbf{P}$) were the polarization observables extracted in this analysis. α (β) was the angle between the transverse polarization of the target (linear polarization of the beam) and the x-axis in the center-of-mass production plane. The orientation of the photon polarization was given in the laboratory frame by an angle ϕ_0 and, thus, $\beta = \phi_{\rm lab} - \pi - \phi_0$. If the diamond crystal was oriented such that the direction of the beam polarization was perpendicular to the floor (PERP data), then $\phi_0 = \pi/2$ and $\beta = \phi_{\rm lab} - 3\,\pi/2$. Otherwise, if the diamond crystal was oriented such that the direction of the beam polarization was parallel to

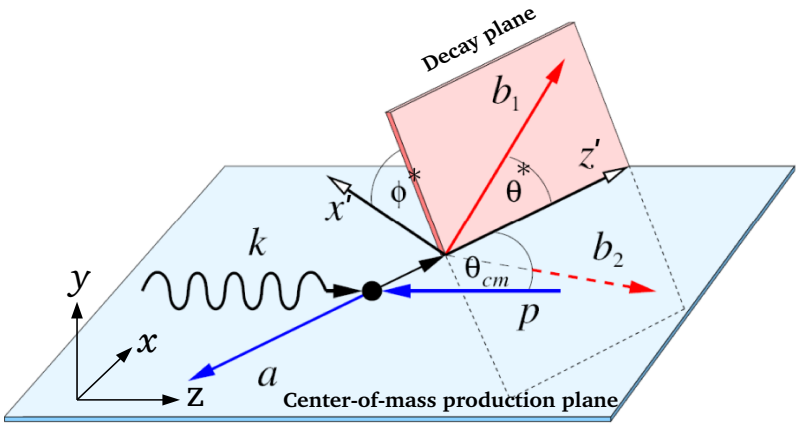

Figure 4.2: A diagram describing the kinematics of the reaction $\gamma p \to p\pi^+\pi^-$. The blue plane represents the center-of-mass production plane composed of the initial photon and one of the final-state particles, whereas the red plane represents the decay plane formed by the other two final-state particles. a, b_1, and b_2 denote the three particles of the final state. The z-axis is chosen along the direction of the incoming photon beam. The y-axis is defined as $\hat{y} = \frac{\hat{p}_{rec} \times \hat{z}}{|\hat{p}_{rec} \times \hat{z}|}$, where $\hat{p}_{rec}$ is a unit vector along the momentum of one of the final-state particles. If the chosen particle is represented by particle a, then the y-axis will point in the direction as shown in the figure. Moreover, k is the momentum of the initial photon and the particle p denotes the polarized proton in the FROST target. If we assume that particle a is the recoiling proton, then b_1 and b_2 will be the two pions, π^+ and π^-. The angle $\Theta_{c.m.}$ denotes the angle between the initial proton and the particle a in the center-of-mass system. Finally, ϕ^* and θ^* indicate the azimuthal and polar angles of the particle b_1 in the rest frame of b_1 and b_2. In our analysis, we chose π^+ as b_1. Hence, we will use the notations ϕ_{π^+} (θ_{π^+}) instead of ϕ^* (θ^*) in our results.

the floor (PARA data), then $\phi_0 = 0$ and $\beta = \phi_{\text{lab}} - \pi$. In our analysis, we chose to define the sign of β as positive if the x-axis was rotated counter-clockwise relative to the beam polarization. We refer to Appendix B for further details on the definition of the angles α and β.

4.3 The $\vec{\gamma}\,\vec{p} \to p\,\pi^+\pi^-$ Polarization Observables

The reaction rate for $\gamma p \to p\,\pi\pi$, in the case of a linearly-polarized photon beam incident on a transversely-polarized target (FROST-g9b) reduced from the form shown in Section 1.4.2 to:

$$\begin{aligned}\frac{d\sigma}{dx_i} = \sigma_0 \{ (1 + \Lambda \cos\alpha \, \mathbf{P_x} + \Lambda \sin\alpha \, \mathbf{P_y}) \\ + \delta_l [\sin 2\beta (\mathbf{I^s} + \Lambda \cos\alpha \, \mathbf{P^s_x} + \Lambda \sin\alpha \, \mathbf{P^s_y}) \\ + \cos 2\beta (\mathbf{I^c} + \Lambda \cos\alpha \, \mathbf{P^c_x} + \Lambda \sin\alpha \, \mathbf{P^c_y})] \} ,\end{aligned} \tag{4.3}$$

where x_i denoted the kinematic variables, σ_0 was the unpolarized cross section, Λ denoted the polarization of the initial nucleon and δ_l was the degree of linear polarization. α (β) was the angle between the transverse polarization of the target (linear polarization of the beam) and the x-axis in the center-of-mass production plane. We refer again to Appendix B for further details on the definition of the angles α and β. The polarization observables ($\mathbf{I^{s,c}}$, $\mathbf{P_{x,y}}$, $\mathbf{P^{s,c}_{x,y}}$) were determined in this analysis.

From Equation 4.3 we can see that two (linear) beam asymmetries, $\mathbf{I^s}$ and $\mathbf{I^c}$, were accessible in the two-pion reaction as compared to just one beam asymmetry, Σ, in the case of a single-pseudoscalar meson reaction. Similarly, more target observables and double-polarization observables arose in the two-pion reaction. This could be attributed to the fact that, in addition to the center-of-mass production plane, we also needed a decay plane (see Figure 4.2) to completely describe the two-pion reaction. All polarization observables for this reaction had either an even or odd parity with respect to ϕ^*, which was simply the angle between the decay plane and the production plane [36]. In the special case when the decay plane coincided with the production plane, ϕ^* was zero and therefore, the observables that were odd in ϕ^* (i.e., they could be expressed in terms of a sine series) vanished. Thus, Equation 4.3 reduced to Equation 4.2 in this special case.

4.4 Analysis Techniques and Notations

4.4.1 General Description of the Unbinned Maximum Likelihood Method

Experiments which utilize a linearly-polarized beam and/or a transversely-polarized target break the typical ϕ_{lab} symmetry of the experimental setup. In such cases, the distribution of events with respect to ϕ_{lab} of any final-state particle reveals the underlying asymmetry. Traditionally, one can display the asymmetry as a distribution of events with different polarization settings

and fit it using the method of least squares to extract the polarization observable(s). However, plotting the asymmetry requires binning the data where the number of bins is governed by the available statistics. Binning the data can therefore hide some of the features of the asymmetry.

A more sophisticated fitting technique is the "unbinned maximum likelihood method". This method utilizes information from each event and does not require any binning, thereby preventing any loss of information. For example, consider the two-pion reaction which is a five-dimensional problem (Section 4.1.2). Ideally, we should determine the polarization observables as a function of all five dimensions. But due to limited statistics, we needed to integrate over some of them. The unbinned maximum likelihood method allowed us to integrate over only two of the five independent variables and yet, yielded good quality results for the observables.

A detailed description of the method and how to use it to fit angular distributions for the determination of polarization observables is given in a CLAS note [83]. In this reference, the method is also compared to a standard binned fit and has been shown to be more effective. Here, we give a short summary.

The likelihood function, L, gives the combined probability density or the *likelihood* of obtaining a particular type of distribution in our experiment, such as an angular distribution or a mass distribution, given a set of parameters that we want to determine. In our case, these parameters are the polarization observables. By maximizing the likelihood function, we can determine the most likely values of the parameters. Equation 4.4 shows the most general form of a Likelihood function, L, for a certain distribution of events:

$$L = \prod_{i=1}^{N} P_i \,, \tag{4.4}$$

where P_i is the probability density of observing the i^{th} event and N is the total number of observed events that form the distribution.

As an example, consider the task of extracting the beam asymmetry, $\mathbf{\Sigma}$, in ω photoproduction using linearly-polarized beam and unpolarized target data. These data have two orthogonal linear-polarization settings, denoted as $\parallel$ and $\perp$. As a reminder, $\parallel$ refers to the case where the electric field vector of the electromagnetic wave (photon) is parallel to the x-axis in the lab frame and therefore, $\phi_0 = 0$ (PARA). On the other hand, $\perp$ denotes the case where the electric field

oscillates perpendicularly to the lab floor and thus, $\phi_0 = \pi/2$ rad (PERP). For simplicity, let us assume that the flux, Φ, and the acceptance, ϵ, of the $\parallel$ and $\perp$ data are the same (these factors will be properly taken into account in the later sections when we will discuss our results on the polarization observables). Then the number of $\parallel$ and $\perp$ events can be derived from the reaction rate (Equation 1.5) and is given by Equation 4.5 and Equation 4.6, respectively:

$$\begin{aligned} N_{\parallel} &= \Phi\, C\, \epsilon\, \sigma_{\parallel} \\ &= \Phi\, C\, \epsilon\, \sigma_0 \{\, 1 - \delta_{\parallel}\, \mathbf{\Sigma} \cos[\, 2\,(\phi^{\mathrm{p}}_{\mathrm{lab}} - \pi - \phi_0)\,]\,\} \\ &= \Phi\, C\, \epsilon\, \sigma_0 \{\, 1 - \delta_{\parallel}\, \mathbf{\Sigma} \cos[\, 2\,(\phi^{\mathrm{p}}_{\mathrm{lab}} - \pi)\,]\,\} \\ &= \Phi\, C\, \epsilon\, \sigma_0 \{\, 1 - \delta_{\parallel}\, \mathbf{\Sigma} \cos 2\phi^{\mathrm{p}}_{\mathrm{lab}}\}\,, \end{aligned} \tag{4.5}$$

$$\begin{aligned} N_{\perp} &= \Phi\, C\, \epsilon\, \sigma_{\perp} \\ &= \Phi\, C\, \epsilon\, \sigma_0 \{\, 1 - \delta_{\perp}\, \mathbf{\Sigma} \cos[\, 2\,(\phi^{\mathrm{p}}_{\mathrm{lab}} - \pi - \phi_0)\,]\,\} \\ &= \Phi\, C\, \epsilon\, \sigma_0 \{\, 1 - \delta_{\perp}\, \mathbf{\Sigma} \cos[\, 2\,(\phi^{\mathrm{p}}_{\mathrm{lab}} - \pi - \pi/2)\,]\,\} \\ &= \Phi\, C\, \epsilon\, \sigma_0 \{\, 1 + \delta_{\perp}\, \mathbf{\Sigma} \cos 2\phi^{\mathrm{lab}}_{\mathrm{p}}\}\,, \end{aligned} \tag{4.6}$$

where Σ is the beam asymmetry we would like to determine, C is the total number of target nucleons which is a constant, $\delta_{\parallel,\,\perp}$ are the degrees of linear beam polarization, and $\phi^{\mathrm{p}}_{\mathrm{lab}}$ is the azimuthal angle of the recoil proton in the lab frame.

The asymmetry, A, is given by:

$$A = \frac{N_{\parallel} - N_{\perp}}{N_{\parallel} + N_{\perp}} = -\,\frac{(\delta_{\parallel} + \delta_{\perp})\, \mathbf{\Sigma} \cos 2\phi^{\mathrm{p}}_{\mathrm{lab}}}{[\, 2 + (\delta_{\perp} - \delta_{\parallel})\, \mathbf{\Sigma} \cos 2\phi^{\mathrm{p}}_{\mathrm{lab}}\,]}\,. \tag{4.7}$$

We can now show how the probability density of each observed event, and therefore the likelihood of observing a particular data distribution, is related to the asymmetry, A. Within each kinematic bin (E_γ, $\cos\Theta^{\omega}_{\mathrm{c.m.}}$), fitting the asymmetry in $\phi^{\mathrm{p}}_{\mathrm{lab}}$ will give us the polarization observable $\mathbf{\Sigma}$. The most common way is to plot the asymmetry by defining bins centered at specific values of $\phi^{\mathrm{p}}_{\mathrm{lab}}$. The unbinned event-based fitting is an extreme case of the binned method in which each $\phi^{\mathrm{p}}_{\mathrm{lab}}$ bin is shrunk until it contains only one or zero event(s). This concept will be used to derive the probability density for each event. The binned method will be discussed first.

Each $\phi_{\rm lab}^{\rm p}$ bin has a certain number of $N_\parallel$ and $N_\perp$ events. The probability of a randomly-selected event in this bin being a $\parallel$ event is then given by r:

$$\begin{aligned} r &= \frac{N_\parallel}{N_\parallel + N_\perp} \\ &= \frac{N_\parallel + N_\perp + N_\parallel - N_\perp}{2\,(N_\parallel + N_\perp)} \\ &= \frac{1}{2}\,(1 + A)\,, \end{aligned} \tag{4.8}$$

and likewise, the probability of a randomly-selected event being a $\perp$ event is given by $1 - r$:

$$1 - r \,=\, 1 \,-\, \frac{1}{2}\,(1 + A) \,=\, \frac{1}{2}\,(1 \,-\, A)\,, \tag{4.9}$$

where A is given by the asymmetry equation which contains the polarization observable. In this particular example, A is given by Equation 4.7. The probability of obtaining $N_\parallel$ and $N_\perp$ events in a $\phi_{\rm lab}^{\rm p}$ bin is:

$$P(N_\parallel,\, N_\perp \,|\, A) \,=\, \frac{1}{Z'}\,(1 \,+\, A)^{N_\parallel}\,(1 - A)^{N_\perp}\,, \tag{4.10}$$

where Z' is a normalization constant. In the unbinned case, the bins contain only one or zero event(s). Then, the probability in Equation 4.10 reduces to:

$$\begin{aligned} P(N_\parallel,\, N_\perp \,=\, 0 \,|\, A) \,&=\, \frac{1}{2}\,(1 \,+\, A)\,, \qquad \text{for every } \parallel \text{ event, and} \\ P(N_\parallel \,=\, 0,\, N_\perp \,|\, A) \,&=\, \frac{1}{2}\,(1 \,-\, A)\,, \qquad \text{for every } \perp \text{ event}\,. \end{aligned} \tag{4.11}$$

The relation between the likelihood function L and the asymmetry in any $(E_\gamma,\, \cos\Theta_{\rm c.m.}^{\omega})$ kinematic bin with $N_{\rm total}$ events is given by:

$$\begin{aligned} L \,&=\, \prod_{i=1}^{N_{\rm total}} P\,(\text{event}\,_i)\,, \\ &\text{where } P\,(\text{event}\,_i) \,=\, \begin{cases} \frac{1}{2}\,(1 \,+\, A), & \text{for } \parallel \text{ setting}\,, \\ \frac{1}{2}\,(1 \,-\, A), & \text{for } \perp \text{ setting}\,. \end{cases} \end{aligned} \tag{4.12}$$

Computationally, it is convenient to minimize $-\ln L$ using standard packages such as MINUIT to obtain the values and errors of the observables. Moreover, in those analyses where each event is assigned its own weight factor w_i — including for example various factors such as the Q-factor,

normalization factors, etc. — the likelihood is given by:

$$L = \prod_{i=1}^{N_{\text{total}}} [\, P\,(\text{event}_i)\,]^{w_i}$$

$$-\ln L = -\sum_{i=1}^{N_{\text{total}}} w_i \ln\left(P\,(\text{event}_i)\right), \tag{4.13}$$

$$\text{where } P\,(\text{event}_i) = \begin{cases} \frac{1}{2}\,(1 + A), & \text{for one pol. setting (e.g. } \|), \\ \frac{1}{2}\,(1 - A), & \text{for the other pol. setting (e.g. } \perp). \end{cases}$$

Equation 4.13 was extensively used in our analysis. A takes on different forms depending on the measurement. In the present example, A depends on the $\mathbf{\Sigma}$ observable, δ_l and $\phi_{\text{lab}}^{\text{p}}$ as shown in Equation 4.7. The latter two variables were experimentally measured for each event and put in the probability density function. Thus, the likelihood is a function of $\mathbf{\Sigma}$ only and maximizing it, gives us the most probable value for the observable.

4.4.2 Notations

We can now proceed to the extraction of the polarization observables for the reactions of interest using the methods described above. A summary of the notations for beam- and target-polarization settings is given below:

1. **Linearly-polarized beam:** PARA or $\|$ denotes an electric field vector oriented parallel to the x-axis in the lab frame. PERP or $\perp$ denotes an electric field vector oriented perpendicular to the lab floor.

2. **Circularly-polarized beam:** The symbol $\rightarrow$ ($\leftarrow$) denotes that the helicity is parallel (antiparallel) to the beam axis.

3. **Transverse target polarization:** A '+' denotes that the transverse polarization points away from the lab floor with an offset of 116.1° or 2.025 rad with respect to the x-axis in the lab frame. A '−' denotes that it points toward the floor and is oriented at an angle of −63.9° or −1.115 rad from the lab x-axis.

Average Degrees of Polarization. We calculated the average beam polarization, $\bar{\delta}_{\text{beam}}^{\text{target}}$, and the average target polarization, $\bar{\Lambda}_{\text{beam}}^{\text{target}}$, of a data set in any chosen kinematic bin as:

$$\bar{\delta}_{\text{beam}}^{\text{target}} = \frac{\sum_{i=1}^{N} Q_i\,\delta_i}{\sum_{i=1}^{N} Q_i}\,, \qquad \bar{\Lambda}_{\text{beam}}^{\text{target}} = \frac{\sum_{i=1}^{N} Q_i\,\Lambda_i}{\sum_{i=1}^{N} Q_i}\,, \tag{4.14}$$

where N denoted the total number of events with a particular beam and target polarization, Q_i was the Q-factor and δ_i (Λ_i) was the degree of beam (target) polarization of the i^{th} event. Each event belonging to a particular run was assigned a degree of target polarization which was equal to the average target polarization for that run. The values are given at g9b_runlist. In the data with a circularly-polarized beam, the event-based degree of beam polarization in each E_γ bin was determined using Equation 3.12, where the electron beam energy was 3.082 GeV. In the case of the linearly-polarized data sets, the degree of beam polarization for each event was obtained from the relevant polarization table (see Section 3.7.4).

Linear Beam Polarization In each coherent-edge data set and any chosen kinematic bin, it was observed that $\delta_\parallel^+ \sim \delta_\parallel^-$. This was evident from Figures 4.3 and 4.4. Therefore, either $\delta_\parallel^+$ or $\delta_\parallel^-$ was replaced with the corresponding average, $\bar{\delta}_\parallel$, in the analysis. Similarly, $\delta_\perp^{(+,-)}$ was replaced with the average, $\bar{\delta}_\perp$. It was further observed that the average target polarization for the same target polarization setting was similar. We used the average, $\Lambda^{\,\text{target}}$, in the analysis, e.g. $\Lambda^{+}_{(\parallel,\perp)} = \bar{\Lambda}^{+}$.

Circular Beam Polarization In each period of the FROST data with a circularly-polarized beam and longitudinal- or transverse-target polarization, the beam polarization flipped rapidly every second and therefore, $\delta^{\text{target}}_{\rightarrow} = \delta^{\text{target}}_{\leftarrow}$ in each kinematic bin for a given target-polarization data set. Moreover, the degree of circular beam polarization depended only on the e^- energy and the electron-beam polarization; it was independent of the target polarization for the period combinations used in our analysis. Hence, in the rest of the section, we will use $\bar{\delta}_\odot$. Likewise, $\Lambda^{\text{target}}_{\rightarrow} = \Lambda^{\text{target}}_{\leftarrow}$ and it will therefore be denoted by $\bar{\Lambda}^{\,\text{target}}$.

Final Remarks. For the ω photoproduction reaction, we chose to consider the lab azimuthal-angle distribution of the recoil proton. For the $\pi^+\pi^-$ photoproduction reaction, we chose the π^+ lab azimuthal angle distribution. Therefore, the angles β and α in Equations 4.2 and 4.3 were given by Equation 4.15 and Equation 4.16, respectively:

$$\beta = \phi_{\text{lab}}^{\text{particle}} - \pi - \phi_0\,, \qquad \text{where } \phi_0 = \begin{cases} 0 & \text{for } \parallel \text{ beam}\,, \\ \frac{\pi}{2}\,\text{rad} & \text{for } \perp \text{ beam}\,, \end{cases} \tag{4.15}$$

and similarly:

$$\begin{aligned} \alpha &= \pi - \phi_{\text{lab}}^{\text{particle}} + \phi_{\text{offset}}\,, \\ &\text{where } \phi_{\text{offset}} = \begin{cases} 2.025 \text{ rad} & \text{for `+' target polarization}\,, \\ 2.025 - \pi \approx -1.115 \text{ rad} & \text{for `}-\text{' target polarization}\,, \end{cases} \end{aligned} \tag{4.16}$$

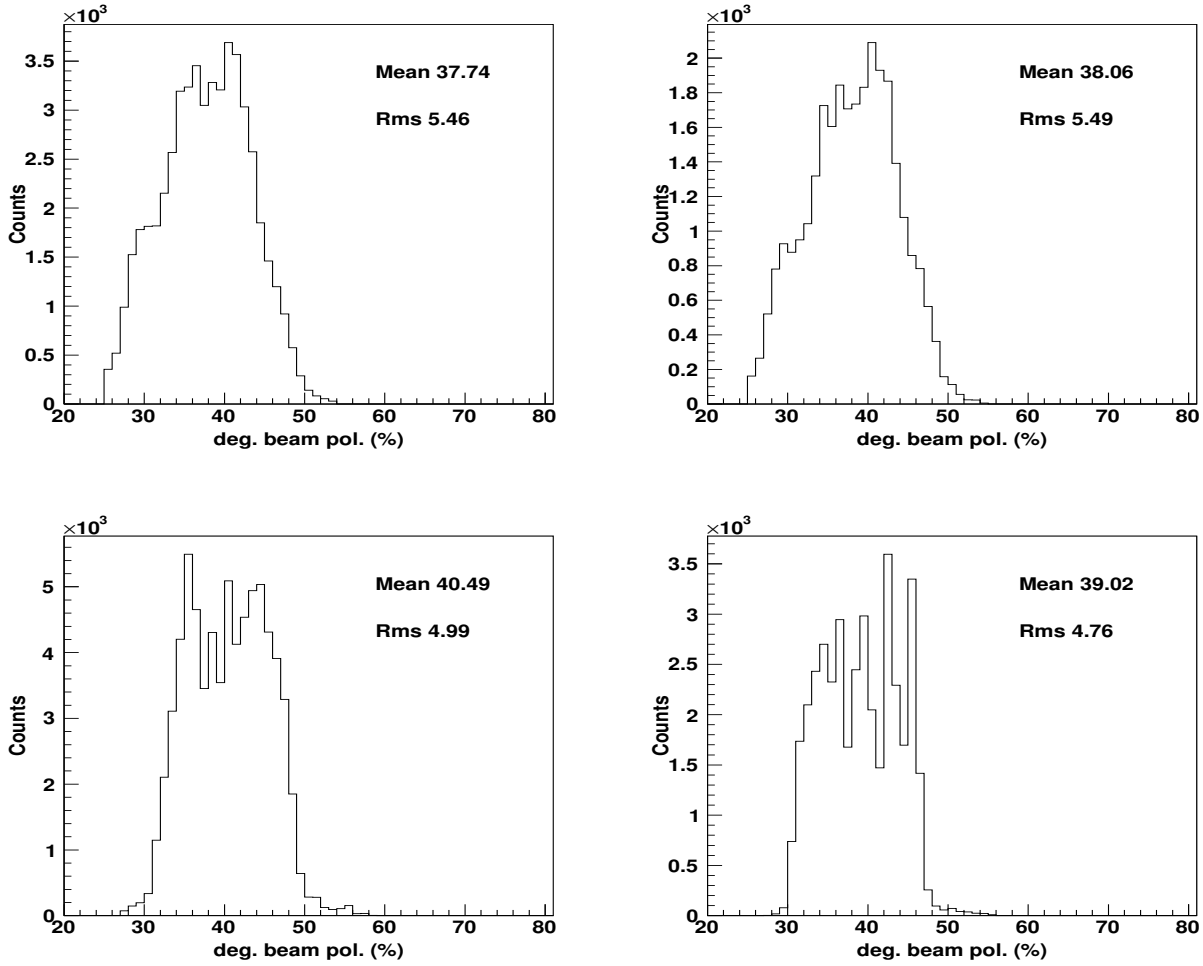

Figure 4.3: Distributions of the Q-value weighted degrees of the photon beam polarization, δ, for PARA setting (top row) and PERP setting (bottom row) in the energy bin $E_\gamma \in [0.9, 1.0]$ GeV. The left plots are for '+' target polarization and the right plots are for '−' target polarization. In conclusion, $\delta_\parallel^+$ and $\delta_\parallel^-$ differed by less than 1 % in this energy bin. In case of the PERP beam polarization, $\delta_\perp^+$ and $\delta_\perp^-$ differed by about 3.6 %.

and the particle was the recoil proton (π^+) for ω production ($\pi^+\pi^-$ production), ϕ_{offset} was the angle of the transverse target polarization with respect to the lab x-axis and ϕ_0 was the angle of the linear polarization with respect to the lab x-axis. The derivations of the above equations are given in Appendix B.

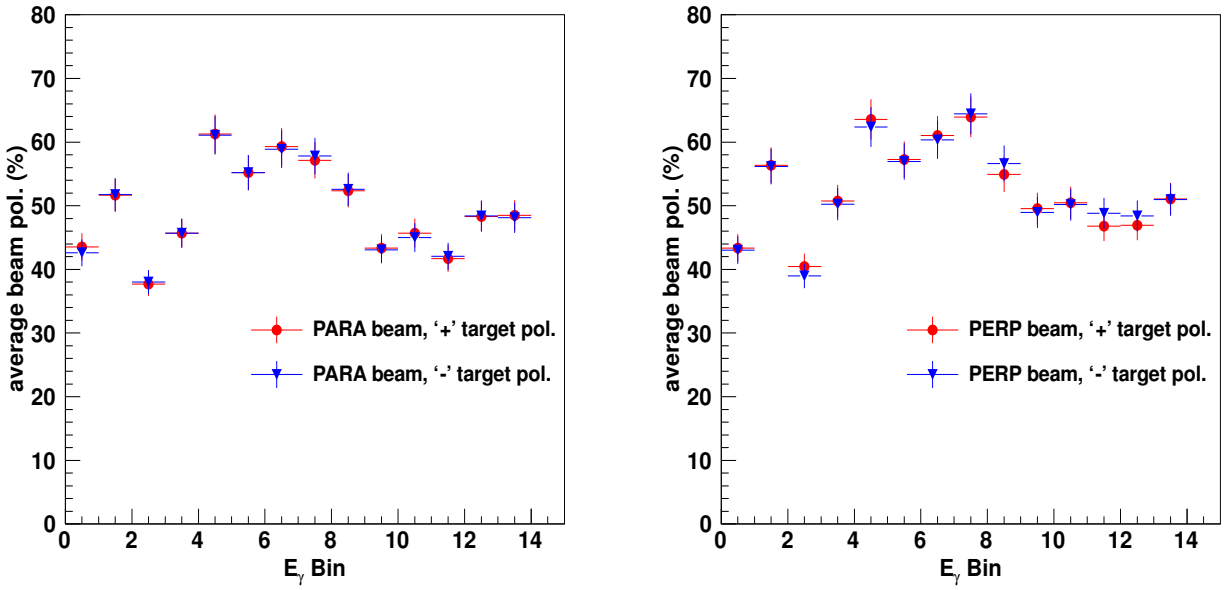

Figure 4.4: A comparison of the average PARA beam polarization (left) and PERP beam polarization (right) for the two target polarization settings ('+' shown in red and '−' shown in blue) in all photon energy bins in the FROST-g9b data. In both plots, bin number one on the x-axis corresponds to the 700-800 MeV energy bin, bin number two corresponds to the 800-900 MeV energy bin, etc. We clearly see from this figure that in any given energy bin, the average degrees of beam polarization for the two target settings were very similar.

The experimentally-observed number of events was related to the reaction rate σ:

$$N_{\text{data}} \;=\; \Phi\, C\, \epsilon\, \sigma\,, \tag{4.17}$$

where Φ denoted the photon flux (Section 3.8), C denoted the total number of target nucleons and ϵ denoted the CLAS acceptance. Since C was a constant, we will drop this term in the rest of the analysis note. The CLAS acceptance and its effect on the polarization observables are discussed separately for the two reactions.

4.4.3 Extraction of Polarization Observables in $\vec{\gamma}\,\vec{p} \to p\,\omega$

Events from Topology 5 (see Table 3.5) were utilized to extract the polarization observables in $\vec{\gamma}\,\vec{p} \to p\,\omega$. At the time of our FROST analyses, a fully-tested and ready-to-be-used-in-an-analysis Monte Carlo simulation for g9b was not available. For this reason, acceptance effects in different

topologies could only be estimated but not be studied in all their details. This was not a big concern in any extraction of an ω observable because we considered only one topology and we binned in all relevant kinematic variables which spanned the phase space for this reaction. In this scenario, the acceptance should largely cancel out when an asymmetry was formed. Furthermore, the CLAS detector acceptance likely did not depend on the relative orientation of the photon's polarization with respect to the detector. The acceptances of orthogonal target polarization settings were *a priori* not known but we assumed that they were very similar since the magnitude of the holding field was fairly small. In a nutshell, we initially concluded that the acceptance terms were the same in a particular kinematic-bin combination for all beam-target polarization settings.

The g9b observables required fitting angular distributions. The number of PARA events with '+' or '−' target polarization was given by (substituting Equations 4.2, 4.15, 4.16 into Equation 4.17):

$$\begin{aligned} N_{\parallel}^{\pm} \;=\; \Phi_{\parallel}^{\pm}\,\epsilon\,\sigma_0\,\{\,1 \;-\; & \bar{\delta}_{\parallel}\,\boldsymbol{\Sigma}\cos 2\phi_{\mathrm{lab}}^{\mathrm{p}} \\ & \mp\; \bar{\delta}_{\parallel}\,\bar{\Lambda}^{\pm}\,\mathbf{H}\cos\left(\pi \;-\; \phi_{\mathrm{lab}}^{\mathrm{p}} \;+\; 2.025\right)\sin 2\phi_{\mathrm{lab}}^{\mathrm{p}} \\ & \pm\; \bar{\Lambda}^{\pm}\,\mathbf{T}\sin\left(\pi \;-\; \phi_{\mathrm{lab}}^{\mathrm{p}} \;+\; 2.025\right) \\ & \mp\; \bar{\delta}_{\parallel}\,\bar{\Lambda}^{\pm}\,\mathbf{P}\sin\left(\pi \;-\; \phi_{\mathrm{lab}}^{\mathrm{p}} \;+\; 2.025\right)\cos 2\phi_{\mathrm{lab}}^{\mathrm{p}}\,\}\,. \end{aligned} \tag{4.18}$$

Likewise, the number of PERP events with '+' or '−' target polarization was given by:

$$\begin{aligned} N_{\perp}^{\pm} \;=\; \Phi_{\perp}^{\pm}\,\epsilon\,\sigma_0\,\{\,1 \;+\; & \bar{\delta}_{\perp}\,\boldsymbol{\Sigma}\cos 2\phi_{\mathrm{lab}}^{\mathrm{p}} \\ & \pm\; \bar{\delta}_{\perp}\,\bar{\Lambda}^{\pm}\,\mathbf{H}\cos\left(\pi \;-\; \phi_{\mathrm{lab}}^{\mathrm{p}} \;+\; 2.025\right)\sin 2\phi_{\mathrm{lab}}^{\mathrm{p}} \\ & \pm\; \bar{\Lambda}^{\pm}\,\mathbf{T}\sin\left(\pi \;-\; \phi_{\mathrm{lab}}^{\mathrm{p}} \;+\; 2.025\right) \\ & \pm\; \bar{\delta}_{\perp}\,\bar{\Lambda}^{\pm}\,\mathbf{P}\sin\left(\pi \;-\; \phi_{\mathrm{lab}}^{\mathrm{p}} \;+\; 2.025\right)\cos 2\phi_{\mathrm{lab}}^{\mathrm{p}}\,\}\,. \end{aligned} \tag{4.19}$$

For the data with a circularly-polarized beam, the number of events with '$\rightarrow$' helicity and '+' or '−' target polarization was given by:

$$\begin{aligned} N_{\rightarrow}^{\pm} \;=\; \Phi^{\pm}\,\epsilon\,\sigma_0\,\{\,1 \;\pm\; & \bar{\Lambda}^{\pm}\,\bar{\delta}_{\odot}\,\mathbf{F}\cos\left(\pi \;-\; \phi_{\mathrm{lab}}^{\mathrm{p}} \;+\; 2.025\right) \\ & \pm\; \bar{\Lambda}^{\pm}\,\mathbf{T}\sin\left(\pi \;-\; \phi_{\mathrm{lab}}^{\mathrm{p}} \;+\; 2.025\right)\,\}\,. \end{aligned} \tag{4.20}$$

Likewise, the number of events with '$\leftarrow$' helicity and '+' or '−' target polarization was given by:

$$\begin{aligned} N_{\leftarrow}^{\pm} \;=\; \Phi^{\pm}\,\epsilon\,\sigma_0\,\{\,1 \;\mp\; & \bar{\Lambda}^{\pm}\,\bar{\delta}_{\odot}\,\mathbf{F}\cos\left(\pi \;-\; \phi_{\mathrm{lab}}^{\mathrm{p}} \;+\; 2.025\right) \\ & \pm\; \bar{\Lambda}^{\pm}\,\mathbf{T}\sin\left(\pi \;-\; \phi_{\mathrm{lab}}^{\mathrm{p}} \;+\; 2.025\right)\,\}\,. \end{aligned} \tag{4.21}$$

The Beam Asymmetry Σ. This observable was a single-polarization observable associated with a linearly-polarized photon beam and an unpolarized target. However, our experimental g9b data had a linearly-polarized beam in combination with a transversely-polarized target (Tables 3.2 and 3.3). To *unpolarize* the target, we combined data with opposite target polarization which had the same beam polarization. This required appropriate normalization factors.

The number of $\parallel$ events, $N_{\parallel}$, after combining data sets with $\parallel$ beam polarization and different target polarization (+ or −), was given by:

$$N_{\parallel} \,=\, N_{\parallel}^{+} \,+\, N_1 \, N_{\parallel}^{-} \;, \tag{4.22}$$

where N_1 was a normalization factor that depended on the photon flux ratio and the average degrees of target polarization of the two data sets:

$$N_1 \,=\, \frac{\Phi_{\parallel}^{+} \, \bar{\Lambda}^{+}}{\Phi_{\parallel}^{-} \, \bar{\Lambda}^{-}} \;. \tag{4.23}$$

By substituting Equation 4.18 into Equation 4.22, we obtained:

$$N_{\parallel} \,=\, \Phi_{\parallel}^{+} \, \epsilon \, \sigma_0 \, (1 \,+\, \bar{\Lambda}_R) \, \{ \, 1 \,-\, \bar{\delta}_{\parallel} \, \boldsymbol{\Sigma} \cos 2\phi_{\rm lab}^{\rm p} \, \} \,=\, \Phi_{\parallel}^{+} \, \epsilon \, \sigma_{\parallel} \, , \tag{4.24}$$

where $\bar{\Lambda}_R$ was defined as $\bar{\Lambda}_R \,=\, \bar{\Lambda}^{+} \,/\, \bar{\Lambda}^{-}$.

In the same way, the number of $\perp$ events, $N_{\perp}$, after combining data sets with $\perp$ beam polarization and different target polarization was given by:

$$N_{\perp} \,=\, N_{\perp}^{+} \,+\, N_2 \, N_{\perp}^{-} \;, \tag{4.25}$$

where N_2 was the normalization factor and had the value $N_2 \,=\, \frac{\Phi_{\perp}^{+}}{\Phi_{\perp}^{-}} \, \bar{\Lambda}_R$. By substituting Equation 4.19 into the above equation, we obtained:

$$N_{\perp} \,=\, \Phi_{\perp}^{+} \, \epsilon \, \sigma_0 \, (1 \,+\, \bar{\Lambda}_R) \, \{ \, 1 \,+\, \bar{\delta}_{\perp} \, \boldsymbol{\Sigma} \cos 2\phi_{\rm lab}^{\rm p} \, \} \,=\, \Phi_{\perp}^{+} \, \epsilon \, \sigma_{\perp} \;. \tag{4.26}$$

The asymmetry between $\parallel$ and $\perp$ data could finally be written as:

$$A \,=\, \frac{N_{\parallel} \,-\, N_{\perp}}{N_{\parallel} \,+\, N_{\perp}} \,=\, \frac{A' \,+\, \Delta\Phi}{1 \,+\, A' \, \Delta\Phi} \;, \tag{4.27}$$

where,

$$
\begin{aligned}
A' \;&=\; \left(\frac{\sigma_{\parallel} \,-\, \sigma_{\perp}}{\sigma_{\parallel} \,+\, \sigma_{\perp}}\right) \;=\; \frac{-\,\tilde{\delta}_l\,\boldsymbol{\Sigma}\cos 2\phi^{\,\mathrm{p}}_{\mathrm{lab}}}{1 \,-\, \tilde{\delta}_l\,\Delta\delta_l\,\boldsymbol{\Sigma}\cos 2\phi^{\,\mathrm{p}}_{\mathrm{lab}}}\;, \\
\Delta\Phi \;&=\; \frac{\Phi^{+}_{\parallel} \,-\, \Phi^{+}_{\perp}}{\Phi^{+}_{\parallel} \,+\, \Phi^{+}_{\perp}}\;, \quad \tilde{\delta}_l \;=\; \frac{\bar{\delta}_{\parallel} \,+\, \bar{\delta}_{\perp}}{2}\;, \quad \Delta\delta_l \;=\; \frac{\bar{\delta}_{\parallel} \,-\, \bar{\delta}_{\perp}}{\bar{\delta}_{\parallel} \,+\, \bar{\delta}_{\perp}}\;.
\end{aligned}
\tag{4.28}
$$

The likelihood of obtaining the observed angular distribution in $\phi^{\,\mathrm{p}}_{\mathrm{lab}}$ in any kinematic bin, using A from Equation 4.27, was then given by:

$$
\begin{aligned}
-\ln L \;&=\; -\sum_{i=1}^{N_{\mathrm{total}}} w_i \ln\left(P\left(\mathrm{event}_{\,\mathrm{i}}\right)\right), \\
&\text{where } P\left(\mathrm{event}_{\,i}\right) \begin{cases} \frac{1}{2}\,(1 \,+\, A) & \text{for } \parallel \text{ events}\,, \\ \frac{1}{2}\,(1 \,-\, A) & \text{for } \perp \text{ events}\,, \end{cases}
\end{aligned}
\tag{4.29}
$$

and N_{total} was the sum of all events for the four beam-target polarization settings used in that kinematic bin. The weight for each event depended on its Q-factor, $Q_{\,\mathrm{event}}$, and the normalization factor for the corresponding data set. From the above discussion, the weight of the i^{th} event was given by:

$$
w_i \;=\; \begin{cases} Q_i, & \text{for } (\parallel,\,+) \text{ or } (\perp,\,+) \text{ events}\,, \\ Q_i\,N_1 & \text{for } (\parallel,\,-) \text{ events}\,, \\ Q_i\,N_2 & \text{for } (\perp,\,-) \text{ events}\,. \end{cases}
\tag{4.30}
$$

Minimizing $-\ln L$ yielded the value and the statistical error of the polarization observable $\boldsymbol{\Sigma}$. Figure 4.5 shows examples of the $\boldsymbol{\Sigma}$ observable in the two energy bins $E \in [1.30,\, 1.40]$ GeV and $E \in [1.40,\, 1.50]$ GeV.

The Target Asymmetry T. The target asymmetry $\mathbf{T}$ in ω photoproduction was a first-time measurement. This observable is a single-polarization observable associated with an unpolarized photon beam and a transversely-polarized target. Since our experimental data were based on a linearly- or a circularly-polarized beam in combination with a transversely-polarized target (Tables 3.2, 3.3, and 3.4), we had to *unpolarize* the beam, similar to *unpolarizing* the target in the previous section.

To unpolarize the beam, we combined data with the same target polarization which had opposite beam polarization settings, again using appropriate normalization factors. Since the method to extract the observable was the same for both linear and circular polarization, we will use labels '1'

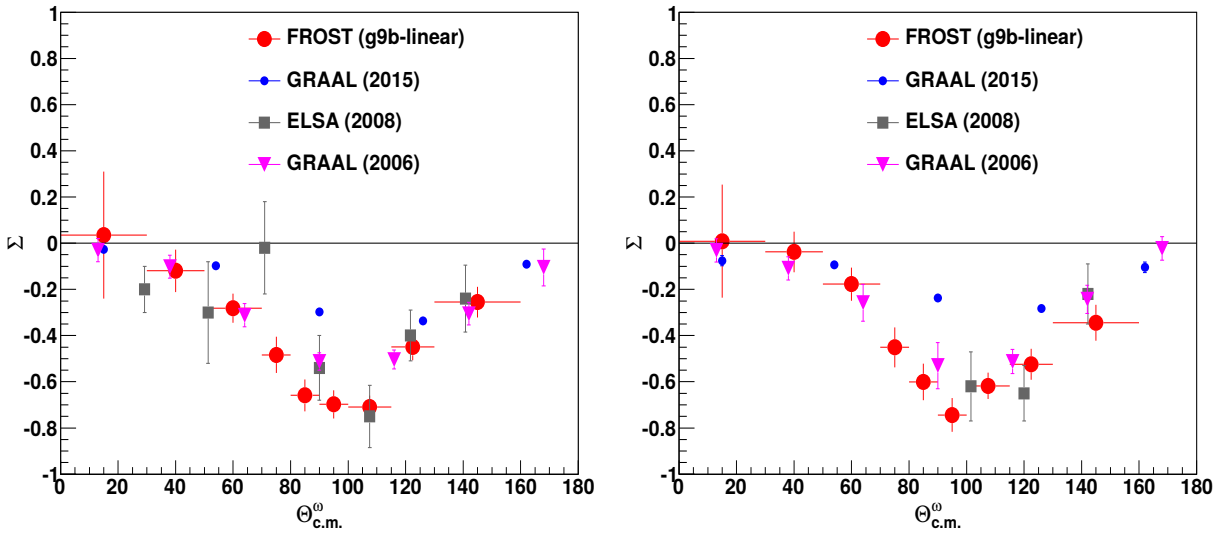

Figure 4.5: Examples of the $\boldsymbol{\Sigma}$ observable from FROST-g9b (red circles) for $E \in [1.30, 1.40]$ GeV (left) and $E \in [1.40, 1.50]$ GeV (right). Our results agree fairly well within statistical uncertainties with results published by the GRAAL Collaboration in 2006 [27] (magenta triangles) and by the CBELSA/TAPS Collaboration in 2008 [28] (gray squares). The angular distributions published by the GRAAL Collaboration in 2015 [29] (blue circles) have a smaller amplitude than our FROST results and the other published results, which could be due to an error in their overall normalization. Furthermore, the good agreement between our results, the GRAAL 2006 results (obtained from the $\pi^+\pi^-\pi^0$ decay mode) and the CBELSA/TAPS 2008 results (obtained from the radiative decay mode) indicates that the acceptance effects on our results are negligible.

and '2' to denote the beam polarization settings. For data sets with a linearly-polarized photon beam, '1' will represent $\parallel$ polarization and '2' will represent $\perp$ polarization, whereas in case of data sets with a circularly-polarized beam, '1' will refer to $\rightarrow$ helicity and '2' will refer to $\leftarrow$ helicity.

The number of '+' events, N^+, after combining data sets with different beam polarization was given by:

$$N^+ \;=\; N_1^+ \;+\; C_2^+ \, N_2^+ \;, \tag{4.31}$$

where C_2^+ was a normalization factor given by $C_2^+ \;=\; \frac{\Phi_1^+}{\Phi_2^+}\,\bar{\delta}_R$. Moreover, $\bar{\delta}_R \;=\; \frac{\bar{\delta}_\parallel}{\bar{\delta}_\perp}$ for linear-beam polarization and $\bar{\delta}_R \;=\; 1$ for circular-beam polarization. The flux ratio was equal to *one* in the case of circularly-polarized photons because of the rapid helicity flips. By substituting the value of C_2^+ into Equation 4.31 and using Equations 4.18 & 4.19 in case of a linearly-polarized beam, and Equations 4.20 & 4.21 in case of a circularly-polarized beam, we obtained:

$$N^+ \;=\; \Phi_1^+ \, \epsilon \, \sigma_0 \, (1 \;+\; \bar{\delta}_R) \, \{\, 1 \;+\; \bar{\Lambda}^+ \, \mathbf{T} \sin\left(\pi \;-\; \phi^{\rm p}_{\rm lab} \;+\; 2.025\right) \} \;=\; \Phi_1^+ \, \epsilon \, \sigma^+ \;. \tag{4.32}$$

Similarly, the number of '$-$' events, N^-, after combining data sets with '$-$' transverse target polarization and different beam polarization, was given by:

$$N^- \,=\, N_1^- \,+\, C_2^-\, N_2^- \;, \tag{4.33}$$

where C_2^- was the normalization factor and had the value $C_2^- \,=\, \frac{\Phi_1^-}{\Phi_2^-}\,\bar{\delta}_R$. Following the same procedure as before, we obtained:

$$N^- \,=\, \Phi_1^-\,\epsilon\,\sigma_0\,(1\,+\,\bar{\delta}_R)\,\{\,1\,-\,\bar{\Lambda}^-\,\mathbf{T}\sin\left(\pi\,-\,\phi^{\rm p}_{\rm lab}\,+\,2.025\right)\,\}\,=\,\Phi_1^-\,\epsilon\,\sigma^-\;. \tag{4.34}$$

The asymmetry between '$+$' and '$-$' data was finally given by:

$$A \,=\, \frac{A'\,+\,\Delta\Phi}{1\,+\,A'\,\Delta\Phi}\;, \tag{4.35}$$

where

$$\begin{aligned} A' \,&=\, \left(\frac{\sigma^+\,-\,\sigma^-}{\sigma^+\,+\,\sigma^-}\right) \,=\, \frac{\tilde{\Lambda}\,\mathbf{T}\sin\left(\pi\,-\,\phi^{\rm p}_{\rm lab}\,+\,2.025\right)}{1\,+\,\tilde{\Lambda}\,\Delta\Lambda\,\mathbf{T}\sin\left(\pi\,-\,\phi^{\rm p}_{\rm lab}\,+\,2.025\right)}\;, \\ \Delta\Phi \,&=\, \frac{\Phi_1^+\,-\,\Phi_1^-}{\Phi_1^+\,+\,\Phi_1^-}\;,\quad \tilde{\Lambda} \,=\, \frac{\bar{\Lambda}^+\,+\,\bar{\Lambda}^-}{2}\;,\quad \Delta\Lambda \,=\, \frac{\bar{\Lambda}^+\,-\,\bar{\lambda}^-}{\bar{\Lambda}^+\,+\,\bar{\Lambda}^-}\;. \end{aligned} \tag{4.36}$$

The likelihood of obtaining the observed angular distribution in $\phi^{\rm p}_{\rm lab}$ in any kinematic bin, using A from Equation 4.35, was then given by:

$$\begin{aligned} -\ln L \,&=\, -\sum_{i=1}^{N_{\rm total}}\, w_i \ln\left(P\left(\text{event}_{\,\rm i}\right)\right), \\ &\text{where } P\left(\text{event}_{\,\rm i}\right) \,=\, \begin{cases} \frac{1}{2}\,(1\,+\,A) & \text{for '+' events}\,, \\ \frac{1}{2}\,(1\,-\,A) & \text{for '$-$' events}\,, \end{cases} \end{aligned} \tag{4.37}$$

and $N_{\rm total}$ was the sum of all events for the four beam-target polarization settings used in that kinematic bin. The weight of the i^{th} event was:

$$w_i \,=\, \begin{cases} Q_i & \text{for (1, +) or (1, $-$) events}\,, \\ Q_i\,C_2^+ & \text{for (2, +) events}\,, \\ Q_i\,C_2^- & \text{for (2, $-$) events}\,. \end{cases} \tag{4.38}$$

The observable $\mathbf{T}$ was then extracted by minimizing $-\ln L$ which was given in Equation 4.37.

The T Observable from Data Sets with Linear and Circular Beam Polarization

As shown in Table 3.4, the circularly-polarized FROST-g9b data were organized in five periods.

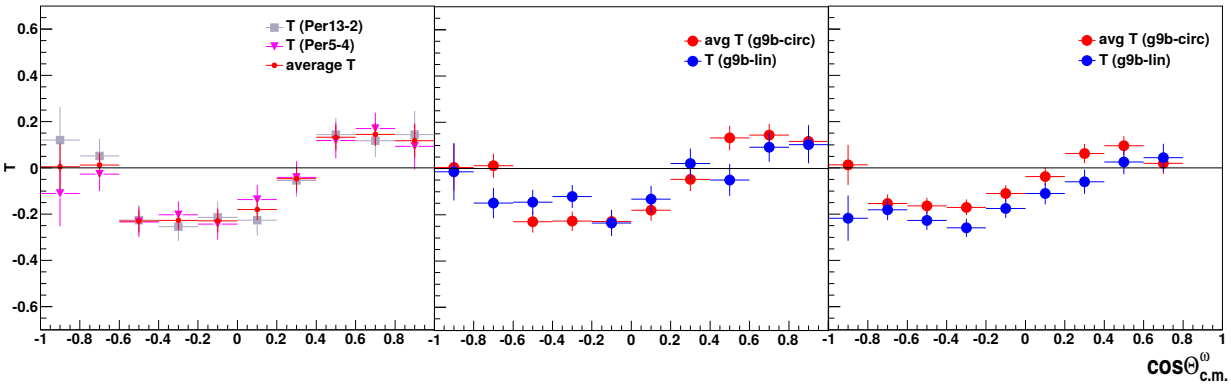

Figure 4.6: (Left) The **T** observable in the energy bin $E_\gamma \in [1.50, 1.60]$ GeV from the g9b Period 13-2 combination (shown in gray) and the Period 5-4 combination (shown in magenta). The red data points denote the uncertainty-weighted average. Center: The **T** observable in the same energy bin from the linearly-polarized g9b data (shown in blue) and the comparison with the averaged **T** result from the circularly-polarized g9b data (shown in red). Again, the two results agree fairly well which indicates that our method to unpolarize the beam by combining data sets worked well. (Right) The **T** observable in a lower-energy bin, $E_\gamma \in [1.30, 1.40]$ GeV, from the linearly-polarized data (shown in blue) and the corresponding circularly-polarized data (shown in red). The two results agree within statistical errors but we see a small systematic shift in the blue data points which might be attributed to the effect of the different holding field orientations.

Periods 1, 2 and 3 had a '+' holding magnet sign and Periods 4 and 5 had a '−' negative holding magnet sign. Furthermore, Periods 1, 3 and 5 had a '+' target polarization and Periods 2 and 4 had a '−' target polarization. This allowed for several ways to form asymmetries in order to extract the **T** observable.

It was observed that the best way to extract the target asymmetry **T** was based on separately analyzing *combination132* and *combination45*. This observation could be explained with the influence of the holding magnet sign on the detector acceptance (see Appendix C for more details). The **T** observables extracted from these two combinations agreed very nicely. An average **T** was then determined by calculating a weighted average of these two results; their respective uncertainties were used as weights according to:

$$\bar{x} = \frac{\sum_i x_i \cdot \frac{1}{\sigma_i^2}}{\sum_i \frac{1}{\sigma_i^2}} , \tag{4.39}$$

where x_i was the observable and σ_i was its error. Figure 4.6 (left) shows an example of the **T** observable from *combination132* and *combination45* as well as their weighted average.

Figure 4.6 (center) shows a comparison of the averaged **T** observable from the g9b data which utilized circular beam polarization with the **T** observable extracted from the g9b data which utilized linear beam polarization (1.7 GeV coherent edge). The two results agreed fairly well within statistical errors. Note that the holding field signs were also the same for the relevant *linear* g9b data (Table 3.2). Thus, the acceptance effects largely canceled out for both the *linear* and the *circular* data sets.

For all FROST data utilizing circular beam polarization, it was always possible to combine data sets such that the relevant terms in the asymmetries had the same holding field sign. In contrast, the holding field signs were mostly different for the relevant g9b *linear* data sets. The 1.7 GeV (coherent edge) data were an exception. Figure 4.6 (right) shows an example from the 1.5 GeV (coherent edge) data set. The **T** observable extracted from the linearly-polarized data (blue data points) agreed within statistical errors with the observable from the data which utilized circular beam polarization (red data points). However, the blue data points appeared to be slightly shifted systematically. We concluded that this small offset might be due to the holding field's influence on the acceptance.

The holding field was not considered in the cooking. When we discovered its influence on the acceptance, we tried to develop corrections for the azimuthal and polar angles of each track (see Section 3.6.4). However, a satisfactory multi-dimensional approach was impossible and some effects remained. Since a correction of the data was not a realistic option, we decided to define the difference between the results from the *linear* and the *circular* data as an overall non-angle-dependent contribution to the systematic uncertainty of the *linear* data. This contribution was determined by averaging the differences between individual data points weighted with their statistical errors to disentangle it from statistical fluctuations.

The Double-Polarization Observable F. The **F** observable in ω photoproduction was also a first-time measurement. This observable was a double-polarization observable associated with a circularly-polarized photon beam and a transversely-polarized target. Since the beam polarization flipped rapidly every second in the recorded data sets, we had $\Phi^{+}_{\rightarrow} = \Phi^{+}_{\leftarrow} = \Phi^{+}$ and $\Phi^{-}_{\rightarrow} = \Phi^{-}_{\leftarrow} = \Phi^{-}$.

From Equations 4.20 and 4.21, we see that combining $N^{+}_{\rightarrow}$ with $N^{-}_{\leftarrow}$ (with an appropriate normalization factor) eliminated the **T** term and retained the term with **F**:

$$\begin{aligned} N_a &= N^{+}_{\rightarrow} + C^{-}\, N^{-}_{\leftarrow} \\ &= \Phi^{+}\,\epsilon\,\sigma_0\,\{\,1 + \bar{\Lambda}_R + 2\bar{\Lambda}^{+}\,\bar{\delta}_{\odot}\,\mathbf{F}\cos\left(\pi - \phi^{\mathrm{p}}_{\mathrm{lab}} + 2.025\right)\} \\ &= \Phi^{+}\,\epsilon\,\sigma_a\ , \end{aligned} \tag{4.40}$$

where

$$C^{-} = \frac{\Phi^{+}}{\Phi^{-}}\frac{\bar{\Lambda}^{+}}{\bar{\Lambda}^{-}}\ , \quad \text{and} \quad \bar{\Lambda}_R = \frac{\bar{\Lambda}^{+}}{\bar{\Lambda}^{-}}\ . \tag{4.41}$$

Similarly, we could combine data sets with $(\rightarrow,\,-)$ & $(\leftarrow,\,+)$ beam-target polarization and obtained:

$$\begin{aligned} N_b &= N^{+}_{\leftarrow} + C^{-}\, N^{-}_{\rightarrow} \\ &= \Phi^{+}\,\epsilon\,\sigma_0\,\{\,1 + \bar{\Lambda}_R - 2\bar{\Lambda}^{+}\,\bar{\delta}_{\odot}\,\mathbf{F}\cos\left(\pi - \phi^{\mathrm{p}}_{\mathrm{lab}} + 2.025\right)\} \\ &= \Phi^{+}\,\epsilon\,\sigma_b\ . \end{aligned} \tag{4.42}$$

The asymmetry between 'a' and 'b' data (after combining data sets as shown in Equations 4.40 and 4.42) was then given by:

$$A = \frac{A' + \Delta\Phi}{1 + A'\,\Delta\Phi}\ , \tag{4.43}$$

where

$$A' = \left(\frac{\sigma_a - \sigma_b}{\sigma_a + \sigma_b}\right) = \frac{2\bar{\Lambda}^{+}\,\bar{\delta}_{\odot}\,\mathbf{F}\cos\left(\pi - \phi^{\mathrm{p}}_{\mathrm{lab}} + 2.025\right)}{1 + \bar{\Lambda}_R}\ , \qquad \Delta\Phi = 0 \tag{4.44}$$

The likelihood of observing a particular angular distribution in $\phi^{\mathrm{p}}_{\mathrm{lab}}$ for any kinematic bin was given by (using A from Equation 4.43):

$$\begin{aligned} -\ln L &= -\sum_{i=1}^{N_{\mathrm{total}}} w_i \ln\left(P\left(\mathrm{event}_{\,\mathrm{i}}\right)\right), \\ &\text{where } P\left(\mathrm{event}_{\,i}\right) = \begin{cases} \frac{1}{2}\left(1 + A\right) & \text{for } (\rightarrow,\,+) \text{ or } (\leftarrow,\,-) \text{ events}, \\ \frac{1}{2}\left(1 - A\right) & \text{for } (\rightarrow,\,-) \text{ or } (\leftarrow,\,+) \text{ events}, \end{cases} \end{aligned} \tag{4.45}$$

and N_{total} was the sum of all events for the four beam-target polarization settings used in that kinematic bin. The weight of the i^{th} event was:

$$w_i = \begin{cases} Q_i & \text{for } (\rightarrow,\,+) \text{ or } (\leftarrow,\,+) \text{ events} \\ Q_i\,C^{-} & \text{for } (\rightarrow,\,-) \text{ or } (\leftarrow,\,-) \text{ events} \end{cases} \tag{4.46}$$

The observable **F** was then extracted by minimizing $-\ln L$ which was given by Equation 4.45.

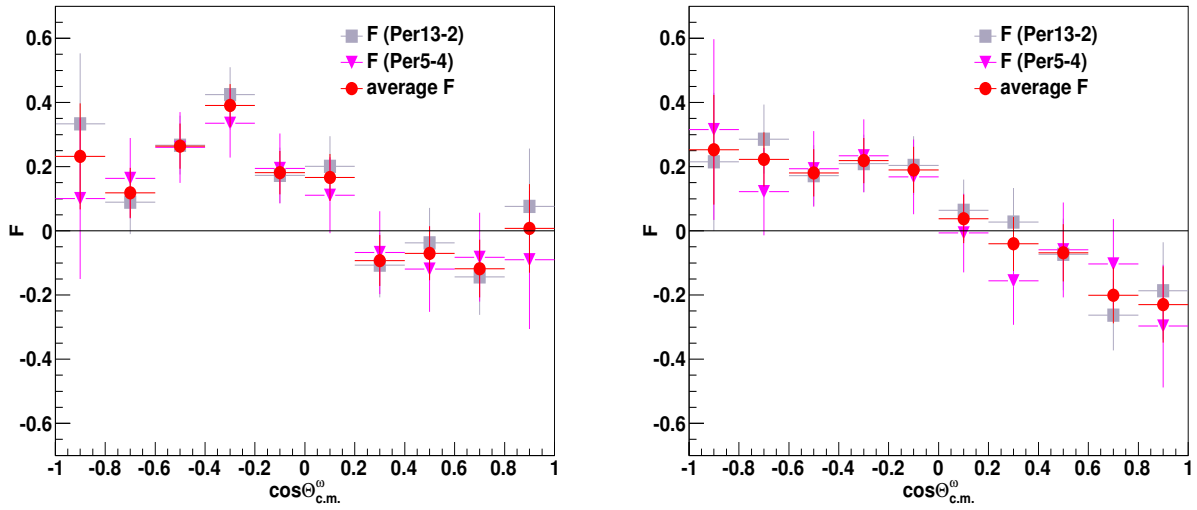

Figure 4.7: Examples of the **F** observable for $E_\gamma \in [1.40, 1.50]$ GeV (left) and $E_\gamma \in [1.50, 1.60]$ GeV (right) from the g9b (circular) data. The data points shown in gray were obtained from combination132. The data points shown in magenta were obtained from combination45. The data shown in red represent uncertainty-weighted average.

***.** The Average F Observable As discussed in the previous section, the best way to form an asymmetry between *circular* data sets from FROST-g9b was to combine those data sets with the same holding magnet sign. Hence, we used *combination-132* and *combination-45*. An average **F** was then determined by weighting the two results with their respective uncertainties. Figure 4.7 shows examples of the **F** observable for the different combinations and weighted average. The data agreed very well.

The Double-Polarization Observable H & Recoil-Polarization Observable P. Both the **H** and the **P** observable in ω photoproduction were first-time measurements. The observable **H** was a double-polarization observable associated with a linearly-polarized photon beam and a transversely-polarized target. The observable **P**, on the other hand, was a single-polarization observable that was associated with recoil polarization, but it could also be extracted from data using linearly-polarized photons and a transversely-polarized target.

From Equations 4.18 and 4.19, we can see that combining $N_{\parallel}^{+}$ and $N_{\perp}^{-}$ data with appropriate normalization factors gave:

$$\begin{aligned} N_1 &= N_{\parallel}^{+} + C_3\, N_{\perp}^{-} \\ &= \Phi_{\parallel}^{+}\,\epsilon\,\sigma_0\,\{\,1 + \bar{\Lambda}_R - \bar{\delta}_{\perp}\,(\bar{\delta}_R - \bar{\Lambda}_R)\,\mathbf{\Sigma}\cos 2\phi_{\rm lab}^{\rm p} \\ &\qquad - 2\bar{\Lambda}^{+}\,\tilde{\delta}\,(\quad \mathbf{H}\cos(\pi - \phi_{\rm lab}^{\rm p} + 2.025)\sin 2\phi_{\rm lab}^{\rm p} \\ &\qquad\qquad + \mathbf{P}\sin(\pi - \phi_{\rm lab}^{\rm p} + 2.025)\cos 2\phi_{\rm lab}^{\rm p}\,)\,\}\,, \end{aligned} \tag{4.47}$$

where

$$C_3 = \frac{\Phi_{\parallel}^{+}}{\Phi_{\perp}^{-}}\frac{\bar{\Lambda}^{+}}{\bar{\Lambda}^{-}}\,, \qquad \bar{\Lambda}_R = \frac{\bar{\Lambda}^{+}}{\bar{\Lambda}^{-}}\,, \qquad \tilde{\delta} = (\frac{\bar{\delta}_{\parallel} + \bar{\delta}_{\perp}}{2})\,. \tag{4.48}$$

In the term $\bar{\delta}_{\perp}\,(\bar{\delta}_R - \bar{\Lambda}_R)\,\mathbf{\Sigma}\cos 2\phi_{\rm lab}^{\rm p}$, $\bar{\delta}_R$ and $\bar{\Lambda}_R$ were ~ 1 and the remaining variables were smaller than *one*; thus, we could discard this term. Then, the above equation reduced to:

$$\begin{aligned} N_1 &= \Phi_{\parallel}^{+}\,\epsilon\,\sigma_0\,\{\,1 + \bar{\Lambda}_R \\ &\qquad - 2\bar{\Lambda}^{+}\,\tilde{\delta}\,(\quad \mathbf{H}\cos(\pi - \phi_{\rm lab}^{\rm p} + 2.025)\sin 2\phi_{\rm lab}^{\rm p} \\ &\qquad\qquad + \mathbf{P}\sin(\pi - \phi_{\rm lab}^{\rm p} + 2.025)\cos 2\phi_{\rm lab}^{\rm p}\,)\,\} \\ &= \Phi_{\parallel}^{+}\,\epsilon\,\sigma_1\,. \end{aligned} \tag{4.49}$$

Similarly, combining $N_{\perp}^{+}$ events with $N_{\parallel}^{-}$ gave:

$$\begin{aligned} N_2 &= \Phi_{\perp}^{+}\,\epsilon\,\sigma_0\,\{\,1 + \bar{\Lambda}_R \\ &\qquad + 2\bar{\Lambda}^{+}\,\tilde{\delta}\,(\quad \mathbf{H}\cos(\pi - \phi_{\rm lab}^{\rm p} + 2.025)\sin 2\phi_{\rm lab}^{\rm p} \\ &\qquad\qquad + \mathbf{P}\sin(\pi - \phi_{\rm lab}^{\rm p} + 2.025)\cos 2\phi_{\rm lab}^{\rm p}\,)\} \\ &= \Phi_{\perp}^{+}\,\epsilon\,\sigma_2\,. \end{aligned} \tag{4.50}$$

The asymmetry between '1' and '2' data was given by (after combining data sets as shown in Equation 4.49 and 4.50):

$$A = \frac{A' + \Delta\Phi}{1 + A'\,\Delta\Phi}\,, \tag{4.51}$$

where

$$\begin{aligned} A' &= \left(\frac{\sigma_1 - \sigma_2}{\sigma_1 + \sigma_2}\right) \\ &= \frac{-2\bar{\Lambda}^{+}\,\tilde{\delta}\,(\,\mathbf{H}\cos(\pi - \phi_{\rm lab}^{\rm p} + 2.025)\sin 2\phi_{\rm lab}^{\rm p} + \mathbf{P}\sin(\pi - \phi_{\rm lab}^{\rm p} + 2.025)\cos 2\phi_{\rm lab}^{\rm p}\,)}{1 + \bar{\Lambda}_R}\,, \end{aligned} \tag{4.52}$$

$$\Delta\Phi = \frac{\Phi_{\parallel}^{+} - \Phi_{\perp}^{+}}{\Phi_{\parallel}^{+} + \Phi_{\perp}^{+}}\,.$$

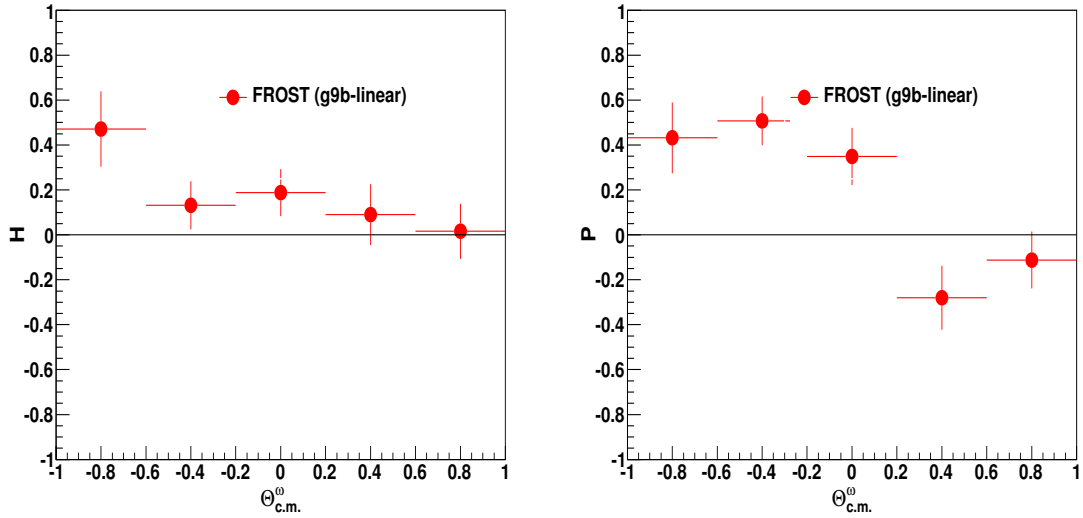

Figure 4.8: Example of the double-polarization observable **H** and the recoil-polarization observable **P** for $E_\gamma \in [1.70, 1.80]$ GeV from the g9b data which utilized a linearly-polarized beam and a transversely-polarized target. As mentioned in Section 4.1.1, a coarser binning scheme is used since the $\phi^{\mathrm{p}}_{\mathrm{lab}}$ angular distributions have a more complicated form (as shown in Equation 4.52).

The likelihood of observing a particular angular distribution in $\phi^{\mathrm{p}}_{\mathrm{lab}}$ for any kinematic bin was given by (using A from Equation 4.51):

$$-\ln L \;=\; -\sum_{i=1}^{N_{\mathrm{total}}} w_i \ln\left(P\left(\mathrm{event_i}\right)\right), \qquad \text{where } P\left(\mathrm{event_i}\right) \;=\; \begin{cases} \frac{1}{2}\left(1 + A\right) & \text{for } (\parallel,+) \text{ or } (\perp,\text{-}) \text{ events}, \\ \frac{1}{2}\left(1 - A\right) & \text{for } (\parallel,\text{-}) \text{ or } (\perp,+) \text{ events}, \end{cases} \tag{4.53}$$

and N_{total} was the sum of all events for the four beam-target polarization settings used in that kinematic bin. The weight of the i^{th} event was:

$$w_i \;=\; \begin{cases} Q_i & \text{for } (\parallel,+) \text{ or } (\perp,+) \text{ events}, \\ Q_i \, \dfrac{\Phi^{+}_{\parallel}}{\Phi^{-}_{\perp}} \, \bar{\Lambda}_R & \text{for } (\perp,-) \text{ events}, \\ Q_i \, \dfrac{\Phi^{+}_{\perp}}{\Phi^{-}_{\parallel}} \, \bar{\Lambda}_R & \text{for } (\parallel,-) \text{ events}. \end{cases} \tag{4.54}$$

The two observables were then extracted by minimizing $-\ln L$ which was given by Equation 4.53. Examples of **H** and **P** are shown in Figure 4.8.

4.4.4 Extraction of Polarization Observables in $\vec{\gamma}\vec{p} \to p\,\pi^+\pi^-$

Three different topologies were considered for the two-pion reaction (see also Table 3.5, Section 3.2). The topologies are listed here as a reminder:

- Topology 1: $\vec{\gamma}\,\vec{p} \to p\pi^+\,(\pi^-)$ – π^- not detected,
- Topology 2: $\vec{\gamma}\,\vec{p} \to p\pi^-\,(\pi^+)$ – π^+ not detected,
- Topology 4: $\vec{\gamma}\,\vec{p} \to p\,\pi^+\pi^-$ – all particles detected.

As mentioned previously, we did not have a *ready-to-be-used-in-an-analysis* Monte Carlo simulation for studying the acceptances of these three topologies. In the ideal situation of infinite statistics, the data could be binned finely in all five kinematic variables and furthermore, the detector acceptance would be independent of the beam-target polarization. For every topology, the acceptance term in each kinematic bin would then be the same for all data sets irrespective of their beam-target polarization and hence, the term would drop out for each asymmetry measurement. In reality, the detector acceptance could still be considered independent of the beam polarization. Moreover, we discussed in Section 4.4.3 that the effect of the target polarization on the acceptance was small, provided that data sets with different holding-field signs were properly combined.

However due to limited statistics, we could bin in only three of the five kinematic variables (see Section 4.1.2). Unfortunately, the acceptance terms associated with the remaining two variables did not cancel out when the asymmetries were formed. To estimate the overall effect of the detector acceptance from integrating over these two remaining variables (e.g. $\cos\Theta_{\mathrm{c.m.}}$ and a mass in our experimental analysis), we carefully compared the observables from the three topologies. The final observables are presented in this thesis as statistics-weighted averages over the three topologies, which also reduced the statistical errors. Note that this was one of the many choices available for presenting the final observables.

The extraction of polarization observables from data sets utilizing linearly-polarized photons and a transversely-polarized target required fitting angular distributions (as described in Section 4.4.1). The number of $\parallel$ events with a '+' or a '−' target polarization was determined by substituting

Equations 4.3, 4.15 and 4.16 into Equation 4.17:

$$\begin{aligned} N_{\parallel}^{\pm} \;=\; \Phi_{\parallel}^{\pm}\,\sigma_0\,\{\,(\,1 \,\pm\, \bar{\Lambda}^{\pm}\cos\alpha_0\,\mathbf{P_x} \,\pm\, \bar{\Lambda}^{\pm}\sin\alpha_0\,\mathbf{P_y}\,) \\ +\; \bar{\delta}_{\parallel}\,[\quad \sin 2\beta_0\,(\,\mathbf{I^s} \,\pm\, \bar{\Lambda}^{\pm}\cos\alpha_0\,\mathbf{P_x^s} \,\pm\, \bar{\Lambda}^{\pm}\sin\alpha_0\,\mathbf{P_y^s}) \\ +\; \cos 2\beta_0\,(\,\mathbf{I^c} \,\pm\, \bar{\Lambda}^{\pm}\cos\alpha_0\,\mathbf{P_x^c} \,\pm\bar{\Lambda}^{\pm}\sin\alpha_0\,\mathbf{P_y^c}\,)\,]\,\}\,, \end{aligned} \tag{4.55}$$

where $\alpha_0 = \pi - \phi_{\rm lab}^{\pi^+} + 2.025$ and $\beta_0 = \phi_{\rm lab}^{\pi^+}$. Note that the number of events was not corrected for the CLAS acceptance.

Similarly, the number of $\perp$ events for the two target settings, without correcting for the CLAS acceptance, could be written as:

$$\begin{aligned} N_{\perp}^{\pm} \;=\; \Phi_{\perp}^{\pm}\,\sigma_0\,\{\,(\,1 \,\pm\, \bar{\Lambda}^{\pm}\cos\alpha_0\,\mathbf{P_x} \,\pm\, \bar{\Lambda}^{\pm}\sin\alpha_0\,\mathbf{P_y}\,) \\ -\; \bar{\delta}_{\perp}\,[\quad \sin 2\beta_0\,(\,\mathbf{I^s} \,\pm\, \bar{\Lambda}^{\pm}\cos\alpha_0\,\mathbf{P_x^s} \,\pm\, \bar{\Lambda}^{\pm}\sin\alpha_0\,\mathbf{P_y^s}) \\ +\; \cos 2\beta_0\,(\,\mathbf{I^c} \,\pm\, \bar{\Lambda}^{\pm}\cos\alpha_0\,\mathbf{P_x^c} \,\pm\bar{\Lambda}^{\pm}\sin\alpha_0\,\mathbf{P_y^c}\,)\,]\,\}\,. \end{aligned} \tag{4.56}$$

Note that any number of events was not corrected for the CLAS acceptance. The above four equations had to be combined appropriately to single out each of the three polarization observables. A recipe for combining the different beam-target settings is discussed in the subsequent sections.

The Beam-Polarization Observables $\mathbf{I^s}$ and $\mathbf{I^c}$. The extraction of the beam-polarization observables was carried out using the same procedure as described in Section 4.4.3 for the extraction of the Σ_ω observable. The only difference was that the event numbers were given by Equations 4.55 and 4.56. Therefore, the mathematical form of the asymmetry was very similar to the one described by Equation 4.28, except for the fact that we had two observables, $\mathbf{I^s}$ and $\mathbf{I^c}$, and we considered the lab azimuthal angle of the π^+.

The asymmetry between $\parallel$ and $\perp$ data (after *unpolarizing* the target) could be written as:

$$A \;=\; \frac{A' \,+\, \Delta\Phi}{1 \,+\, A'\,\Delta\Phi}\;, \tag{4.57}$$

where

$$\begin{aligned} A' \;=\; \Big(\frac{\sigma_{\parallel} \,-\, \sigma_{\perp}}{\sigma_{\parallel} \,+\, \sigma_{\perp}}\Big) \;=\; \frac{\tilde{\delta}_l\,(\,\mathbf{I^s}\sin 2\phi_{\rm lab}^{\pi^+} \,+\, \mathbf{I^c}\cos 2\phi_{\rm lab}^{\pi^+}\,)}{1 \,+\, \tilde{\delta}_l\,\Delta\delta_l\,(\,\mathbf{I^s}\sin 2\phi_{\rm lab}^{\pi^+} \,+\, \mathbf{I^c}\cos 2\phi_{\rm lab}^{\pi^+}\,)} \\ \Delta\Phi \;=\; \frac{\Phi_{\parallel}^{+} \,-\, \Phi_{\perp}^{+}}{\Phi_{\parallel}^{+} \,+\, \Phi_{\perp}^{+}}\;, \qquad \tilde{\delta}_l \;=\; \frac{\bar{\delta}_{\parallel} \,+\, \bar{\delta}_{\perp}}{2}\;, \qquad \Delta\delta_l \;=\; \frac{\bar{\delta}_{\parallel} \,-\, \bar{\delta}_{\perp}}{\bar{\delta}_{\parallel} \,+\, \bar{\delta}_{\perp}}\;. \end{aligned} \tag{4.58}$$

The likelihood of observing a particular angular distribution in $\phi^{\pi^+}_{\text{lab}}$ in any kinematic bin was given by (using A from Equation 4.57):

$$
\begin{aligned}
-\ln L \;&=\; -\sum_{i=1}^{N_{\text{total}}} w_i \ln\left(P\left(\text{event}_{\,\text{i}}\right)\right), \\
&\text{where } P\left(\text{event}_{\,i}\right) \;=\; \begin{cases} \frac{1}{2}\left(1 \,+\, A\right) & \text{for } \parallel \text{ events}, \\ \frac{1}{2}\left(1 \,-\, A\right) & \text{for } \perp \text{ events}, \end{cases}
\end{aligned}
\tag{4.59}
$$

and N_{total} was the sum of all events for the four beam-target polarization settings used in that kinematic bin. The weight of the i^{th} event was:

$$
w_i \;=\; \begin{cases} Q_i & \text{if } (\parallel, +) \text{ or } (\perp, +) \text{ event}, \\ Q_i \,\frac{\Phi^+_{\parallel}}{\Phi^-_{\parallel}}\,\frac{\bar{\Lambda}^+}{\Lambda^-} & \text{if } (\parallel, -) \text{ event}, \\ Q_i \,\frac{\Phi^+_{\perp}}{\Phi^-_{\perp}}\,\frac{\bar{\Lambda}^+}{\Lambda^-}\,. & \text{if } (\perp, -) \text{ event} \end{cases}
\tag{4.60}
$$

Minimizing the negative log of the likelihood gave us the values and the statistical errors of the beam-polarization observables.

Comparing Results from Different Topologies Figures 4.10 and 4.11 shows comparisons between results from the three topologies in the $[1.3, 1.4]$ GeV energy bin. The comparisons were made separately for two independent CLAS experiments, the FROST-g9b experiment (left plots) and the CLAS-g8b experiment [44] (right plots) which utilized an unpolarized hydrogen target. The results from the CLAS-g8b experiment have been approved by the collaboration and are currently in preparation for publication. In the majority of the kinematic bins, the topologies agreed well within errors in both experiments. However, in certain kinematic bins significant disagreements between topologies could also be observed. The discrepancies were visible in the same kinematic bins and with very similar overall features in both experiments. Since the two experiments and their analyses were completely independent of each other, this indicated that the different behavior of the individual topologies in these kinematic bins was not analysis-specific; rather, it was topology-dependent and related to the CLAS acceptance of the two kinematic variables we integrated over. This was also evident from Figure 4.9 where the averages of the observables over all topologies from FROST-g9b (red data points) were compared with the averages over topologies from CLAS-g8b (blue data points) and they were found to be in excellent agreement with each other.

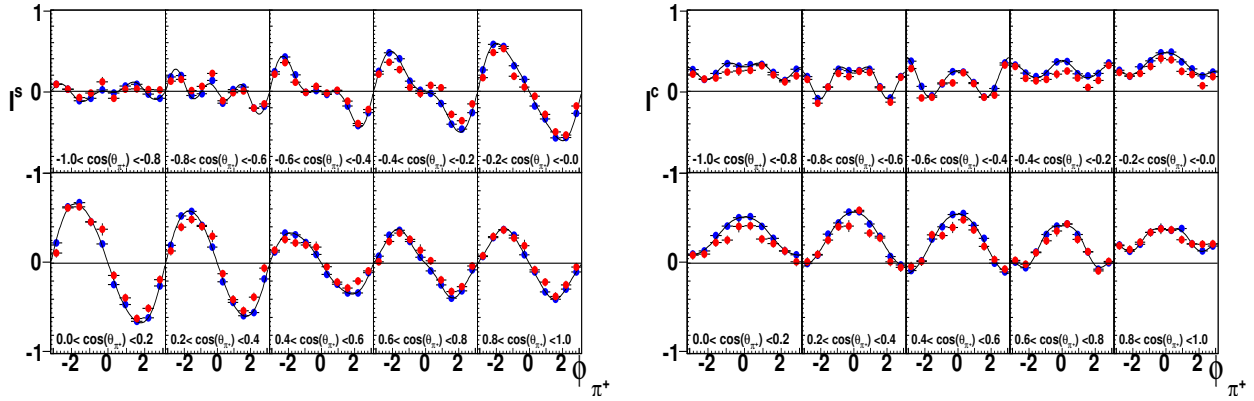

Figure 4.9: Observables $\mathbf{I^s}$ (left) and $\mathbf{I^c}$ (right) in the energy bin $E_\gamma \in [1.3, 1.4]$ GeV after performing a statistics-weighted average over results from the three topologies. The averaged observables from the FROST-g9b experiment (shown in red) are in excellent agreement with the averaged results from the CLAS-g8b experiment (shown in blue). The solid curves are third-order Fourier sine (cosine) fits to the $\mathbf{I^s}$ ($\mathbf{I^c}$) results from CLAS-g8b.

Figure 4.12 shows the distributions of the differences between the averages from all topologies (referred to as Topology 0) and the results from each individual topology integrated over all kinematic bins. Since Topology 1 had the largest statistics, the averaged results were close to the results from Topology 1. Hence, the distributions of the differences between results from Topology 0 and Topology 1 were narrow and nicely centered at zero. The distribution of the difference between Topology 0 and Topology 2 for $\mathbf{I^c}$ was centered at about 0.1 which showed that the acceptance effects lead to slightly different observables in Topology 2 relative to the other topologies. These acceptance effects were not noticeable in the distribution of the difference between $\mathbf{I^s}$ from Topology 0 and Topology 2 because of the odd parity of this observable with respect to ϕ_{π^+}. The differences took either positive or negative signs depending on the value of ϕ_{π^+} and hence, the distribution of the difference turned out to be symmetric with its center at zero. Last not least, acceptance effects were revealed as a small negative offset in the distribution of the difference between $\mathbf{I^c}$ from Topology 0 and Topology 4.

The Target-Polarization Observables $\mathbf{P_x}$ and $\mathbf{P_y}$. Both the $\mathbf{P_x}$ and the $\mathbf{P_y}$ observable were first-time measurements. These observables were determined using a procedure which was very similar to the one described in Section 4.4.3 for the extraction of the target-polarization observable

T for the ω channel. The only differences, as pointed out in the previous section, were the usage of the Equations 4.55, 4.56 and $\phi_{\rm lab}$ of the π^+ meson. The asymmetry between the '+' and '−' data (after *unpolarizing* the beam) could be written as:

$$A \,=\, \frac{A' \,+\, \Delta\Phi}{1 \,+\, A'\,\Delta\Phi}\,, \tag{4.61}$$

where

$$\begin{aligned} A' \,&=\, \frac{\tilde{\Lambda}\,[\,\mathbf{P_x}\cos\left(\pi \,-\, \phi^{\pi^+}_{\rm lab} \,+\, 2.025\right) \,+\, \mathbf{P_y}\sin\left(\pi \,-\, \phi^{\pi^+}_{\rm lab} \,+\, 2.025\right)\,]}{1 \,+\, \tilde{\Lambda}\,\Delta\Lambda\,[\,\mathbf{P_x}\cos\left(\pi \,-\, \phi^{\pi^+}_{\rm lab} \,+\, 2.025\right) \,+\, \mathbf{P_y}\sin\left(\pi \,-\, \phi^{\pi^+}_{\rm lab} \,+\, 2.025\right)\,]} \\ \Delta\Phi \,&=\, \frac{\Phi^+_\parallel \,-\, \Phi^-_\parallel}{\Phi^+_\parallel \,+\, \Phi^-_\parallel}\,, \qquad \tilde{\Lambda} \,=\, \frac{\bar{\Lambda}^+ \,+\, \bar{\Lambda}^-}{2}\,, \qquad \Delta\Lambda = \frac{\bar{\Lambda}^+ \,-\, \bar{\Lambda}^-}{\bar{\Lambda}^+ \,+\, \bar{\Lambda}^-}. \end{aligned} \tag{4.62}$$

The likelihood was then given by:

$$\begin{aligned} -\ln L \,&=\, -\sum_{i=1}^{N_{\rm total}} w_i \ln\left(P\left(\text{event}_{\rm i}\right)\right), \\ \text{where } P\left(\text{event}_i\right) \,&=\, \begin{cases} \frac{1}{2}\left(1 \,+\, A\right) & \text{for '}+'\text{ events}, \\ \frac{1}{2}\left(1 \,-\, A\right) & \text{for '}-\text{' events}, \end{cases} \end{aligned} \tag{4.63}$$

and $N_{\rm total}$ was the sum of all events for the four beam-target polarization settings used in that kinematic bin. The weight of the i^{th} event was:

$$w_i \,=\, \begin{cases} Q_i, & \text{if } (\parallel,\,+) \text{ or } (\parallel,\,-) \text{ event} \\ Q_i\,\frac{\Phi^+_\parallel}{\Phi^+_\perp}\,\frac{\bar{\delta}_\parallel}{\bar{\delta}_\perp} & \text{if } (\perp,\,+) \text{ event} \\ Q_i\,\frac{\Phi^-_\parallel}{\Phi^-_\perp}\,\frac{\bar{\delta}_\parallel}{\bar{\delta}_\perp} & \text{if } (\perp,\,-) \text{ event} \end{cases} \tag{4.64}$$

Comparing Results from Different Topologies Figure 4.13 shows a comparison of the results on the observable $\mathbf{P_x}$ from the individual topologies (top rows) and their averages (bottom rows) in the energy bin $E \in [0.8, 0.9]$ GeV. The same is shown for the observable $\mathbf{P_y}$ in Figure 4.14. The results agreed fairly well with each other within statistical errors in most of the kinematic bins. However, the acceptance effects were significant in some cases. They lead to small disagreements between results from the individual topologies, as we can see in some of the kinematic bins shown in the figure. Figure 4.15 shows the distributions of the differences between the averaged results and the results from each topology, integrated over all kinematic bins. The distributions were narrow and centered at zero. Based on these distributions, we concluded that the overall acceptance effects

owing to integrating over the two kinematic variables were very small unlike in the previous section. Since the target-polarization observable was much smaller than the beam-polarization observable, it appeared not to vary much over the two remaining kinematic variables (not used for binning).

Again, these observables were first-time measurements. Based on parity conservation, it has been predicted that $\mathbf{P_x}$ ($\mathbf{P_y}$) have an odd (even) parity with respect to ϕ_{π^+} [36]. This behavior was clearly seen in our results. As an example, we show the averaged results in the energy bin $E \in [0.8, 0.9]$ GeV in Figures 4.13 and 4.14 (bottom rows). The results could be nicely fitted with a second-order Fourier sine or cosine series (shown as black solid curves).

The Double-Polarization Observables $\mathbf{P^{s,c}_{x,y}}$. All four double-polarization observables were first-time measurements. The procedure for the extraction was the same as outlined in Section 4.4.3. Using Equations 4.55 and 4.56, the asymmetry could be written as:

$$A = \frac{A' + \Delta\Phi}{1 + A'\,\Delta\Phi}\,, \tag{4.65}$$

where

$$\begin{aligned} A' &= \frac{2\,\bar{\Lambda}^+\,\tilde{\delta}\,(\,\mathbf{P^s_x}\sin 2\beta_0\cos\alpha_0 \,+\, \mathbf{P^s_y}\sin 2\beta_0\sin\alpha_0 \,+\, \mathbf{P^c_x}\cos 2\beta_0\cos\alpha_0 \,+\, \mathbf{P^c_y}\cos 2\beta_0\sin\alpha_0\,)}{1 \,+\, \bar{\Lambda}_R} \\ \Delta\Phi &= \frac{\Phi^+_\parallel - \Phi^+_\perp}{\Phi^+_\parallel + \Phi^+_\perp}\,, \qquad \bar{\Lambda}_R = \frac{\bar{\Lambda}^+}{\bar{\Lambda}^-}\,, \qquad \tilde{\delta} = \left(\frac{\bar{\delta}_\parallel + \bar{\delta}_\perp}{2}\right), \end{aligned} \tag{4.66}$$

and $\alpha_0 = \pi - \phi^{\pi^+}_{\rm lab} + 2.025$, $\beta_0 = \phi^{\pi^+}_{\rm lab}$. The likelihood of observing a particular angular distribution in $\phi^{\pi^+}_{\rm lab}$ in any kinematic bin was then given by (using A from Equation 4.65):

$$\begin{aligned} -\ln L &= -\sum_{i=1}^{N_{\rm total}} w_i \ln\left(P\left(\text{event}_i\right)\right), \\ &\text{where, } P\left(\text{event}_i\right) = \begin{cases} \frac{1}{2}\,(1 + A) & \text{for } (\parallel, +) \text{ or } (\perp, -) \text{ events}, \\ \frac{1}{2}\,(1 - A) & \text{for } (\parallel, -) \text{ or } (\perp, +) \text{ events}, \end{cases} \end{aligned} \tag{4.67}$$

and $N_{\rm total}$ was the sum of all events for the four beam-target polarization settings used in that kinematic bin. The weight of the i^{th} event was:

$$w_i = \begin{cases} Q_i & \text{if } (\parallel, +) \text{ or } (\perp, +) \text{ event}, \\ Q_i\,\frac{\Phi^+_\parallel}{\Phi^-}\,\bar{\Lambda}_R & \text{if } (\perp, -) \text{ event}, \\ Q_i\,\frac{\Phi^+_\perp}{\Phi^-_\parallel}\,\bar{\Lambda}_R & \text{if } (\parallel, -) \text{ event}. \end{cases} \tag{4.68}$$

As discussed in Section 4.1.2, the data in this case were binned in quasi-three dimensions: 100 MeV wide photon energy bins, 2 bins in $\cos\theta_{\pi^+}$ and 10 bins in ϕ_{π^+}.

Comparing Results from Different Topologies Figure 4.16 shows a comparison between the individual topologies and their weighted average in the energy bin $E_\gamma \in [0.8, 0.9]$ GeV. In addition to the acceptance effects due to integrating over the two remaining kinematic variables, there were likely also acceptance effects due to the coarse binning in $\cos\theta_{\pi^+}$. Similar to the discussion in the previous section, the acceptance effects appeared smaller than those observed in Section 4.4.4, which might be due to the fact that the observable itself was small (less than 0.3 in magnitude) and did not vary as much as the observables $I^{s,c}$ over $\cos\theta_{\pi^+}$ and the unbinned variables. This was also evident from the distributions of the differences between the averaged results and the results from the individual topologies integrated over all kinematic bins (Figure 4.18). Note that the distributions of the differences were not as smooth as the distributions presented in the previous two sections because the number of entries in each of these distributions decreased by a factor of five (owing to the coarse binning in $\cos\theta_{\pi^+}$).

Figure 4.17 shows the weighted average of the results over all topologies for the four observables in the energy bin $E_\gamma \in [0.8, 0.9]$ GeV. The observables $\mathbf{P_x^c}$ and $\mathbf{P_y^s}$ exhibited an odd symmetry with respect to ϕ_{π^+}. The other two observables, $\mathbf{P_x^s}$ and $\mathbf{P_y^c}$ exhibited an even symmetry with respect to ϕ_{π^+}. These observations were consistent with theoretical predictions based on parity conservation and support our results.

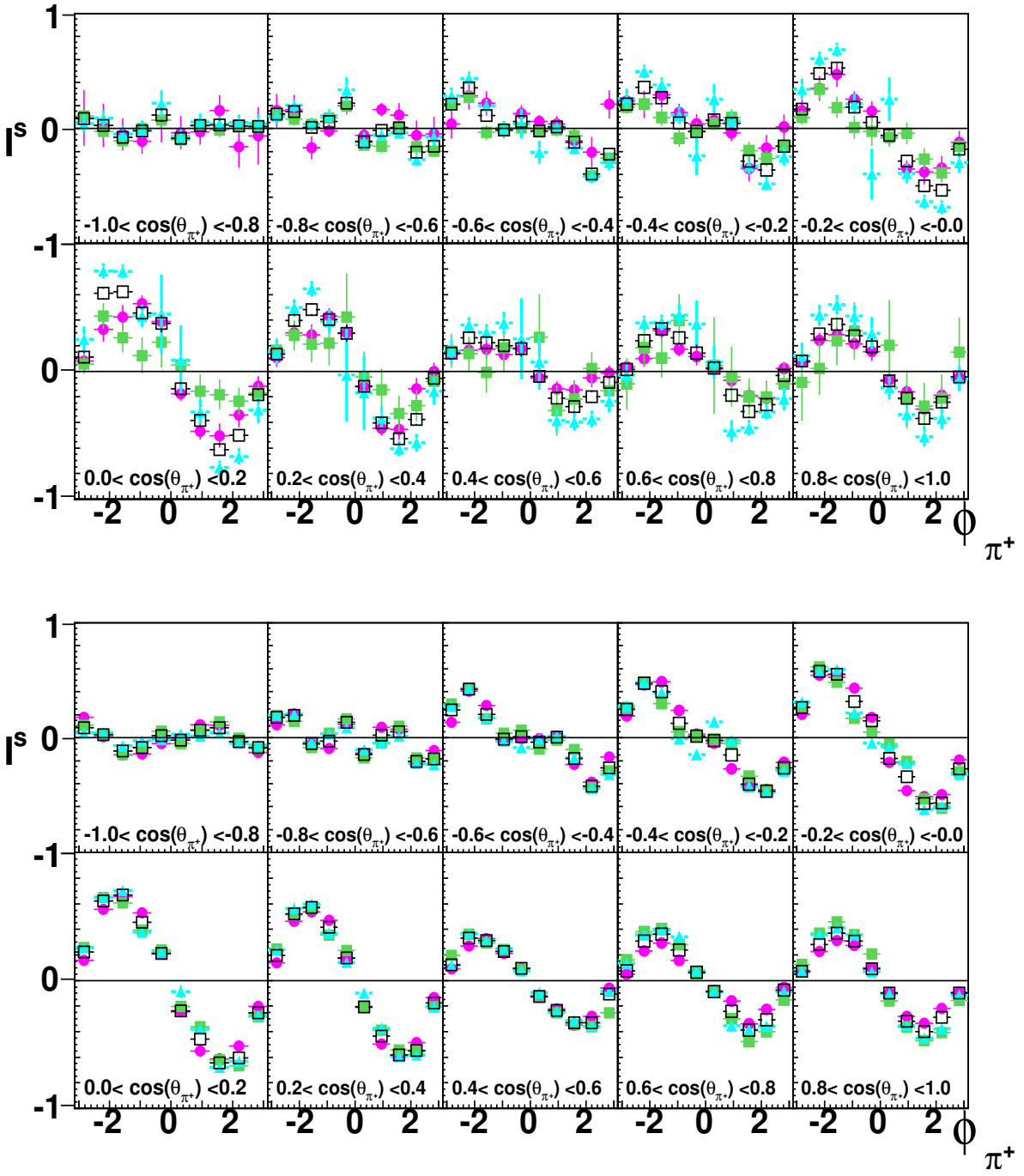

Figure 4.10: A comparison between results on $\mathbf{I^s}$ from Topology 1 (magenta circles), Topology 2 (green squares), Topology 4 (light blue triangles) and their average (black open squares) in the energy bin $E_\gamma \in [1.3, 1.4]$ GeV. Results are shown as a function of $\cos\theta_{\pi^+}$ and ϕ_{π^+} from two independent experiments, the g9b experiment (top) and the CLAS-g8b experiment (bottom).

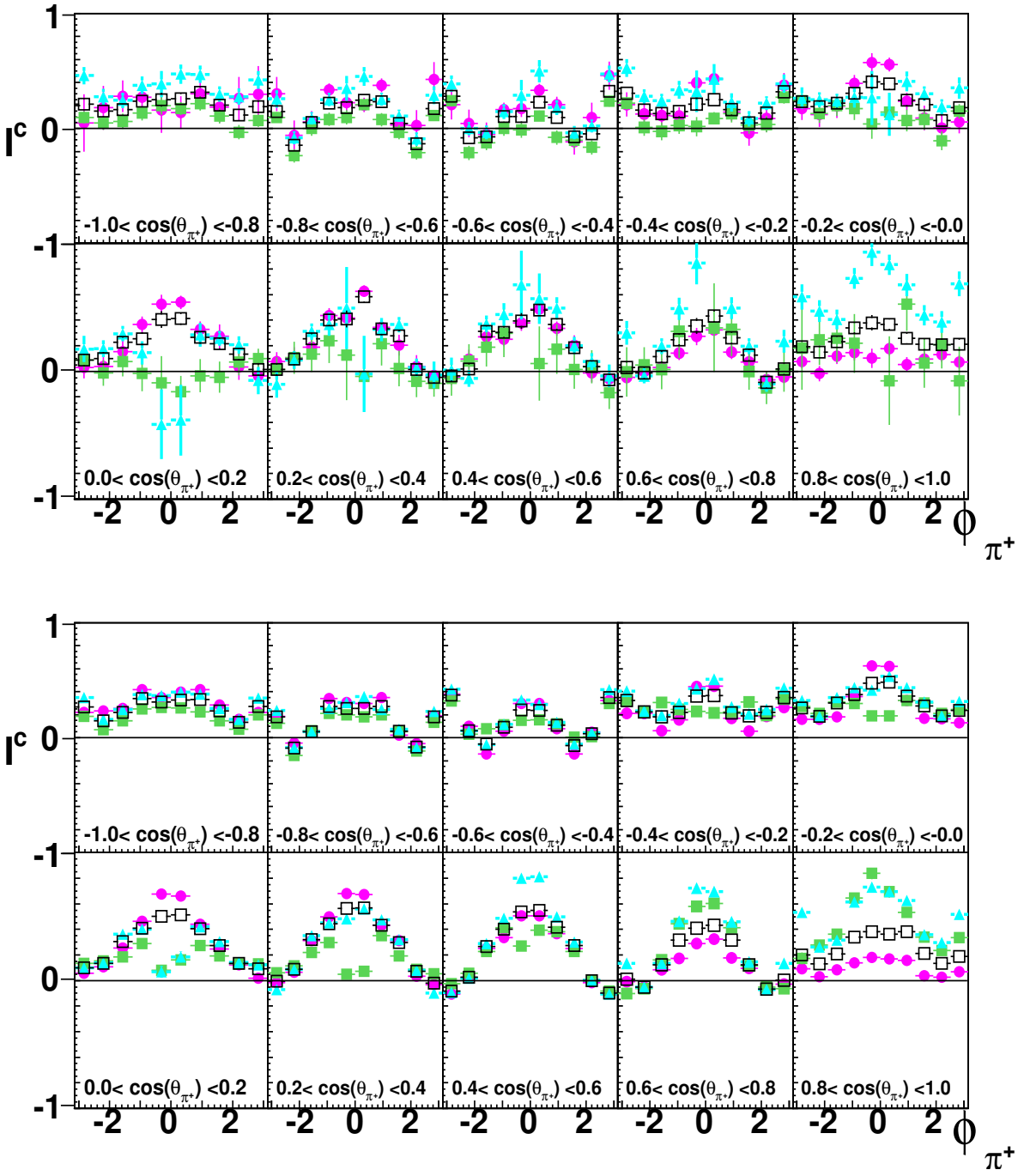

Figure 4.11: A comparison between results on $\mathbf{I^c}$ from Topology 1 (magenta circles), Topology 2 (green squares), Topology 4 (light blue triangles) and their average (black open squares) in the energy bin $E_\gamma \in [1.3, 1.4]$ GeV. Results are shown as a function of $\cos\theta_{\pi^+}$ and ϕ_{π^+} from two independent experiments, the g9b experiment (top) and the CLAS-g8b experiment (bottom).

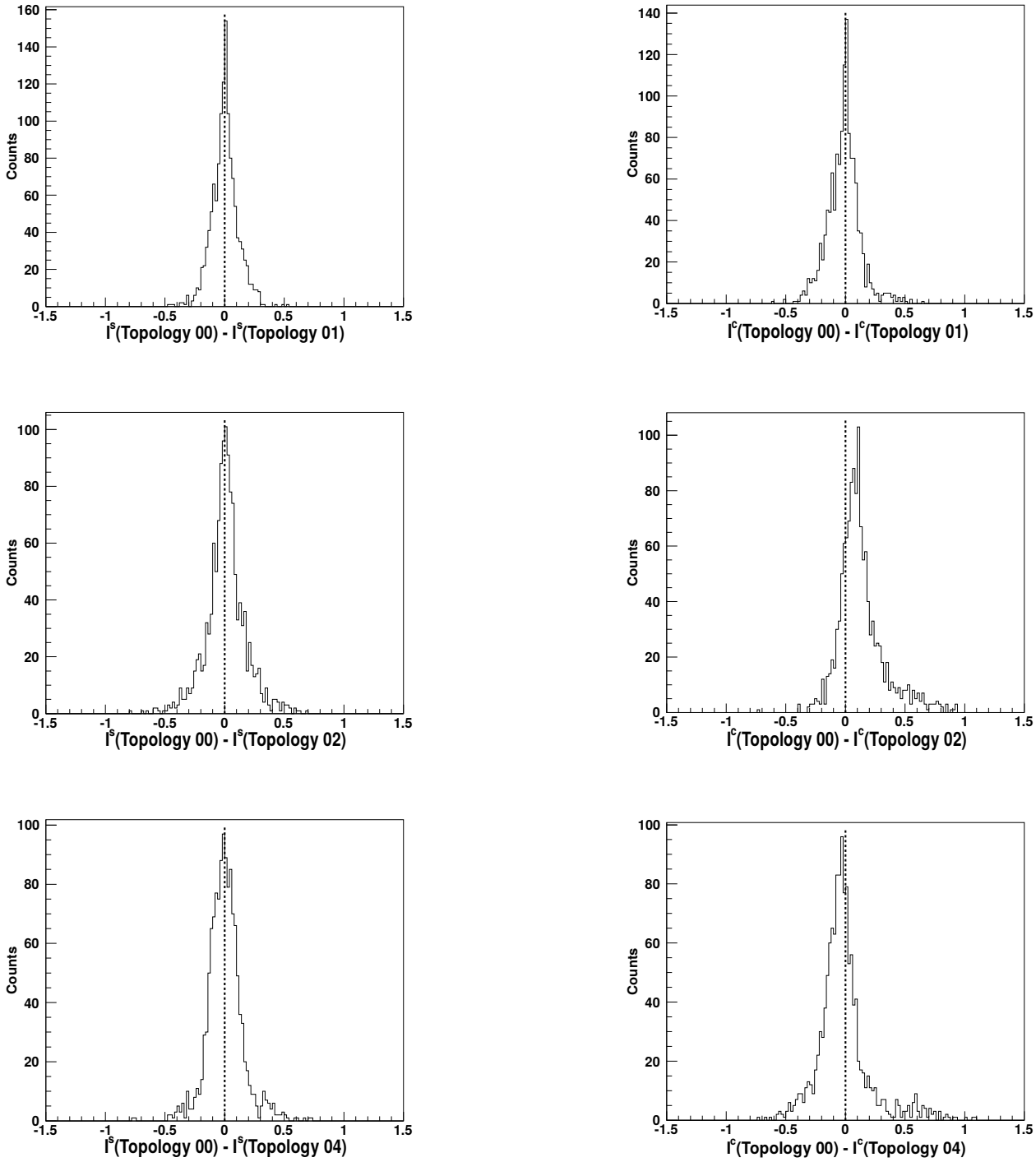

Figure 4.12: The differences between Topology 0 and the individual topologies for the observables $\mathbf{I^s}$ (left) and observables $\mathbf{I^c}$ (right) extracted from the FROST-g9b experiment. Here, Topology 0 denotes the weighted average of the three topologies. The differences presented here are integrated over all kinematic bins.

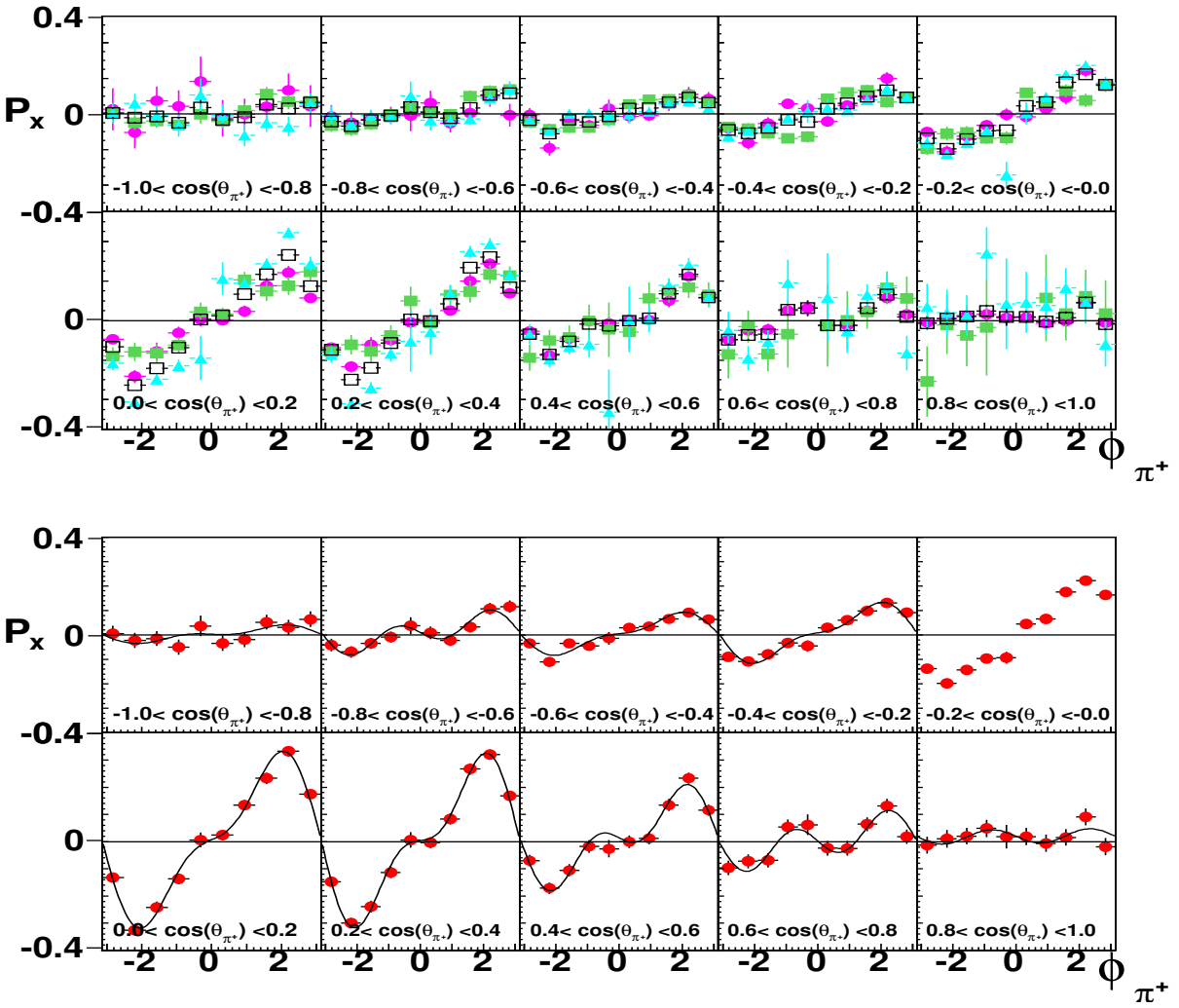

Figure 4.13: A comparison between results on $\mathbf{P_x}$ from Topology 1 (magenta circles), Topology 2 (green squares), Topology 4 (light blue triangles) and their average (black open squares) in the energy bin $E_\gamma \in [0.8, 0.9]$ GeV. Results are shown as a function of $\cos\theta_{\pi^+}$ and ϕ_{π^+}. The bottom half shows the final results as averages (red circles) over all topologies in the same energy bin. The solid curves are second-order Fourier sine fits to the final results for $\mathbf{P_x}$.

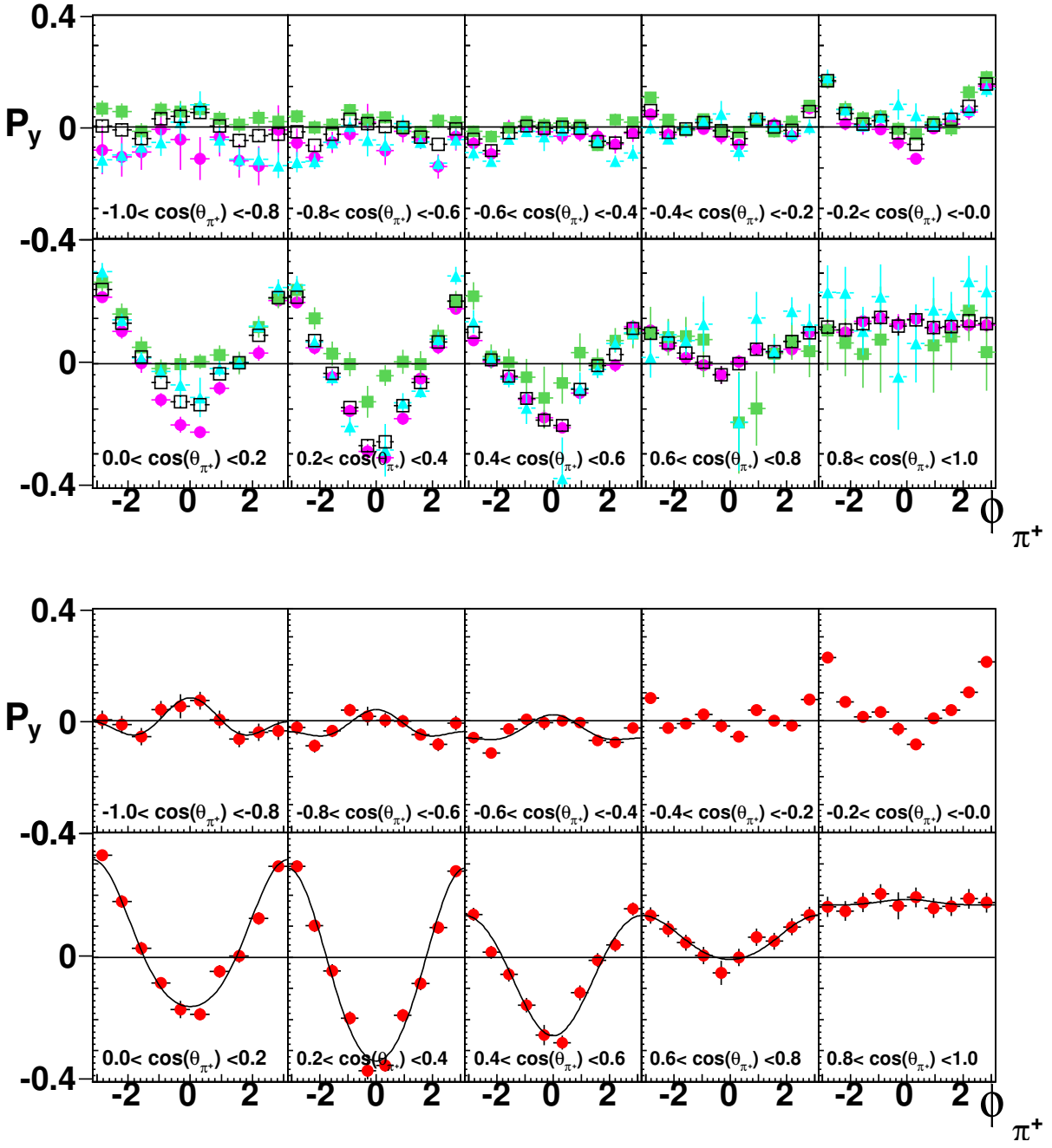

Figure 4.14: A comparison between results on $\mathbf{P_y}$ from Topology 1 (magenta circles), Topology 2 (green squares), Topology 4 (light blue triangles) and their average (black open squares) in the energy bin $E_\gamma \in [0.8, 0.9]$ GeV. Results are shown as a function of $cos\,\theta_{\pi^+}$ and ϕ_{π^+}. The bottom half shows the final results as averages (red circles) over all topologies in the same energy bin. The solid curves are second-order Fourier cosine fits to the final results for $\mathbf{P_y}$.

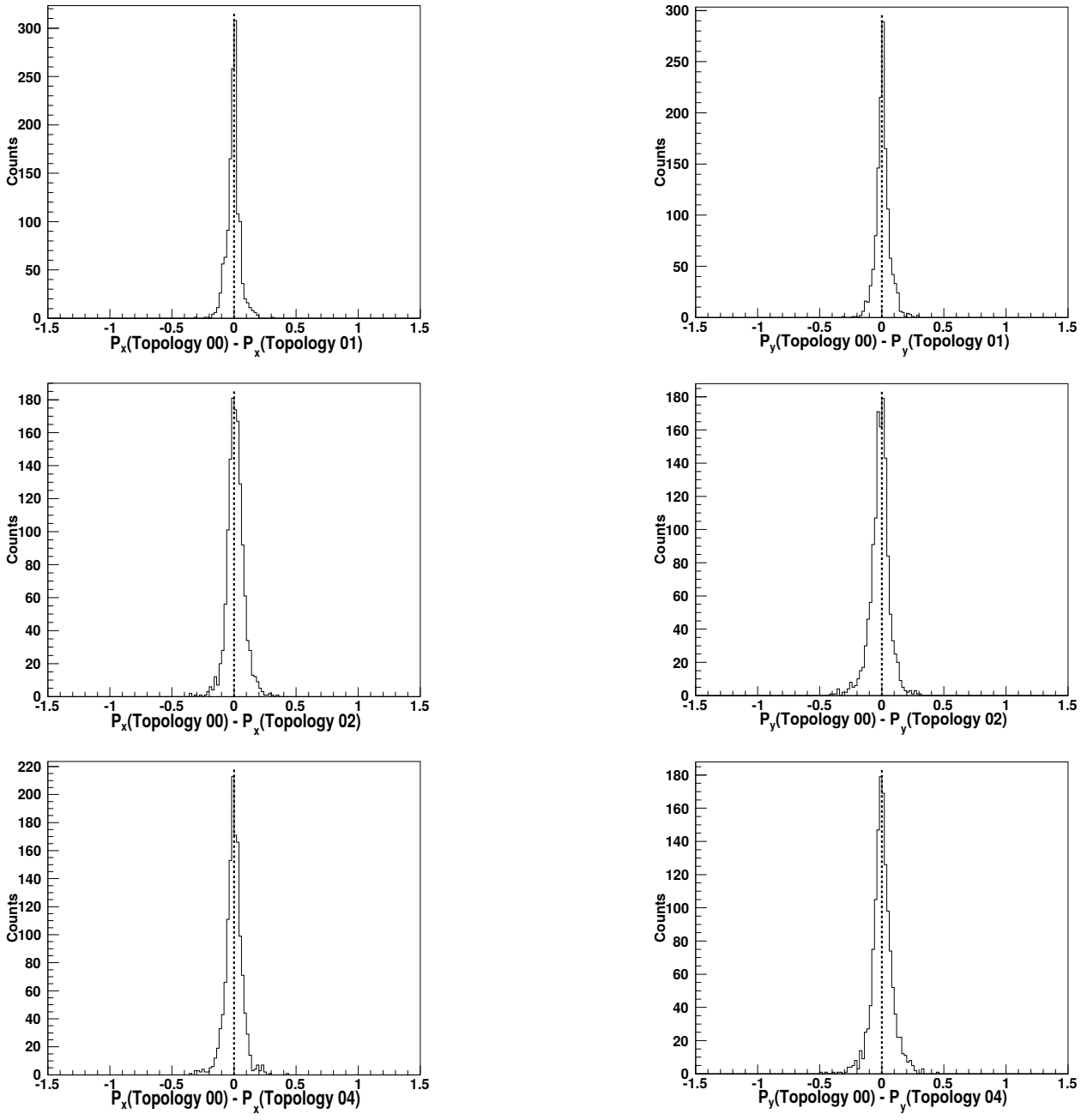

Figure 4.15: The differences between Topology 0 and the individual topologies for the observables $\mathbf{P_x}$ (left) and $\mathbf{P_y}$ (right) extracted from the FROST-g9b experiment. Topology 0 corresponds to the average of the three topologies. The presented differences are integrated over all kinematic bins.

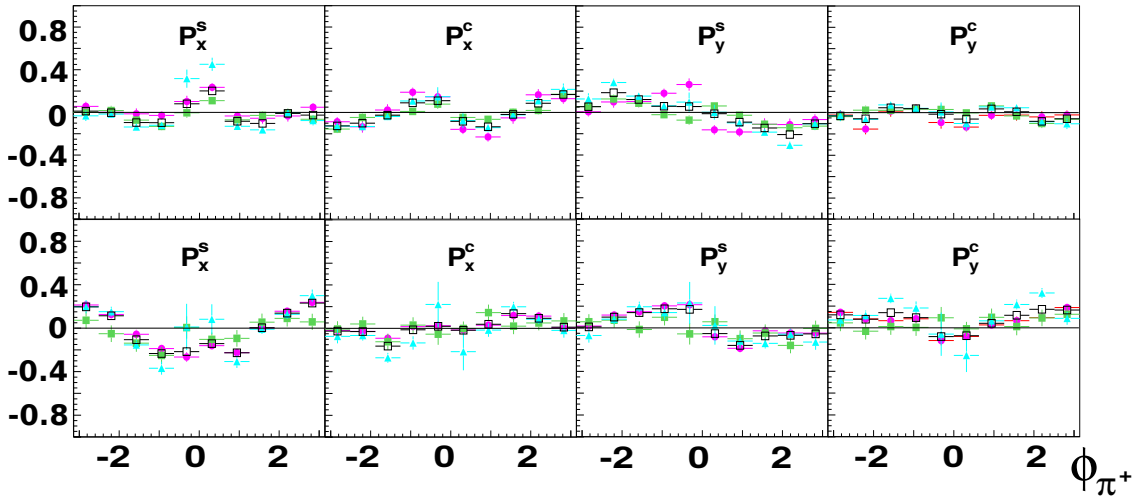

Figure 4.16: A comparison between results from Topology 1 (magenta circles), Topology 2 (green squares), Topology 4 (light blue triangles), and their average (black open squares) in the energy bin $E_\gamma \in [0.8, 0.9]$ GeV. Results are shown for the angle bins $-1.0 < \cos\theta_{\pi^+} < 0.0$ (top) and $0.0 < \cos\theta_{\pi^+} < 1.0$ (bottom) for the observable $\mathbf{P_x^s}$ (first column), $\mathbf{P_x^c}$ (second column), $\mathbf{P_y^s}$ (third column) and $\mathbf{P_y^c}$ (fourth column). In each $\cos\theta_{\pi^+}$ bin, the data are plotted as a function of ϕ_{π^+}.

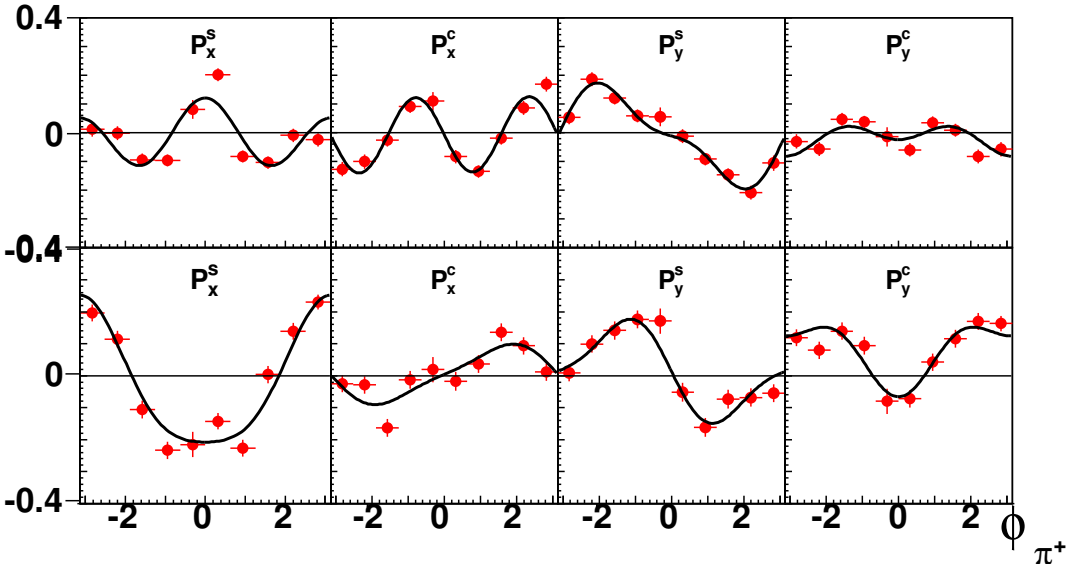

Figure 4.17: The weighted average of the results over all topologies for the observables $\mathbf{P_x^s}$ (first column), $\mathbf{P_x^c}$ (second column), $\mathbf{P_y^s}$ (third column), and $\mathbf{P_y^c}$ (fourth column) in $E_\gamma \in [0.8, 0.9]$ GeV. Results are shown for the angle bins $-1.0 < \cos\theta_{\pi^+} < 0.0$ (top row) and $0.0 < \cos\theta_{\pi^+} < 1.0$ (bottom row). The x-axis is ϕ_{π^+}. The solid curves are second-order Fourier sine (cosine) fits to the averaged results on $\mathbf{P_x^c}$, $\mathbf{P_y^s}$ ($\mathbf{P_x^s}$, $\mathbf{P_y^c}$).

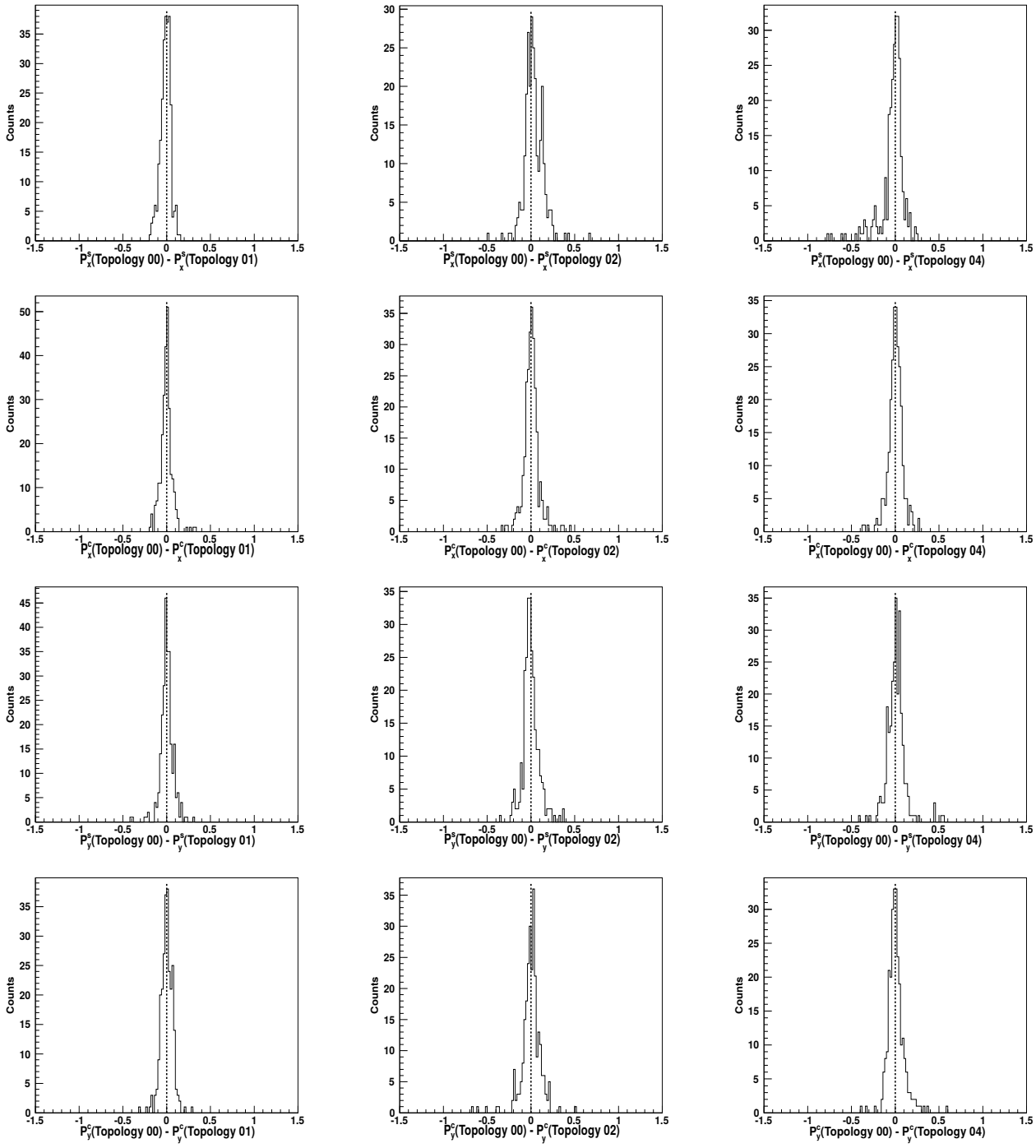

Figure 4.18: Distributions of differences between results from Topology 0 and the individual topologies on the observables $\mathbf{P_x^s}$ (first row), $\mathbf{P_x^c}$ (second row), $\mathbf{P_y^s}$ (third row), and $\mathbf{P_y^c}$ (fourth row). Topology 0 denotes the average of the three topologies. The differences presented here are integrated over all kinematic bins.

CHAPTER 5

SYSTEMATIC ERRORS

5.1 Contribution from the Q-Factor Method

Propagating the Q-value errors analytically was very difficult since angular distributions in $\phi_{\rm lab}$ needed to be fitted in the extraction of polarization observables, for example in the determination of the beam-polarization observables $\mathbf{I}^{\rm s}$ and $\mathbf{I}^{\rm c}$. Therefore an alternative approach was applied. We changed the Q-value of each event by σ_{Q_i} where σ_{Q_i} was the fit error in the Q-value of the i^{th} event. Then the error in the yield in any $\phi_{\rm lab}$ bin was equal to the sum over all σ_{Q_i} within the bin. Thus, this method corresponded to the case when the events are assumed to be 100% correlated (over-estimation of errors). In the next step, we determined the asymmetry and re-extracted the polarization observable by using these modified Q-values. The difference between the original polarization observable and the slightly modified observable, was considered a contribution to the overall systematic uncertainty. An important question was whether the Q-value of the event should be increased or decreased by the fit errors. Three different cases were studied:

1) increasing all Q-values by their individual fit errors,

2) decreasing all Q-values by their individual errors,

3) increasing the Q-values of the events with one type of polarization and decreasing the Q-values of the events with the opposite type of polarization.

It was observed that, on average, the magnitudes of the changes in the polarization observable in 1. and 2. were very similar and bigger than in case 3. We therefore employed case 1. and determined the the absolute value of the change in the observable in each kinematic bin; this number was then quoted as the absolute uncertainty in the observable *due to the Q-factor method*. In Section 6 the gray band at the bottom of each plot shows the *total* systematic uncertainty for each observable.

Table 5.1: Average percentage errors in $\mathbf{I^s}$ and $\mathbf{I^c}$ in various energy bins due to the Q-value method.

Energy Range (MeV)	$\mid \Delta \mathbf{I^s}/\mathbf{I^s} \mid (\%)$	$\mid \Delta \mathbf{I^c}/\mathbf{I^c} \mid (\%)$
1100 - 1200	6.1	10.1
1400 - 1500	8.6	9.0
1600 - 1700	10.1	9.5

Furthermore, to develop an overall estimate of the average percentage error (over all kinematic bins within an energy bin), the following equation was used:

$$\left|\frac{\Delta x}{x}\right|_{av.} \text{(in \%)} = \left(\frac{\sum_{i=1}^{\text{all bins}} \{ \left|\frac{x-x'}{x}\right| \left(\frac{1}{\sigma_x}\right)^2 \}}{\sum_{i=1}^{\text{all bins}} \left(\frac{1}{\sigma_x}\right)^2} \right) \times 100\,\%\,, \tag{5.1}$$

where x was the original polarization observable, x' was the re-calculated polarization observable and σ_x was the statistical error in x. Table 5.1 lists the average percentage errors, using Equation 5.1, for the observables $\mathbf{I^s}$ and $\mathbf{I^c}$ at various energies.

The above method to determine the contribution from the Q-factor method to the overall systematic uncertainty was based on the assumption that our choice for the background and signal shapes was appropriate. This was not always true in energy bins close to the threshold region for the ω reaction (1.1 - 1.3 GeV) where the background subtraction was more difficult. Since the phase space had a fairly sharp cut-off on the right-hand side of the ω peak, a combination of an Argus function and a second-order Chebychev polynomial was utilized to define the background pdf, as described in Section 3.9.3. Yet, the available background did not always sufficiently constrain the event-based likelihood fits. We refer to Figure 3.27 (top right) as an example, which corresponds to the [1.2 - 1.3] GeV photon energy bin. In the background, a dip-like structure under the ω peak was observed. To estimate the systematics associated with this, the background distribution obtained from the Q-factor method was fitted with a second-order polynomial in the range $\omega_{\text{peak}} \pm 5\sigma$, as shown in Figure 5.1 (right). This was done separately for the four sub-data sets: (PARA, +), (PARA, −), (PERP, +), and (PERP, −). The fractional difference between the background and the fit in the range ω peak $\pm\ 2\sigma$ was determined to be about 5 - 7 % on average. In order to quantify the effect of this fractional difference on the final observables, we developed the following strategy:

Since the background was under-estimated in the region $\omega_{\text{peak}} \pm 2\sigma$, which was equivalent to the signal being over-estimated, we *decreased* the Q-value of those events belonging to this mass range by 7 %. In addition, the Q-values of all events were also increased by their fit errors. The final observables were then re-determined and the fractional difference between the original observables and the modified observables was quoted as the systematic uncertainty for the observable due to the Q-factor method.

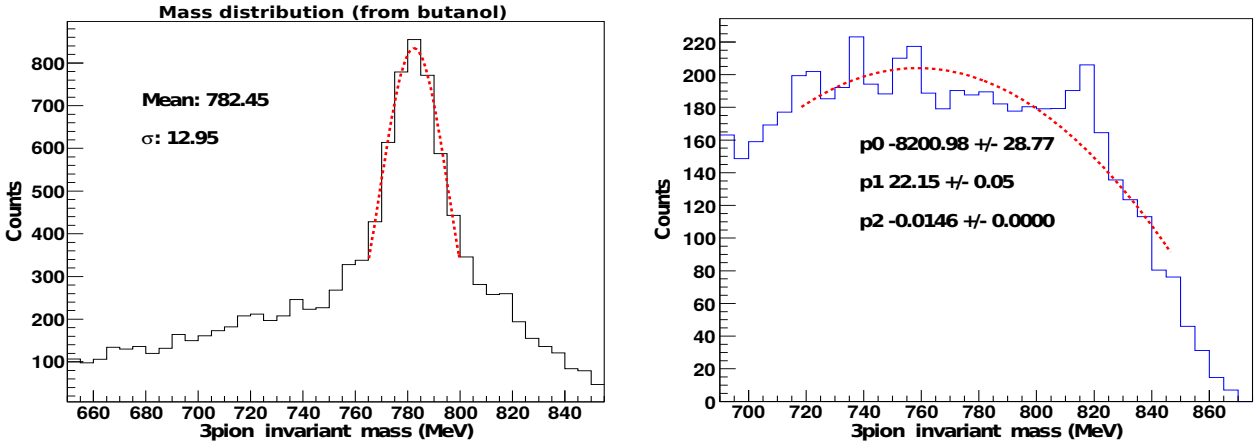

Figure 5.1: (Left) An invariant-mass distribution of the $(\pi^+\pi^-\pi^0)$ system obtained from the butanol target for $E \in [1.2, 1.3]$ GeV. The ω peak was fitted with a Gaussian function (red dashed curve) and the corresponding mean and σ were determined. (Right) The mass distribution was then weighted by $(1 - Q)$ and the region lying within $[\omega_{peak} \pm 5\sigma]$ was fitted with a second-order polynomial function (red dashed curve). Data used: 1.3 GeV coherent edge data set with PARA beam and '+' target polarization.

We found that the uncertainty in the ω beam asymmetry $\mathbf{\Sigma}$ for the bin $E \in [1.2, 1.3]$ GeV increased from 3.6 % (considering only the Q-fit errors) to 4.8 % when we also included the fractional difference between the Q-factor background description and the polynomial fit.

5.2 Contribution from the Beam Polarization

The observables Σ, **F**, **H**, and **P** in the ω reaction and the observables $\mathbf{I}^{s,c}$ and $\mathbf{P}^{s,c}_{x,y}$ in the $\pi^+\pi^-$ reaction were extracted by fitting angular distributions. The amplitudes were proportional to the product of the average degree of beam polarization and the relevant polarization observable. Therefore, the contribution to the systematic uncertainty in the observable was the same as

the percentage error in the degree of beam polarization. For example, we showed earlier for the observables $\mathbf{I}^{s,\,c}$ (Equation 4.58) that:

$$A' = \left(\frac{\sigma_{\parallel} - \sigma_{\perp}}{\sigma_{\parallel} + \sigma_{\perp}}\right) = \frac{\tilde{\delta}_l \,(\,\mathbf{I^s} \sin 2\phi^{\pi^+}_{\text{lab}} + \mathbf{I^c} \cos 2\phi^{\pi^+}_{\text{lab}}\,)}{1 + \tilde{\delta}_l\,\Delta\delta_l\,(\,\mathbf{I^s} \sin 2\phi^{\pi^+}_{\text{lab}} + \mathbf{I^c} \cos 2\phi^{\pi^+}_{\text{lab}}\,)}\,, \tag{5.2}$$

where $\tilde{\delta}_l = \frac{\bar{\delta}_{\parallel} + \bar{\delta}_{\perp}}{2}$ and the term, $\tilde{\delta}_l\,\Delta\delta_l = \frac{\bar{\delta}_{\parallel} - \bar{\delta}_{\perp}}{2}$, were significantly smaller than *one* in all kinematic bins. Hence, the amplitudes were essentially equal to $\tilde{\delta}_l\,\mathbf{I^s}$ and $\tilde{\delta}_l\,\mathbf{I^c}$. Since the polarization observables were extracted by dividing the amplitude (returned by the fitter) by the average degree of the beam polarization, any error in the determination of the average beam polarization led to the same percentage error in the observable.

As discussed earlier, in case of circular beam polarization, the statistical uncertainty in the electron-beam polarization was 1.5 % and the systematic uncertainty was 3 % [74]. This led to a total uncertainty of 3.4 % in FROST-g9b. The linearly-polarized photon beam had an average uncertainty of 5 % (as the upper limit) *"mostly due to the determination of the baseline and the assumption that the spread in enhancement, and hence polarization, due to beam divergence, crystal thickness etc. could be modelled as one Gaussian"* [1]. Thus, the contribution to the systematic error in the observables can be summarized in the following table:

Table 5.2: Contribution from the beam polarization to the systematic uncertainties for various polarization observables.

Beam-Polarization	Observables	$\lvert\,\Delta$obs./obs.$\,\rvert$ (%)
Circular	$\mathbf{F}$ (for ω)	$< 4\,\%$
Linear	$\mathbf{\Sigma}$, $\mathbf{H}$, $\mathbf{P}$ (for ω); $\mathbf{I}^{s,\,c}$, $\mathbf{P}^{s,\,c}_{x,\,y}$ (for $\pi^+\pi^-$)	$< 5\,\%$

The effect of the uncertainty in the beam polarization on the target-polarization observables will be discussed in Section 5.5 since we used them as normalization factors when combining data sets to "unpolarize" the beam.

5.3 Contribution from the Target Polarization

Following the same argument as discussed in the previous section, it was evident from the equations for the asymmetries that the contribution to the overall systematic uncertainties in the

[1] K. Livingston, private communication, 2 June 2015.

target-polarization observables and the double-polarization observables was equal to the percentage error in the degree of the target polarization. As mentioned in Section 3.7.6, the uncertainty was $\sim$ 1.7 %[2]. The contribution to the systematic uncertainties in the observables is summarized in Table 5.3.

Table 5.3: Contribution from the target polarization to the overall systematic uncertainty for various polarization observables.

Observables	$\lvert \Delta$obs./obs.$\rvert$ (%)
H, **P**, **F**, **T** (for ω)	$< 2\,\%$
$\mathbf{P}_{x,y}$, $\mathbf{P}^{s,c}_{x,y}$ (for $\pi^+\pi^-$)	$< 2\,\%$

The effect of the uncertainty in the degree of target polarization on the beam-polarization observables will be discussed in Section 5.5 since they were used as normalization factors when combining data sets to "unpolarize" the target.

5.4 Contribution from the Target Offset Angle

The uncertainty in the target offset angle of the transversely-polarized target was 0.4° (see Section 3.7.6). To determine the effect of this uncertainty on the polarization observables, the angle was varied by $\pm\sigma$ and the target-polarization observables $P_{x,y}$ were extracted again. This was done at various energies. In each energy bin, the average percentage error in the observable was calculated over all kinematic bins (10 $\cos\theta_{\pi^+}$ bins and 10 ϕ_{π^+} bins) using Equation 5.1. The average percentage errors are listed in the table shown below.

Since the average percentage error should be independent of the energy, we quoted the average of the uncertainties presented in the above table, which is $\sim$ 2.3 %, as the contribution of the offset-angle uncertainty to the overall systematic uncertainties in the observables $\mathbf{P}_{x,y}$. Note that this uncertainty did not affect the beam-polarization observables since we "unpolarized" the target to determine these observables. This did not require any accurate knowledge of the angle.

[2]Natalie Walford used an educated guess of 4-5 % in her Ph. D. dissertation as the upper limit [59].

Table 5.4: Average percentage errors in $\mathbf{P_x}$ and $\mathbf{P_y}$ in various energy bins due to the error in the target offset angle.

Energy Range (MeV)	$\mid \Delta \mathbf{P}_x/\mathbf{P}_x \mid$ (%)	$\mid \Delta \mathbf{P}_y/\mathbf{P}_y \mid$ (%)
700 - 800	2.2	2.5
1100 - 1200	2.7	2.0
1500 - 1600	2.2	2.5
1900 - 2000	2.3	1.8

5.5 Contribution from the Normalization Factors

The necessity of normalization factors has been explained in Section 3.8. These factors were a product of flux ratios and the ratios of the degrees of beam- or target polarization. Hence, the uncertainty in a normalization factor was related to the uncertainties in the ratios:

$$\frac{\sigma_{\text{norm.}}}{\text{norm.}} = \sqrt{\left(\frac{\sigma_{R_1}}{R_1}\right)^2 + \left(\frac{\sigma_{R_2}}{R_2}\right)^2}, \tag{5.3}$$

where R_1 denotes the flux ratio and R_2 denotes the ratio of the degrees of polarization. The ratios were determined from the CH_2 target since the gflux files were not available. In order to assess the systematic uncertainty originating from the flux ratios using the CH_2 target, these ratios were also compared with the ratios obtained from the C target. The flux ratios from both targets were determined by integrating over all reconstructed events and hence, could be affected by the detector acceptance. Therefore, this method was further compared with gflux ratios using FROST-g9a data and with ratios obtained from fitting asymmetries using FROST-g9b data. The full details are given in Appendix D. Our studies showed that the uncertainty associated with the flux normalization factors obtained from CH_2 was less than 2 %.

Circular Beam Polarization The extraction of observables by appropriately normalizing or scaling data sets can sometimes lead to substantial systematic errors if several normalization factors are involved in the analysis [84]. For data sets with a circularly-polarized photon beam, this was not a concern since only one normalization factor was required, i.e. the normalization factor between data with different target settings. Hence, these data sets did not suffer from a huge systematic uncertainty due to normalization. For example, the overall normalization factor to extract the target

Table 5.5: Average percentage uncertainties in $\mathbf{T}$ and $\mathbf{F}$ in various energy bins due to the uncertainty in the normalization factors.

Energy Range (MeV)	$\lvert \Delta \mathbf{T}/\mathbf{T} \rvert$ (%)	$\lvert \Delta \mathbf{F}/\mathbf{F} \rvert$ (%)
1400 - 1500	1.3	0.8
1500 - 1600	1.3	0.9
1700 - 1800	1.3	0.2
2000 - 2100	0.5	0.9
2200 - 2300	1.7	1.0

asymmetry $\mathbf{T}$ in the ω reaction was $\Phi_R = \Phi^+ / \Phi^-$ which had an uncertainty of 2 % at the most. In order to estimate the systematic uncertainty in $\mathbf{T}$ due to the normalization factor, the factor was changed by 2 % and the observable was re-determined. We then estimated the percentage difference between the modified $\mathbf{T}$ and the original $\mathbf{T}$ and found it to be 1.7 % at the most (see Table 5.5). The table also shows the percentage difference observed in the observable $\mathbf{F}$ when the normalization factor was varied by its systematic uncertainty. For this observable, the normalization factor was $(\Phi^+ \Lambda^+) / (\Phi^- \Lambda^-)$. The uncertainty in this factor was 3.5 % from error propagation (Equation 5.3) since both the flux ratio and the target polarization had an uncertainty of 2 %. This finally led to a systematic uncertainty of less than 1 % in $\mathbf{F}$.

Linear Beam Polarization In the FROST-g9b data set with a linearly-polarized beam, three normalization factors were required. We tried to avoid some of the scaling by fitting the normalization but this procedure did not work well for the two-pion reaction since the fit function for an asymmetry between unscaled data sets had too many fit parameters ($\mathbf{I^s}$, $\mathbf{I^c}$, $\mathbf{P_x}$, $\mathbf{P_y}$, $\mathbf{P_x^s}$, $\mathbf{P_x^c}$, $\mathbf{P_y^s}$, $\mathbf{P_y^c}$), which gave the fit too much freedom. We encountered similar problems for the ω reaction when fitting the asymmetries between unscaled data sets. A combination of too many fit parameters and insufficient statistics led to inconclusive results.

Given three normalization factors, our estimates for the systematic uncertainties in the polarization observables for this (linear) data set were higher (compared to the circularly-polarized data set) but they were not substantial. For example, consider the beam-polarization observables, $\mathbf{I}^s$

Table 5.6: Average percentage uncertainties in $\mathbf{I^s}$ and $\mathbf{I^c}$ in various energy bins due to the uncertainty in the normalization factors.

Energy Range (MeV)	$\mid \Delta\, \mathbf{I^s}/\mathbf{I^s} \mid$ (%)	$\mid \Delta\, \mathbf{I^c}/\mathbf{I^c} \mid$ (%)
1100 - 1200	3.2	1.2
1500 - 1600	2.3	2.07
1900 - 2000	5.12	3.8

and $\mathbf{I^c}$. Three normalization factors were required (see Section 4.4.4):

$$N_1 = \left(\frac{\Phi^+_\parallel}{\Phi^-_\parallel}\, \bar{\Lambda}_R \right) \qquad \text{and} \qquad N_2 = \left(\frac{\Phi^+_\perp}{\Phi^-_\perp}\, \bar{\Lambda}_R \right) \tag{5.4}$$

to "unpolarize" the target in the PARA and PERP data sets, respectively, and:

$$\Phi_R = \frac{\Phi^+_\parallel}{\Phi^+_\perp} \tag{5.5}$$

to normalize the PARA and PERP data sets (after "unpolarizing" the target). The uncertainty in the normalization factors N_1 and N_2 was determined to be 7 % (using Equation 5.3) since the uncertainty in the polarization was always less than 5 % (Sections 5.2 and 5.3) and the uncertainty in the flux normalization factor was less than 2 %. The uncertainty in Φ_R was 2 %. Each normalization factor could be changed by $\pm\sigma$ and thus, we performed all possible permutations and re-extracted the observables; this was done at various energies. In each energy bin and for each permutation, the average percentage uncertainty in the observable was calculated over all kinematic bins using Equation 5.1. Table 5.6 shows the highest (over all permutations) average percentage uncertainty in the observable at various energy bins. Based on the values listed in the table, we quoted 5 % and 4 % as the maximum contribution to the overall systematic uncertainties for the polarization observables $\mathbf{I^s}$ and $\mathbf{I^c}$, respectively.

5.6 Contribution from the Accidental Photons

In Section 3.3.1 we explained how initial photons were selected. Even after following the full selection procedure, some accidental photons remained. The fraction could be estimated from a comparison in the yields between the central peak with the neighboring beam buckets in the

Table 5.7: Summary of the contribution from various sources to the systematic uncertainty in the polarization observables. The total systematic uncertainty was calculated by adding the individual contributions in quadrature. Here, "g9b-lin." denotes the g9b experiment which utilized a linearly-polarized photon beam and "g9b-circ." denotes the g9b experiment which utilized a circularly-polarized photon beam.

Systematics	$\lvert\,\Delta$ Obs./Obs.$\,\rvert$ (%)		
	g9b-lin.		g9b-circ.
	$\gamma p \to p\,\pi^+\pi^-$	$\gamma p \to p\,\omega$	$\gamma p \to p\,\omega$
Q-factor method	10	4-5 (threshold E_γ)	4-5 (threshold E_γ)
		7-9 (higher E_γ)	7-9 (higher E_γ)
Beam-polarization	5	5	4
Target-polarization	2	2	2
Target-offset angle	2	2	2
Normalization	5	5	2
Beam-charge asym.	-	-	< 0.2
Accidental photons	Unknown	Unknown	Unknown
σ_{total}	13	9 (threshold E_γ)	7 (threshold E_γ)
		12 (higher E_γ)	11 (higher E_γ)

coincidence-time distribution (for example, see figure 3.1). However, the effect of the accidental photons on the modulations, and hence on the polarization observables, could not be determined.

5.7 Contribution from the Beam-Charge Asymmetry

Section 3.7.5 discussed the beam-charge asymmetry in detail. Since they were small (< 0.003 in FROST-g9a and $< 0.2\,\%$ in FROST-g9b), their effect on the observables was considered negligible.

5.8 Summary

Table 5.7 shows a summary of the contributions from various sources to the overall systematic uncertainty. The numbers represent percentage errors. Not surprisingly, the biggest contributions come from the Q-value method, especially from the background description close to the reaction thresholds. We believe that our *good faith* estimates discussed in this section appear reasonable.

The listed uncertainties are comparable with the corresponding quoted systematic errors of other experiments. For the total systematic uncertainty, we first determined the absolute value of the change in observable (Δ Obs.) due to the Q-value method (discussed in details in Section 5.1). This was done for every observable in each kinematic bin. We then added this number in quadrature to the absolute uncertainties (estimated using the knowledge of the percentage uncertainties) from the other contributing factors.

CHAPTER 6

FINAL RESULTS

6.1 Results for the $\vec{\gamma}\vec{p} \to p\,\omega$ Reaction

The following sections present and discuss our final results for a large variety of single- and double-polarization observables in the reaction $\vec{\gamma}\vec{p} \to p\,\omega \to p\,\pi^+\pi^-\pi^0$.

6.1.1 The Beam-Asymmetry Σ

Figure 6.1 shows our FROST results (red circles) for the full energy range, $E_\gamma \in [1.1, 2.1]$ GeV, which was accessible in this experiment. The reaction threshold is at $E_\gamma \approx 1109$ MeV. The FROST data points above 1.7 GeV are first-time measurements. Also shown in the figure are two sets of published results from the GRAAL collaboration [29, 27]. The GRAAL-2006 data cover the energy range from the reaction threshold up to 1.5 GeV and were extracted from the $\omega \to \pi^+\pi^-\pi^0$ decay mode (shown as magenta triangles in the figure). The GRAAL-2015 data cover the same energy range but represent a statistics-weighted average of results obtained from the $\pi^+\pi^-\pi^0$ and the radiative $\pi^0\gamma$ decay modes. Moreover, the CBELSA/TAPS collaboration published results in 2008 for energies below < 1.5 GeV obtained from the $\omega \to \pi^0\gamma$ decay mode [28] (shown as gray squares in the figure).

The overall agreement of the angular distributions from all experiments ranges from good to fair with some more serious discrepancies in particular $\Theta^{\omega}_{\text{c.m.}}$ bins. For example, the CBELSA/TAPS data points tend to be slightly lower than all other results, in particular in the angle range, $\Theta^{\omega}_{\text{c.m.}} \in [80, 120]^\circ$ of the first two energy bins. The GRAAL collaboration aimed at resolving this issue with additional measurements but the results published in 2015 (blue circles) exhibited even greater inconsistencies, especially between the two GRAAL measurements themselves. The more recent results appear to be significantly smaller in magnitude in the central region around $\Theta^{\omega}_{\text{c.m.}} = 90^\circ$.

The $E_\gamma \in [1.1, 1.5]$ GeV range

In the lower-energy range below 1.5 GeV, our results can be compared with the previously published results. The FROST results are in very good agreement with the GRAAL 2006 and in fair agreement

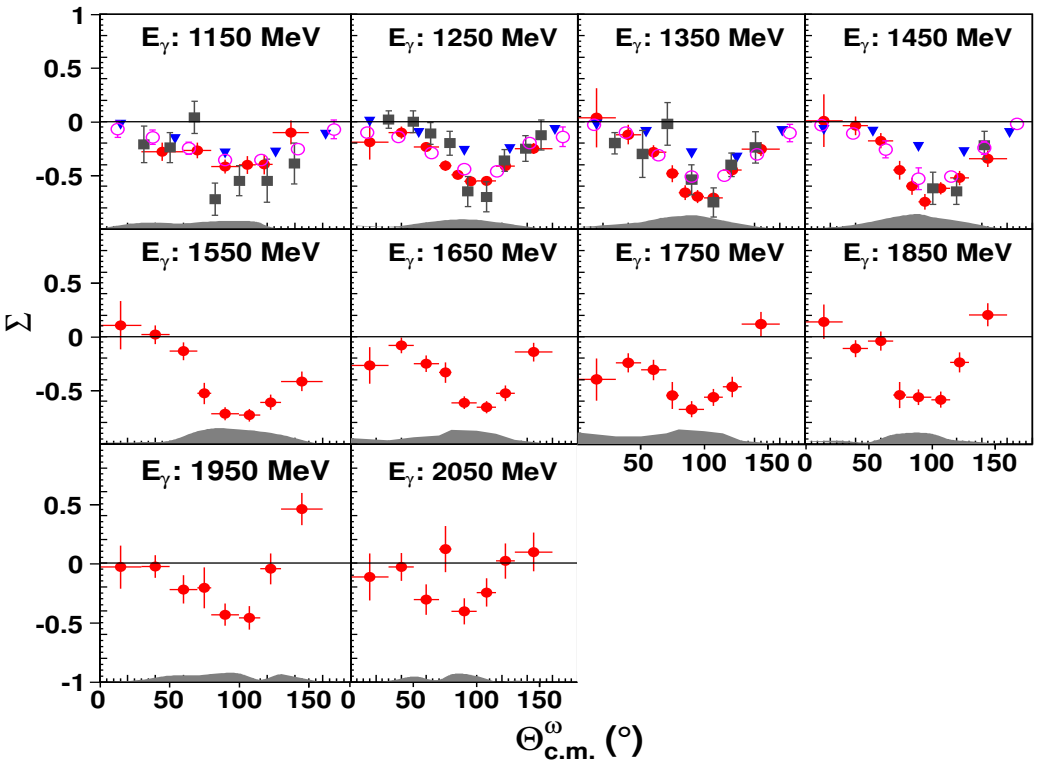

Figure 6.1: Measurement of the beam-asymmetry Σ associated with a linearly-polarized photon beam and an unpolarized target in the reaction $\gamma p \to p\,\omega$. Results are shown for the whole energy range $E_\gamma \in [1.1, 2.1]$ GeV. The FROST results (red circles) are compared with previously published results from the GRAAL collaboration in 2006 using the $\pi^+\pi^-\pi^0$ decay mode [27] (magenta open circles), the CBELSA/TAPS collaboration in 2008 using the radiative decay channel [28] (gray squares) and a weighted average of results from both decay modes determined by the GRAAL collaboration in 2015 [29] (blue inverted triangles). The gray band at the bottom of each panel shows the total systematic uncertainty associated with the FROST observables.

with the GRAAL 2015 results close to the threshold. The CBELSA/TAPS data points suffer from significantly larger statistical errors but the agreement with our FROST results is fair and mostly within errors. All this provides confidence in the FROST results and also resolves the inconsistency between the two GRAAL measurements in favor of the 2006 results.

At this point, the overall disagreement with the GRAAL-2015 results remains unresolved. Although the distribution (of the blue GRAAL points) is smooth, the issue could be either an overall scaling effect (perhaps owing to an incorrectly determined degree of polarization) or a problem with the angular distribution around $\Theta^{\omega}_{c.m.} = 90°$ (perhaps due to poorly understood detector acceptance

or trigger effects).

The $E_\gamma \in [1.5, 2.1]$ GeV range

We present high-quality results for $\mathbf{\Sigma}$ in the energy range 1.5 - 1.7 GeV with a total of 15 data points at various $\Theta^{\omega}_{c.m.}$ bins, which is about three times more than the number of data points from the only other published measurement by the CBELSA/TAPS [28] for this energy range (not shown in the Figure). The results in the energy range 1.7 - 2.1 GeV are first-time measurements. In every energy bin, we see that the beam asymmetry acquires large values, which is only possible if s- and/or u-channel contribution are involved in the production at these energies.

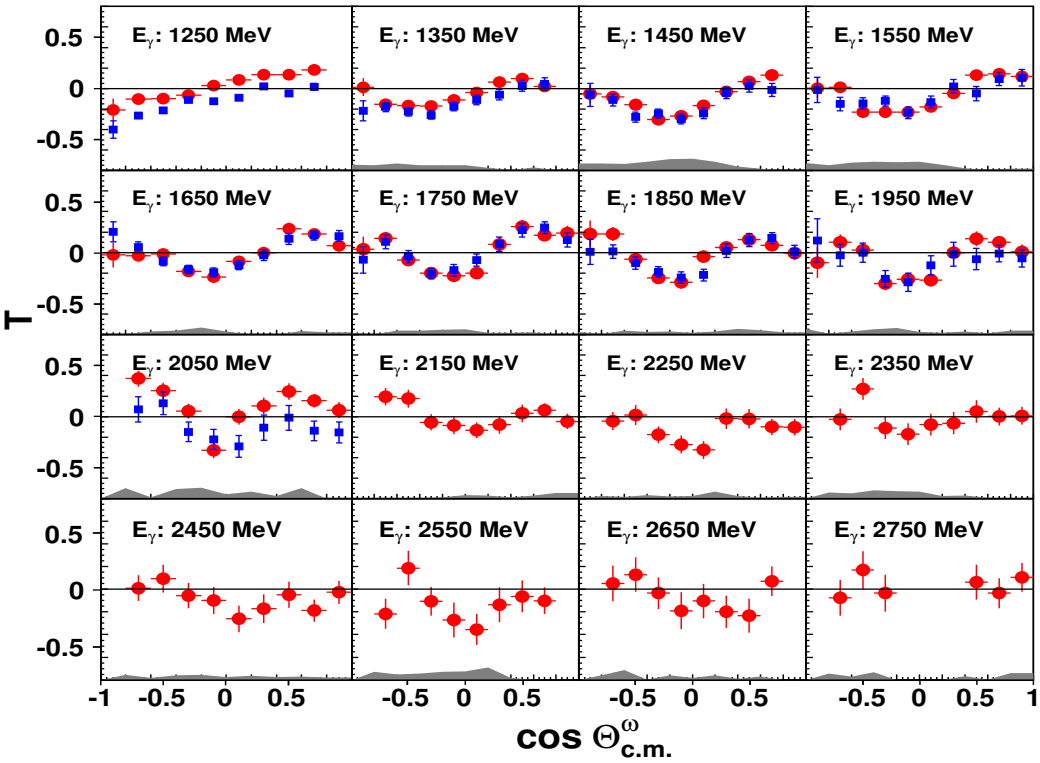

Figure 6.2: First-time measurement of the target-asymmetry $\mathbf{T}$ for the reaction $\gamma p \to p\,\omega$. Results are shown for the energy range $E_\gamma \in [1.2, 2.1]$ GeV from the data that utilized a linearly-polarized photon beam (blue squares) and for the energy range $E_\gamma \in [1.2, 2.8]$ GeV from the data that utilized a circularly-polarized photon beam (red circles). The gray band at the bottom of each panel shows the total systematic uncertainty associated with the observables shown in red circles.

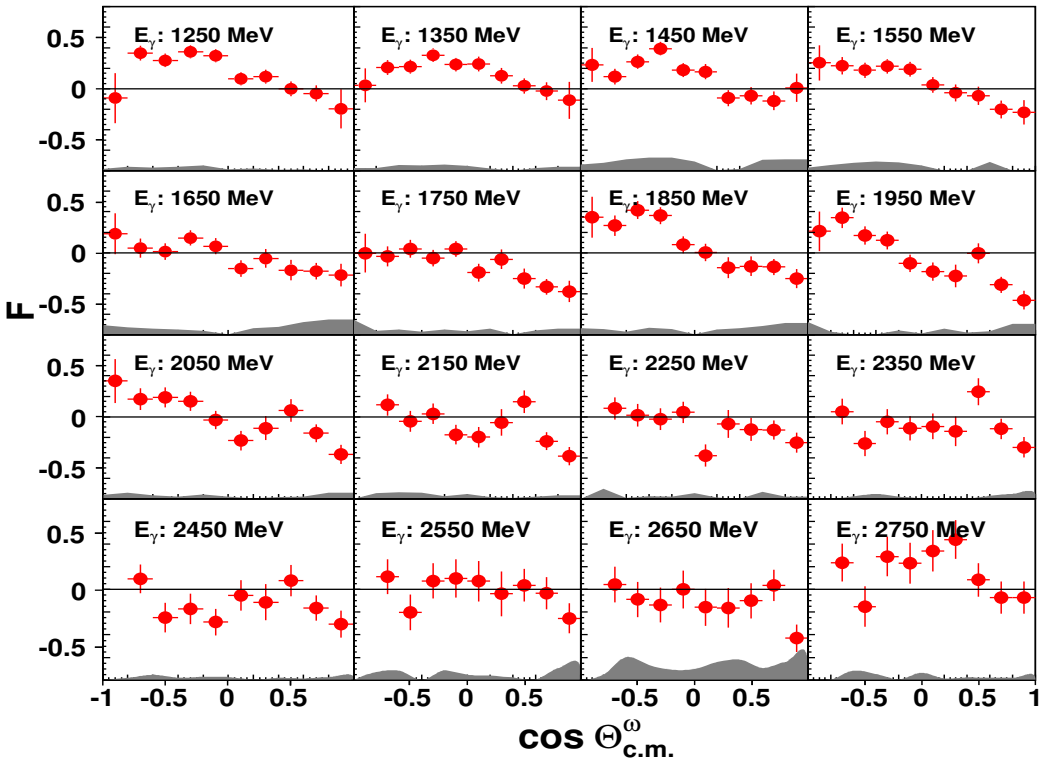

Figure 6.3: First-time measurement of the double-polarization observable **F** in the reaction $\gamma p \to p\omega$ utilizing a circularly-polarized photon beam and a transversely-polarized target. Results are shown for the whole photon energy range $E_\gamma \in [1.2, 2.8]$ GeV. The gray band at the bottom of each panel shows the total systematic uncertainty associated with the FROST observables.

6.1.2 The Target-Asymmetry T

Figure 6.2 shows the first-time measurement of the target-asymmetry **T** associated with a transversely-polarized target for the energy range $E_\gamma \in [1.2, 2.1]$ GeV from the FROST-g9b data set that utilized a linearly-polarized photon beam and for the energy range $E_\gamma \in [1.2, 2.8]$ GeV from the FROST-g9b data set that utilized a circularly-polarized photon beam. The data are given in 100 MeV wide energy bins. The available statistics was sufficient for 10 data points in $\cos\Theta^{\omega}_{\text{c.m.}}$. The two experimental results are in good agreement at all energies, thereby providing a reliability check of the new results.

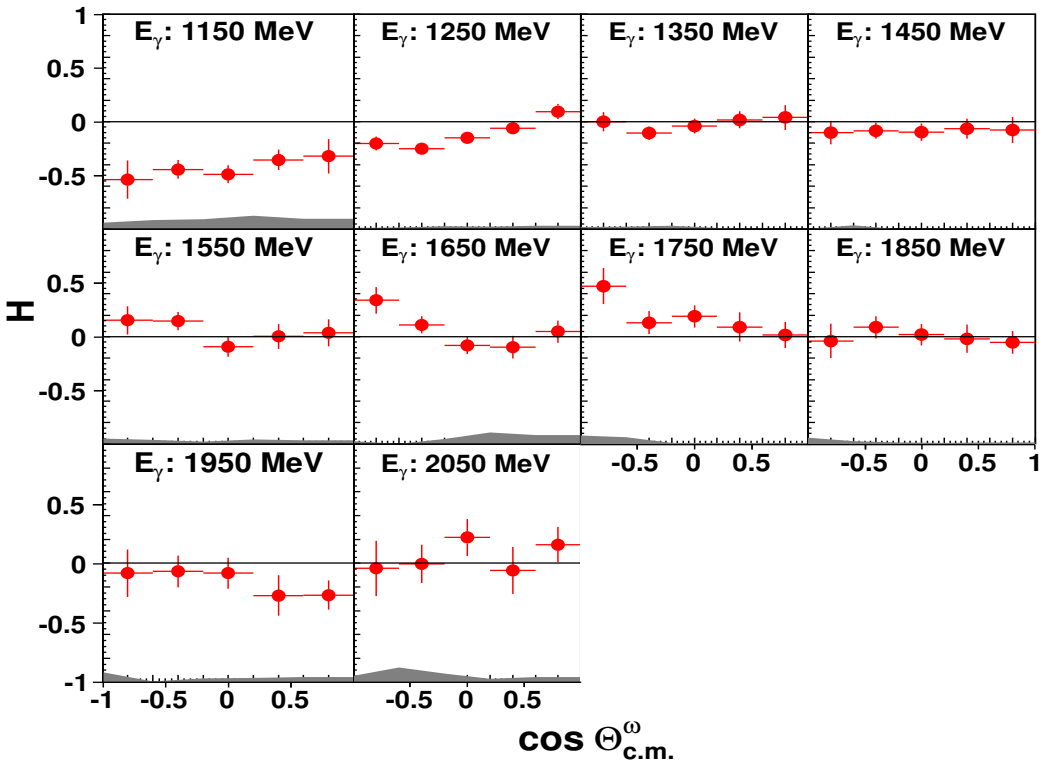

Figure 6.4: First-time measurement of the double-polarization observable **H** in the reaction $\gamma p \to p\omega$ utilizing a linearly-polarized photon beam and a transversely-polarized target. Results are shown for the whole photon energy range $E_\gamma \in [1.1, 2.1]$ GeV. The gray band at the bottom of each panel shows the total systematic uncertainty associated with the FROST observables.

6.1.3 The Double-Polarization Observable F

Figure 6.3 shows the first-time measurement of the double-polarization observable **F** associated with a transversely-polarized target and a circularly-polarized beam for the whole available energy range $E_\gamma \in [1.2, 2.8]$ GeV. The data are given in 100 MeV wide energy bins. The available statistics was sufficient for 10 data points in $\cos\Theta^{\omega}_{\text{c.m.}}$.

6.1.4 The Double-Polarization Observable H

Figure 6.4 shows the first-time measurement of the double-polarization observable **H** associated with a transversely-polarized target and a linearly-polarized beam for the whole available energy

range $E_\gamma \in [1.1, 2.1]$ GeV. The data are given in 100 MeV wide energy bins. The available statistics was sufficient for five data points in $\cos\Theta^{\omega}_{\text{c.m.}}$.

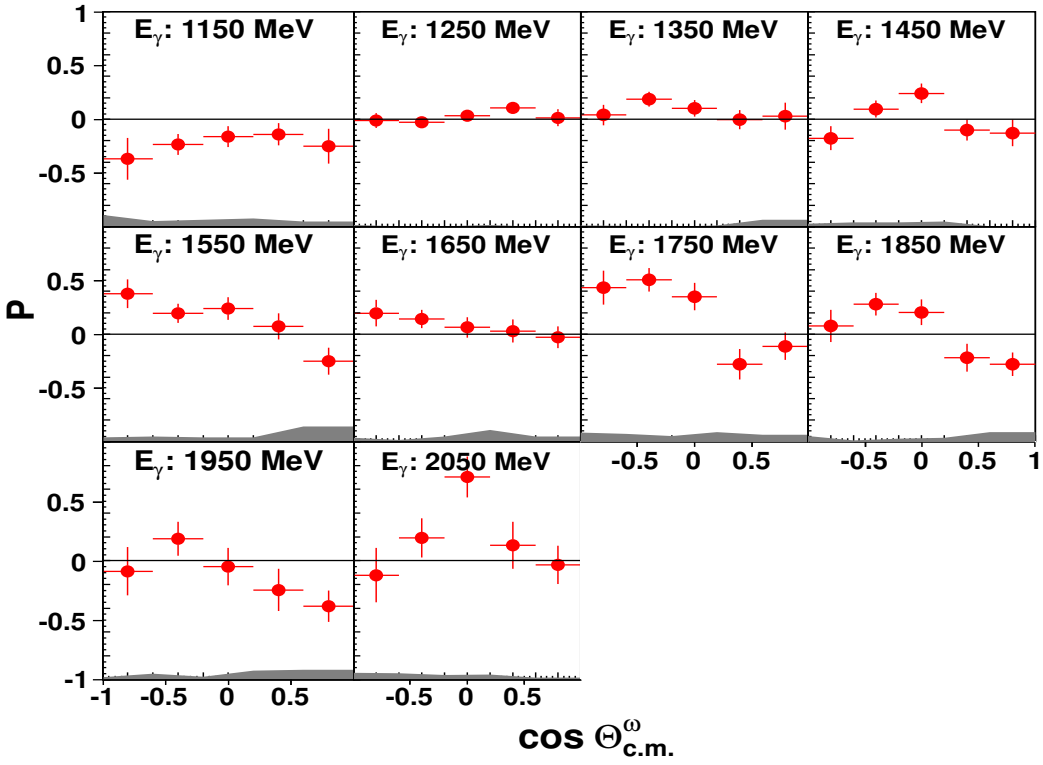

Figure 6.5: First-time measurement of the recoil-polarization observable **P** in the reaction $\gamma p \to p\,\omega$ utilizing a linearly-polarized photon beam and a transversely-polarized target. Results are shown for the whole photon energy range $E_\gamma \in [1.1, 2.1]$ GeV. The gray band at the bottom of each panel shows the total systematic uncertainty associated with the FROST observables.

6.1.5 The Double-Polarization Observable P

Figure 6.5 shows the first-time measurement of the recoil-polarization observable **P** associated with a transversely-polarized target and a linearly-polarized beam for the whole available energy range $E_\gamma \in [1.1, 2.1]$ GeV. The data are given in 100 MeV wide energy bins. The available statistics was sufficient for five data points in $\cos\Theta^{\omega}_{\text{c.m.}}$.

6.2 Results for the $\vec{\gamma}\vec{p} \to p\,\pi^+\,\pi^-$ Reaction

In the following sections, final results from this analysis for a large variety of single- and double-polarization observables in the reaction $\vec{\gamma}\vec{p} \to p\,\pi^+\pi^-$ will be discussed.

6.2.1 The Beam-Asymmetries $\mathbf{I^s}$ and $\mathbf{I^c}$

Figures 6.6-6.19 show our results on $\mathbf{I^s}$ and Figures 6.20-6.33 show our results on $\mathbf{I^c}$, all based on weighted averages over topologies 1, 2 and 4. Each figure shows results for a 100 MeV wide photon energy bin, with the full set of figures covering the entire energy range of 0.7 GeV to 2.1 GeV spanned by the FROST experiment. In each energy bin, the observable is plotted for 10 $\cos\theta_{\pi^+}$ bins and 10 ϕ_{π^+} bins, however the data are not binned in $\cos\Theta_{\text{c.m.}}$ and the mass variable due to limited statistics. As a reminder, note that this is one of the many ways available for presenting the final observables. We chose ϕ_{π^+} as the x-axis since it allowed us to check whether the parity of the observable with respect to this variable is consistent with theoretical predictions. Based on parity conservation, $\mathbf{I^s}$ ($\mathbf{I^c}$) is predicted to have odd (even) parity with respect to ϕ_{π^+}. The figures show that the third-order Fourier sine (cosine) fits to $\mathbf{I^s}$ ($\mathbf{I^c}$) describe the data well, thus confirming that our results are consistent with theory.

No published results are currently available for these beam asymmetries. However, CLAS collaboration-approved results from the g8 experiment at Jefferson Lab are in preparation for publication. Our results are compared with results from g8, which are also shown as weighted averages over topologies 1, 2 and 4, in the photon energy range $E_\gamma \in [1.1, 2.1]$ GeV. The two experimental results are observed to be in very good agreement, barring a few kinematic regions where the discrepancy can be attributed to the method of averaging over the three topologies. In those regions, the g8 observable is averaged over all three topologies whereas in case of FROST, some topologies did not have enough statistics to measure the observable, resulting in averaging over less than three topologies. It should be noted here that the g8 experiment had a much simpler target, a liquid hydrogen target, than the FROST-g9b experiment. Therefore, the overall agreement between the two experiments provides support for our analysis, in particular the background subtraction technique.

6.2.2 The Target-Asymmetries $\mathbf{P_x}$ and $\mathbf{P_y}$

Figures 6.34-6.47 show first-time measurement of $\mathbf{P_x}$ and Figures 6.48-6.61 show first-time measurement of $\mathbf{P_y}$, all based on weighted averages over topologies 1, 2 and 4. Similar to the beam-asymmetries, each figure shows results for a 100 MeV wide photon energy bin, with the full set of figures covering the entire energy range of 0.7 GeV to 2.1 GeV spanned by the FROST experiment. In each energy bin, the observable is plotted for 10 $\cos\theta_{\pi^+}$ bins and 10 ϕ_{π^+} bins, while the data are integrated over $\cos\Theta_{\text{c.m.}}$ and the mass variable due to limited statistics. Again, note that this is one of the many ways available for presenting the final observables. Based on parity conservation, $\mathbf{P_x}$ ($\mathbf{P_y}$) is predicted to have odd (even) parity with respect to ϕ_{π^+}. The figures show that the second-order Fourier sine (cosine) fits to $\mathbf{P_x}$ ($\mathbf{P_y}$) describe the data well within errors, thus confirming that our results are consistent with theory. The target-asymmetries are observed to be fairly smaller than the beam-asymmetries. However, a significant variation in the shape of these observables is observed as we go from one energy bin to the next, and even from one $\cos\theta_{\pi^+}$ bin to the next within the same energy bin.

6.2.3 The Double-Polarization Observables $\mathbf{P}^{\mathbf{s,\,c}}_{\mathbf{x,\,y}}$

Figures 6.62-6.69 show results for all four observables, all of which are first-time measurements. These results are based on weighted averages over topologies 1, 2 and 4. Due to limited statistics, the data are plotted for only 2 $\cos\theta_{\pi^+}$ bins, covering a range of $[-1,\,0]$ and $[0,\,1]$, respectively. Each figure shows results for a $\cos\theta_{\pi^+}$ bin, which is specified in the figure caption. The figure is further divided into 14 sub-figures which correspond to 100 MeV wide photon energy bins, with the full set of sub-figures covering the entire energy range of 0.7 GeV to 2.1 GeV spanned by the FROST experiment. Within each sub-figure, the results are plotted for 10 ϕ_{π^+} bins. The data are integrated over the remaining two kinematic variables for this reaction. Again, note that this is one of the many ways available for presenting the final observables. Based on parity conservation, $\mathbf{P^s_x}$ and $\mathbf{P^c_y}$ are predicted to have even parity with respect to ϕ_{π^+}, while $\mathbf{P^s_y}$ and $\mathbf{P^c_x}$ are predicted to have odd parity with respect to ϕ_{π^+}. The figures show that the parity of our results are consistent with theory. The double-polarization observables are observed to be small in magnitude (about 0.3 or less) at all energies, with an overall tendency to become even smaller as we go to higher energies.

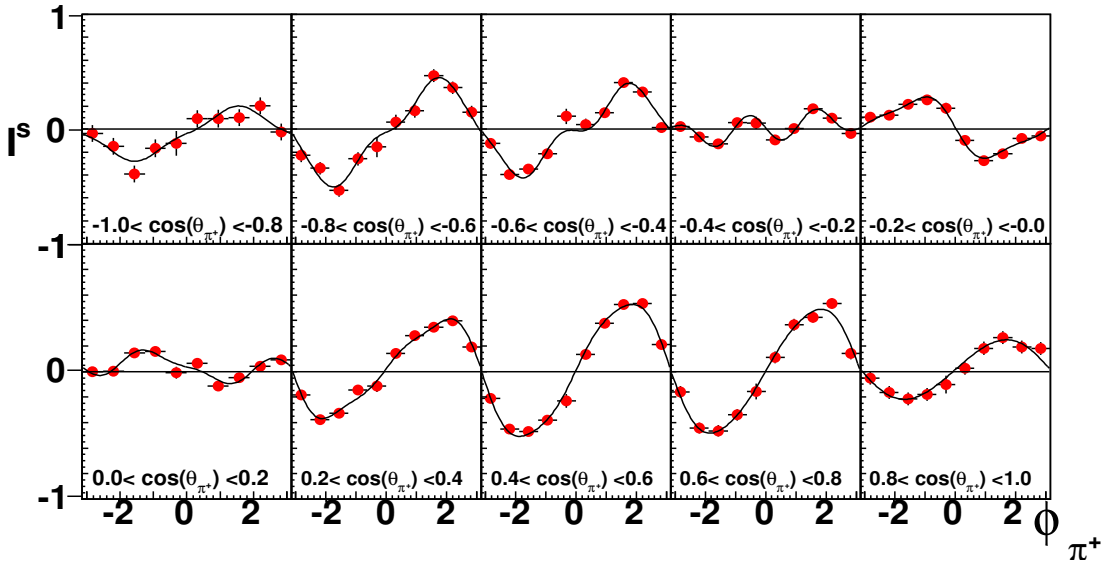

Figure 6.6: A 3-D plot showing first-time measurement of the observable $\mathbf{I^s}$ in the energy bin $E_\gamma \in [0.7, 0.8]$ GeV. The error bars show the statistical uncertainties of the observables. The solid curves are third-order Fourier sine fits to the $\mathbf{I^s}$ results. See text for further discussion.

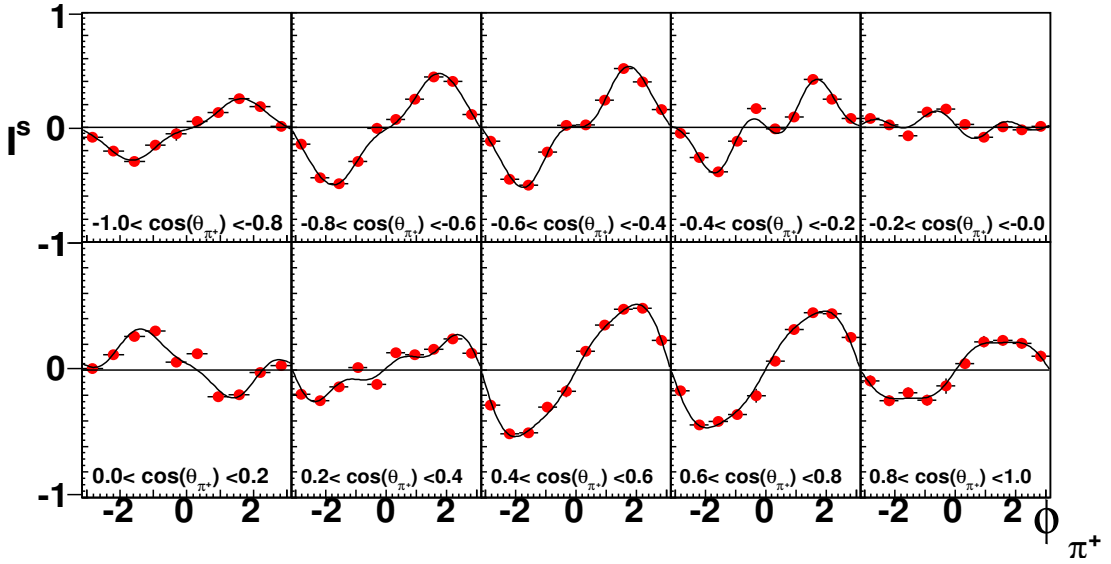

Figure 6.7: A 3-D plot showing first-time measurement of the observable $\mathbf{I^s}$ in the energy bin $E_\gamma \in [0.8, 0.9]$ GeV. The error bars show the statistical uncertainties of the observables. The solid curves are third-order Fourier sine fits to the $\mathbf{I^s}$ results. See text for further discussion.

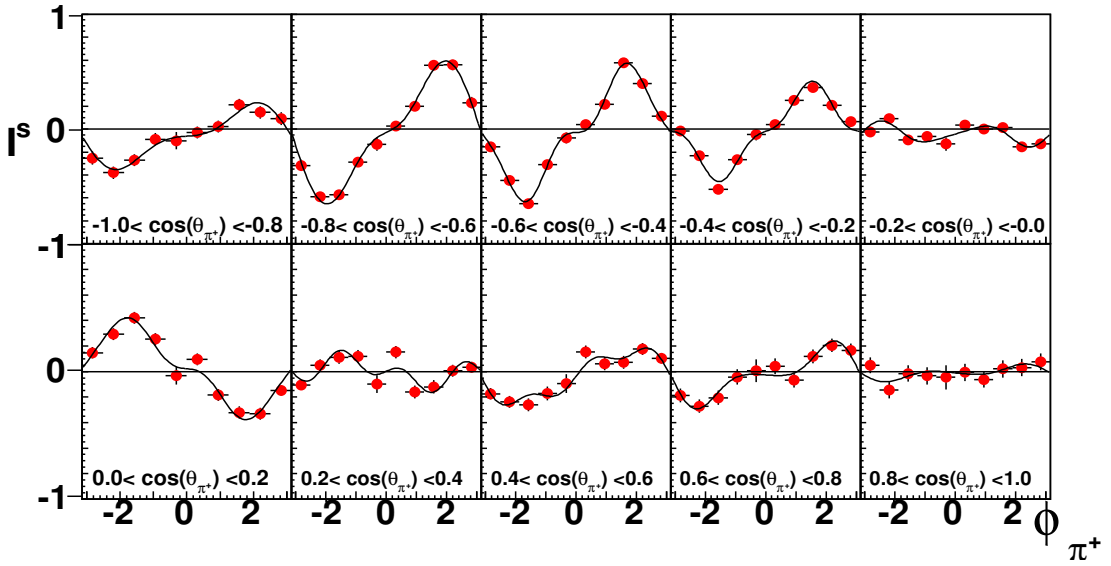

Figure 6.8: A 3-D plot showing first-time measurement of the observable $\mathbf{I^s}$ in the energy bin $E_\gamma \in [0.9, 1.0]$ GeV. The error bars show the statistical uncertainties of the observables. The solid curves are third-order Fourier sine fits to the $\mathbf{I^s}$ results. See text for further discussion.

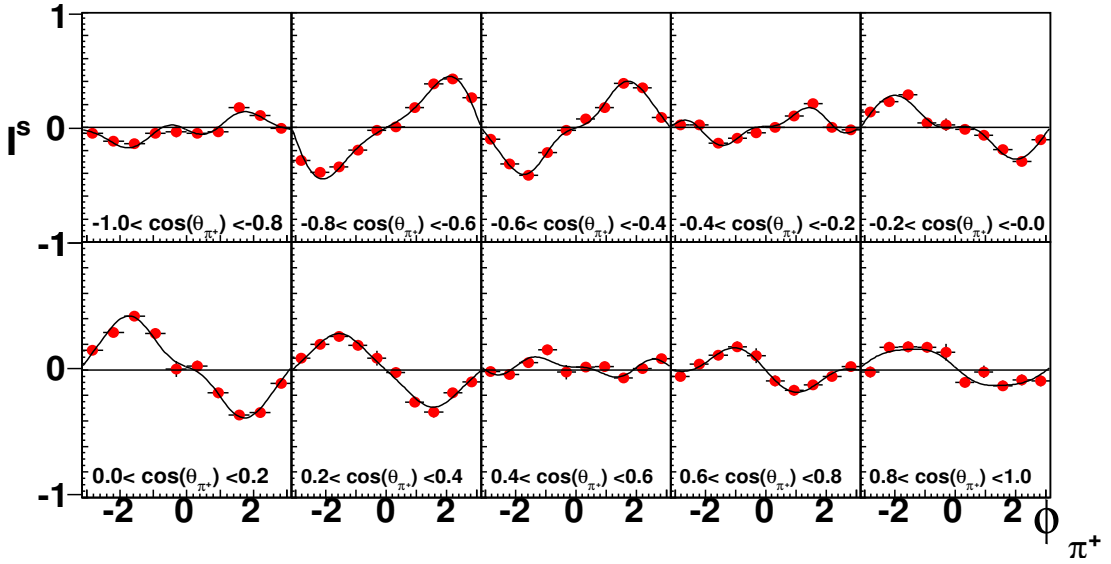

Figure 6.9: A 3-D plot showing first-time measurement of the observable $\mathbf{I^s}$ in the energy bin $E_\gamma \in [1.0, 1.1]$ GeV. The error bars show the statistical uncertainties of the observables. The solid curves are third-order Fourier sine fits to the $\mathbf{I^s}$ results. See text for further discussion.

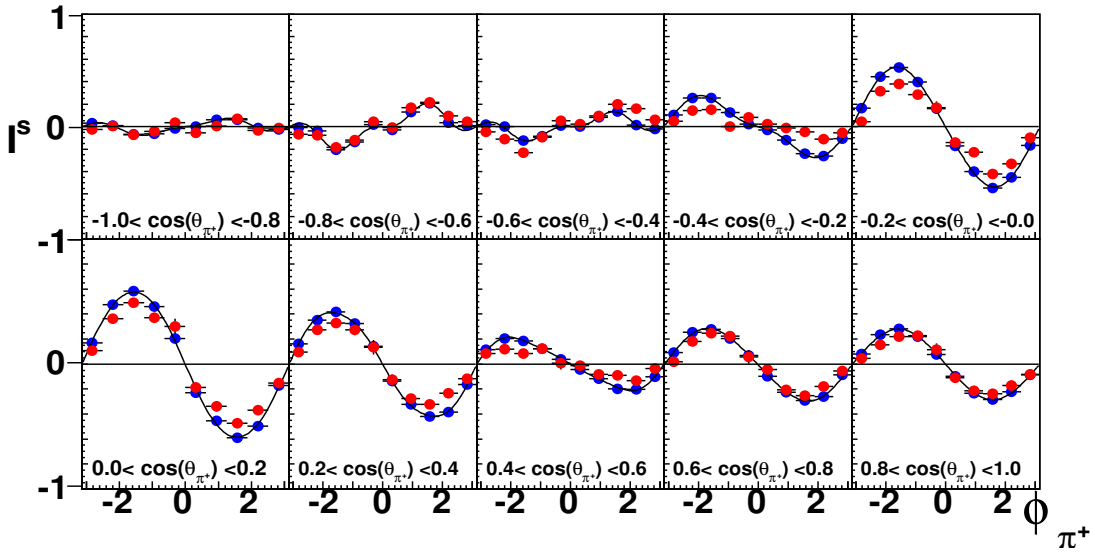

Figure 6.10: A 3-D plot of the observable $\mathbf{I^s}$ from FROST (shown in red) and Clas-g8 (shown in blue) in the energy bin $E_\gamma \in [1.1, 1.2]$ GeV. The error bars show the statistical uncertainties of the observables. The solid curves are third-order Fourier sine fits to the Clas-g8 results. See text for further discussion.

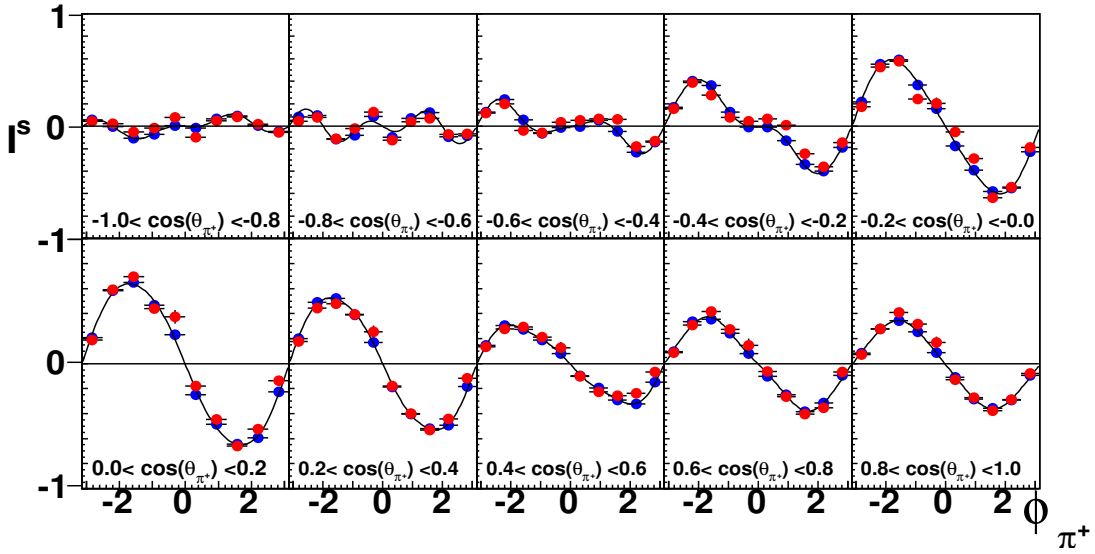

Figure 6.11: A 3-D plot of the observable $\mathbf{I^s}$ $\mathbf{I^s}$ from FROST (shown in red) and Clas-g8 (shown in blue) in the energy bin $E_\gamma \in [1.2, 1.3]$ GeV. The error bars show the statistical uncertainties of the observables. The solid curves are third-order Fourier sine fits to the Clas-g8 results. See text for further discussion.

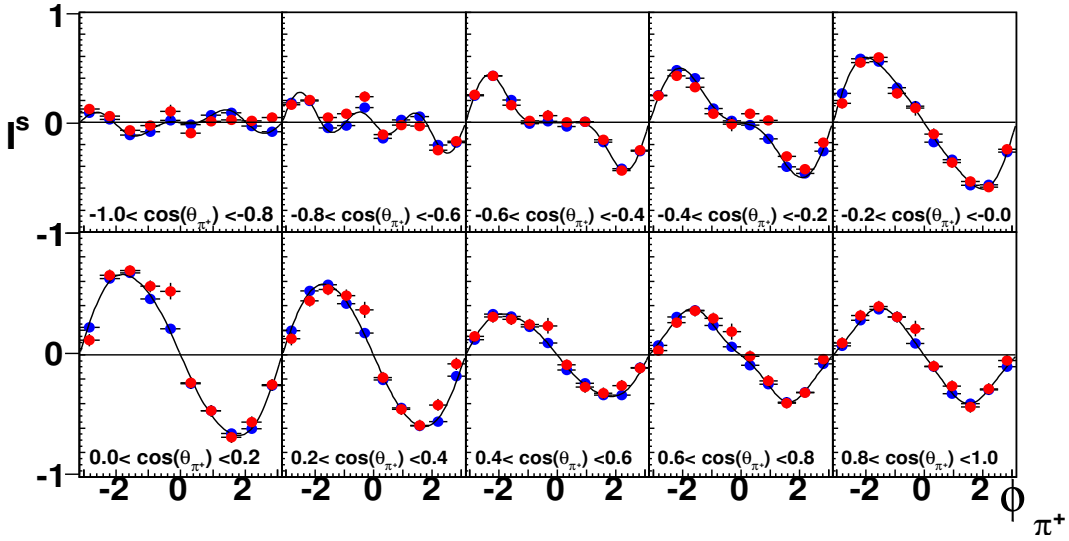

Figure 6.12: A 3-D plot of the observable $\mathbf{I^s}$ from FROST (shown in red) and Clas-g8 (shown in blue) in the energy bin $E_\gamma \in [1.3, 1.4]$ GeV. The error bars show the statistical uncertainties of the observables. The solid curves are third-order Fourier sine fits to the Clas-g8 results. See text for further discussion.

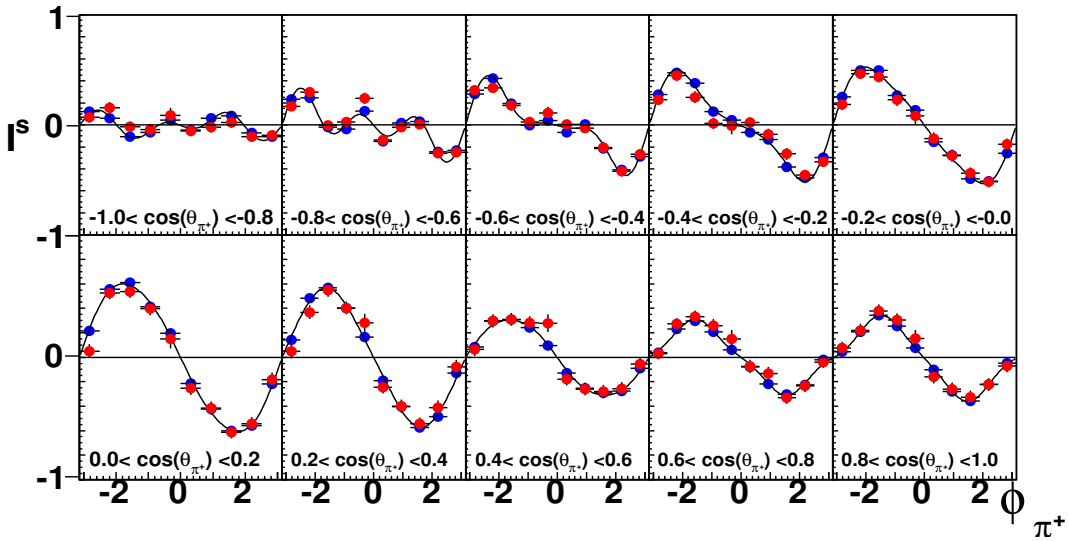

Figure 6.13: A 3-D plot of the observable $\mathbf{I^s}$ from FROST (shown in red) and Clas-g8 (shown in blue) in the energy bin $E_\gamma \in [1.4, 1.5]$ GeV. The error bars show the statistical uncertainties of the observables. The solid curves are third-order Fourier sine fits to the Clas-g8 results. See text for further discussion.

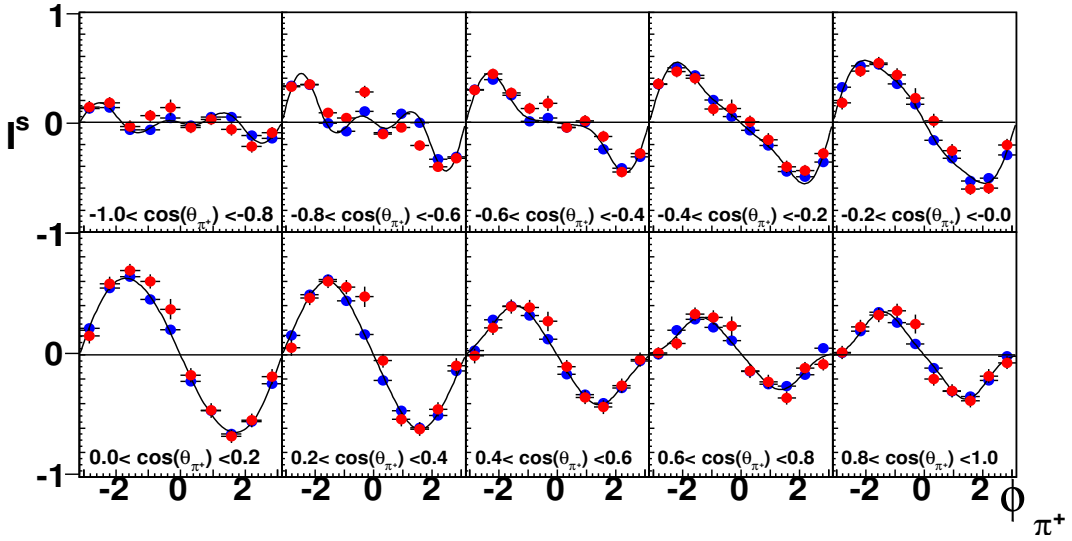

Figure 6.14: A 3-D plot of the observable $\mathbf{I^s}$ from FROST (shown in red) and Clas-g8 (shown in blue) in the energy bin $E_\gamma \in [1.5, 1.6]$ GeV. The error bars show the statistical uncertainties of the observables. The solid curves are third-order Fourier sine fits to the Clas-g8 results. See text for further discussion.

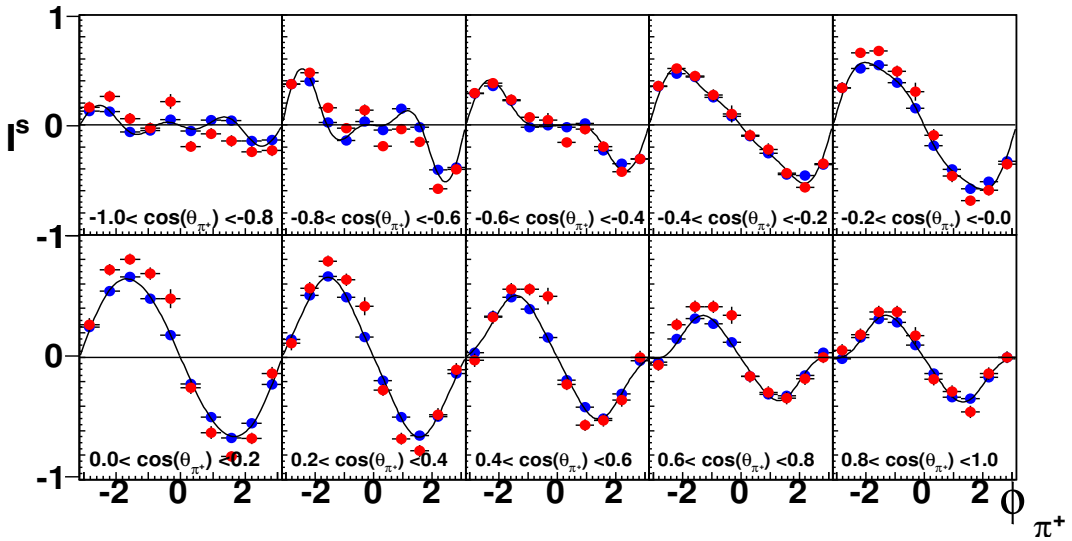

Figure 6.15: A 3-D plot of the observable $\mathbf{I^s}$ from FROST (shown in red) and Clas-g8 (shown in blue) in the energy bin $E_\gamma \in [1.6, 1.7]$ GeV. The error bars show the statistical uncertainties of the observables. The solid curves are third-order Fourier sine fits to the Clas-g8 results. See text for further discussion.

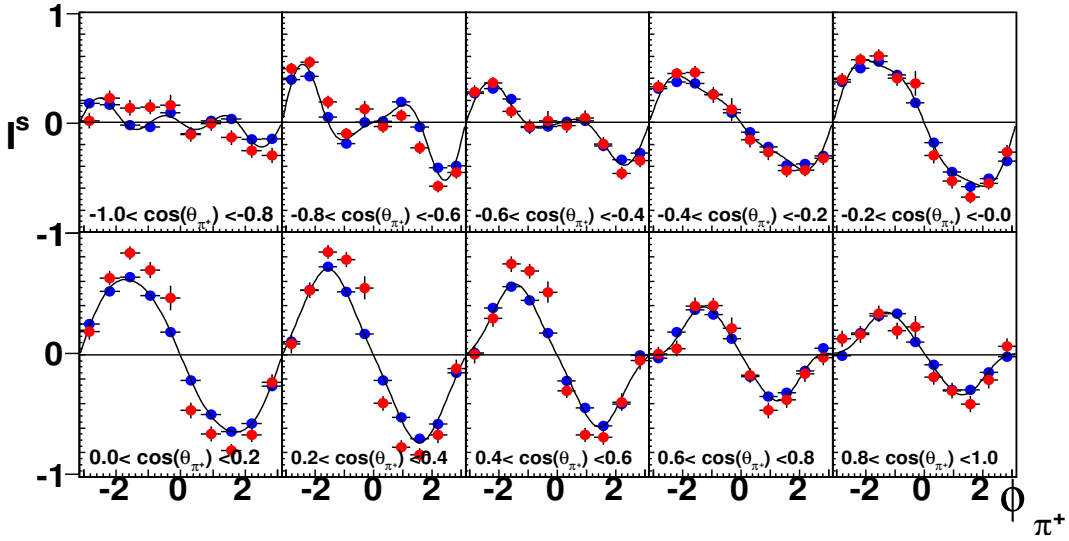

Figure 6.16: A 3-D plot of the observable $\mathbf{I^s}$ from FROST (shown in red) and Clas-g8 (shown in blue) in the energy bin $E_\gamma \in [1.7, 1.8]$ GeV. The error bars show the statistical uncertainties of the observables. The solid curves are third-order Fourier sine fits to the Clas-g8 results. See text for further discussion.

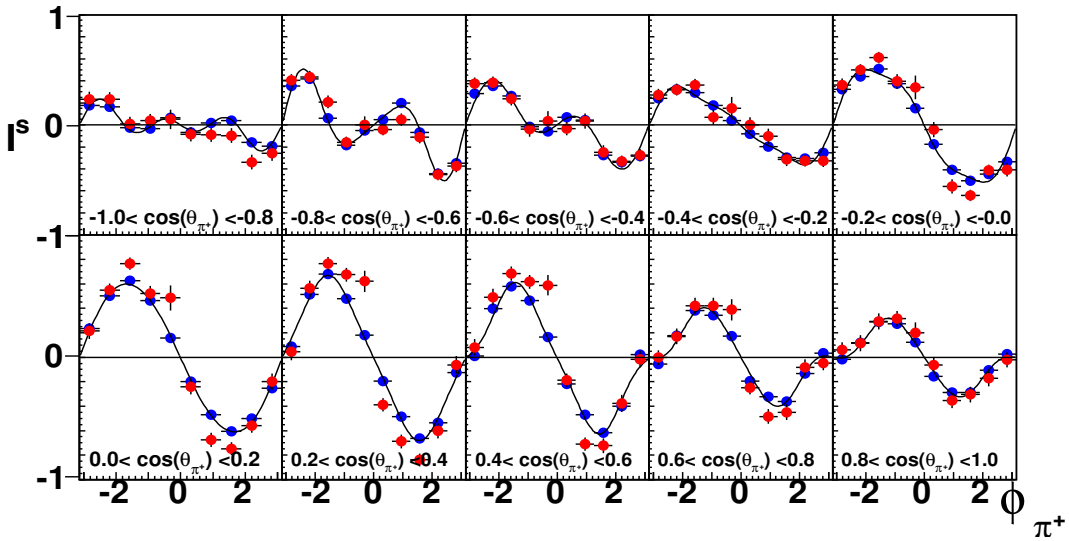

Figure 6.17: A 3-D plot of the observable $\mathbf{I^s}$ from FROST (shown in red) and Clas-g8 (shown in blue) in the energy bin $E_\gamma \in [1.8, 1.9]$ GeV. The error bars show the statistical uncertainties of the observables. The solid curves are third-order Fourier sine fits to the Clas-g8 results. See text for further discussion.

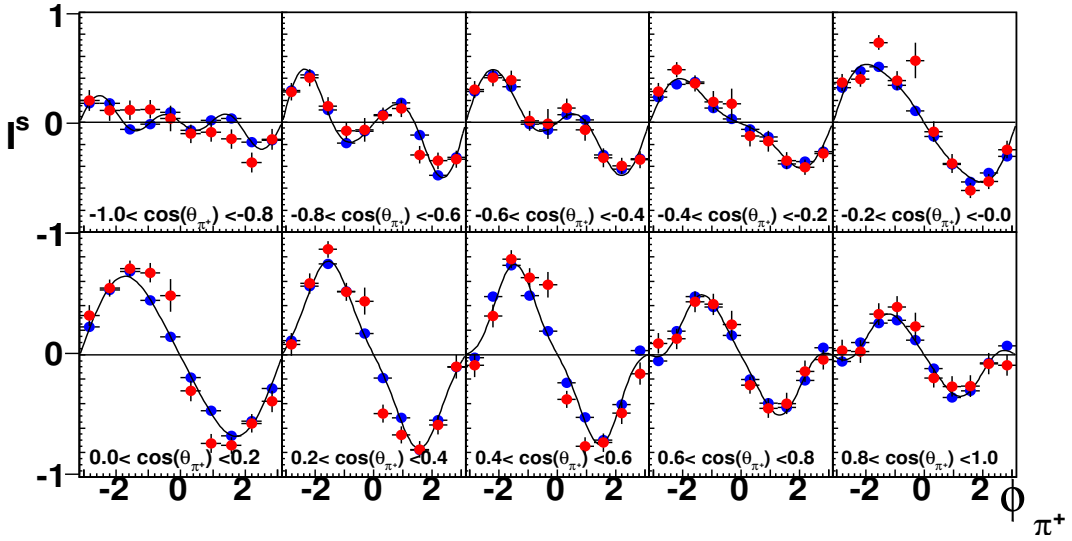

Figure 6.18: A 3-D plot of the observable $\mathbf{I^s}$ from FROST (shown in red) and Clas-g8 (shown in blue) in the energy bin $E_\gamma \in [1.9, 2.0]$ GeV. The error bars show the statistical uncertainties of the observables. The solid curves are third-order Fourier sine fits to the Clas-g8 results. See text for further discussion.

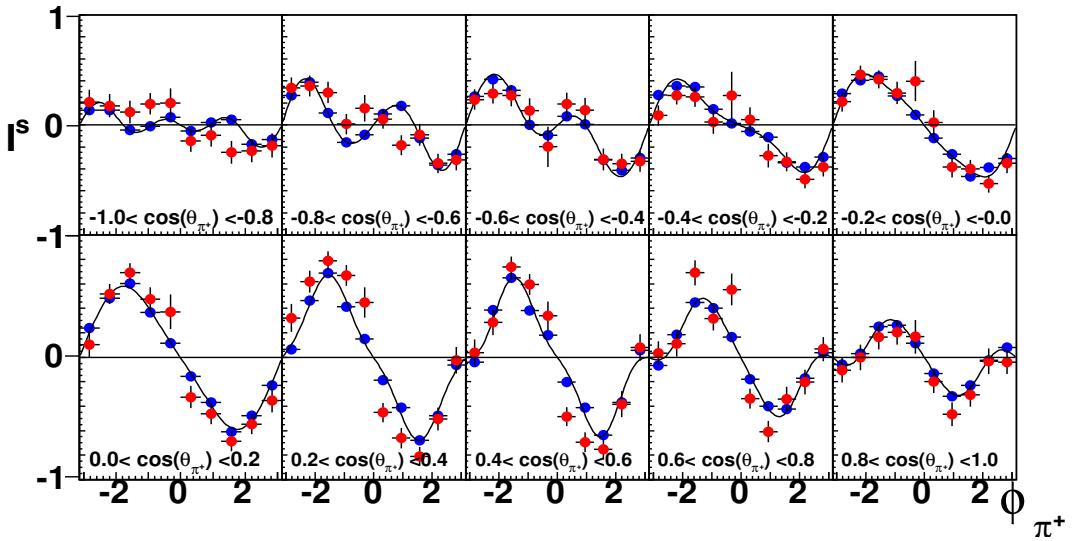

Figure 6.19: A 3-D plot of the observable $\mathbf{I^s}$ from FROST (shown in red) and clas-g8 (shown in blue) in the energy bin $E_\gamma \in [2.0, 2.1]$ GeV. The error bars show the statistical uncertainties of the observables. The solid curves are third-order Fourier sine fits to the clas-g8 results. See text for further discussion.

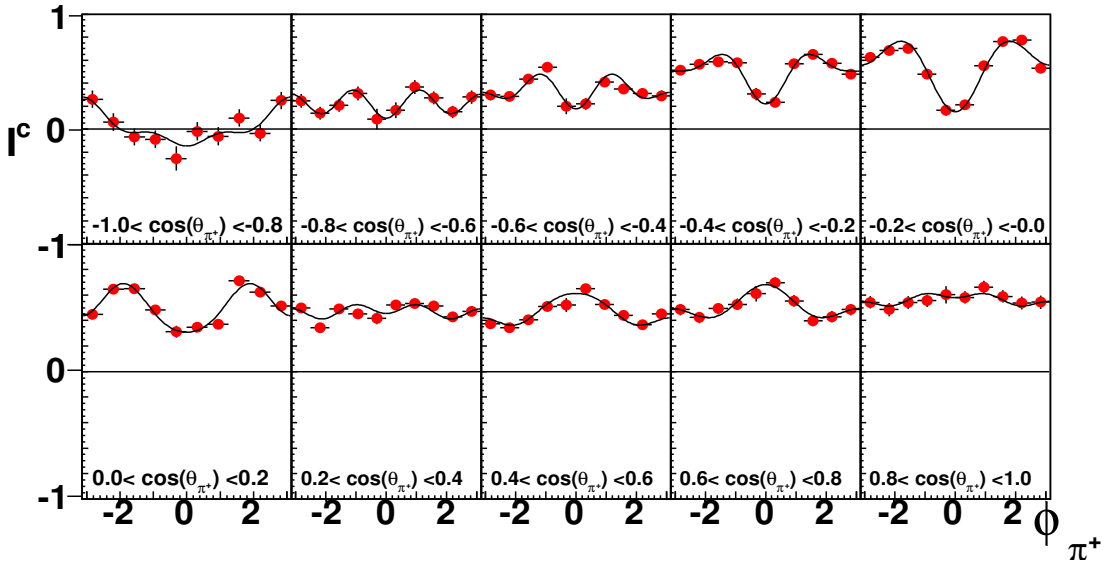

Figure 6.20: A 3-D plot showing first-time measurement of the observable $\mathbf{I^c}$ in the energy bin $E_\gamma \in [0.7, 0.8]$ GeV. The error bars show the statistical uncertainties of the observables. The solid curves are third-order Fourier cosine fits to the $\mathbf{I^c}$ results. See text for further discussion.

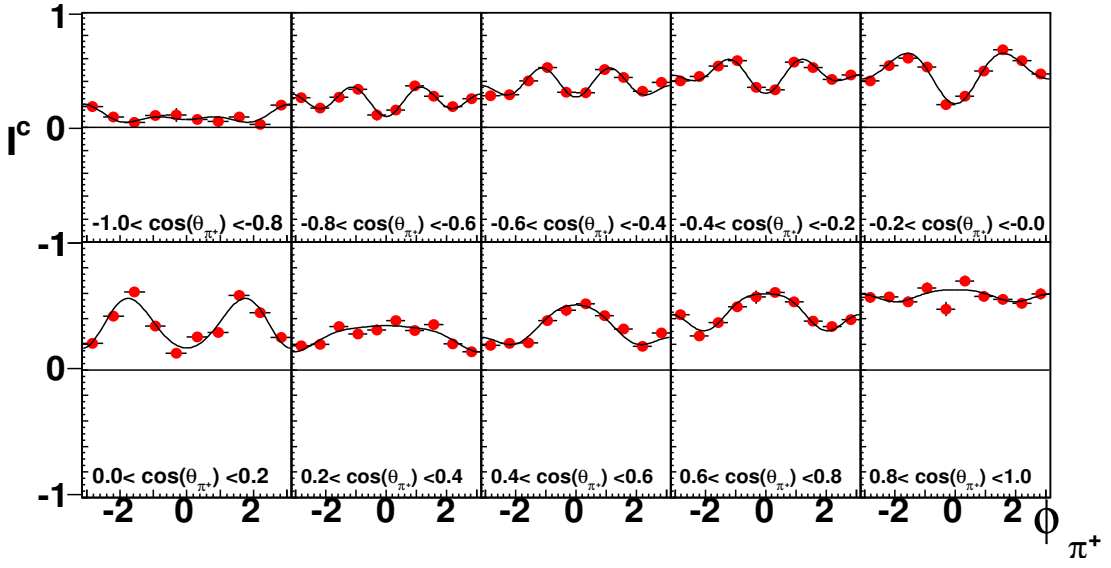

Figure 6.21: A 3-D plot showing first-time measurement of the observable $\mathbf{I^c}$ in the energy bin $E_\gamma \in [0.8, 0.9]$ GeV. The error bars show the statistical uncertainties of the observables. The solid curves are third-order Fourier cosine fits to the $\mathbf{I^c}$ results. See text for further discussion.

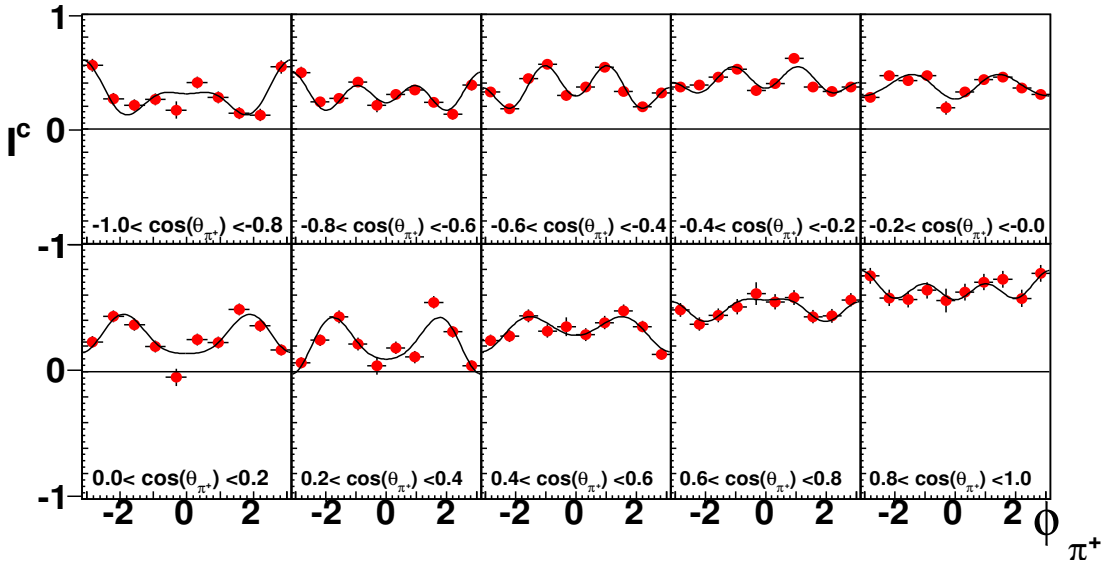

Figure 6.22: A 3-D plot showing first-time measurement of the observable $\mathbf{I^c}$ in the energy bin $E_\gamma \in [0.9, 1.0]$ GeV. The error bars show the statistical uncertainties of the observables. The solid curves are third-order Fourier cosine fits to the $\mathbf{I^c}$ results. See text for further discussion.

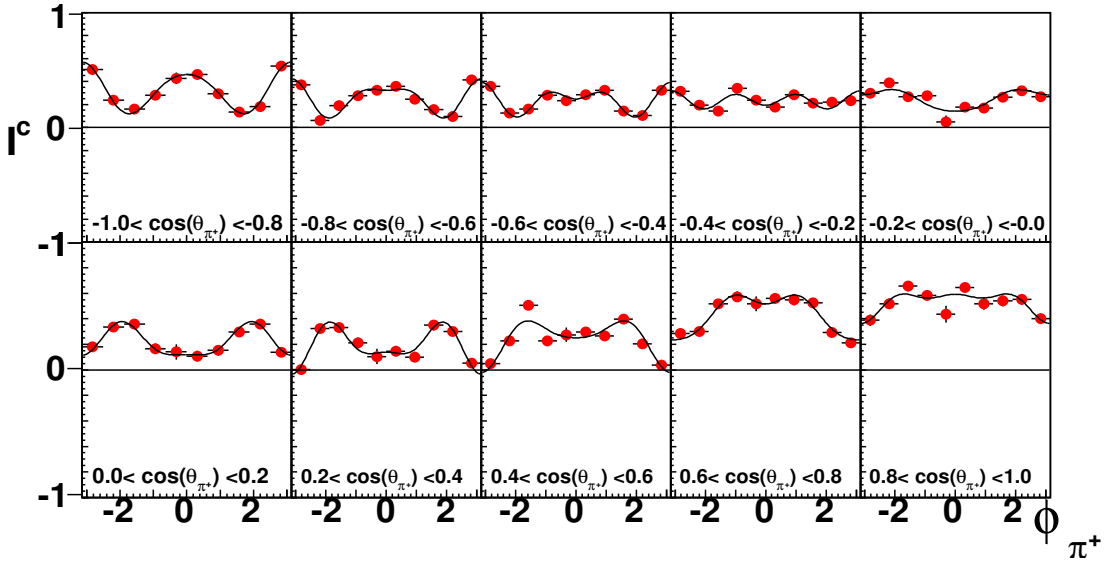

Figure 6.23: A 3-D plot showing first-time measurement of the observable $\mathbf{I^c}$ in the energy bin $E_\gamma \in [1.0, 1.1]$ GeV. The error bars show the statistical uncertainties of the observables. The solid curves are third-order Fourier cosine fits to the $\mathbf{I^c}$ results. See text for further discussion.

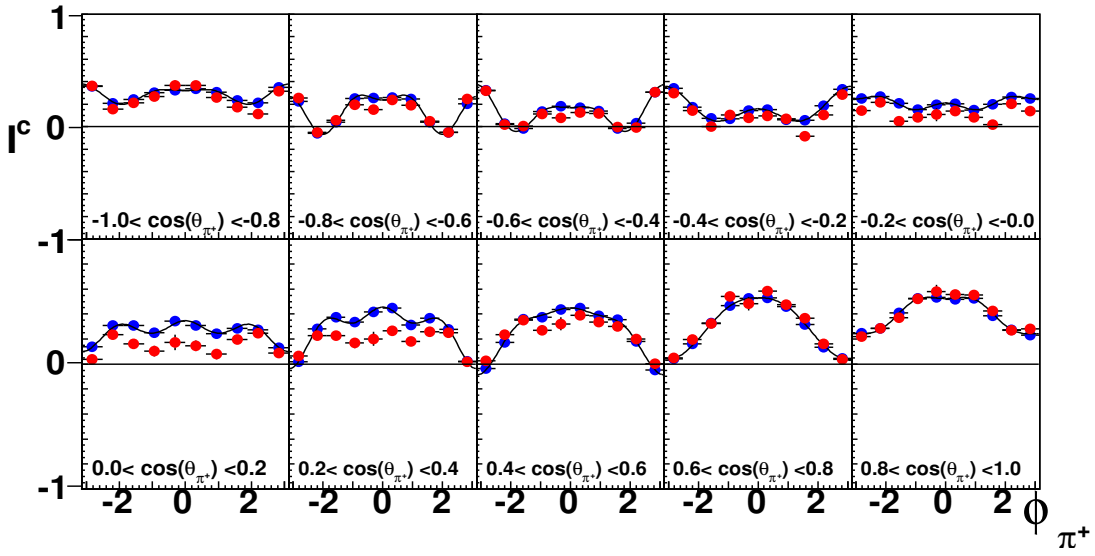

Figure 6.24: A 3-D plot of the observable $\mathbf{I^c}$ from FROST (shown in red) and Clas-g8 (shown in blue) in the energy bin $E_\gamma \in [1.1, 1.2]$ GeV. The error bars show the statistical uncertainties of the observables. The solid curves are third-order Fourier cosine fits to the Clas-g8 results. See text for further discussion.

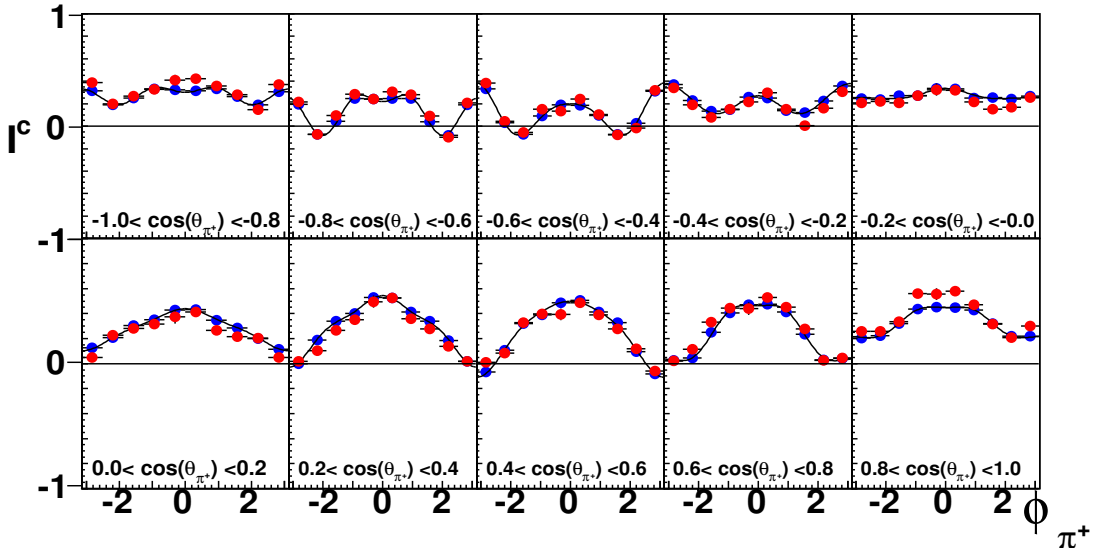

Figure 6.25: A 3-D plot of the observable $\mathbf{I^c}$ from FROST (shown in red) and Clas-g8 (shown in blue) in the energy bin $E_\gamma \in [1.2, 1.3]$ GeV. The error bars show the statistical uncertainties of the observables. The solid curves are third-order Fourier cosine fits to the Clas-g8 results. See text for further discussion.

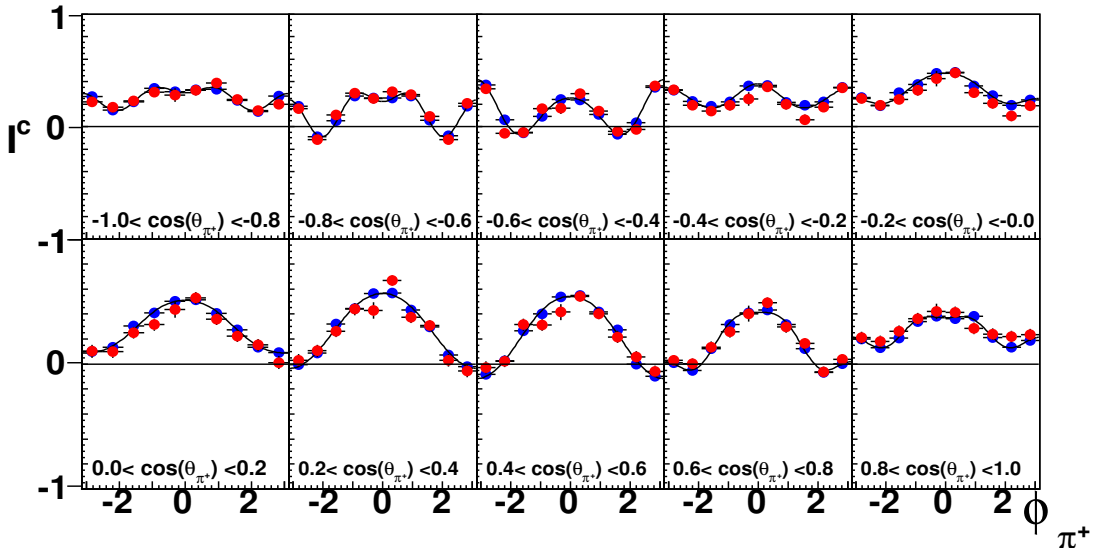

Figure 6.26: A 3-D plot of the observable $\mathbf{I^c}$ from FROST (shown in red) and Clas-g8 (shown in blue) in the energy bin $E_\gamma \in [1.3, 1.4]$ GeV. The error bars show the statistical uncertainties of the observables. The solid curves are third-order Fourier cosine fits to the Clas-g8 results. See text for further discussion.

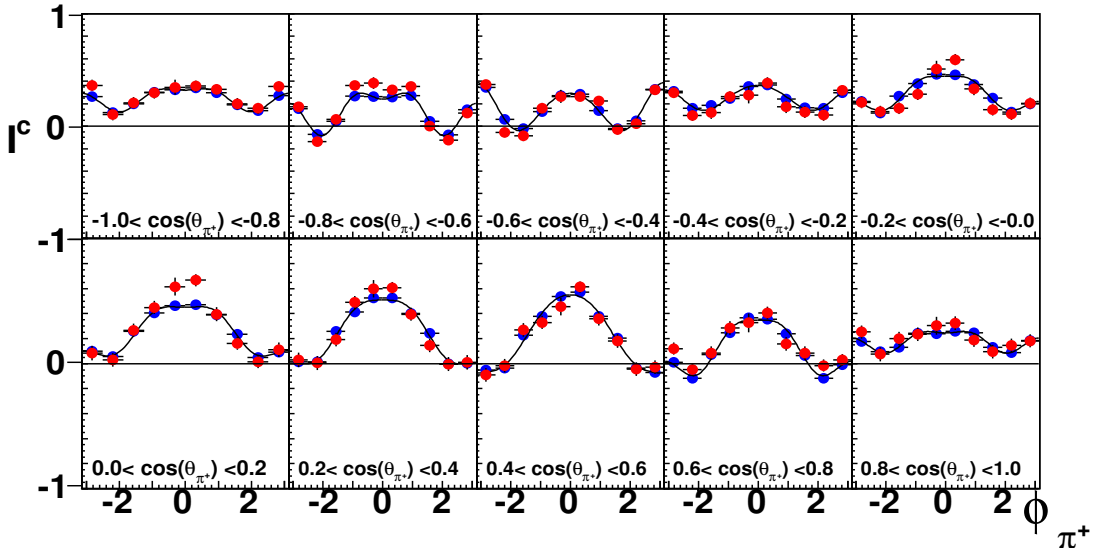

Figure 6.27: A 3-D plot of the observable $\mathbf{I^c}$ from FROST (shown in red) and Clas-g8 (shown in blue) in the energy bin $E_\gamma \in [1.4, 1.5]$ GeV. The error bars show the statistical uncertainties of the observables. The solid curves are third-order Fourier cosine fits to the Clas-g8 results. See text for further discussion.

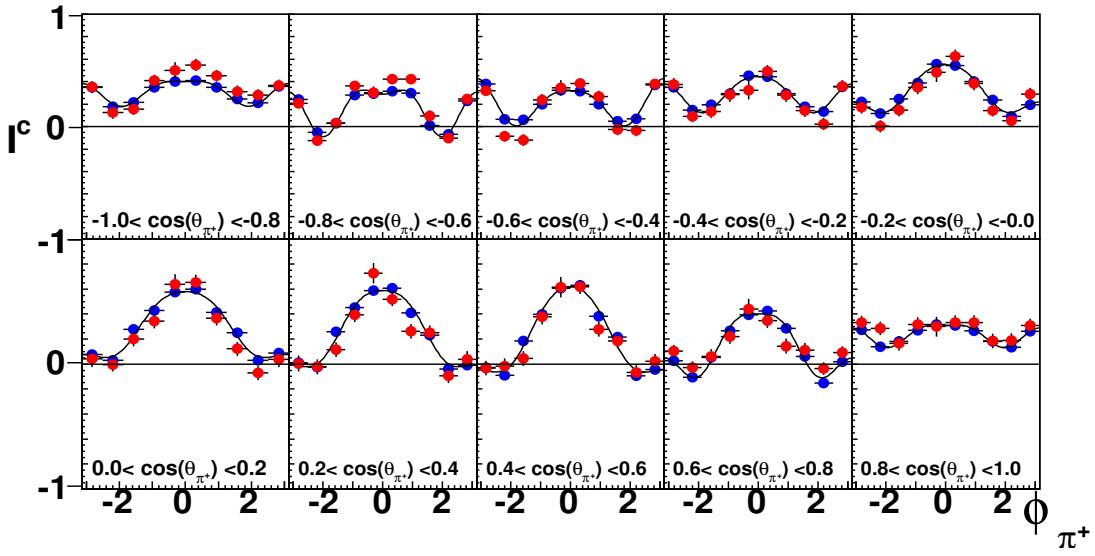

Figure 6.28: A 3-D plot of the observable $\mathbf{I^c}$ from FROST (shown in red) and Clas-g8 (shown in blue) in the energy bin $E_\gamma \in [1.5, 1.6]$ GeV. The error bars show the statistical uncertainties of the observables. The solid curves are third-order Fourier cosine fits to the Clas-g8 results. See text for further discussion.

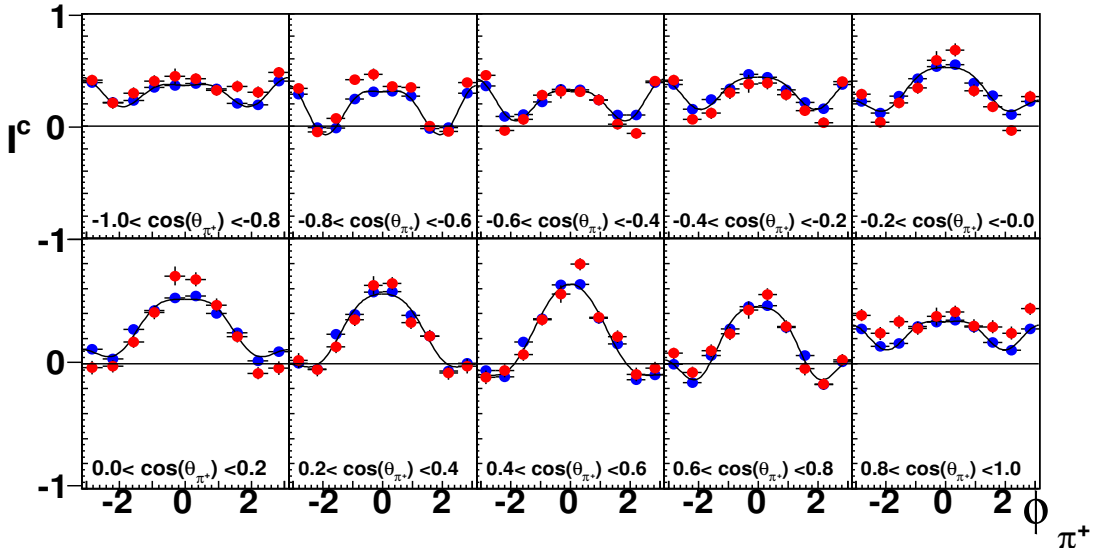

Figure 6.29: A 3-D plot of the observable $\mathbf{I^c}$ from FROST (shown in red) and Clas-g8 (shown in blue) in the energy bin $E_\gamma \in [1.6, 1.7]$ GeV. The error bars show the statistical uncertainties of the observables. The solid curves are third-order Fourier cosine fits to the Clas-g8 results. See text for further discussion.

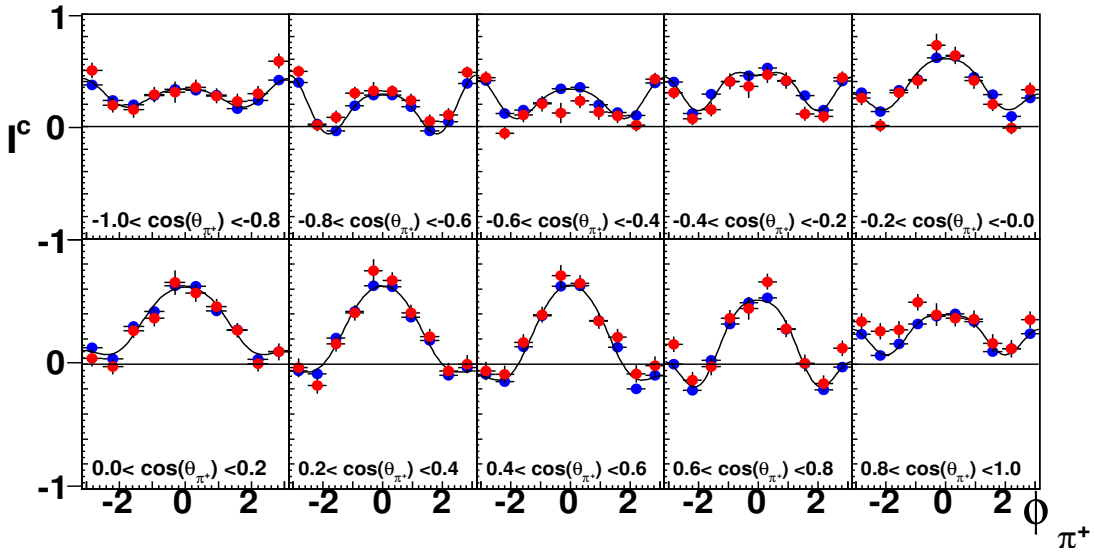

Figure 6.30: A 3-D plot of the observable $\mathbf{I^c}$ from FROST (shown in red) and Clas-g8 (shown in blue) in the energy bin $E_\gamma \in [1.7, 1.8]$ GeV. The error bars show the statistical uncertainties of the observables. The solid curves are third-order Fourier cosine fits to the Clas-g8 results. See text for further discussion.

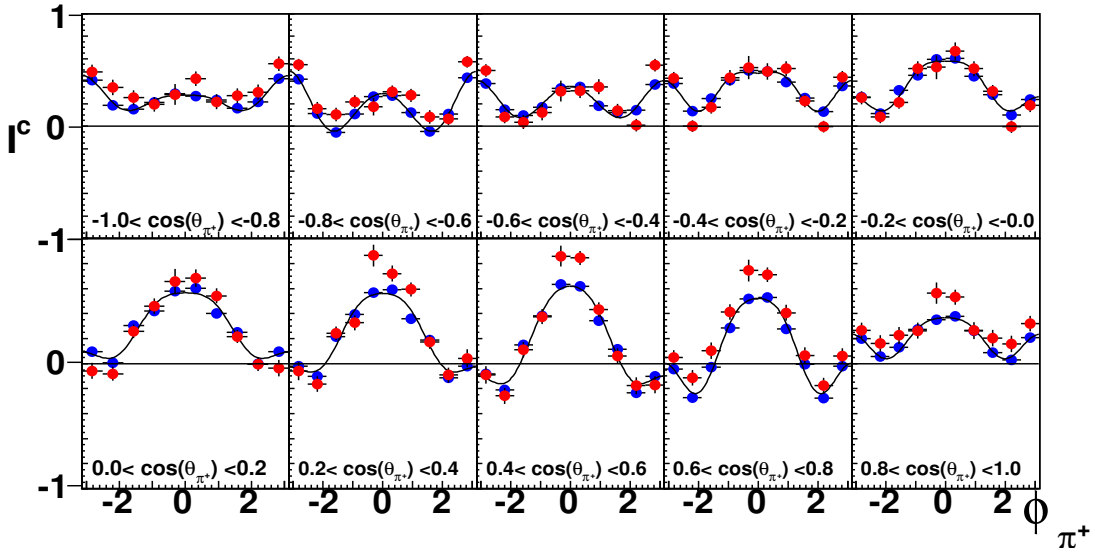

Figure 6.31: A 3-D plot of observable $\mathbf{I^c}$ from FROST (shown in red) and Clas-g8 (shown in blue) in the energy bin $E_\gamma \in [1.8, 1.9]$ GeV. The error bars show the statistical uncertainties of the observables. The solid curves are third-order Fourier cosine fits to the Clas-g8 results. See text for further discussion.

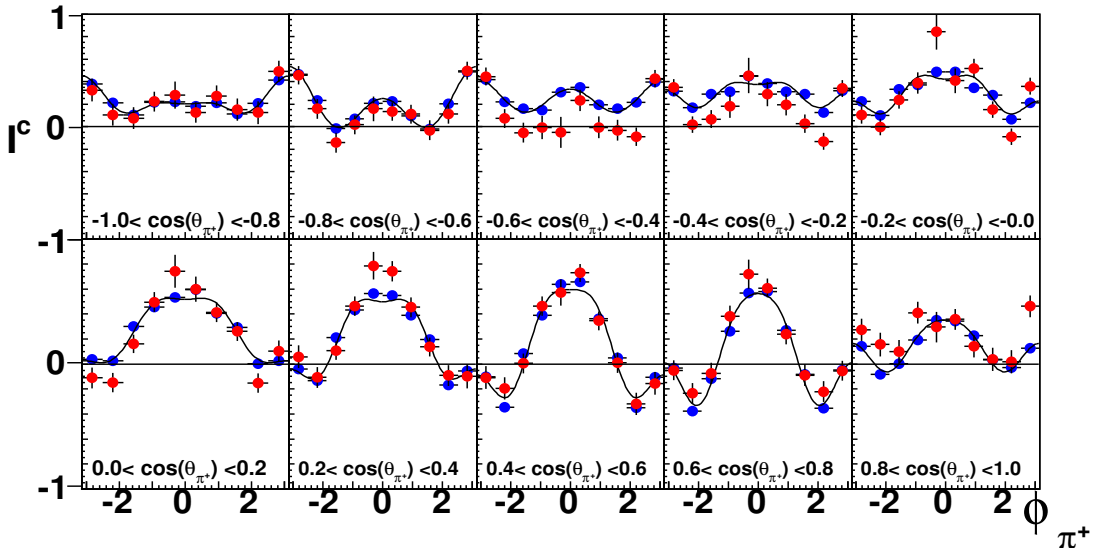

Figure 6.32: A 3-D plot of the observable $\mathbf{I^c}$ from FROST (shown in red) and Clas-g8 (shown in blue) in the energy bin $E_\gamma \in [1.9, 2.0]$ GeV. The error bars show the statistical uncertainties of the observables. The solid curves are third-order Fourier cosine fits to the Clas-g8 results. See text for further discussion.

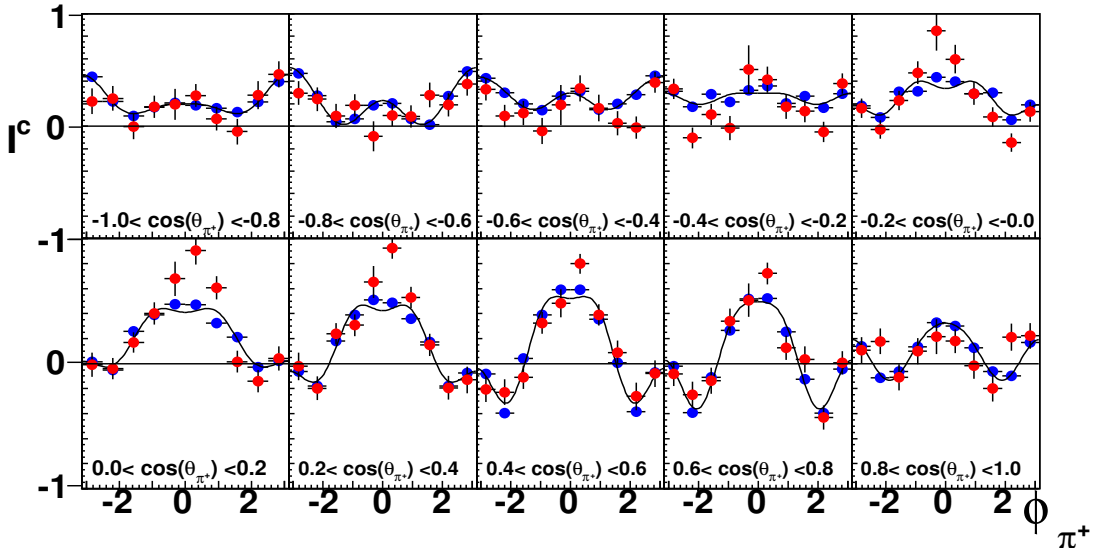

Figure 6.33: A 3-D plot of the observable $\mathbf{I^c}$ from FROST (shown in red) and Clas-g8 (shown in blue) in the energy bin $E_\gamma \in [2.0, 2.1]$ GeV. The error bars show the statistical uncertainties of the observables. The solid curves are third-order Fourier cosine fits to the Clas-g8 results. See text for further discussion.

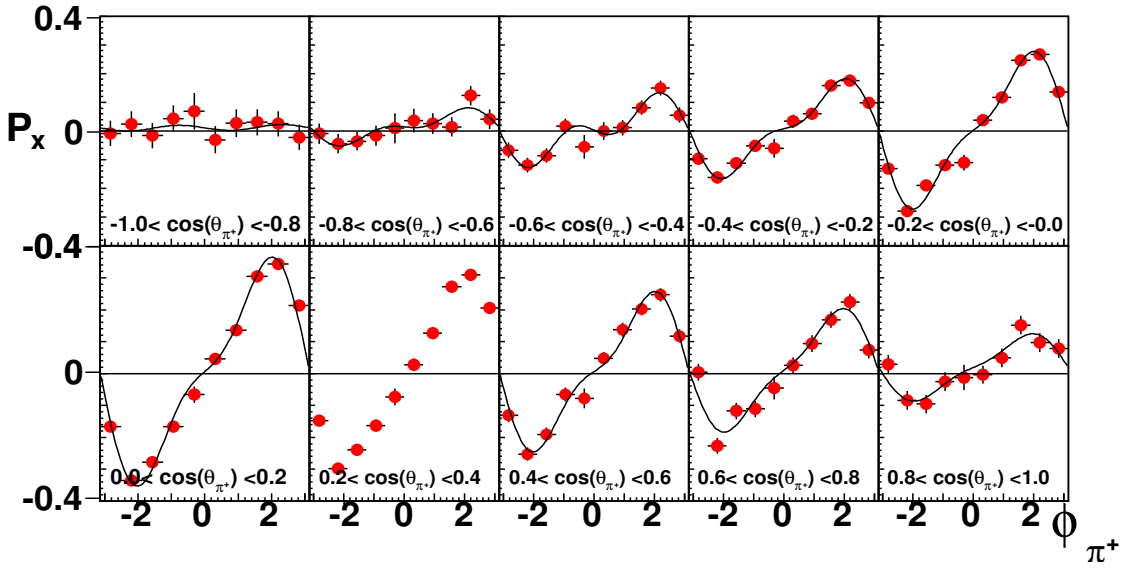

Figure 6.34: A 3-D plot showing first-time measurement of the observable $\mathbf{P_x}$ in the energy bin $E_\gamma \in [0.7, 0.8]$ GeV. The error bars show the statistical uncertainties of the observables. The solid curves are second-order Fourier sine fits to the $\mathbf{P_x}$ results. See text for further discussion.

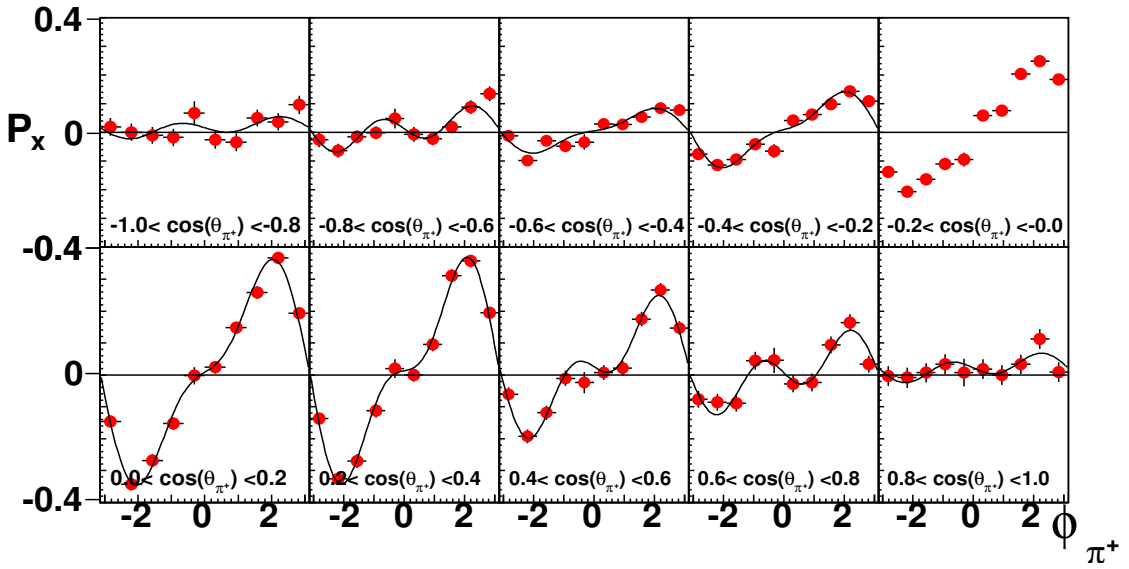

Figure 6.35: A 3-D plot showing first-time measurement of the observable $\mathbf{P_x}$ in the energy bin $E_\gamma \in [0.8, 0.9]$ GeV. The error bars show the statistical uncertainties of the observables. The solid curves are second-order Fourier sine fits to the $\mathbf{P_x}$ results. See text for further discussion.

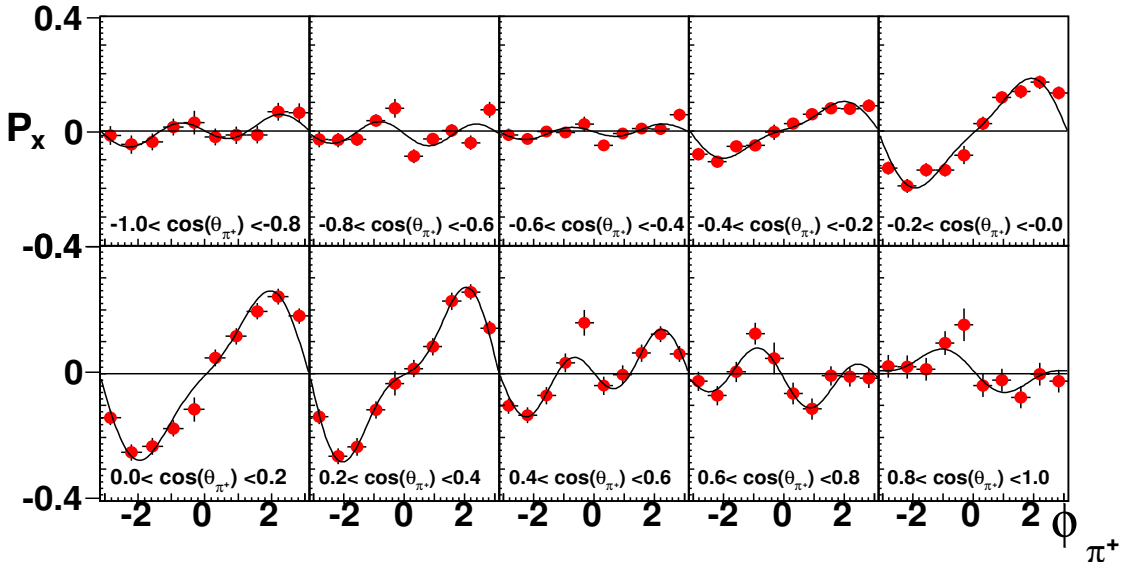

Figure 6.36: A 3-D plot showing first-time measurement of the observable $\mathbf{P_x}$ in the energy bin $E_\gamma \in [0.9, 1.0]$ GeV. The error bars show the statistical uncertainties of the observables. The solid curves are second-order Fourier sine fits to the $\mathbf{P_x}$ results. See text for further discussion.

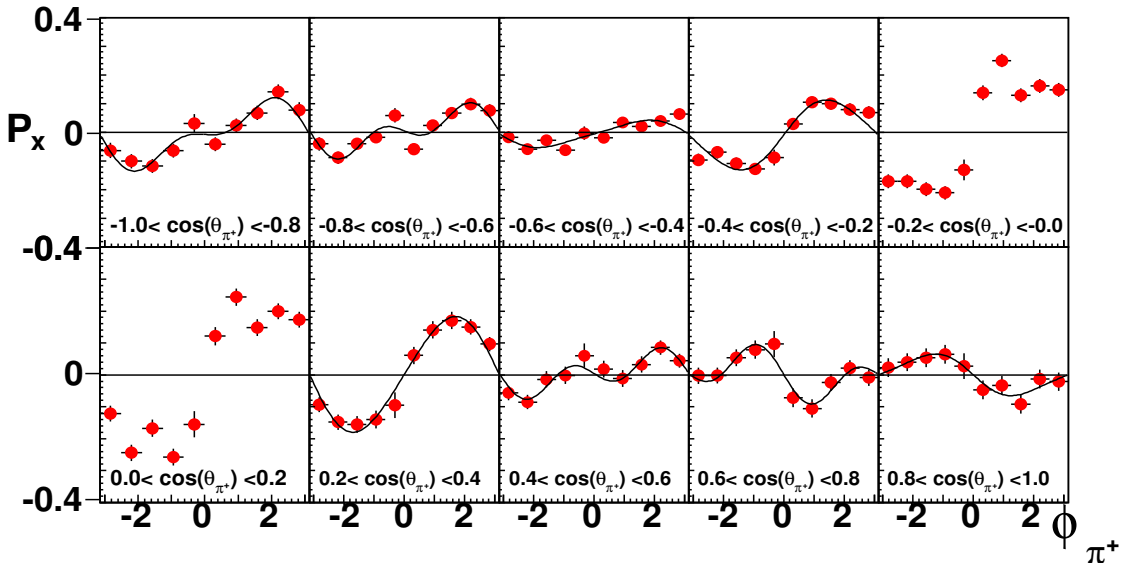

Figure 6.37: A 3-D plotshowing first-time measurement of the observable $\mathbf{P_x}$ in the energy bin $E_\gamma \in [1.0, 1.1]$ GeV. The error bars show the statistical uncertainties of the observables. The solid curves are second-order Fourier sine fits to the $\mathbf{P_x}$ results. See text for further discussion.

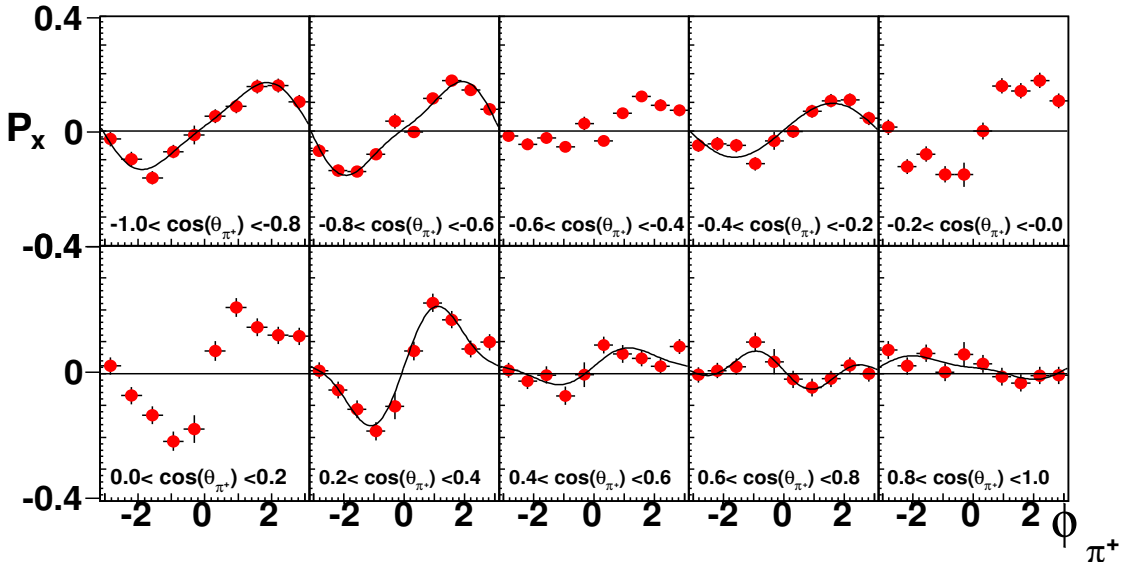

Figure 6.38: A 3-D plot showing first-time measurement of the observable $\mathbf{P_x}$ in the energy bin $E_\gamma \in [1.1, 1.2]$ GeV. The error bars show the statistical uncertainties of the observables. The solid curves are second-order Fourier sine fits to the $\mathbf{P_x}$ results. See text for further discussion.

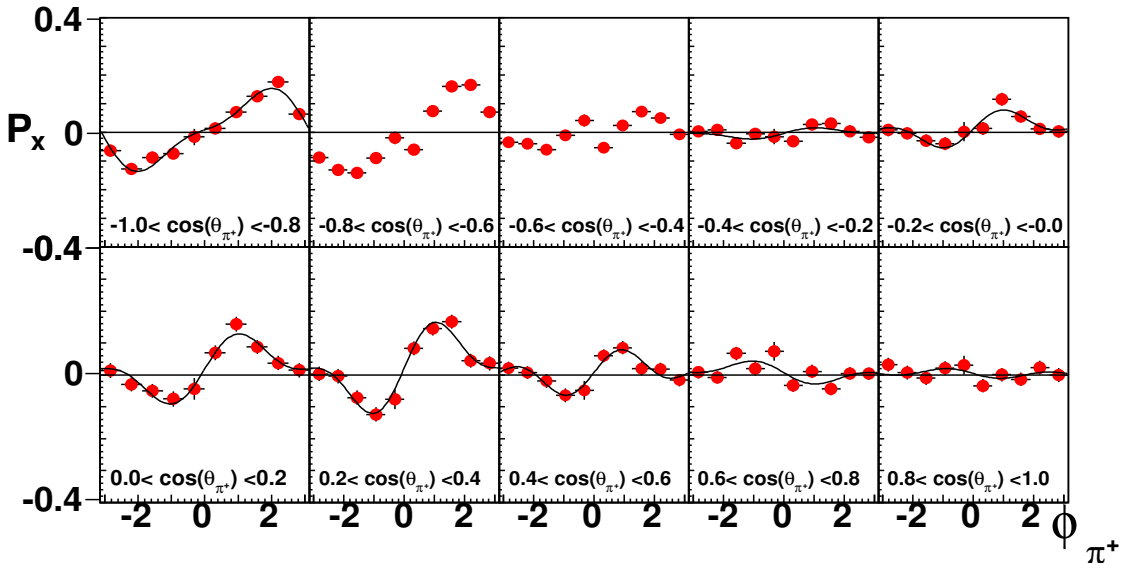

Figure 6.39: A 3-D plot showing first-time measurement of the observable $\mathbf{P_x}$ in the energy bin $E_\gamma \in [1.2, 1.3]$ GeV. The error bars show the statistical uncertainties of the observables. The solid curves are second-order Fourier sine fits to the $\mathbf{P_x}$ results. See text for further discussion.

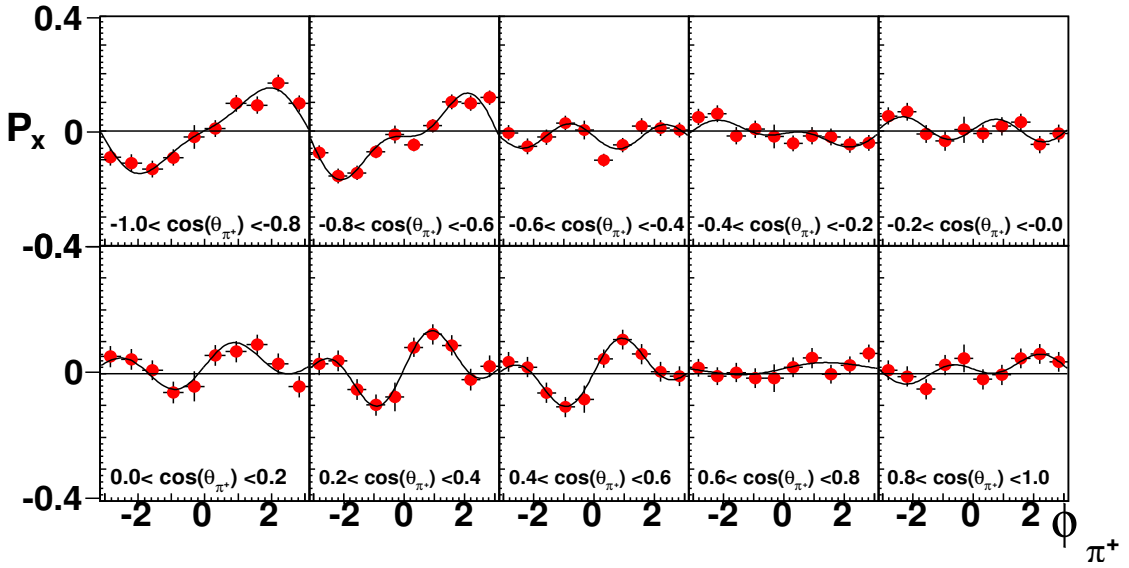

Figure 6.40: A 3-D plot showing first-time measurement of the observable $\mathbf{P_x}$ in the energy bin $E_\gamma \in [1.3, 1.4]$ GeV. The error bars show the statistical uncertainties of the observables. The solid curves are second-order Fourier sine fits to the $\mathbf{P_x}$ results. See text for further discussion.

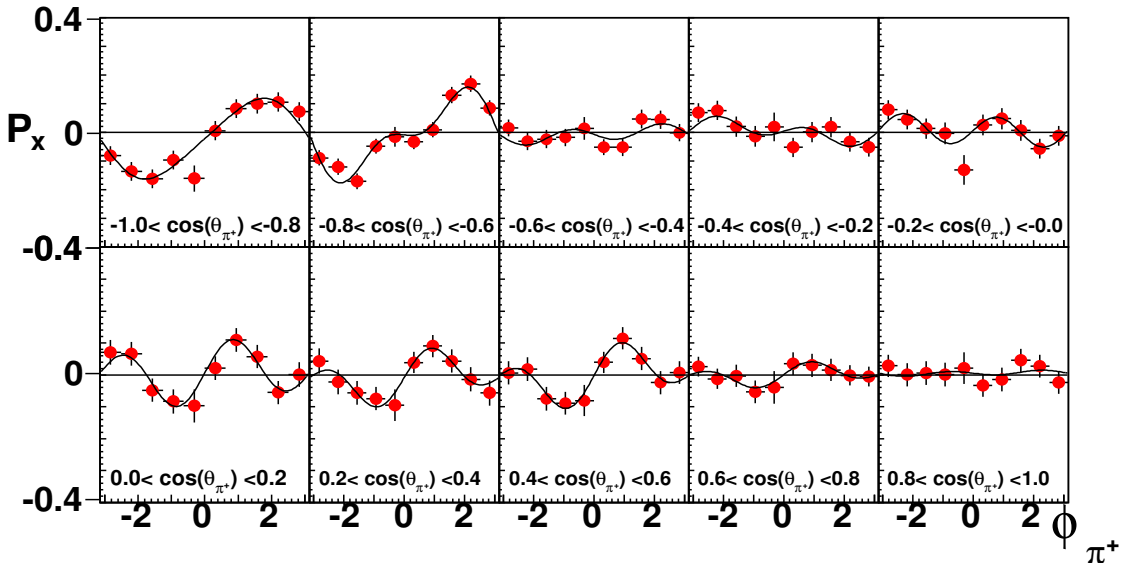

Figure 6.41: A 3-D plot showing first-time measurement of the observable $\mathbf{P_x}$ in the energy bin $E_\gamma \in [1.4, 1.5]$ GeV. The error bars show the statistical uncertainties of the observables. The solid curves are second-order Fourier sine fits to the $\mathbf{P_x}$ results. See text for further discussion.

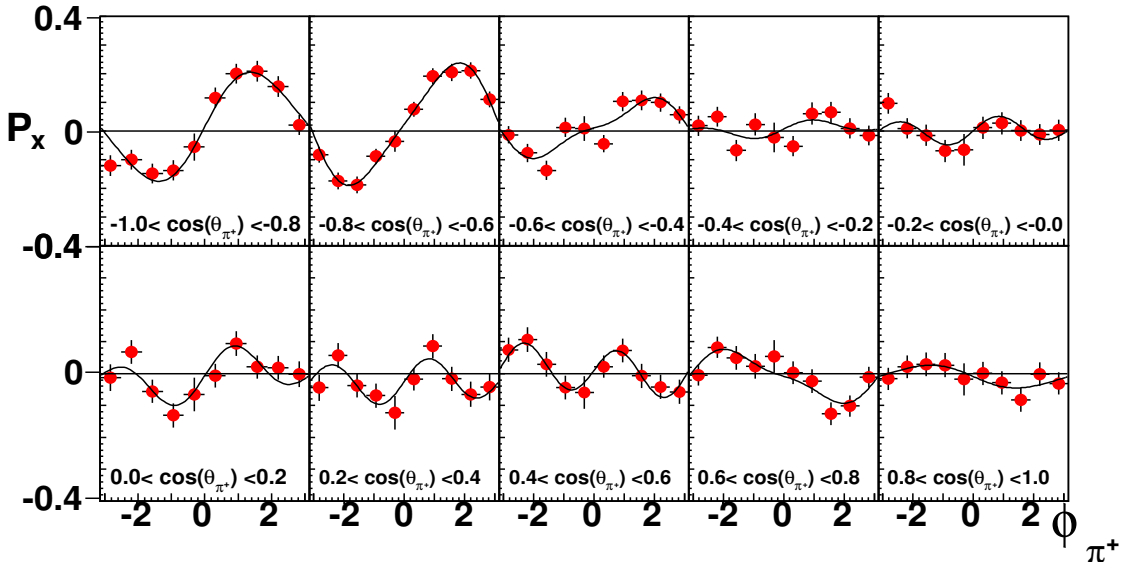

Figure 6.42: A 3-D plot showing first-time measurement of the observable $\mathbf{P_x}$ in the energy bin $E_\gamma \in [1.5, 1.6]$ GeV. The error bars show the statistical uncertainties of the observables. The solid curves are second-order Fourier sine fits to the $\mathbf{P_x}$ results. See text for further discussion.

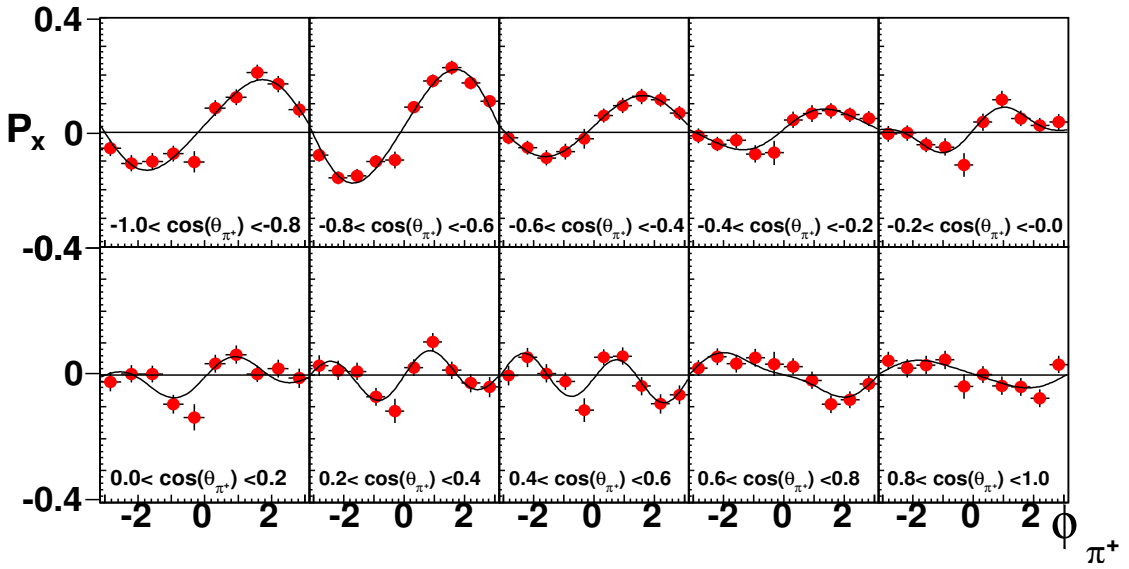

Figure 6.43: A 3-D plot showing first-time measurement of the observable $\mathbf{P_x}$ in the energy bin $E_\gamma \in [1.6, 1.7]$ GeV. The error bars show the statistical uncertainties of the observables. The solid curves are second-order Fourier sine fits to the $\mathbf{P_x}$ results. See text for further discussion.

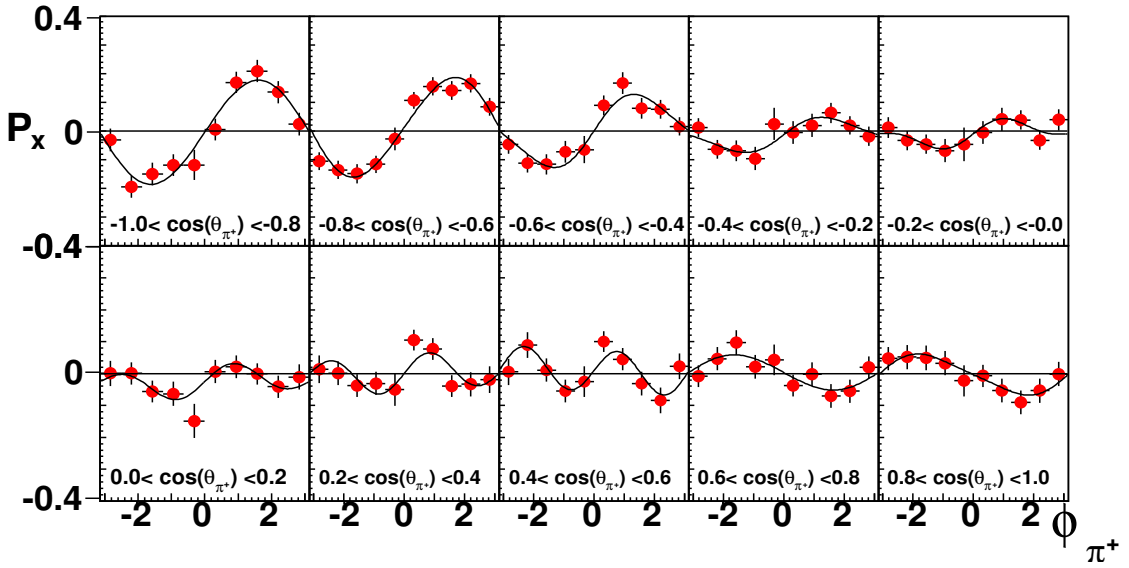

Figure 6.44: A 3-D plot showing first-time measurement of the observable $\mathbf{P_x}$ in the energy bin $E_\gamma \in [1.7, 1.8]$ GeV. The error bars show the statistical uncertainties of the observables. The solid curves are second-order Fourier sine fits to the $\mathbf{P_x}$ results. See text for further discussion.

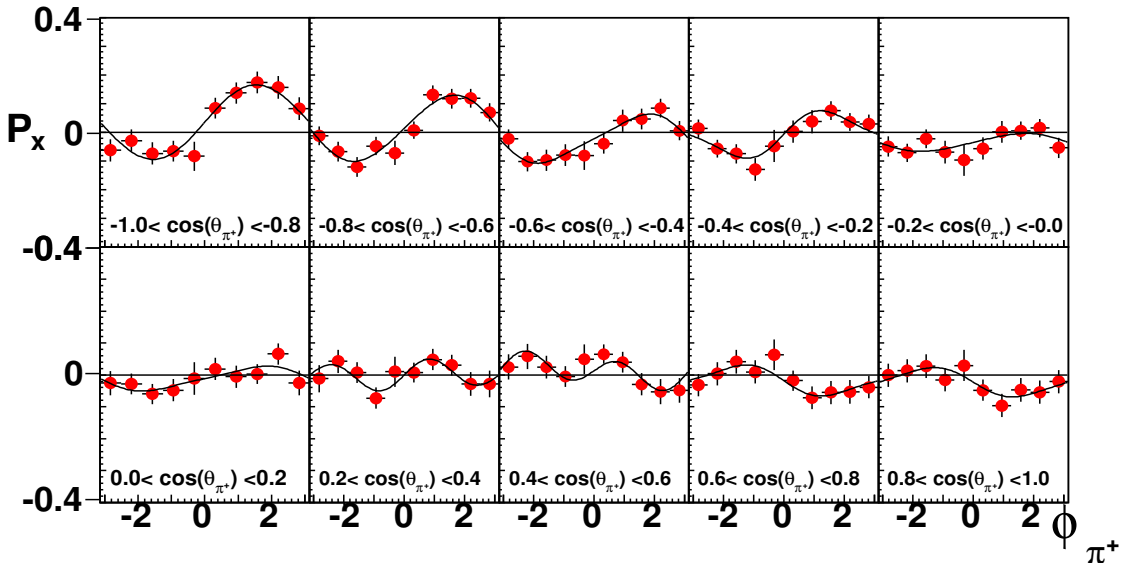

Figure 6.45: A 3-D plot showing first-time measurement of the observable $\mathbf{P_x}$ in the energy bin $E_\gamma \in [1.8, 1.9]$ GeV. The error bars show the statistical uncertainties of the observables. The solid curves are second-order Fourier sine fits to the $\mathbf{P_x}$ results. See text for further discussion.

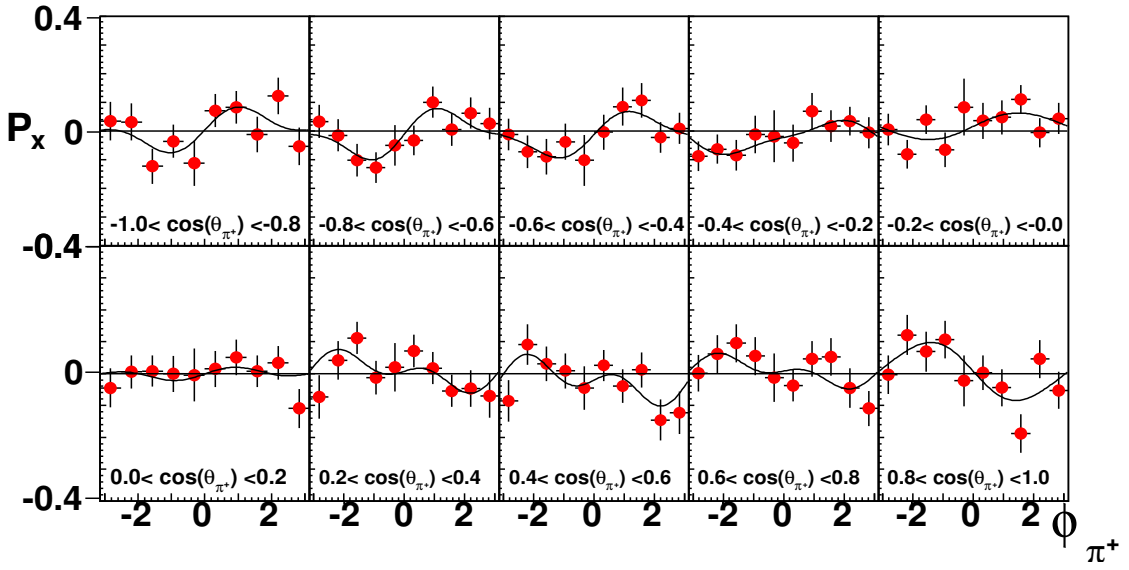

Figure 6.46: A 3-D plot showing first-time measurement of the observable $\mathbf{P_x}$ in the energy bin $E_\gamma \in [1.9, 2.0]$ GeV. The error bars show the statistical uncertainties of the observables. The solid curves are second-order Fourier sine fits to the $\mathbf{P_x}$ results. See text for further discussion.

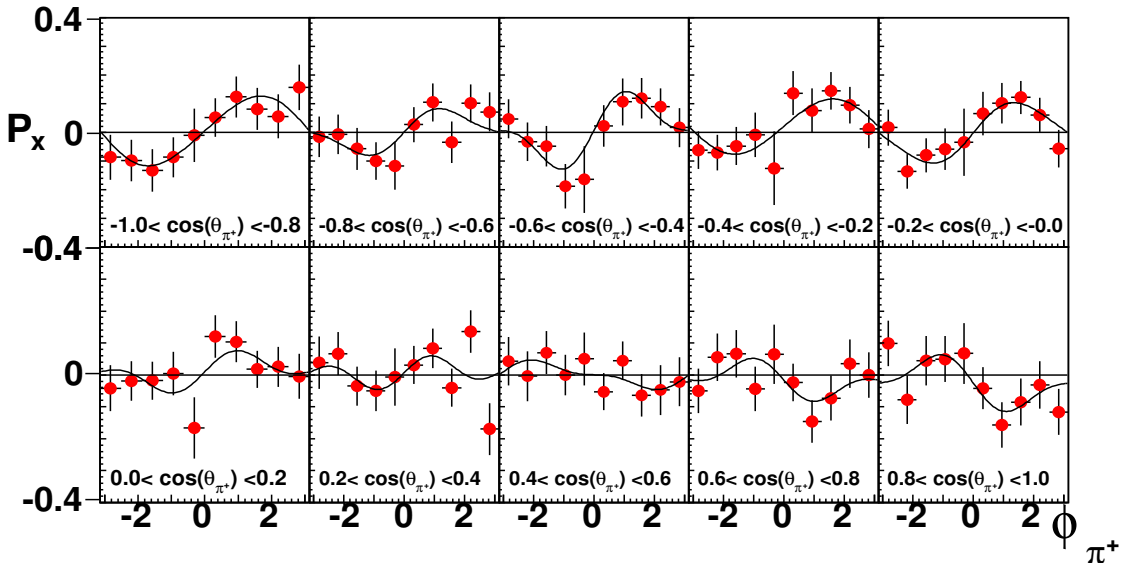

Figure 6.47: A 3-D plot showing first-time measurement of the observable $\mathbf{P_x}$ in the energy bin $E_\gamma \in [2.0, 2.1]$ GeV. The error bars show the statistical uncertainties of the observables. The solid curves are second-order Fourier sine fits to the $\mathbf{P_x}$ results. See text for further discussion.

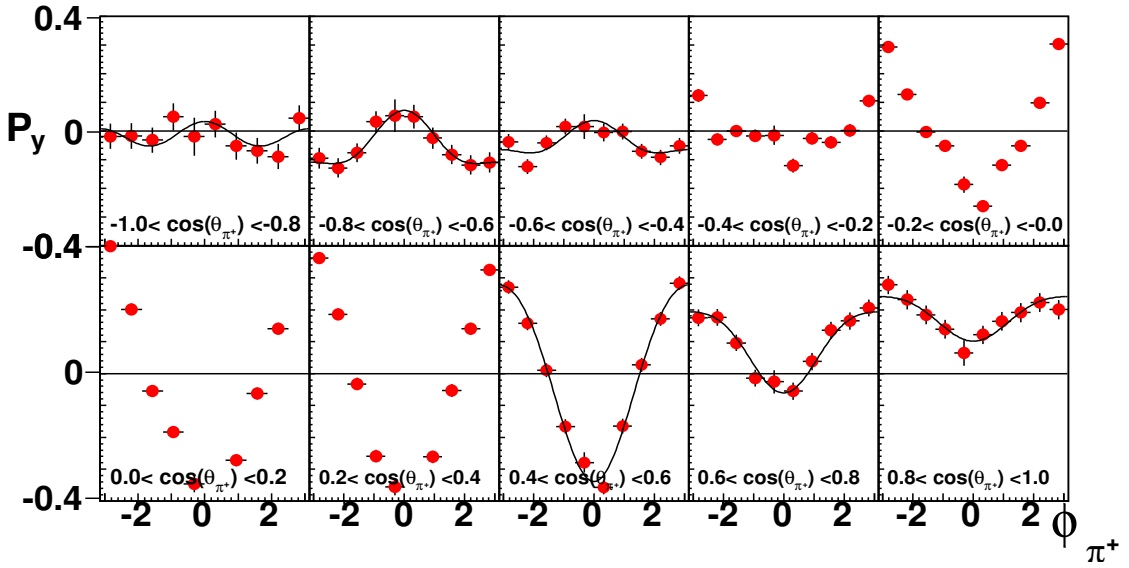

Figure 6.48: A 3-D plot showing first-time measurement of the observable $\mathbf{P_y}$ in the energy bin $E_\gamma \in [0.7, 0.8]$ GeV. The error bars show the statistical uncertainties of the observables. The solid curves are second-order Fourier cosine fits to the $\mathbf{P_y}$ results. See text for further discussion.

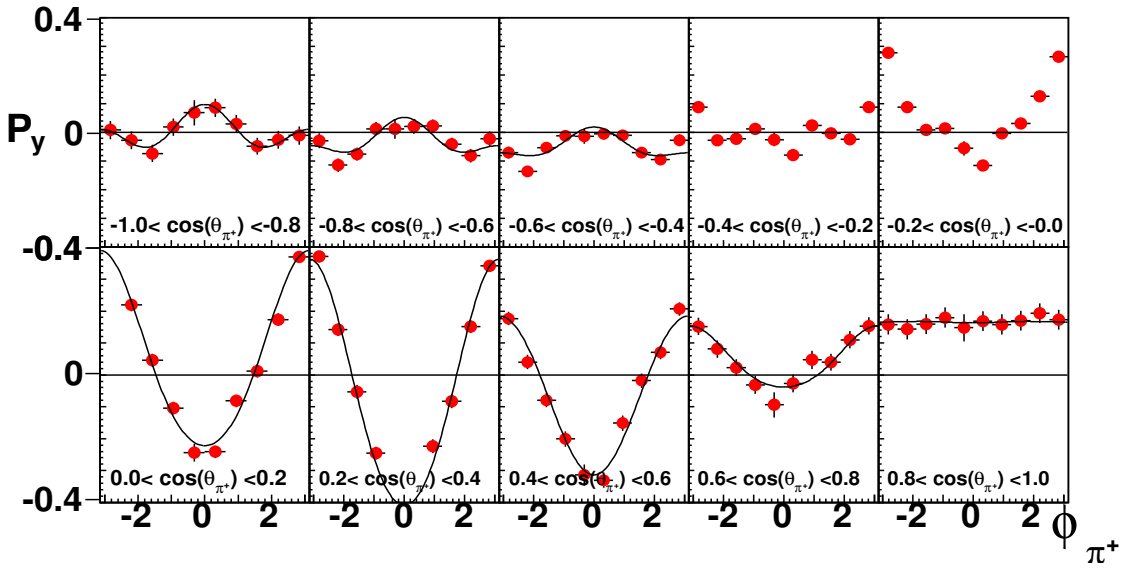

Figure 6.49: A 3-D plot showing first-time measurement of observable $\mathbf{P_y}$ in the energy bin $E_\gamma \in [0.8, 0.9]$ GeV. The error bars show the statistical uncertainties of the observables. The solid curves are second-order Fourier cosine fits to the $\mathbf{P_y}$ results. See text for further discussion.

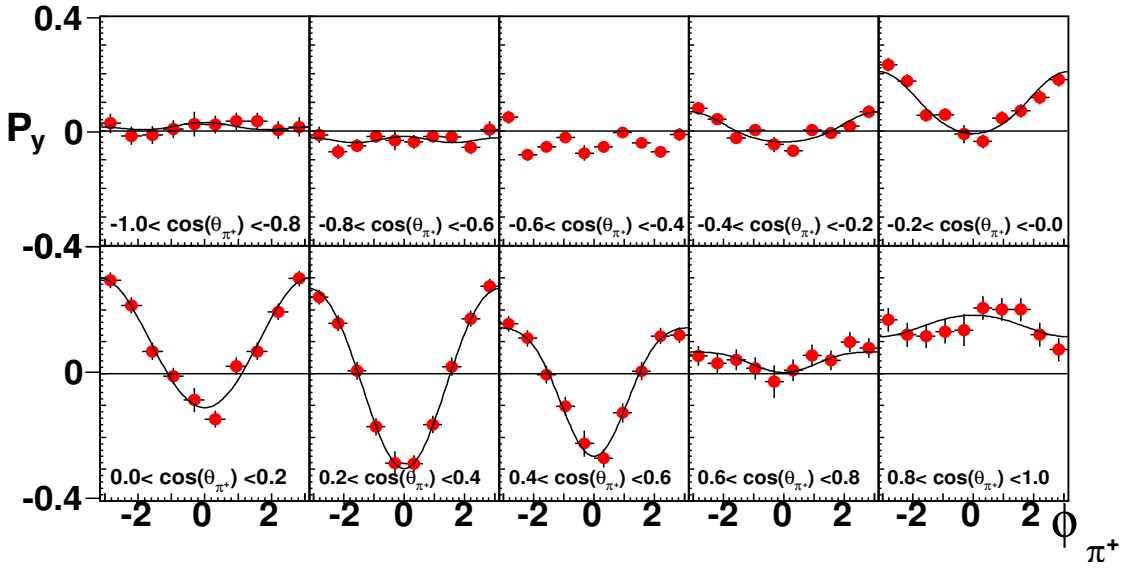

Figure 6.50: A 3-D plot showing first-time measurement of the observable $\mathbf{P_y}$ in the energy bin $E_\gamma \in [0.9, 1.0]$ GeV. The error bars show the statistical uncertainties of the observables. The solid curves are second-order Fourier cosine fits to the $\mathbf{P_y}$ results. See text for further discussion.

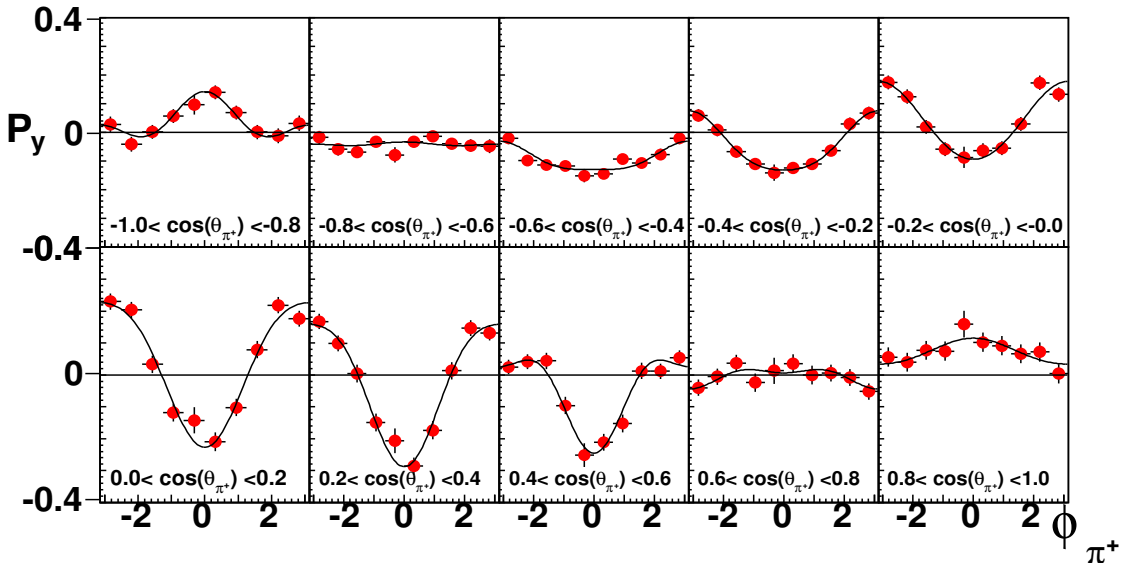

Figure 6.51: A 3-D plot showing first-time measurement of the observable $\mathbf{P_y}$ in the energy bin $E_\gamma \in [1.0, 1.1]$ GeV. The error bars show the statistical uncertainties of the observables. The solid curves are second-order Fourier cosine fits to the $\mathbf{P_y}$ results. See text for further discussion.

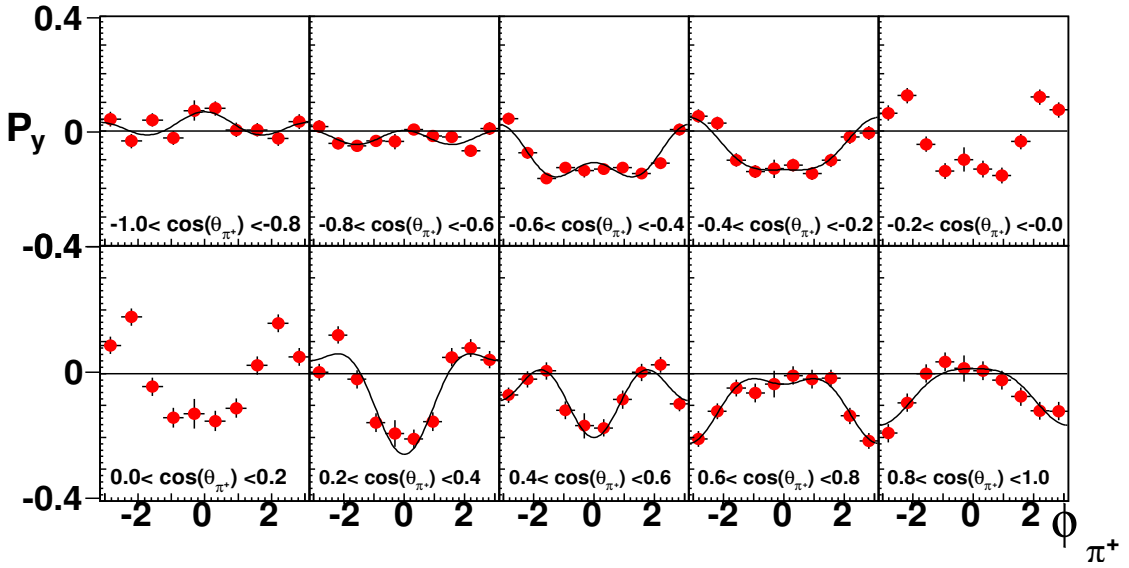

Figure 6.52: A 3-D plot showing first-time measurement of the observable $\mathbf{P_y}$ in the energy bin $E_\gamma \in [1.1, 1.2]$ GeV. The error bars show the statistical uncertainties of the observables. The solid curves are second-order Fourier cosine fits to the $\mathbf{P_y}$ results. See text for further discussion.

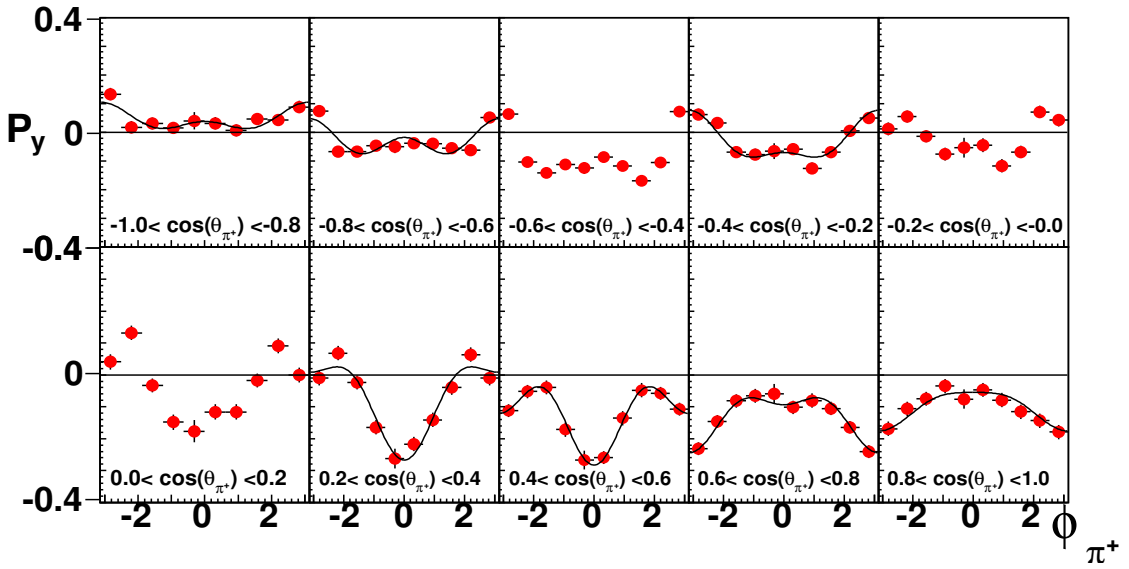

Figure 6.53: A 3-D plot showing first-time measurement of the observable $\mathbf{P_y}$ in the energy bin $E_\gamma \in [1.2, 1.3]$ GeV. The error bars show the statistical uncertainties of the observables. The solid curves are second-order Fourier cosine fits to the $\mathbf{P_y}$ results. See text for further discussion.

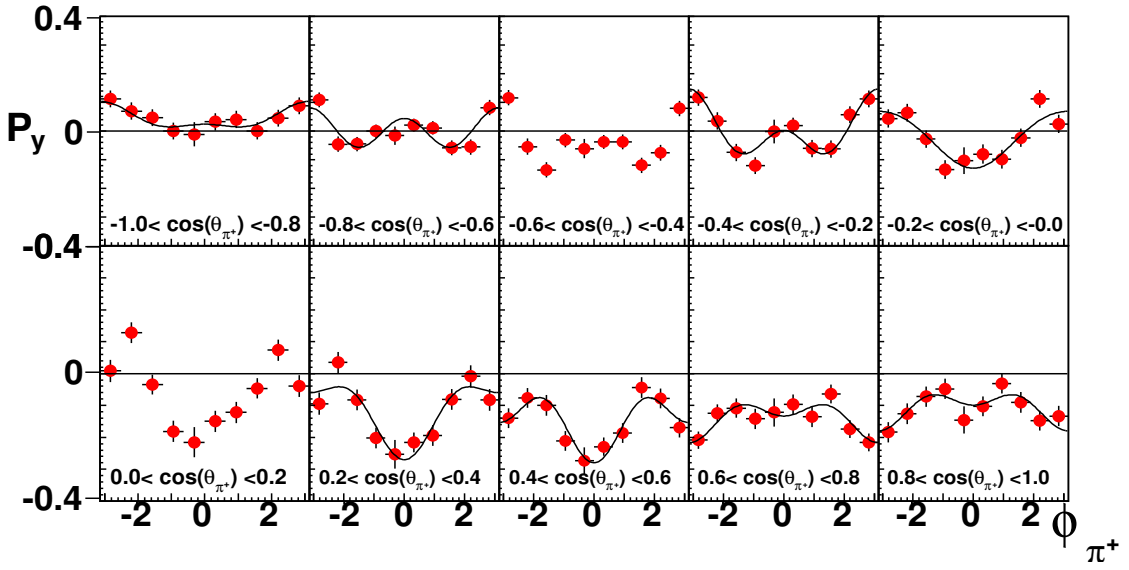

Figure 6.54: A 3-D plot showing first-time measurement of the observable $\mathbf{P_y}$ in the energy bin $E_\gamma \in [1.3, 1.4]$ GeV. The error bars show the statistical uncertainties of the observables. The solid curves are second-order Fourier cosine fits to the $\mathbf{P_y}$ results. See text for further discussion.

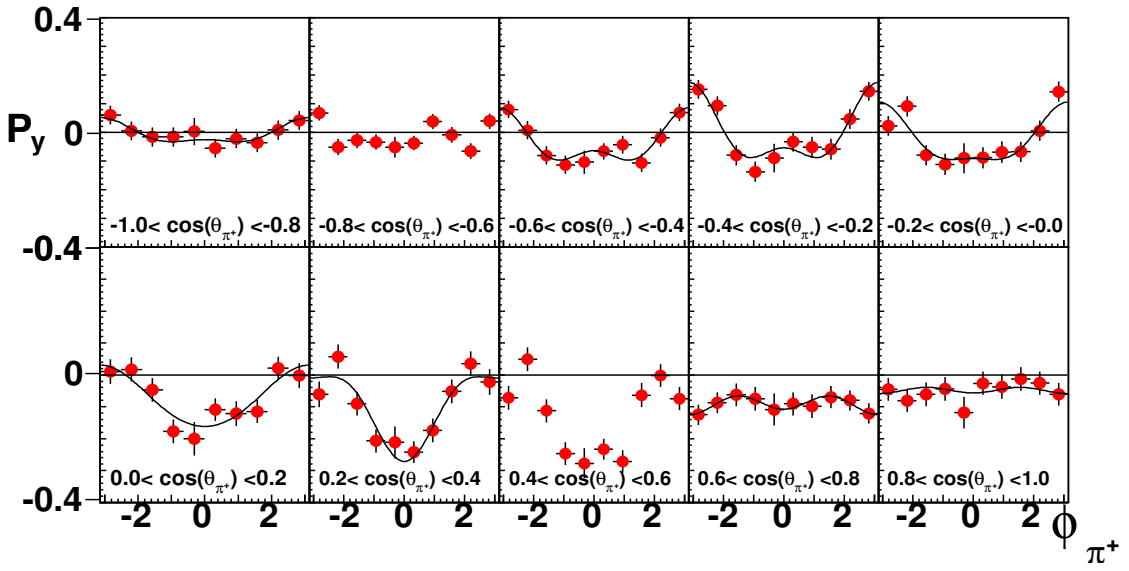

Figure 6.55: A 3-D plot showing first-time measurement of the observable $\mathbf{P_y}$ in the energy bin $E_\gamma \in [1.4, 1.5]$ GeV. The error bars show the statistical uncertainties of the observables. The solid curves are second-order Fourier cosine fits to the $\mathbf{P_y}$ results. See text for further discussion.

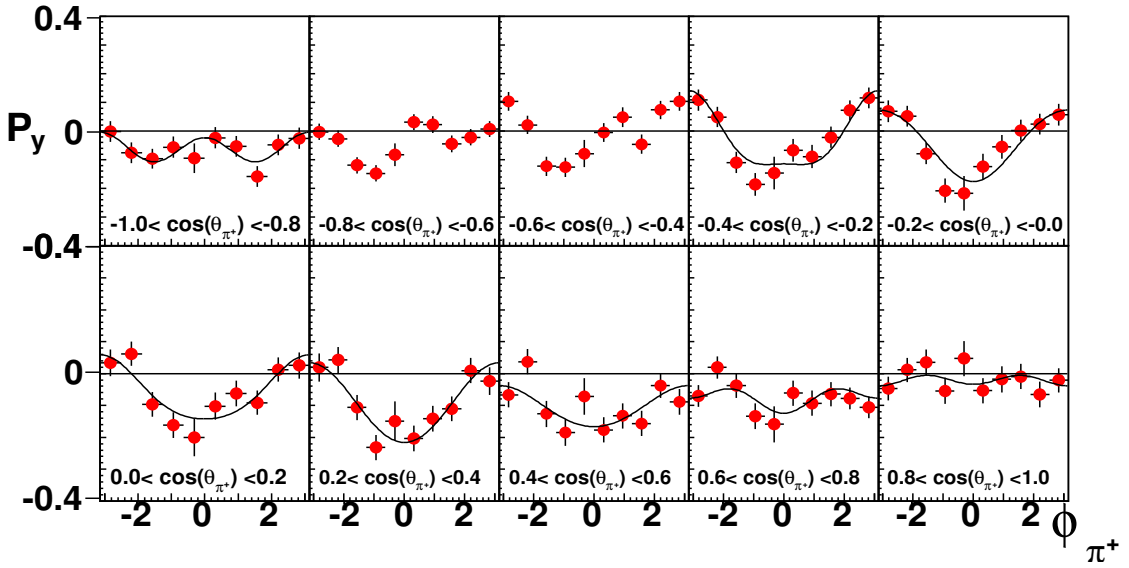

Figure 6.56: A 3-D plot showing first-time measurement of the observable $\mathbf{P_y}$ in the energy bin $E_\gamma \in [1.5, 1.6]$ GeV. The error bars show the statistical uncertainties of the observables. The solid curves are second-order Fourier cosine fits to the $\mathbf{P_y}$ results. See text for further discussion.

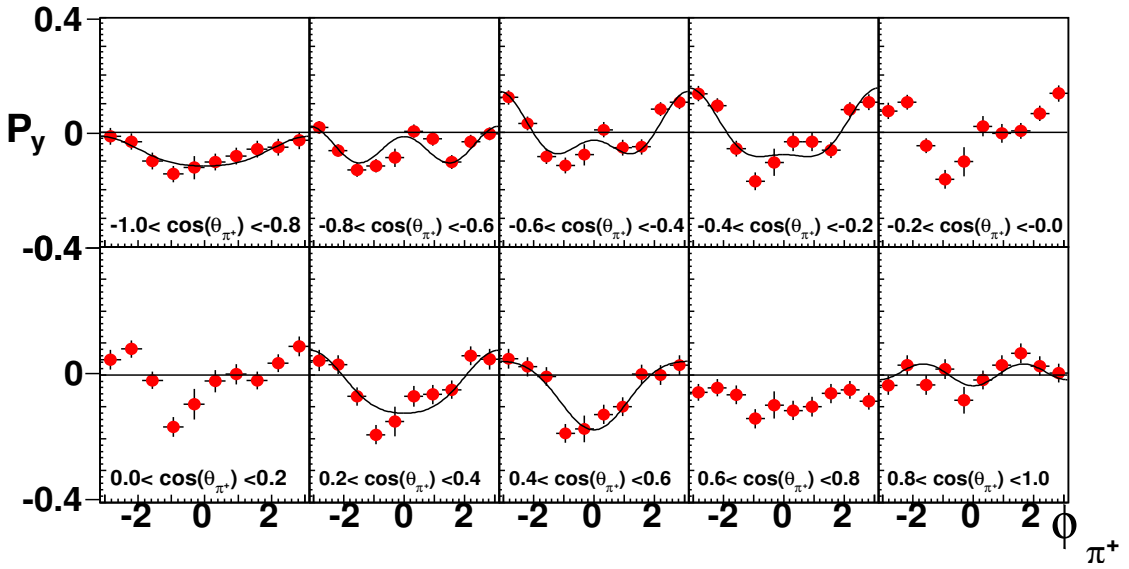

Figure 6.57: A 3-D plot showing first-time measurement of the observable $\mathbf{P_y}$ in the energy bin $E_\gamma \in [1.6, 1.7]$ GeV. The error bars show the statistical uncertainties of the observables. The solid curves are second-order Fourier cosine fits to the $\mathbf{P_y}$ results. See text for further discussion.

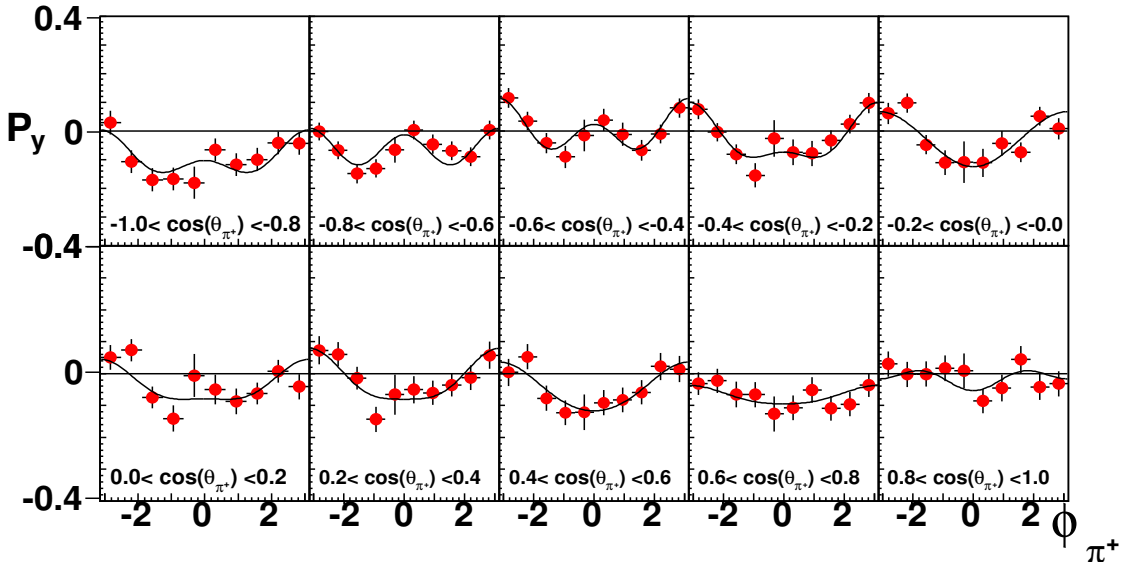

Figure 6.58: A 3-D plot showing first-time measurement of the observable $\mathbf{P_y}$ in the energy bin $E_\gamma \in [1.7, 1.8]$ GeV. The error bars show the statistical uncertainties of the observables. The solid curves are second-order Fourier cosine fits to the $\mathbf{P_y}$ results. See text for further discussion.

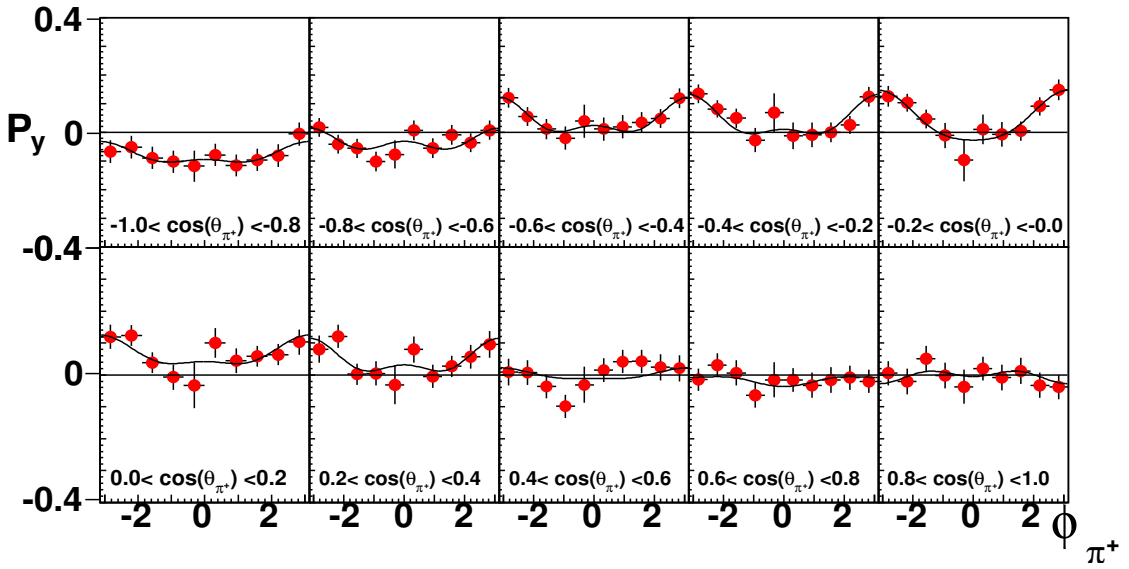

Figure 6.59: A 3-D plot showing first-time measurement of the observable $\mathbf{P_y}$ in the energy bin $E_\gamma \in [1.8, 1.9]$ GeV. The error bars show the statistical uncertainties of the observables. The solid curves are second-order Fourier cosine fits to the $\mathbf{P_y}$ results. See text for further discussion.

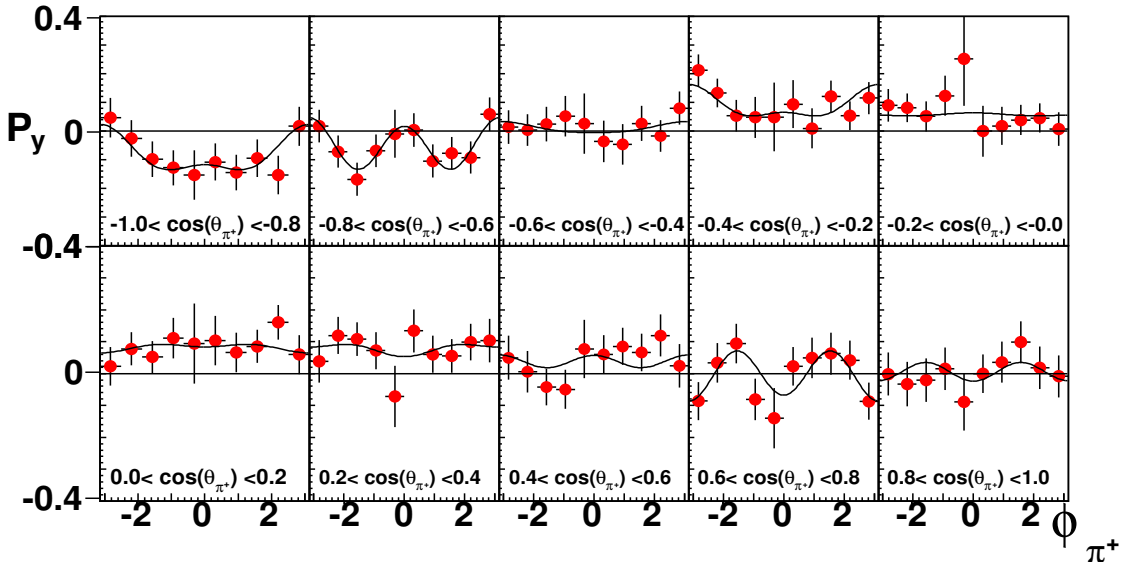

Figure 6.60: A 3-D plot showing first-time measurement of observable $\mathbf{P_y}$ in the energy bin $E_\gamma \in$ [1.9, 2.0] GeV. The error bars show the statistical uncertainties of the observables. The solid curves are second-order Fourier cosine fits to the $\mathbf{P_y}$ results. See text for further discussion.

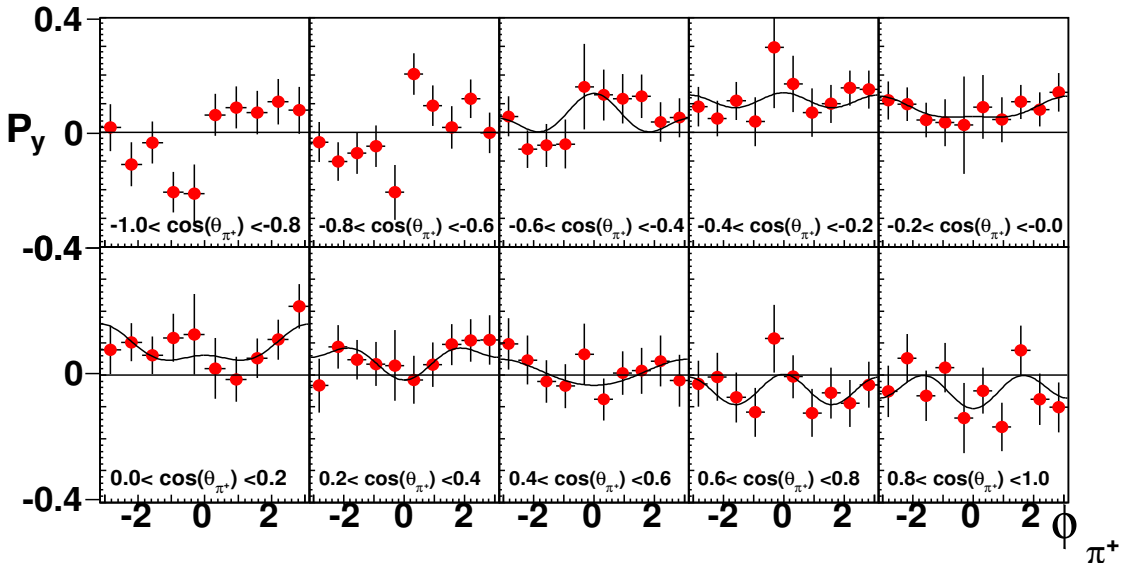

Figure 6.61: A 3-D plot showing first-time measurement of the observable $\mathbf{P_y}$ in the energy bin $E_\gamma \in$ [2.0, 2.1] GeV. The error bars show the statistical uncertainties of the observables. The solid curves are second-order Fourier cosine fits to the $\mathbf{P_y}$ results. See text for further discussion.

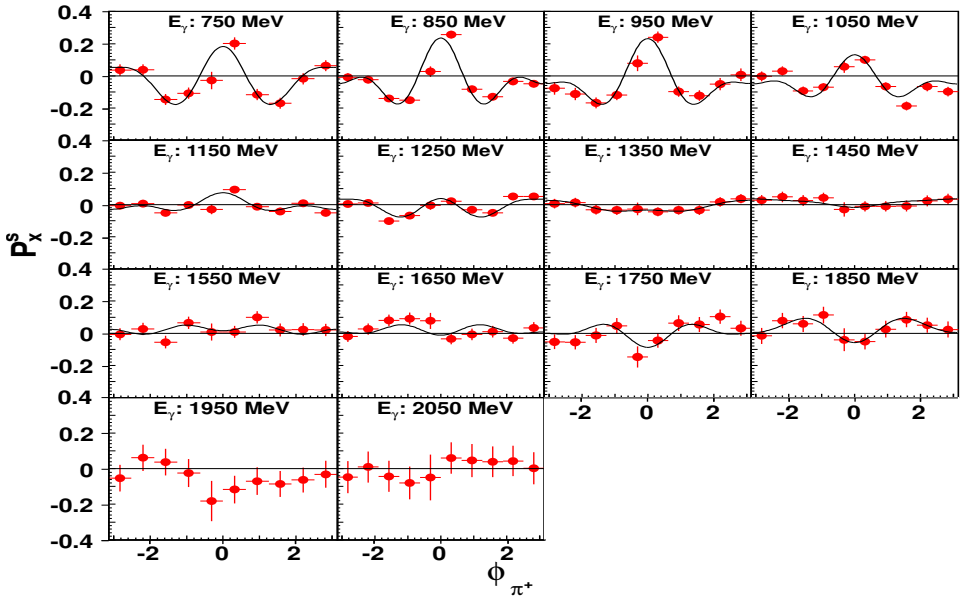

Figure 6.62: A quasi-3D plot showing first-time measurement of $\mathbf{P_x^s}$ along with third-order Fourier cosine fits. Results are shown for $-1.0 < \cos\theta_{\pi^+} < 0.0$. The error bars shown are statistical only.

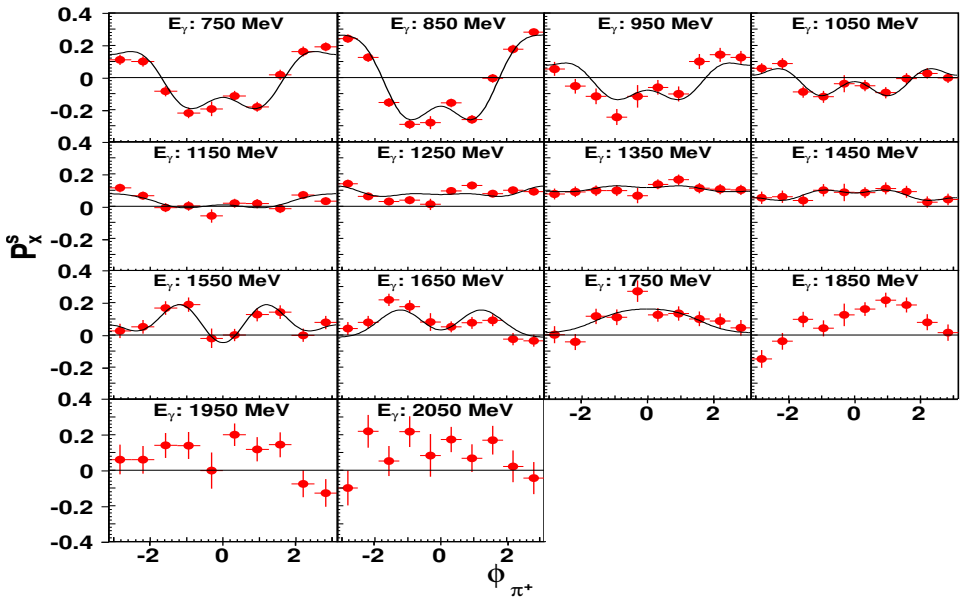

Figure 6.63: A quasi-3D plot showing first-time measurement of $\mathbf{P_x^s}$ along with third-order Fourier cosine fits. Results are shown for $0.0 < \cos\theta_{\pi^+} < 1.0$. The error bars shown are statistical only.

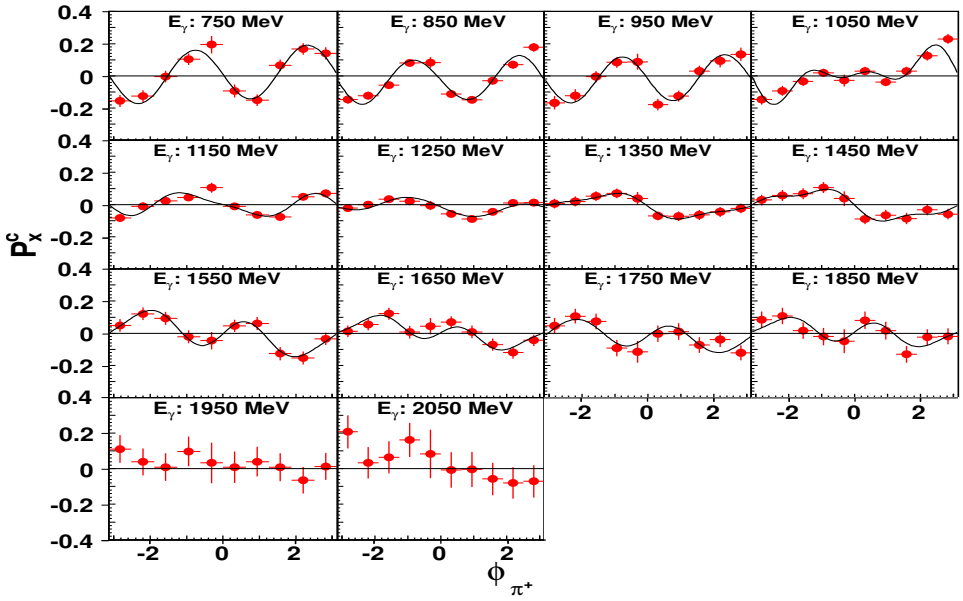

Figure 6.64: A quasi-3D plot showing first-time measurement of $\mathbf{P_x^c}$ along with third-order Fourier sine fits. Results are shown for $-1.0 < \cos\theta_{\pi^+} < 0.0$. The error bars shown are statistical only.

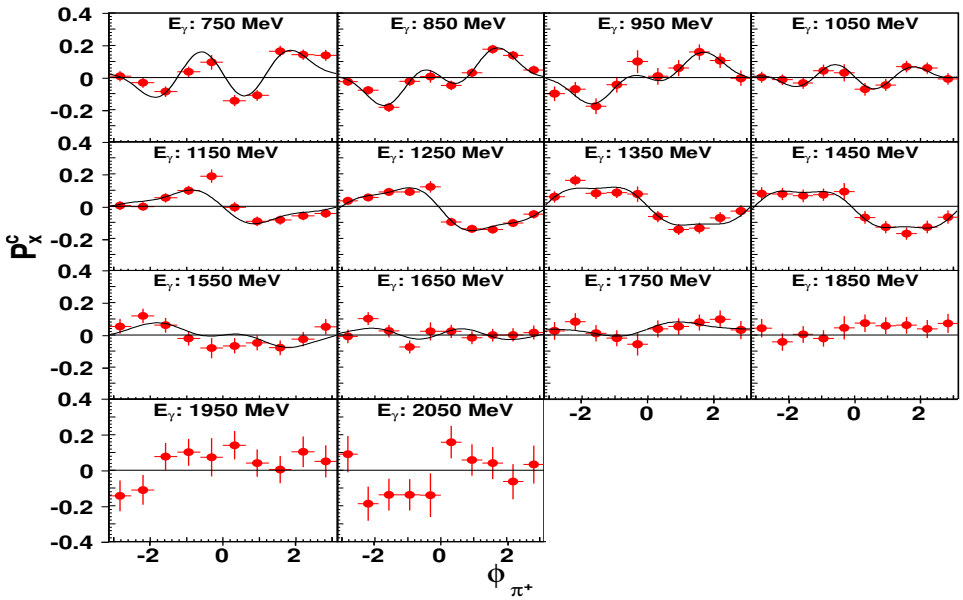

Figure 6.65: A quasi-3D plot showing first-time measurement of $\mathbf{P_x^c}$ along with third-order Fourier sine fits. Results are shown for $0.0 < \cos\theta_{\pi^+} < 1.0$. The error bars shown are statistical only.

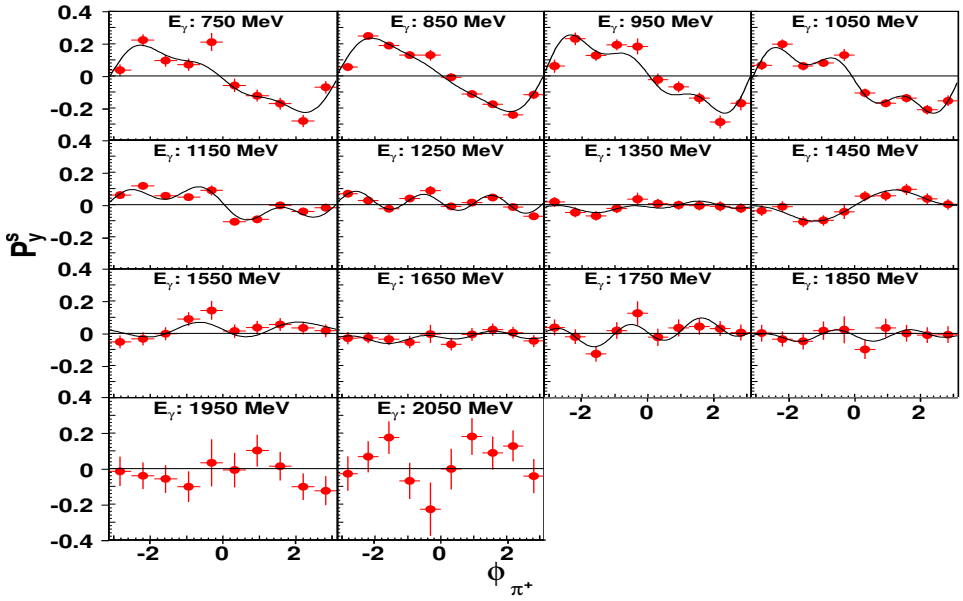

Figure 6.66: A quasi-3D plot showing first-time measurement of $\mathbf{P_y^s}$ along with third-order Fourier sine fits. Results are shown for $-1.0 < \cos\theta_{\pi^+} < 0.0$. The error bars shown are statistical only.

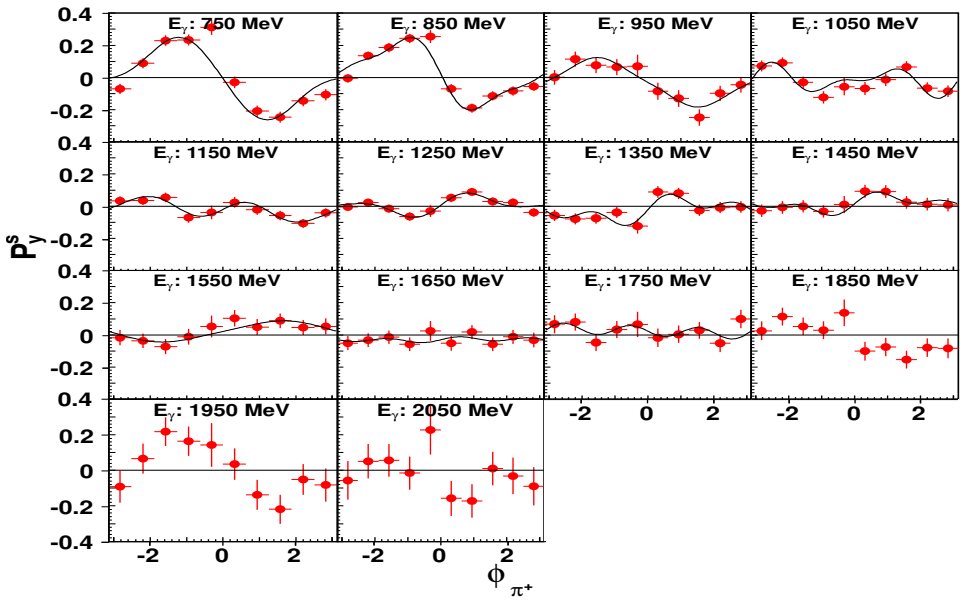

Figure 6.67: A quasi-3D plot showing first-time measurement of $\mathbf{P_y^s}$ along with third-order Fourier sine fits. Results are shown for $0.0 < \cos\theta_{\pi^+} < 1.0$. The error bars shown are statistical only.

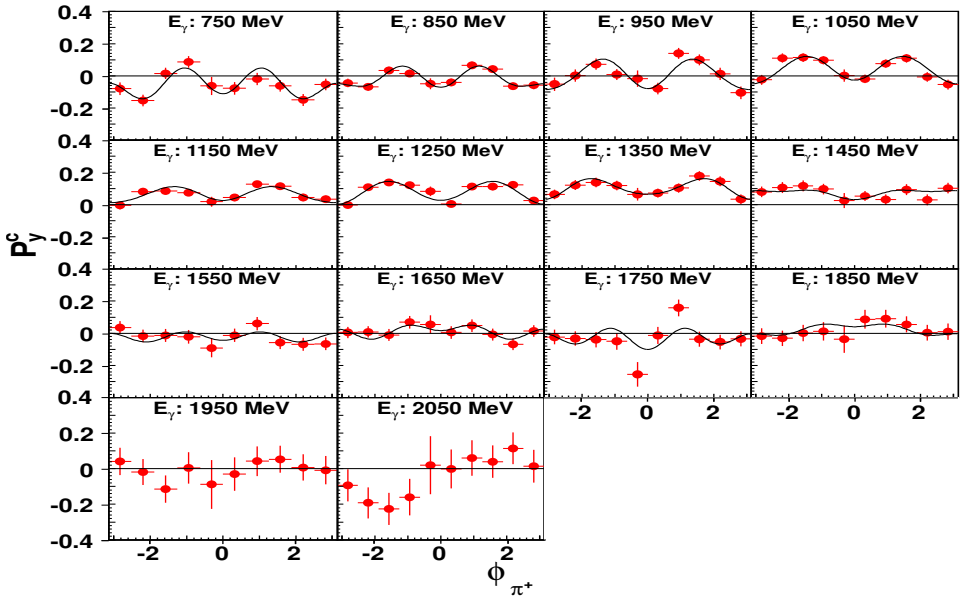

Figure 6.68: A quasi-3D plot showing first-time measurement of $\mathbf{P_y^c}$ along with third-order Fourier cosine fits. Results are shown for $-1.0 < \cos\theta_{\pi^+} < 0.0$. The error bars shown are statistical only.

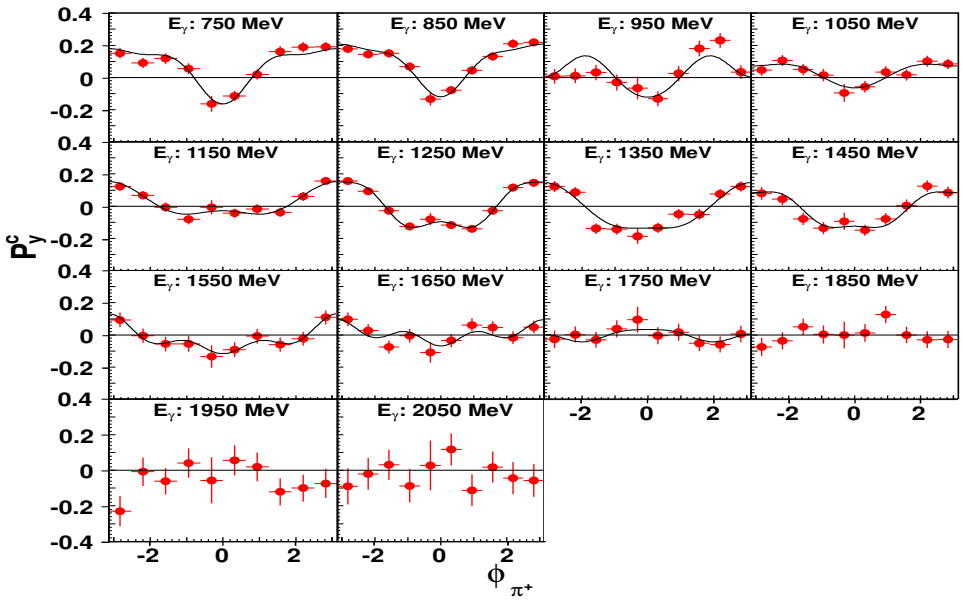

Figure 6.69: A quasi-3D plot showing first-time measurement of $\mathbf{P_y^c}$ along with third-order Fourier cosine fits. Results are shown for $0.0 < \cos\theta_{\pi^+} < 1.0$. The error bars shown are statistical only.

CHAPTER 7

SUMMARY AND OUTLOOK

One of the most challenging problems faced by the nuclear physics community at present is understanding how quark-gluon interactions give rise to protons and neutrons, the building blocks of matter. In this non-perturbative energy regime, confinement — the phenomena which keeps quarks *confined* within nucleons — is observed, however its origin is not well understood. Since Quantum Chromodynamics, the theory of strong force, cannot be analytically solved in this energy regime, physicists resort to other smart tools, such as baryon spectroscopy, to answer these questions. Similar to the way atomic spectroscopy plays a crucial role in understanding electromagnetic interactions in an atom, baryon spectroscopy illuminates QCD interactions in a baryon, which is a nucleon constituting three valence quarks. By studying the overall features of the baryon spectrum, one can get an insight into the underlying effective degrees of freedom in baryons and their evolution with the energy of the system. However, unlike atomic spectroscopy, baryon spectroscopy is very complicated due to the broad and overlapping nature of the baryon resonances, and the situation is exacerbated by the presence of a very complex background. Therefore, it is absolutely crucial to perform polarized experiments and extract certain observables called 'polarization observables' in addition to the differential cross sections in order to disentangle the resonances.

Currently, the baryon spectrum is not well understood, particularly above ~ 1.7 GeV/c^2 where many excited states have been predicted by various phenomenological models as well as lattice-QCD calculations but they have not been experimentally observed. A possible explanation for these *missing* resonances is that they perhaps do not couple strongly to the probes which have been predominantly used to perform spectroscopy, namely the pion beams. Furthermore, most of the reactions which have been studied in the past involved only a single (light) pseudoscalar meson in the final state, such as $N\,\pi$. It has been predicted that the high mass resonances couple strongly to photon beams instead of pion beams and preferably decay into heavier mesons, such as the vector mesons ω and ρ, or decay sequentially into multi-pion final states via intermediate resonances. As a matter of fact, the two-pion photoproduction reaction is the dominant contributor

to the total photo-absorption cross section at high energies where the problem of missing resonances needs to be examined. In addition to revealing many missing resonances, the study of vector meson and two-pion photoproduction reactions can also help in further investigating poorly understood properties of various known resonances. However, the data base of polarization observables for these reactions has remained rather sparse till date. These factors motivated the extraction of polarization observables for ω and $\pi^+\pi^-$ photoproduction reactions in this thesis. The $\pi^+\pi^-$ reaction offers an additional advantage: the resonances which decay to the (broad) ρ vector meson along with a proton can be extracted indirectly from this reaction in a partial-wave analysis. The polarization observables were extracted using data from the FROST experiment, a vigorous program conducted at Jefferson Lab between 2007 and 2010 to perform polarized measurements with all possible beam and target polarizations covering energies up to about 2.3 GeV in center-of-mass.

In this thesis, five ($\mathbf{\Sigma}$, $\mathbf{T}$, $\mathbf{H}$, $\mathbf{P}$, $\mathbf{F}$) out of the seven polarization observables associated with beam and/or target polarizations have been extracted for the $\vec{\gamma}\vec{p} \to p\omega$ reaction, where the ω meson was reconstructed from the $\pi^+\pi^-\pi^0$ decay mode. The observables $\mathbf{\Sigma}$ (the beam asymmetry), $\mathbf{H}$ and $\mathbf{P}$ (double-polarization observables) have been measured from the reaction threshold to $W = 2.2$ GeV, while $\mathbf{T}$ (the target asymmetry) and $\mathbf{F}$ (a double-polarization observable) have been measured in the energy range $W \in [1.77, 2.48]$ GeV. All measurements, except for $\mathbf{\Sigma}$ below $W = 2.0$ GeV, are first-time measurements. Furthermore, eight out of 13 polarization observables accessible from the FROST experiment for the reaction $\vec{\gamma}\vec{p} \to p\pi^+\pi^-$ have been extracted in this analysis, covering the energy range $W \in [1.5, 2.2]$ GeV. They are $\mathbf{I^{s,c}}$ (beam-polarization observables), $\mathbf{P_{x,y}}$ (target-polarization observables) and $\mathbf{P^{s,c}_{x,y}}$ (double-polarization observables). All of them are first-time measurements.

Thus, this thesis represents a comprehensive analysis of vector meson photoproduction decaying to multi-pion final states, which are the ω and ρ mesons, as well as the $\pi^+\pi^-$ photoproduction reaction. The results presented here, all of which (except for $\mathbf{\Sigma}$ at low energies) are first-time measurements, will significantly expand the world database of polarization observables for the ω and $\pi^+\pi^-$ photoproduction reactions. The inclusion of these observables in partial-wave analyses and other model-based fits is highly expected to introduce tighter constraints and thus greatly aid in the identification of the resonant contributions to these reactions with minimal ambiguities. For instance, the recent addition of polarization observables $\mathbf{\Sigma}$, $\mathbf{E}$, $\mathbf{G}$ and polarized SDMEs for ω

photoproduction to the BnGa data base [35] provided further evidence for eight resonances including four poorly known resonances with $(* *)$ rating ($N(1880)1/2^+$, $N(1895)1/2^-$, $N(2000)5/2^+$, $N(2120)3/2^-$) in their partial-wave fits. Their analysis also provided suggestive evidence for at least one new state at about 2.2 GeV. The inclusion of many more high-quality single- as well as double-polarization observables from this analysis is expected to shed more light on the contribution of these states and also reveal more resonances. Our results have been recently approved by the CLAS collaboration and we are working closely with the BnGa group for obtaining partial-wave fits to the new data using a coupled-channel approach. Many publications are being planned for the near future.

Several other analyses on polarization observables using the FROST data are nearing completion. While the results from the FROST experiment will deeply enhance our knowledge about the N^* and Δ members of the multiplets of the light baryon spectrum, the new capabilities of the 12 GeV upgrade at Jefferson Lab will provide complementary information on the strange members of the light baryon multiplets. These information, put together with existing and upcoming results on heavy flavor baryons from facilities abroad, such as from LHCb and BELLE, will present a complete study of the baryon spectrum. The knowledge gained from such studies will immensely contribute to our understanding of the manifestation of QCD in baryons.

APPENDIX A

DETERMINATION OF AZIMUTHAL AND POLAR ANGLE CORRECTIONS

The holding field surrounding the butanol target was 0.5 T in strength and considerably weaker than the polarizing field of 5 T. Nevertheless, it was observed that the holding field exerted a magnetic force on charged particles leaving the target which was not accounted for in the *cooking*. This effect led to small deviations in the reconstruction from the true trajectory. The issue was discussed in Section 3.6.4. We utilized 4C kinematic fitting (no missing particle) to determine the angle corrections. Thus, events from Topology 4 were used for this purpose. Our aim was to develop β_z-dependent angle corrections to simplify this multi-dimensional problem. We acknowledge that this approach cannot be the full solution but represents the best we could do in this analysis. A description of the procedure is given in this appendix.

We applied ELoss and momentum corrections to the four-vectors of all final-state particles and extracted the azimuthal angles, $\phi_{\text{exp.}}$, from the particles' three-momenta. The events were

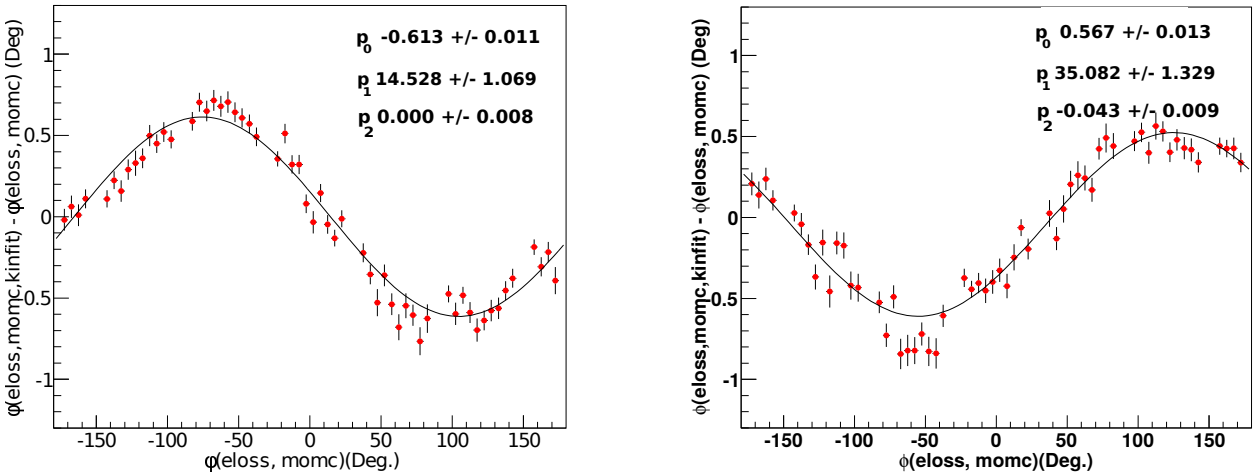

Figure A.1: Examples of $(\phi_{\text{fit.}} - \phi_{\text{exp.}})$ versus ϕ_{exp} distributions for the π^+ from FROST-g9b data. Left: A positive holding field. Right: A negative holding field. Note the flip in sign of the modulation when the direction of the holding field is reversed. The two distributions were obtained from events with $\beta_z \in [0.6, 0.7]$.

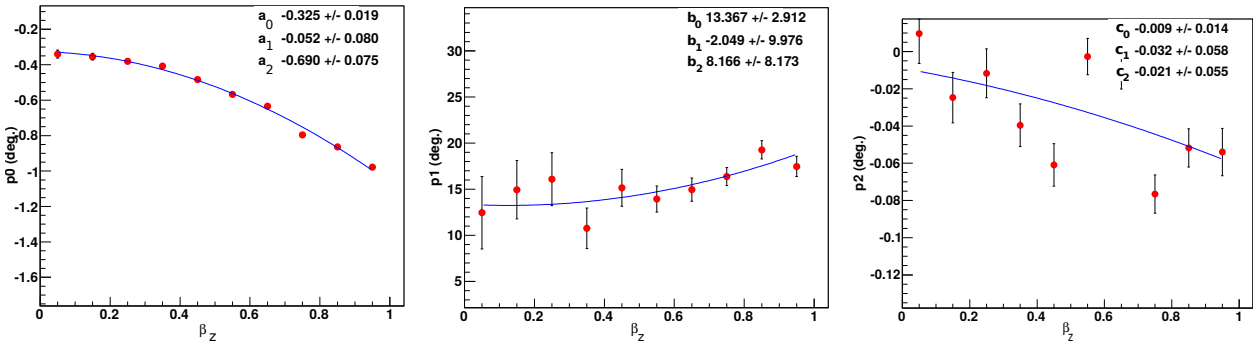

Figure A.2: Example of the β_z dependence of the fit parameters p_0 (left), p_1 (center) and p_2 (right) obtained from fitting $(\phi_{\,\mathrm{fit}} - \phi_{\,\mathrm{exp.}})$ versus $\phi_{\,\mathrm{exp.}}$ histograms for the π^+ in various β_z bins. The plots are based on FROST-g9b data with a positive holding field.

then kinematically fitted in order to extract the expected azimuthal angles, $\phi_{\,\mathrm{fit}}$. To develop β_z-dependent angle corrections, the data were divided into various β_z bins and a $(\phi_{\,\mathrm{fit}} - \phi_{\,\mathrm{exp.}})$ versus $\phi_{\,\mathrm{exp.}}$ histogram was prepared for each of these bins. The distributions were fitted with a function of the form:

$$\phi_{\,\mathrm{fit}} - \phi_{\,\mathrm{exp.}} \;=\; p_0 \sin\left(\frac{\pi}{180}\,(\phi_{\,\mathrm{exp.}} - p_1)\right) + p_2\,, \tag{A.1}$$

where the angles and fit parameters, p_i, were in degrees. Figure A.1 shows examples of $(\phi_{\,\mathrm{fit}} - \phi_{\,\mathrm{exp.}})$ versus $\phi_{\,\mathrm{exp.}}$ distributions in a $\beta_z \in [0.6, 0.7]$ bin. We see that the modulation changed its phase by 180° when the direction of the holding field was reversed. This was a clear indication that the observed modulations could be traced back to the holding field. Overall, the azimuthal angle is shifted by less than a degree and can be considered fairly small for an individual track. To find the functional dependence of the fit parameters p_0, p_1, and p_2 on β_z, they were plotted versus β_z (an example is shown in Figure A.2) and fitted with polynomial functions:

$$\begin{aligned}
p_0^{\mathrm{particle}} &= a_0 \,+\, a_1\,\beta_z^{\mathrm{particle}} \,+\, a_2\,(\beta_z^{\mathrm{particle}})^2 \\
p_1^{\mathrm{particle}} &= b_0 \,+\, b_1\,\beta_z^{\mathrm{particle}} \,+\, b_2\,(\beta_z^{\mathrm{particle}})^2 \\
p_2^{\mathrm{particle}} &= c_0 \,+\, c_1\,\beta_z^{\mathrm{particle}} \,+\, c_2\,(\beta_z^{\mathrm{particle}})^2
\end{aligned} \tag{A.2}$$

The values of the fit parameters a_0, a_1, a_2, etc. are given in Table A.1. We then finalized the correction functions for the azimuthal angles by combining the above information:

$$\phi_{\,\mathrm{corrected}} \;=\; \phi_{\,\mathrm{uncorrected}} \,+\, p_0 \sin\left(\frac{\pi}{180}\,(\phi_{\,\mathrm{uncorrected}} - p_1)\right) + p_2\,, \tag{A.3}$$

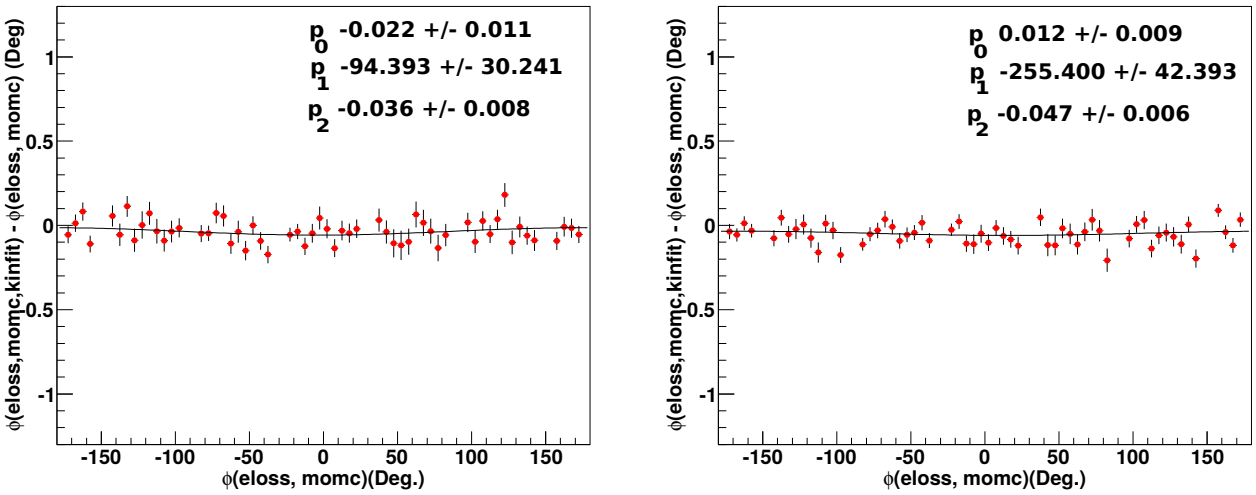

Figure A.3: The $(\phi_{\text{fit}} - \phi_{\text{exp.}})$ versus $\phi_{\text{exp.}}$ histograms of the π^+ from Figure A.1 after applying the azimuthal angle corrections. The previously-observed modulations were successfully removed.

The fit parameters p_0, p_1 and p_2 have different values depending on the particle type, β_z of the particle and the sign of the holding field, which is evident from Equation A.2 and Table A.1.

To demonstrate the effectiveness of our efforts, Figure A.3 shows the $(\phi_{\text{fit}} - \phi_{\text{exp.}})$ versus $\phi_{\text{exp.}}$ histograms from Figure A.1 after applying our corrections. The figure clearly shows that the modulations disappeared.

Table A.1: Values of the polynomial fit parameters that describe the behaviour of p_0, p_1 and p_2 as a function of β_z (see Equation A.2). The function form of p_0, p_1 and p_2 could be used in Equation A.3 to obtain the β_z-dependent azimuthal angle corrections for FROST-g9b.

Field Sign	Particle	Parameters for p_0			Parameters for p_1			Parameters for p_2		
		a_0 (°)	a_1 (°)	a_2 (°)	b_0 (°)	b_1 (°)	b_2 (°)	c_0 (°)	c_1 (°)	c_2 (°)
+	proton	0.34	−4.56	4.40	18.0	0.0	0.0	−0.06	0.0	0.0
	π^+	−0.33	−0.05	−0.69	13.4	−2.0	8.2	0.0	0.0	0.0
	π^-	−0.59	−0.70	−0.11	6.6	121.3	−191.7	0.0	0.0	0.0
−	proton	−0.21	4.1	−4.0	43.1	−31.4	30.4	−0.07	0.0	0.0
	π^+	0.28	0.24	0.46	38.0	−17.0	16.6	0.0	0.0	0.0
	π^-	0.53	−0.73	0.21	42.1	−111.6	200.8	0.0	0.0	0.0

The same procedure was employed to determine correction functions for the lab polar angles, $\theta_{\rm lab}$. The data were again separated into various β_z bins as explained above. Figure A.4 (top row) shows examples of $(\theta_{\rm fit} - \theta_{\rm exp.})$ versus $\phi_{\rm exp.}$ distributions. The observed modulations are smaller but still significant. The histograms were fitted with a sine function (given by Equation A.4 below) and the extracted fit parameters were then plotted versus β_z:

$$\theta_{\rm fit} - \theta_{\rm exp.} \;=\; P_0 \sin\left(\frac{\pi}{180}\left(\phi_{\rm exp.} - P_1\right)\right) \;+\; P_2\,, \tag{A.4}$$

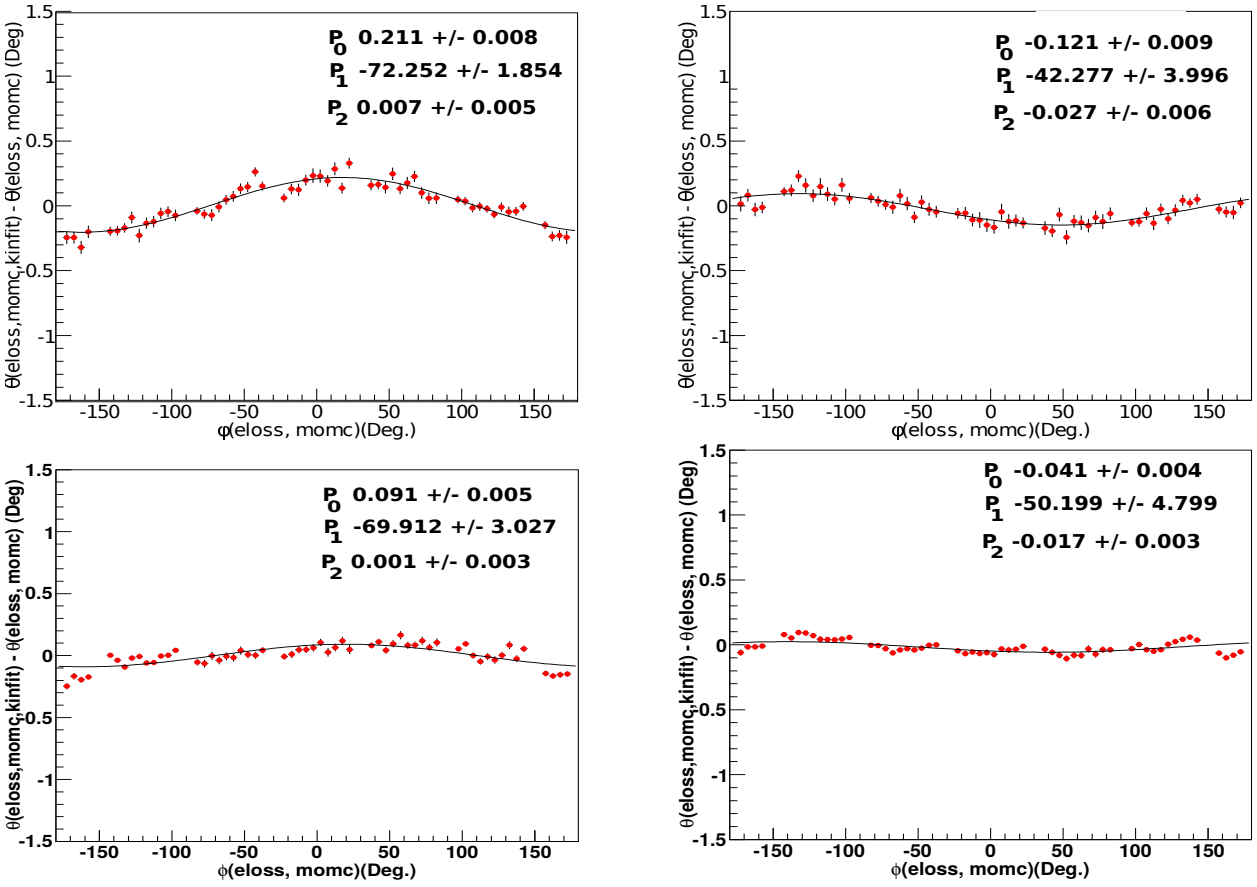

Figure A.4: Examples of $(\theta_{\rm fit.} - \theta_{\rm exp.})$ versus $\phi_{\rm exp.}$ distributions for the π^+ from FROST-g9b data before (top row) and after (bottom row) applying our polar-angle corrections. The plots shown are for $\beta_z \in [0.6, 0.7]$ and were obtained from a data set with a positive (negative) holding field, respectively. The developed polar-angle corrections effectively removed the observed modulations.

Similar to the procedure for the azimuthal angles, these distributions were fitted with polynomial functions to find the β_z-dependence of the parameters:

$$\begin{aligned} P_0^{\text{particle}} &= A_0 + A_1\,\beta_z^{\text{particle}} + A_2\,(\beta_z^{\text{particle}})^2 \\ P_1^{\text{particle}} &= B_0 + B_1\,\beta_z^{\text{particle}} + B_2\,(\beta_z^{\text{particle}})^2 \\ P_2^{\text{particle}} &= C_0 + C_1\,\beta_z^{\text{particle}} + C_2\,(\beta_z^{\text{particle}})^2 \end{aligned} \tag{A.5}$$

The values of the polynomial fit parameters A_0, A_1, A_2 etc. are given in Table A.2. We finally obtained the correction functions for the polar angles by using Equation(s) A.5 along with the values from Table A.2:

$$\theta_{\text{corrected}} = \theta_{\text{uncorrected}} + P_0 \sin\left(\frac{\pi}{180}\,(\phi_{\text{exp.}} - P_1)\right) + P_2\,. \tag{A.6}$$

Figure A.4 (bottom row) shows that the polar-angle corrections were successful in removing the previously-observed modulations in $(\theta_{\text{fit}} - \theta_{\text{exp.}})$ versus $\phi_{\text{exp.}}$ distributions shown in the top row. Last not least, it is worth mentioning that we used the same corrections for the linearly- as well as circularly-polarized g9b data.

Table A.2: Values of the polynomial fit parameters that describe the behaviour of P_0, P_1 and P_2 as a function of β_z (see Equation A.5). The function form of P_0, P_1 and P_2 could be used in Equation A.6 to obtain the β_z-dependent polar-angle corrections for FROST-g9b.

Field Sign	Particle	Parameters for P_0			Parameters for P_1			Parameters for P_2		
		$A_0\,(^\circ)$	$A_1\,(^\circ)$	$A_2\,(^\circ)$	$B_0\,(^\circ)$	$B_1\,(^\circ)$	$B_2\,(^\circ)$	$C_0\,(^\circ)$	$C_1\,(^\circ)$	$C_2\,(^\circ)$
+	proton	0.04	1.4	−1.6	−92.9	82.6	−54.5	−0.36	1.3	−1.14
	π^+	0.09	−0.07	0.4	−54.0	−38.3	23.7	−0.10	0.32	−0.24
	π^-	0.0	0.0	0.0	0.0	0.0	0.0	0.0	0.0	0.0
−	proton	−0.14	−0.9	1.1	−46.3	−41.2	29.4	−0.07	0.0	0.0
	π^+	−0.03	0.17	−0.52	−160.6	289.8	−189.9	−0.05	0.0	0.0
	π^-	−0.21	0.59	−0.50	−242.6	−19.3	−12.8	0.0	0.0	0.0

APPENDIX B

DEFINITION OF THE ANGLES α AND β

The angle β denoted the angle of inclination of the polarization of a linearly-polarized beam relative to the x-axis in the center-of-mass production plane. It would be defined as positive if the x-axis was rotated counter-clockwise from the beam polarization. The definition of the x, y, z coordinate system:

- The z-axis was chosen to be along the direction of the incoming photon beam.
- The y-axis was defined as:

$$\hat{y} = \frac{\hat{p}_{recoil} \times \hat{z}}{|\hat{p}_{recoil} \times \hat{z}|}, \tag{B.1}$$

  where $\hat{p}_{recoil}$ was a unit vector along the momentum of the chosen recoil particle.

Figure B.1 illustrates β and its relation with the lab azimuthal angle of the recoil particle.

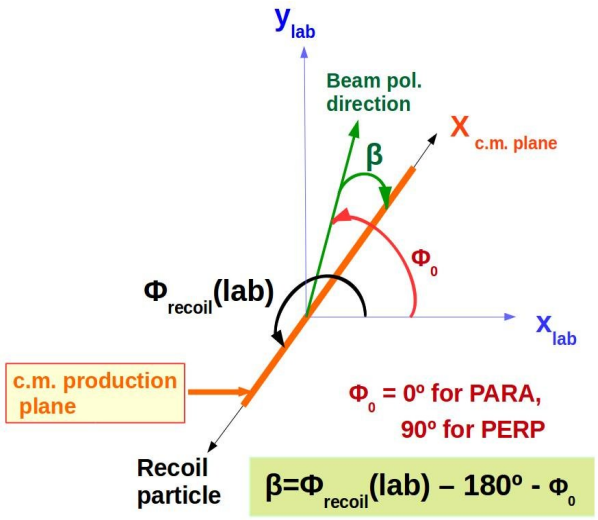

Figure B.1: A schematic diagram for β, which was defined as the angle between the linear-beam polarization and the x-axis in the center-of-mass plane. The diagram also shows the relation between β and the azimuthal angle of the recoil particle in the laboratory frame, ϕ_{recoil} (lab).

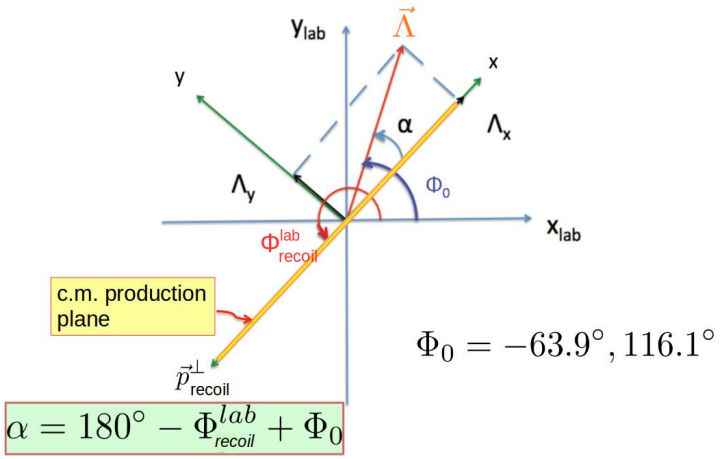

Figure B.2: A schematic diagram to depict α, which was defined as the angle between the transverse target polarization and the x-axis in the center-of-mass plane. The figure also shows the relation between α, the target offset, ϕ_0, and the azimuthal angle of the recoil particle in the laboratory frame, ϕ^{lab}_{recoil}). Courtesy of Aneta Netz (University of South Carolina).

The angle α was defined as the angle between the transverse polarization of the target and the x-axis in the center-of-mass production plane, such that it would be positive if the x-axis was rotated clockwise from the target polarization. In FROST, the transverse target polarization (when positively polarized) was inclined at an angle $\phi_0 = 116.1°$ with respect to the laboratory floor. Figure B.2 shows a schematic diagram to illustrate the definition of α.

APPENDIX C

COMPARISON OF T FROM DIFFERENT PERIOD COMBINATIONS

The FROST-g9b *circular* data sets were divided into five periods, as shown in Table 3.4. Out of these, Periods 2 and 4 had a negatively-polarized target and the remaining periods had a positively-polarized target. The possible ways to combine the periods to form asymmetries and extract the target-polarization observable **T** for the ω reaction were:

Per1-2, Per3-2, Per5-2, Per1-4, Per3-4 and Per5-4.

The **T** observable was extracted using each of the above combinations and the results were compared with each other. It was observed that only three out of the six combinations gave consistent results. These were:

Per1-2, Per3-2 and Per5-4.

Upon studying these results, we noticed that Periods 1, 2 and 3 had the same holding field sign ('+' sign). As a matter of fact, Periods 1 and 3 had the same overall run conditions. Periods 4 and 5 also had the same holding field sign ('−' sign). This suggested that the *good* period combinations were the ones that had the same holding field sign, possibly because any effect of the holding field on the acceptance was canceled out in the asymmetry measurement. Figure C.1 (left) shows a comparison between **T** extracted from Per1-2 (red circles), Per3-2 (magenta triangles) and Per5-4 (gray squares) in various energy bins. The observables were in good agreement. On the other hand, we see in Figure C.1 (right) that the observables extracted from Per1-4 (blue circles), Per3-4 (blue triangles) and Per5-2 (brown squares) are consistently shifted above or below the average of the results from Per1-2, Per3-2 and Per5-4 (red circles). This was observed at all energies, some of which are shown here as examples. Other analyses that used the same data to study other channels [85, 86] confirmed that the best combination of periods to extract the observables were the combinations Per1-2, Per3-2 and Per5-4, indeed. Since Periods 1 and 3 had the same run conditions, they were combined in our analysis and referred to as Per13.

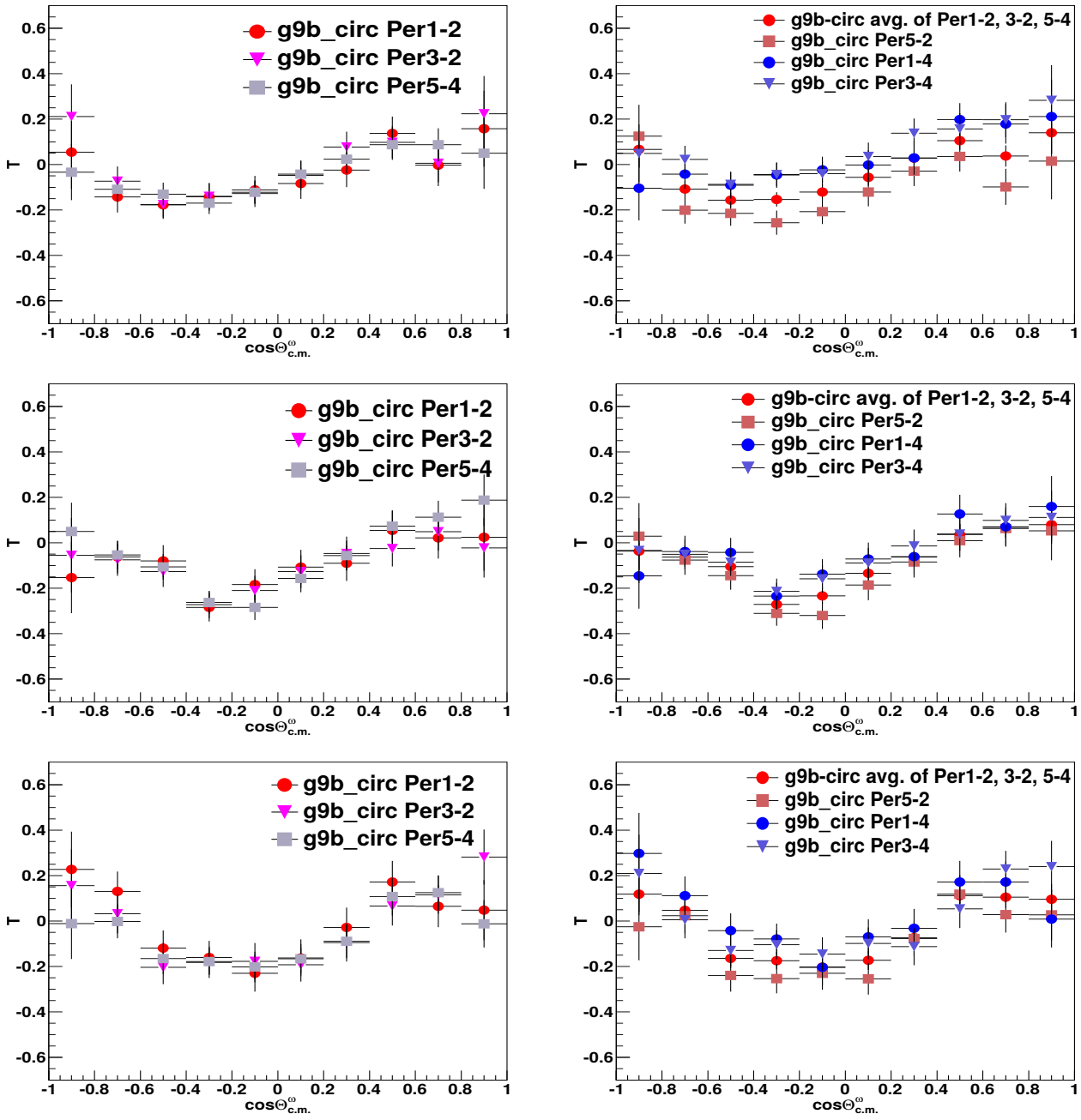

Figure C.1: (Left) A comparison between **T** extracted from Per1-2 (red circles), Per3-2 (magenta triangles) and Per5-4 (gray squares) in the energy bins $E \in [1.3, 1.4]$ GeV (top), $[1.4, 1.5]$ GeV (middle) and $[1.5, 1.6]$ GeV (bottom). The observables are in a good agreement within errors in all energy bins. (Right) A comparison between **T** extracted from Per1-4 (blue circles), Per3-4 (blue triangles), Per5-2 (brown squares) and the uncertainty-weighted average of the results from Per1-2, Per3-2 and Per5-4 (red circles) in the energy bins $E \in [1.3, 1.4]$ GeV (top), $[1.4, 1.5]$ GeV (middle) and $[1.5, 1.6]$ GeV (bottom). The results from Per1-4, Per3-4 and Per5-2 are consistently shifted either above or below the averaged results from Per1-2, Per3-2 and Per5-4 in all energy bins.

APPENDIX D

SYSTEMATIC UNCERTAINTY IN FROST-G9B FLUX NORMALIZATION

The normalization factors were determined from the CH_2 target since the gflux files were not available. One way to estimate the uncertainty in the flux normalization was to find the relative difference between the ratios obtained from the different targets, i.e. from carbon and CH_2. Figure D.1 shows a comparison of the ratios from these two targets as a function of energy (numerical values taken from Table 3.16). We found that the relative difference was always $< 2\,\%$ at all energies in g9b (linearly- as well as circularly-polarized data sets). Furthermore, to assess any systematic effect of the detector acceptance in these flux ratios, results from this method were compared with two other methods.

D.0.4 Ratios from gflux in FROST-g9a

Since gflux files were available in FROST-g9a, the two methods were compared using these data. Table D.1 and Figure D.2 (left) show the results for the three period combinations which were made based on opposite target polarizations. It was observed in the 'combination-32' that the flux ratio between Period 3 (runs 55556-55595) and Period 2 (55521-55555) from CH_2 was lower than the ratio from gflux by only $1.3\,\%$. Similarly, in 'combination-67' (where Period 6 consisted of runs 56164-56193 and Period 7 consisted of runs 56196-56233), the ratio from CH_2 was lower by only $1.6\,\%$. However, in 'combination-45' (where Period 4 consisted of runs 55604-55625 and Period 5 consisted of runs 55630-55678) the ratio obtained from CH_2 was found to be higher by about $10\,\%$. This discrepancy seemed to be a significant overestimation since the differences were much smaller (and fairly consistent) for the other period combinations; these data were taken before and after Periods 4 & 5, respectively. Therefore, we quoted the fractional difference in the ratios obtained from gflux and CH_2 to be less than $2\,\%$.

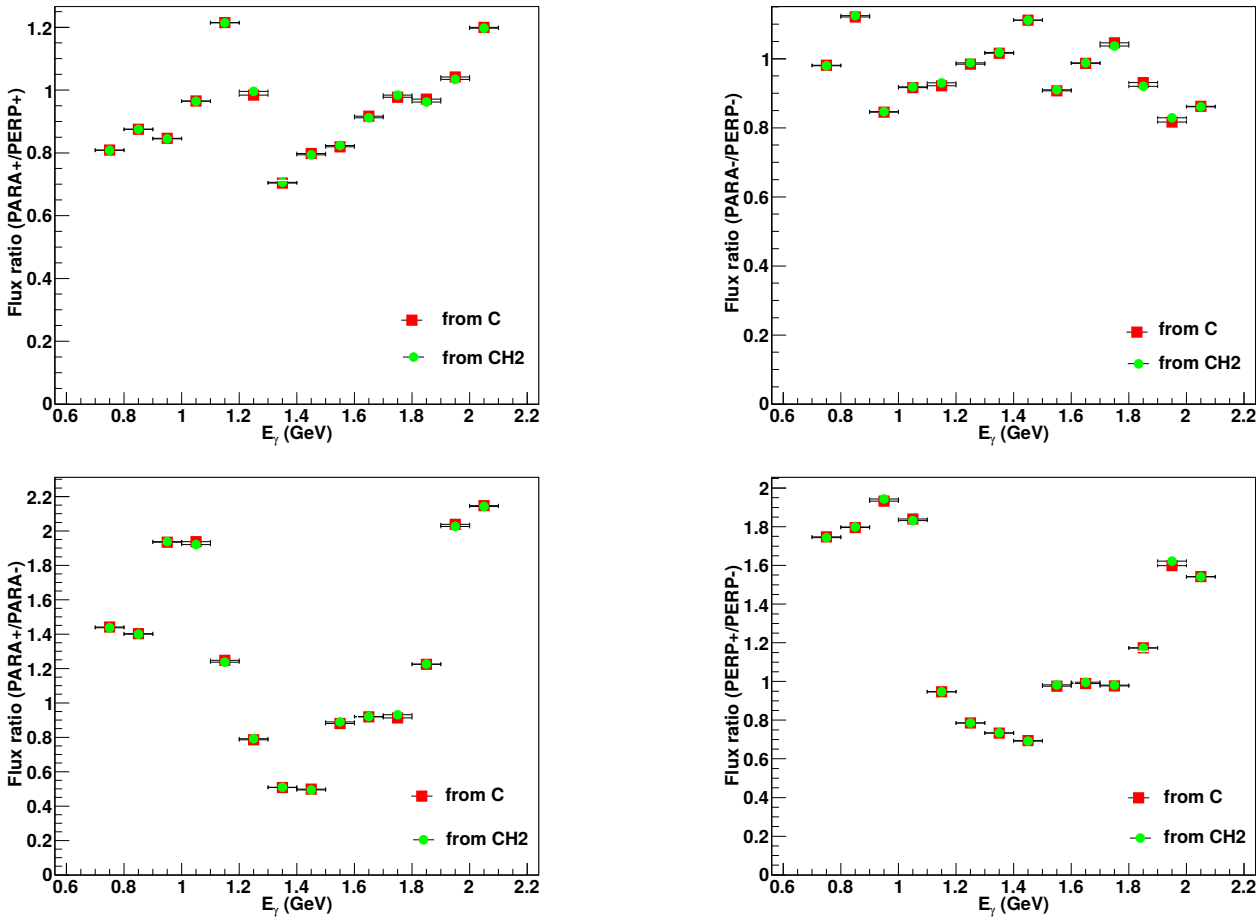

Figure D.1: A comparison of the flux ratios in FROST-g9b (with linearly-polarized photons) from the carbon target (red squares) and the CH_2 target (green circles). The top row shows the comparison of the flux ratios for data sets with the same target setting but different beam settings and the bottom row shows the comparison for data sets with the same beam setting but different target settings. The ratios are compared at all available 100 MeV wide energy bins ranging from 0.7 to 2.1 GeV.

D.0.5 Ratios from fitting angular distributions in FROST-g9b

Another way to determine the flux ratios was by using them as fit parameters when extracting the asymmetries. The reaction $\gamma p \to p\,\omega$ was utilized to perform this study since it was a simpler reaction with fewer kinematic variables and polarization observables than in the $\pi^+\pi^-$ reaction. Our study was along the lines of the procedure that was described in [84].

In FROST-g9b with circularly-polarized photons, flux ratios for the period combinations 13-2

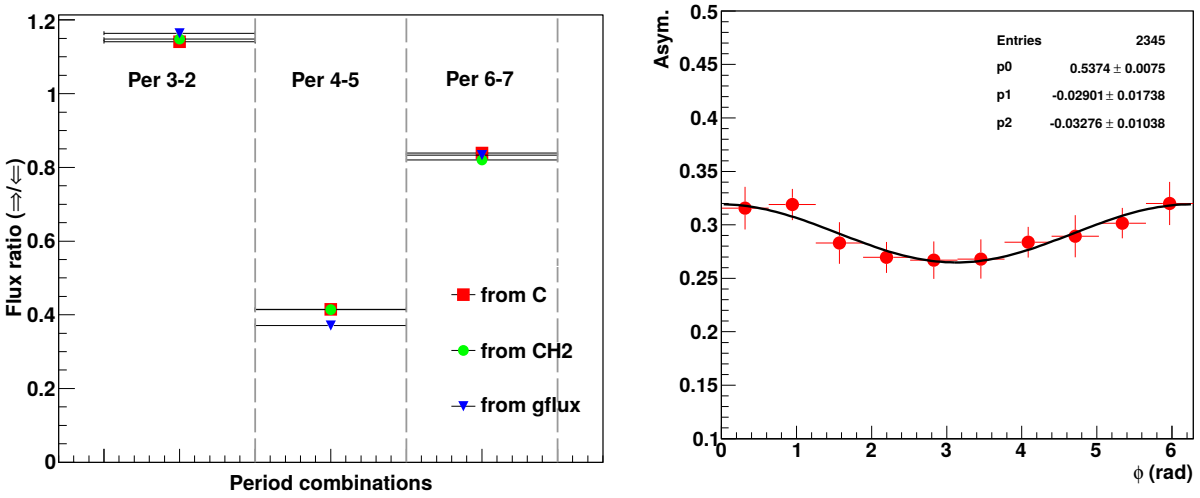

Figure D.2: (Left) A comparison of the photon flux ratios in FROST-g9a obtained from the C target (red squares), CH_2 target (green circles) and gflux files (blue inverted triangles) to assess the systematic error in the flux normalization. (Right) A plot of the asymmetry (red circles) between unscaled Period(s) 13 and Period 2 data sets from FROST-g9b with positive helicities. The data were integrated over all $\cos\Theta^{\omega}_{\text{c.m.}}$ angles and photon energies. The asymmetry was fitted with the fit function given by Equation D.1 with Φ_R, $\mathbf{T}$ and $\mathbf{F}$ as fit parameters.

Table D.1: A comparison of the photon flux ratios in FROST-g9a obtained from the C target, CH_2 target and gflux files. The ratios obtained from CH_2 were lower than the ratios from gflux files by less than 2 % in combinations-32 and 67. In combination-45, the fractional difference was 10 % which seems to be a significant overestimation.

Flux Ratio from	Ratio $N = \Phi(\Rightarrow)/\Phi(\Leftarrow)$		
	per-3/per-2	per-4/per-5	per-6/per-7
C	1.141	0.415	0.839
CH_2	1.148	0.414	0.820
GFLUX	1.164	0.371	0.833

and 5-4 were required. To determine $\Phi(\rightarrow, +)\,/\,\Phi(\rightarrow, -)$ between Per-13 and Per-2, an asymmetry was formed between the two data sets *without* scaling either of them. The asymmetry could be expressed as:

$$A(\phi) = \frac{(1 - \Phi_R) + (1 + \Phi_R P_R)\,(\bar{\Lambda}^+\,\bar{\delta}_\odot\,\mathbf{F}\cos(\phi - \phi_0) + \bar{\Lambda}^+\,\mathbf{T}\sin(\phi - \phi_0)\,)}{(1 + \Phi_R) + (1 - \Phi_R P_R)\,(\bar{\Lambda}^+\,\bar{\delta}_\odot\,\mathbf{F}\cos(\phi - \phi_0) + \bar{\Lambda}^+\,\mathbf{T}\sin(\phi - \phi_0)\,)}\,, \qquad \text{(D.1)}$$

where $\Phi_R = \Phi(\rightarrow, -) \,/\, \Phi(\rightarrow, +) = \Phi(-) \,/\, \Phi(+)$, $P_R = \bar{\Lambda}^- \,/\, \bar{\Lambda}^+$, and ϕ_0 represented the target offset angle defined in Section 3.7.6. The flux ratio Φ_R and the polarization observables **T** and **F** were used as fit parameters. Note that if P_R was also used as a fit parameter, then the fit would fail to converge since it had too much freedom. The asymmetries between the Q-value-weighted $\phi_{\rm lab}$ histograms were made by integrating over all $\cos\Theta^{\omega}_{\rm c.m.}$ angles since ideally, the flux ratios should be independent of this variable. Furthermore, the ratios were also independent of energy, so the data were integrated over all energies to increase the statistics. The fitted asymmetry between the Per 13 and Per 2 data sets with positive beam helicity is shown in Figure D.2 (right). The same procedure was repeated for the negative helicity data sets from the Per 13 - Per 2 combination and also for both helicities from the Per 5 - Per 4 combination. The results are shown in Table D.2. It was observed that the flux ratios from CH_2 were systematically lower by about 1.3 % and 1.9 % than the average ratios obtained from the fitting technique for Per 2-13 and Per 4-5, respectively. Unfortunately, this latter method could not be used to find reliable values for the different coherent-edge data sets in FROST-g9b, mainly because there were more fit parameters (flux ratio, **Σ**, **T**, **H**, and **P**) compared to the circularly-polarized data set but not enough statistics.

In conclusion, the above studies showed that the systematic uncertainty in the flux normalization factors from CH_2 was less than 2 % in FROST-g9a as well as in FROST-g9b with a circularly-polarized photon beam. Since neither gflux nor any fitting technique could be used in FROST-g9b with linearly-polarized photons, the same estimate of 2 % was also used for this data set.

Table D.2: A comparison of the photon flux ratios in FROST-g9b obtained from fitting asymmetries and the ratios obtained from the C and CH_2 targets. The flux ratios obtained from CH_2 were found to be systematically lower by 1.3 % and 1.9 % than the average ratios obtained from the fitting technique for Periods 2-13 and Periods 4-5, respectively.

$\frac{\Phi(-)}{\Phi(+)}$	From fitting technique			From C	From CH_2
	Pos. helicity data	Neg. helicity data	Average		
Combination 2-13	0.537 ± 0.008	0.568 ± 0.008	0.553	0.546	0.546
Combination 4-5	1.311 ± 0.029	1.370 ± 0.016	1.341	1.299	1.316

APPENDIX E

POLARIZATION OBSERVABLES IN THE REACTION $\gamma p \to p\,\eta$

We extracted the polarization observable **T** from FROST-g9b data, respectively. Since we used the $\eta \to \pi^+\pi^-\pi^0$ decay mode and reconstructed the π^0 as a missing particle, the η analyses followed the exact same procedure as has been described in this analysis for the corresponding polarization observables in ω photoproduction. With the exception of the event-based background subtraction (Q-value method), which used the η peak rather than the ω peak, the **T** analysis for the η are essentially identical to the ω analyses. Some representative g9b η-mass distributions including the Q-factor-based signal and background distributions are presented in Figure E.1. Given the considerably smaller statistics in the η channel, we chose 200 MeV-wide energy bins.

Figure E.2 show our results for **T**. The observable in Figure E.2 is shown in comparison with published data from MAMI [87] and the Phoenics experiment in Bonn [88]. Our results are statistically not competitive and we have no plans to publish these results. However, from the plots we can clearly see that our definition of the target offset led to consistent results from our analysis and published results from other collaborations.

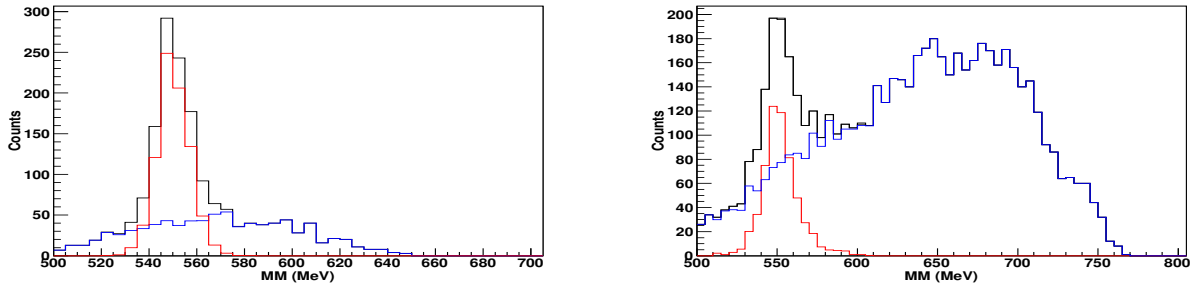

Figure E.1: Examples of g9b invariant $\pi^+\pi^-\pi^0$ distributions for the reaction $\gamma p \to p\,\eta$. Shown are 200-MeV wide energy bins with $E_\gamma \in [700, 900]$ MeV (left) and $E_\gamma \in [900, 1100]$ MeV (right). The black distributions denote the full mass distributions in each energy bin; the red and the blue distributions represent the Q-value weighted signal and background contributions, respectively.

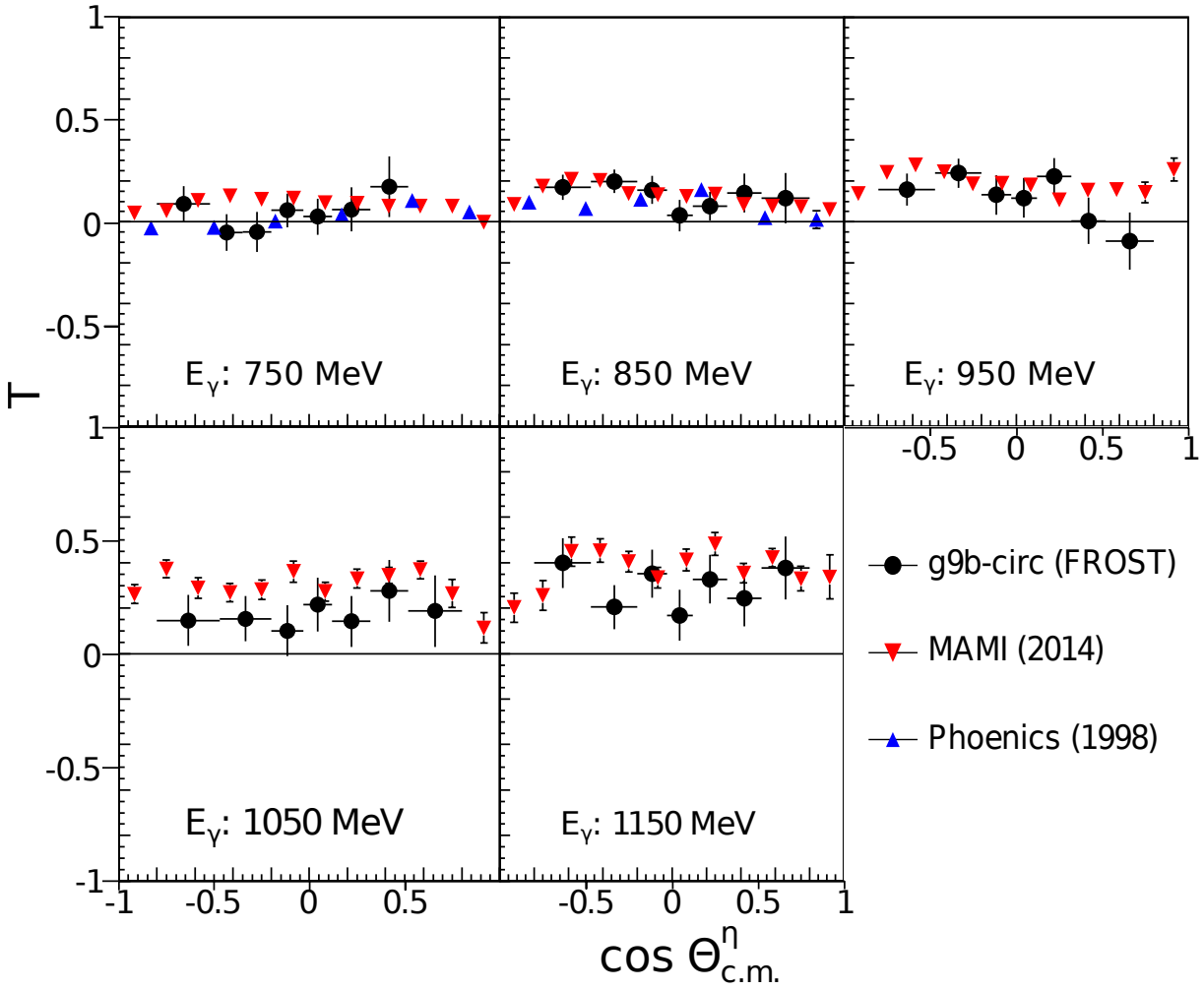

Figure E.2: Measurement of the target asymmetry in the reaction $\gamma p \to p\,\eta$ utilizing a circularly-polarized photon beam and a transversely-polarized target. The results are shown for the photon energy range $E_\gamma \in [\,750,\,1150\,]$ MeV.

BIBLIOGRAPHY

[1] D. J. Gross, "Twenty Five Years of Asymptotic Freedom," Nuclear Physics B (Proc. Suppl.) **74**, 426-446 (1999).

[2] S. Bethke, "Experimental Tests of Asymptotic Freedom," Prog. Part. Nucl. Phys. **58**, 351-386 (2007).

[3] V. Crede and W. Roberts, "Progress Towards Understanding Baryon Resonances," Rept. Prog. Phys. **76**, 076301 (2013).

[4] D. B. Lichtenberg *et al.*, "Quark-Diquark Model of Baryons and SU(6)," Phys. Rev. **167**, 1535 (1968).

[5] E. Oset *et al.*, "Dynamically Generated Resonances," Prog. Theor. Phys. Suppl. **186**, 124-133 (2010).

[6] S. Capstick and N. Isgur, "Baryons in a Relativized Quark Model with Chromodynamics," Phys. Rev. D **34**, 2809 (1986).

[7] K. Nakamura *et al.* (Particle Data Group), J. Phys. G **37**, 075021 (2010).

[8] R. Bradford *et al.*, "First Measurement of Beam-Recoil Observables C_x and C_z in Hyperon Photoproduction," Phys. Rev. C **75**, 035205 (2007).

[9] V. A. Nikonov *et al.*, "Further Evidence for $N(1900)P_{13}$ from Photoproduction of Hyperons," Phys. Lett. B **662**, 245 (2008).

[10] V. Sokhoyan *et al.*, "High Statistics Study of the Reaction $\gamma p \to p2\pi^0$," Eur. Phys. J. A **51**, no. 8, 95 (2015).

[11] I. G. Aznauryan *et al.*, "Electroexcitation of Nucleon Resonances from CLAS Data on Single Pion Electroproduction," Phys. Rev. C **80**, 055203 (2009).

[12] R. G. Edwards *et al.*, "Excited State Baryon Spectroscopy from Lattice QCD," Phys. Rev. D **84**, 074508 (2011).

[13] M. Williams, "Measurement of Differential Cross Sections and Spin Density Matrix Elements along with a Partial Wave Analysis for $\gamma p \to p\omega$ using CLAS at Jefferson Lab," Ph. D. thesis, Carnegie Mellon University (2007).

[14] M. Gottschall *et al.*, "First Measurement of the Helicity Asymmetry for $\gamma p \to p\pi^0$ in the Resonance Region," Phys. Rev. Lett. **112**, 012003 (2014).

[15] K. A. Olive *et al.* (Particle Data Group), Chin. Phys. C **38**, 090001 (2015).

[16] M. Pichowsky, C. Savkli and F. Tabakin, "Polarization Observables in Vector Meson Photoproduction," Phys. Rev. C **53**, 593 (1996).

[17] K. Schilling, P. Seyboth and G. Golf, "On the Analysis of Vector-Meson Production by Polarized Photons," Nucl. Phys. B **15**, 397 (1970).

[18] J. Ballam *et al.*, "Vector-Meson Production by Polarized Photons at 2.8, 4.7, and 9.3 GeV," Phys. Rev. D **7**, 3150 (1973).

[19] R. W. Clift *et al.*, "Observation of a Baryon Exchange Dip and Parton Effects in Backward Photoproduction of ω," Phys. Lett. B **72**, 144 (1977).

[20] D. P. Barber *et al.*, "A Study of the Reactions Gamma P to Omega P and Gamma P to Omega Delta+," Z. Phys. C **26**, 343 (1984).

[21] M. Battaglieri *et al.*, "Photoproduction of the ω Meson on the Proton at Large Momentum Transfer," Phys. Rev. Lett. **90**, 022002 (2003).

[22] J. Barth *et al.*, "Low-Energy Photoproduction of ω-Mesons," Eur. Phys. J. A **18**, 117 (2003).

[23] M. Williams *et al.*, "Differential Cross Sections and Spin Density Matrix Elements for the Reaction $\gamma p \to p\omega$," Phys. Rev. C **80**, 065208 (2009).

[24] M. Williams *et al.*, "Partial Wave Analysis of the Reaction $\gamma p \to p\omega$ and the Search for Nucleon Resonances," Phys. Rev. C **80**, 065209 (2009).

[25] A. Wilson *et al.*, "Photoproduction of ω Mesons off the Proton," Phys. Lett. B **749**, 407 (2015).

[26] I. I. Strakovsky *et al.*, "Photoproduction of the ω Meson on the Proton Near Threshold," Phys. Rev. C **91**, no. 4, 045207 (2015).

[27] J. Ajaka *et al.*, "Evidence for Nucleon-Resonance Excitation in ω-Meson Photoproduction," Phys. Rev. Lett. **96**, 132003 (2006).

[28] F. Klein *et al.*,"Beam Asymmetries in Near-threshold ω Photoproduction off the Proton," Phys. Rev. D **78**, 117101 (2008).

[29] V. Vegna *et al.*, "Measurement of the Σ Beam Asymmetry for the ω Photoproduction off the Proton and the Neutron at the GRAAL Experiment," Phys. Rev. C **91**, 065207 (2015).

[30] H. Eberhardt *et al.*, "Measurement of Double Polarisation Asymmetries in ω-Photoproduction,"

[31] Q. Zhao, "Nucleonic Resonance Excitations with Linearly Polarized Photons in $\gamma p \to \omega p$," Phys. Rev. C **63**, 025203 (2001).

[32] A. I. Titov and T. S. H. Lee, "Effective Lagrangian Approach to the ω Photoproduction Near Threshold," Phys. Rev. C **66**, 015204 (2002).

[33] G. Penner and U. Mosel, "Vector meson production and nucleon resonance analysis in a coupled-channel approach for energies $m_N < \sqrt{s} < 2$ GeV. II. Photon-induced results," Phys. Rev. C **66**, 055212 (2002).

[34] V. Shklyar *et al.*, "Coupled-channel analysis of ω-meson production in πN and γN reactions for c.m. energies up to 2 GeV," Phys. Rev. C **71**, 055206 (2005).

[35] I. Denisenko *et al.*, "N^* Decays to $N\omega$ from New Data on $\gamma p \to \omega p$," Phys. Lett. B **755**, 97 (2016).

[36] W. Roberts and T. Oed, "Polarization Observables for Two-Pion Production off the Nucleon," Phys. Rev. C **71**, 055201 (2005) [nucl-th/0410012].

[37] B. Krusche and S. Schadmand, "Study of Non-Strange Baryon Resonances with Meson Photoproduction," Prog. Part. Nucl. Phys. **51**, 399 (2003).

[38] J. A. Gomez Tejedor and E. Oset, "Double Pion Photoproduction on the Nucleon: Study of the Isospin Channels," Nucl. Phys. A **600**, 413 (1996).

[39] L. Y. Murphy and J. M. Laget, DAPHNIA/SPhN 96-10 (1996).

[40] K. Ochi *et al.*, "Photoabsorption on a Nucleon in the D(13) Resonance Energy Region," Phys. Rev. C **56**, 1472 (1997).

[41] S. Strauch *et al.* [CLAS Collaboration], "Beam-Helicity Asymmetries in Double-Charged-Pion Photoproduction on the Proton," Phys. Rev. Lett. **95**, 162003 (2005) [hep-ex/0508002].

[42] D. Krambrich *et al.* [Crystal Ball at MAMI Collaboration], "Beam-Helicity Asymmetries in Double Pion Photoproduction off the Proton," Phys. Rev. Lett. **103**, 052002 (2009).

[43] J. Ahrens *et al.* [GDH and A2 Collaborations], "First measurement of the helicity dependence for the $\gamma p \to p\pi^+\pi^-$ reaction," Eur. Phys. J. A **34**, 11 (2007).

[44] C. Hanretty, "Measurement of the Polarization Observables I^s and I^c for $\vec{\gamma}p \to p\pi^+\pi^-$ using the CLAS Spectrometer," Ph.D. thesis, Florida State University (2011).

[45] `https://www.flickr.com/photos/jeffersonlab/`.

[46] M. Crofford *et al.*, "The RF System for the CEBAF Polarized Photoinjector". Technical Report, Thomas Jefferson National Accelerator Facility, 1993.

[47] `http://education.jlab.org/sitetour/guidedtour05.1.alt.html`.

[48] U. Timm, "Coherent Bremsstrahlung of Electrons in Crystals," Fortschritte der Physik, 1969.

[49] `http://nuclear.gla.ac.uk/~clasg8/linpol/1330-1360PARA.gif`.

[50] W. J. Briscoe *et al.* NSF Major Research Instrumentation, NSF Award 9724489. Technical report.

[51] D. I. Sober *et al.*, "The Bremsstrahlung Tagged Photon Beam in Hall B at JLab," Nucl. Instrum. Meth. A **440**, 263 (2000).

[52] C. D. Keith *et al.*, "The Jefferson Lab Frozen Spin Target," Nucl. Instrum. Meth. A **684**, 27 (2012) [arXiv:1204.1250 [physics.ins-det]].

[53] `https://userweb.jlab.org/~ckeith/Frozen/Frozen.html`.

[54] B. A. Mecking *et al.*, "The CEBAF Large Acceptance Spectrometer (CLAS)," Nucl. Instrum. Meth. A **503**, 513 (2003).

[55] `https://www.jlab.org/Hall-B/album/`.

[56] S. Taylor *et al.*, "The CLAS Start Counter", Nucl. Instr. Meth. A **462**, 484 (2001).

[57] M. D. Mestayer, "The CLAS Drift Chamber System," Nucl. Instr. Meth. A **449**, 81 (2000).

[58] E. Smith *et al.*, "The Time-of-Flight System for CLAS," Nucl. Instr. Meth. A **432**, 265 (1999).

[59] N. Walford, "The Search for Missing Resonances in $\gamma p \to K^+ + \Lambda$ and $K^+ + \Sigma^0$ using Circularly Polarized Photons on a Transversely Polarized Frozen Spin Target," Ph.D. thesis, Catholic University of America (2014).

[60] E. Pasyuk, "A Brief User Guide to GPID," CLAS Note 2007-008 (2007).

[61] A. Netz, TOF offsets in FROST-g9b,
`https://www.jlab.org/Hall-B/secure/g9/anetanet/Mean_Delta_TOF_Per_Paddle.pdf`.

[62] F. Klein, clas for TOF corrections,
`https://clasweb.jlab.org/rungroups/g9/wiki/index.php/TSCtimeCorr`.

[63] F. Klein, Procedure for TOF Corrections,
`https://clasweb.jlab.org/rungroups/g9/wiki/index.php/G9b_TOF_problems`.

[64] S. Strauch, "Hydrogen Content of the C12 and CH2 Targets" https://clasweb.jlab.org/rungroups/g9/wiki/index.php/Steffen%27s_analysis_page.

[65] M. Williams, C. A. Meyer, "Kinematic Fitting in CLAS," CLAS Note 2003-017 (2003).

[66] E. Pasyuk, "Energy Loss Corrections for Charged Particles in CLAS," CLAS Note 2007-016 (2007).

[67] S. Stepanyan *et al.*, "Energy Calibration of the JLab Bremsstrahlung Tagging System," Nucl. Instrum. Meth. A **572**, 654 (2007) [physics/0608302 [physics.ins-det]].

[68] M. Dugger, C. Hanretty, "Correction to the Incident Photon Energy for g8b Data," CLAS Note 2009-030 (2009).

[69] M. Dugger, P. Roy, N. Walford, "Momentum Corrections for π^+ and Protons in g9b Data," CLAS Note 2013-011 (2013).

[70] H. Olsen and L. C. Maximon,"Photon and Electron Polarization in High-Energy Bremsstrahlung and Pair Production with Screening," Phys. Rev. **114**, 887 (1959).

[71] K. Livingston, "Polarization from Coherent Bremsstrahlung Enhancement," CLAS Note 2011-020 (2011).

[72] K. Livingston, http://nuclear.gla.ac.uk/~kl/g8b/linpol/polarization.html.

[73] M. Anderson, K. Livingston, "Fits to g9b Polarization Enhancements" http://nuclear.gla.ac.uk/~marka/g9b_pol_plots/beamPolPass1.html.

[74] Polarization of Circularly Polarized Photon Beam in g9b, https://clasweb.jlab.org/rungroups/g9/wiki/index.php/Circular_Beam_Polarization. polarisation," Nucl. Instrum. Meth. B **211**, 465 (2003).

[75] S. Park, "Measurement of Polarization Observables in $\vec{\gamma}\vec{p} \to p\pi^+\pi^-$ using Circular Beam and Longitudinal Target Polarization and the CLAS Spectrometer at Jefferson Laboratory," Ph.D. thesis, Florida State University (2013).

[76] Y. Mao, "Determination of the Target Polarization for g9b from NMR Measurements," https://www.jlab.org/Hall-B/secure/g9/yuqing/CLAS_note.pdf.

[77] R. Tucker B. G. Ritchie and M. Dugger, "Analysis of g9b Target Offset Angle," CLAS note 2014-001 (2014).

[78] R. Tucker, "Spin Observables in η Meson Photoproduction on the Proton," Ph. D. thesis, Arizona State University (2016).

[79] J. Ball and E. Pasyuk, "Photon Flux Determination through Sampling of "Out-of-Time" Hits with the Hall B Photon Tagger," CLAS note 2005-002 (2005).

[80] M. Dugger, B. G. Ritchie, "DRAFT of CLAS-note: Phase Space Dependent Scale Factors for FROST g9a Data."

[81] M. Williams, M. Bellis and C. A. Meyer, "Separating Signals from Non-Interfering Backgrounds using Probabilistic Event Weightings," arXiv:0804.3382 [physics.data-an].

[82] W. Verkerke, D. Kirkby, "RooFit Users Manual v2.91," Document version 2.91-33, October 14th (2008).

[83] D. G. Ireland, "Extracting Polarization Observables in Pseudoscalar Photoproduction Reactions," CLAS note 2011-010 (2011).

[84] Ken Livingston, "Procedure for Extracting Σ and G Making the Best of all Available Data," `http://www.nuclear.gla.ac.uk/~kl/G/G4.pdf`

[85] A. Netz, "Different Run Periods Comparison," `https://www.jlab.org/Hall-B/secure/g9/anetanet/FROST_062515.pdf`.

[86] M. Dugger, "Study of T Asymmetry for Different Run Sets," `https://userweb.jlab.org/~dugger/frost/setStudyV3.pdf`.

[87] C. S. Akondi *et al.* [A2 at MAMI Collaboration], "Measurement of the Transverse Target and Beam-Target Asymmetries in η Meson Photoproduction at MAMI," Phys. Rev. Lett. **113**, no. 10, 102001 (2014).

[88] A. Bock *et al.*, "Measurement of the Target Asymmetry of η and π_0 Photoproduction on the Proton," Phys. Rev. Lett. **81**, 534 (1998).

BIOGRAPHICAL SKETCH

I was born in Jodhpur, a city in the Thar Desert of Rajasthan, India. My childhood was spent in about 10 different places in India due to my father's occupation as an Air Force officer. I received my high school degree from Air Force Golden Jubilee Institute, New Delhi in 2004. In school, I was mostly interested in physics and applied mathematics, so I decided to pursue a Bachelor of Science degree in physics.

I was offered admission for the same at Miranda House college in the University of Delhi, where I spent three wonderful years learning more about science. During my time at Miranda House, I competed at the All India level to seek admission in a Master of Science program in one of the most prestigious Indian universities, and was overjoyed to receive an offer from the Indian Institute of Technology Kanpur (IIT Kanpur). In 2008, I completed my Bachelor degree securing third rank in B.Sc. Physics (Honors) at the university level, and joined IIT Kanpur later that year.

Close to the completion of my first year in the M. Sc. program, I started exploring various research opportunities in India. In summer 2009, I was selected for the Visiting Students' Research Program at Tata Institute of Fundamental Research in Mumbai where I spent my summer studying absorption in semiconductors using photo-thermal deflection spectroscopy. After coming back, I started working on my Masters thesis for which I utilized a home-made Scanning Tunneling Microscope with the ability for *in-situ* annealing of samples to study the properties of Bismuth Telluride topological insulator. Simultaneously, I began applying for admission in doctoral programs within as well as outside India.

Upon graduation with a Master of Science degree from IIT Kanpur in 2010, I joined the doctoral program at the Department of Physics, Florida State University in the Fall of that year. For the first two years, I worked at a Molecular Beam Epitaxy facility at the National High Magnetic Field Laboratory. Our work led to a publication in 2013 in the Nature Communications journal (M. P. Warusawithana, C. Richter, J. A. Mundy, P. Roy *et al.*, Nat. Commun. **4**, 2351 (2013)).

Towards the end of 2012, I switched my field of research and joined the hadronic physics group with Professor Volker Crede as my thesis advisor, which naturally led to the work presented here. Over the course of this work, I gave several talks: an invited talk at the Excited QCD workshop in

Portugal, a Plenary talk at the CLAS collaboration meeting in 2016, four contributed talks including two at International conferences, and two seminar talks at Florida State University. In April 2015, I was awarded the John. D. Fox award in nuclear physics by the Department of Physics at Florida State University for my work. In 2016, I published a peer-reviewed conference proceedings in "AIP Conf. Proc. **1735**, 040009 (2016)". My research was approved by the CLAS collaboration in May 2016 and several papers as a result of this analysis are currently in preparation.